Hyperpolarized noble gas magnetic resonance imaging of the *ex vivo* rodent lung

by

Dr. David M.L. Lilburn, BSc., MB.ChB., MSc.

Sir Peter Mansfield Magnetic Resonance Centre

School of Medicine

Thesis submitted to the University of Nottingham

for the degree of Doctor of Philosophy,

July 2015

List of contents

Abstract

The work described within this thesis was conducted at the University of Nottingham between April 2011 and March 2014. Due to the inter-disciplinary nature of this work it was undertaken by the author in conjunction with the other scientists in the Translational Imaging group at the Sir Peter Mansfield Magnetic Resonance Centre, University of Nottingham and collaborators in both the Pulmonary Biology group, University of Nottingham and the Respiratory Pharmacology group, Imperial College London.

Pulmonary hyperpolarized (hp) noble gas magnetic resonance imaging (MRI) has seen increasing development and utility over the past two decades. However the application of this relatively new pulmonary imaging modality to small animal models is technically challenging. *Ex vivo* lung models have allowed for the investigation of functional respiratory measurements in small animals but have yet to be utilized with hp noble gas MRI.

The *ex vivo* lung model presented within this work allowed for the study of pulmonary physiology using hp ^{129}Xe and hp ^{83}Kr MR imaging in intact lungs from both healthy rodents and rat models of respiratory disease. Novel hp ^{129}Xe imaging protocols were developed to provide measurements of functional respiratory parameters and to gather information of regional gas distribution in healthy excised rodent lungs. Furthermore the developed ^{129}Xe methodology was used to study regional responses in an *ex vivo* model of human asthma after intravenous deliveries of increasing quantities of the bronchoconstricting agent methacholine.

The *ex vivo* model provided the platform to develop the novel lung imaging technique of hp ^{83}Kr surface quadrupolar relaxation (SQUARE) MRI with this new methodology used to study an excised rat model of emphysema potentially providing the first application for this quadrupolar noble gas isotope in the field of respiratory medicine.

PUBLCIATIONS RESULTING FROM THESIS:

1. Lilburn D M L, Pavlovskaya G E and Meersmann T 2013 Perspectives of hyperpolarized noble gas MRI beyond He-3 *J Magn Reson* 229 173-86
2. Lilburn D M L, Hughes-Riley T, Six J S, Stupic K F, Shaw D E, Pavlovskaya G E and Meersmann T 2013 Validating Excised Rodent Lungs for Functional Hyperpolarized Xenon-129 MRI *PLOS ONE* 8
3. Six J S, Hughes-Riley T, Lilburn D M, Dorkes A C, Stupic K F, Shaw D E, Morris P G, Hall I P, Pavlovskaya G E and Meersmann T 2013 Pulmonary MRI contrast using Surface Quadrupolar Relaxation (SQUARE) of hyperpolarized Kr *Magn Reson Imaging*
4. Hughes-Riley T, Six J S, Lilburn D M, Stupic K F, Dorkes A C, Shaw D E, Pavlovskaya G E and Meersmann T 2013 Cryogenics free production of hyperpolarized Xe and Kr for biomedical MRI applications *J Magn Reson* 237C 23-33

GLOSSARY OF COMMONLY USED TERMS AND ABBREVIATIONS

Hp	Hyperpolarized
MRI	Magnetic Resonance Imaging
NMR	Nuclear Magnetic Resonance
I	Nuclear Spin
γ	Gyromagnetic ratio of a nuclear spin
h	Planck's Constant ($6.62606957 \times 10^{-34}$ J s)
w_0	Larmor Frequency
^{1}H	Proton
^{3}He	Helium-3
^{129}Xe	Xenon-129
SEOP	Spin Exchange Optical Pumping
P_{app}	Apparent Polarization
FOV	Field of View
SNR	Signal-to-Noise Ratio
TE	Echo Time
TR	Repetition Time
FLASH	Fast-Low-Angle-Shot
VFA	Variable Flip Angle
CT	Computed Tomography
SPECT	Single Photon Emission Computed Tomography
PET	Positron Emission Tomography
RV	Residual Volume
FRC	Functional Residual Capacity
TLC	Total Lung Capacity

VC	Vital Capacity
AHR	Airway Hyper-Responsiveness
V_i	Volume Inhaled
V_S	Suction Volume (applied to the artificial pleural cavity)
V_B	Hp Storage Volume (in transfer line located below the breathing apparatus)
MCh	Methacholine
OVA	Ovalbumin
PBS	Phosphate Buffer Solution
BAL	Bronchoalveolar Lavage
S/V	Surface-to-Volume Ratio
COPD	Chronic Obstructive Pulmonary Disease
MAA	Mean Alveolar Area

ACKNOWLEDGEMENTS

The work contained within this thesis would not have been possible if not for the numerous people who have helped through either direct assistance or the significant amount of encouragement and moral support I have received during the past 3 years. You know who you are. I owe you all my heartfelt thanks. I am greatly indebted to you all for your kindness, generosity, good humour and fellowship.

I would however specifically like to thank my supervisors Dr. Dominick Shaw and Prof. Thomas Meersmann for their help, guidance and hard-work during the term of this thesis. I know it has not always been easy but with a lot of blood, sweat and a few tears it has finally come to fruition.

I would also like to thank my close friends and laboratory colleagues Dr. Karl Stupic, Mr. (now Dr.) Joseph Six, and Mr. (also now Dr.) Theodore Hughes-Riley. All of you have been dear to me over the past few years and without you guys it would have been far, far more difficult and much less rewarding. Please know that wherever we all end up, each one of you has a friend in whom you can trust to be there if ever you need me.

I would also like to thank Ms. Clémentine Lesbats and wish you the best of luck with continuing the work we have started- I look forward to seeing the *in vivo* images in print in the not-too-distant future. Thank-you also to Dr. Galina Pavlovskaya for technical assistance, useful discussions, and the development of some of the experimental apparatus. I would also like to thank Clive Dixon, Mike Olsen, Ian Taylor, and particularly Alan Dorkes for the fabrication of specialized glassware and equipment used in this work.

Finally, I would like to thank my grandmother Mrs. Anne Croft. You have been there for me through everything- I would not be where I am without your help, care and straightforward attitude to life.

DEDICATION

In loving memory of Ann Cecilia Lilburn

Chapter 1: Introduction

1.1. Motivation

1.1.1. The burden of lung disease

Lung disorders form a large part of the burden of human disease worldwide with respiratory diseases amongst the leading causes of death [1] and accounting for ~7% of all hospital admissions in European countries [2]. By 2030 it is expected that this burden will rise and that one in five deaths worldwide will be caused by respiratory disease [1].

The study of functional respiratory parameters has proven important in both the diagnosis and monitoring of human lung disease due to the close link between alteration in lung function and underlying structural change [3]. With the absence of current alternative methods to study function in the intact organ, the use of animal models is necessary.

1.1.2. Small animal models in the study of respiratory disease

Small animal models of respiratory disease, typically utilizing members of the lowest order of the mammalian clade, *rodentia*, including mice, rats, guinea pigs and rabbits, have been widely used in the development of new pharmacological treatments and in safety pharmacology and toxicological testing [4-7]. Rodent models in particular have allowed for rapid

throughput investigation in the study of respiratory disease because of the relative ease in setting up and the comparatively low costs due to the animals' small size and short lifecycles.

Much of the study of lung function in small animals has involved the use of techniques initially developed in humans and other large mammals. However, the downscaling has resulted in additional requirements for sensitive, highly precise equipment with measurements *in vivo* proving technically challenging [4, 5, 8, 9].

By comparison, several investigators have utilized *ex vivo* rodent lung models to study lung ventilatory physiology [10-12], lung vascular function [13-15] and the monitoring of inflammatory responses to noxious stimuli [16-19]. In addition isolated and perfused murine lungs have been used to investigate the pharmacokinetics of inhaled aerosols [20, 21].

1.1.3. Hyperpolarized noble gas magnetic resonance imaging (MRI)

The study of hyperpolarized (hp) noble gas MRI techniques has similarly seen the necessary downscaling to take advantage of small animal models of disease in the quest to provide new biomarkers. This has had the effect of further increasing the complexity and cost of already technically demanding lung function experiments in small animals [22, 23], limiting the application of this imaging modality in animal models to a few, highly specialized, research centres.

1.1.4. Purpose of this thesis

The purpose of this thesis is threefold. Firstly, it will demonstrate that the *ex vivo* model offers the opportunity to reduce the experimental complexity of hp noble gas MRI in small animal models, facilitating the rapid development and testing of novel imaging protocols and technologies. Secondly, it will be shown that the *ex vivo* rodent lung model permits the study of lung structure and function in healthy and disease models with hp noble gas MRI and that the combination provides additional benefits and insights beyond those already acquired using *in vivo* techniques. Finally this thesis will demonstrate the intrinsic usefulness of hp gas MR imaging as a tool to study respiratory disease, able to further the understanding of pulmonary disease and assist with the development of new therapies.

1.2. Basic anatomy and physiology of the lung

There are an extensive number of texts on the subject of mammalian lung anatomy and physiology (see for example [24-28]) but in this section there will be a brief overview of the points most pertinent to understand the relationship between lung structure and function. A particular focus will be on the rat lung as this is the species most used in this thesis.

The primary function of the lung is for gas exchange, that is, to allow the free diffusion of oxygen (O_2) from the air and the elimination of carbon dioxde (CO_2) from venous blood [26]. To this end the lung has evolved into an organ that, in health, allows the easy passage of air from the upper respiratory tract to the distal airways where the key respiratory unit of the alveolus is found, across which gas diffusion occurs.

The rat respiratory system illustrated in Fig. 1.1 consists of the upper airways of the nasal and oral cavities, pharynx and larynx and the series of successively branching tubes of the conducting airways starting with the trachea and ending with the respiratory bronchioles in the terminal respiratory unit of the acinus (See Fig. 1.2). With each successive airway branching in the conducting airway there is a reduction in cross section and length and an increase in the level of airway smooth muscle. In rats there are around 16 branchings [29] until the highest order of terminal bronchioles after which the respiratory zone begins. These conducting airways do not take part in gas exchange and make up part of the

anatomical dead space. Table 1.1 illustrates the comparative anatomy of the human and rat lung.

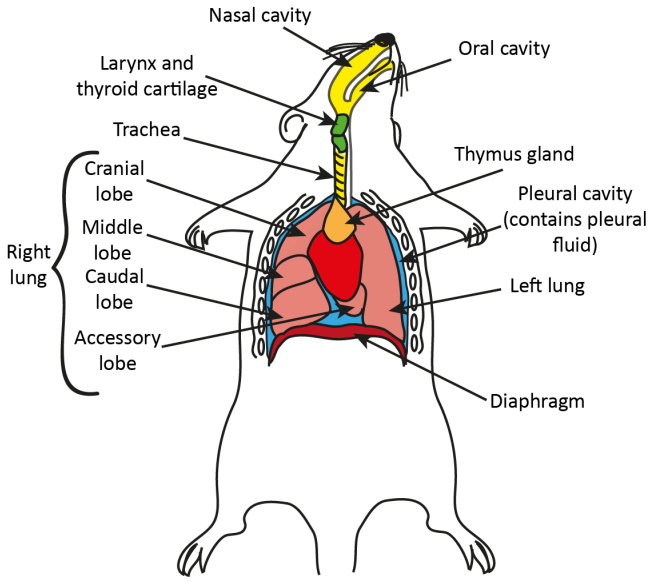

Figure 1.1. Anatomy of the rat respiratory system.

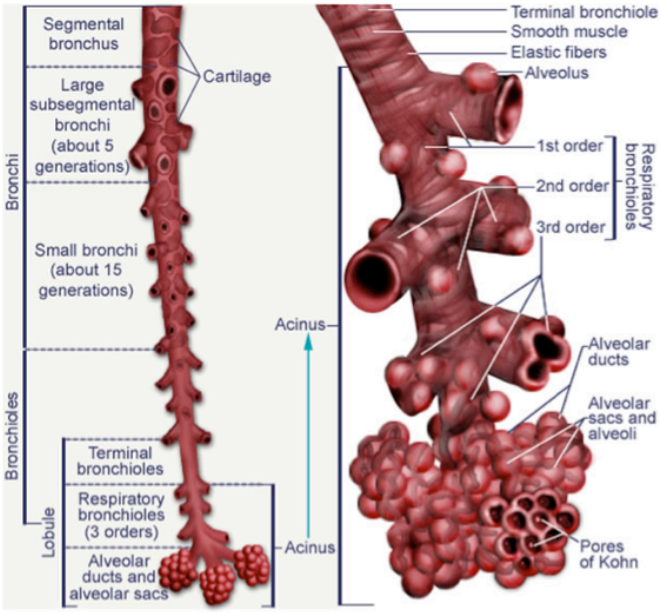

Figure 1.2. Branching of airways in the human lung from segmental bronchi to respiratory bronchioles and termination in alveolar sacs. Note the reduction in cartilage from segmental bronchus to the bronchioles where no cartilage is found. The alveoli communicate within alveolar ducts and the Pores of Kohn in the alveolar sacs themselves. Reproduced with permission form [30].

The acinus starts with respiratory bronchioles off which there are small numbers of alveolar buds. Respiratory bronchioles, present in human airways but not in rodents, then branch into alveolar ducts where alveolar budding is more numerous. The acinus finally terminates in clusters of alveoli called alveolar sacs where the surface area for gas exchange is the greatest.

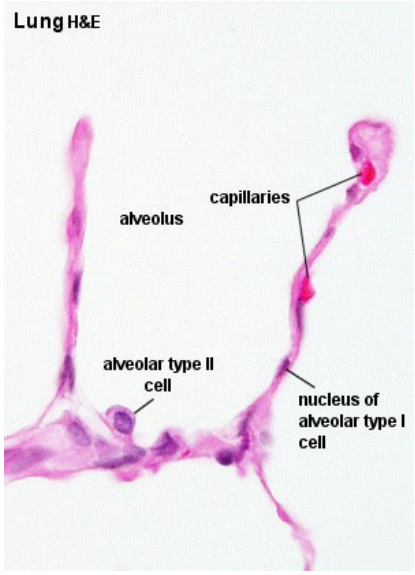

Figure 1.3. Histological structure of the human alveolus. Light microscopy image stained using haematoxylin and eosin (H&E) demonstrating principle cellular components. Note the cuboidal shape with the thin walls composed of type I and type II alveolar cells. Reproduced with permission from [31].

The alveolus is the key unit for gas exchange (Fig. 1.3). The mean diameter of alveoli in rats varies with age and between strains but is generally considered to measure 90 μm in mature rats when inflated to total lung capacity [32], compared to 270 μm in humans [33]. Several key features of the alveolus should be noted. Firstly the alveolus is roughly cuboidal in shape, rather than spherical as it is routinely depicted. Secondly, the alveolar wall is a very thin structure composed of type I and type II alveolar epithelial cells, the former being exceptionally delicate, providing the greatest surface for gas exchange, whilst the latter are largely thought to have a secretory and repair role [34]. Thirdly, the alveolus is

surrounded by an extensive capillary network where the capillary lumens are extremely narrow, being of the order of 7 – 10 μm, allowing for the passage of a single red blood cell at a time. The result of the above situation is to allow for the maximal uptake of O_2 from inside the alveolus into the blood plasma where the O_2 is rapidly absorbed by the haemoglobin in the red blood cell with CO_2 taking the opposite route.

	Human	**Rat**
Number lung lobes (numbers off left and right main bronchi)	5 in total (3 right / 2 left)	5 in total (4 right / 1 left)
Number generations large bronchi and conducting bronchioles	16	15*
Number terminal bronchioles	27,000 – 65,000#	2,500
Number generations of respiratory bronchioles until alveolar sacs	6 - 8	0
Alveolar diameter (μm)	270	90

Table 1.1. Comparison of human and rat lung anatomy. Values from references [26, 35, 36]. #Note: competing measurements currently available with wide ranges.

The vasculature of the lung is such that the full cardiac output, of around 85 mL/min/kg [26] in humans and 200 mL/min/kg in rats [37] passes through the low resistance pulmonary circulation with a low pulmonary arterial pressure. This situation allows the alveolar membrane to be incredibly thin but means that it is rather intolerant to increases in

pressure, with potential flooding of the alveolus if the capillary pressure rapidly increases.

The lung itself is a very elastic structure allowing it to expand during inspiration and contract by recoiling during resting expiration when the inspiratory pressures in the pleural cavity outside the lung have returned to resting (less negative) values. The thin structure of the alveoli would be inherently unstable if it were not for the fibrous support structures which pervade the entire lung [3] with: axial fibres to provide inward traction towards the hilum (lung root); peripheral fibres providing outward traction to the outer pleural lining; and septal fibres between the two. Collapse is also avoided by the inner surface of the alveolus being lined with secretions that smooth out surface irregularities and prevent epithelial damage through drying and microbial attack.

The surface tension of the internal fluid film would exert a significant resistance to expansion of the alveolus [26]. However, type II alveolar cells produce a substance called surfactant, composed of phospholipids and proteins, which is profoundly hydrophobic and so interrupts the fluid film lining the interior of the alveolus, reducing the surface tension particularly at end-expiration when alveolar volume is at a minimum [38].

The process by which inhaled gas gets to the alveoli, where gas exchange occurs, is ventilation. During inhalation the lung inflates with inspired gas as the result of an increase in the thoracic volume. Contraction and flattening of the diaphragm; and contraction of the external intercostal

muscles pulling the ribs upward and forward are the process by which thoracic volume normally increases. Expiration of gas during resting respiration is however principally a result of the passive elastic recoil of the chest wall and the lung itself with a return of the diaphragm to its' resting (dome-shape) dimensions. Control of ventilation rate and depth occurs by a variety of neural and local mechanisms [26] which as they are out-with the context of this thesis will not be covered further. The theory of ventilation will however be further developed under the relevant tests of lung function in section 1.3.

One final important concept in the study of lung physiology in the context of this thesis is that of airway tone. As mentioned, the airways are composed of varying degrees of airway smooth muscle (ASM). The degree of contraction of this muscle is an important determinant of airway resistance with changes brought about by a variety of mechanisms [39]. The parasympathetic cholinergic fibres of the vagus nerve provide a stable, relatively reversible, baseline level of ASM tone under normal circumstances [40] with tone regulated by, for instance, local irritant and pulmonary stretch receptors [26]. However factors beyond the vagal parasympathetic ganglion also affect changes in ASM tone [41]. Indirect sympathetic control via inhibition of parasympathetic ganglion neurones and β_2-adrenoceptors on the ASM themselves tends to counteract high levels of cholinergic activity [39], although further mechanisms have also been identified [41]. Measurement of airway tone with further detail on the theory will be covered in section 1.3.2.

1.3. Tests of lung function

As described earlier, tests of lung function initially devised for humans and large mammals have been adapted for use with small animals. There have often been several competing techniques devised to measure a certain aspect of lung function each with their own advantages and disadvantages [7, 42, 43]. The use of non-invasive measurements on conscious animals has the advantage that they are often quicker, easier, and repeatable over long studies with the animal being studied in a situation close to the normal physiological state. However, non-invasive measurements are often prone to artefacts due to animal movement and include the contribution of the upper airways producing uncertainty about the site and nature of any functional changes. Additionally, compared to performing the tests in man where a certain degree of cooperation with manoeuvres is available, in small animals certain manoeuvres such as prolonged breath holds or deep inspirations are simply not possible whilst the animal is conscious. Therefore the need for general anaesthesia and often paralysis with neuromuscular blocking drugs is necessary which themselves introduce changes in ventilation and smooth muscle tone .

1.3.1. Measurement of lung volumes

The most basic measurements of respiratory physiology are those of lung volumes. As can be seen from Fig. 1.4 the tidal volume (TV) is the volume of gas moved during resting steady state respiration and is usually around 1.5 mL in the 300g adult rat [44]. The total lung capacity (TLC) includes

the vital capacity (*VC*), the maximal amount of gas that can be expired (approximately 12.3 mL in the rat [45]), and the residual volume (*RV*), which includes the dead space gas (~1.2 mL in the adult rat [46]). The functional residual capacity (*FRC*) includes both the residual volume and the volume of gas expired during forced expiration from tidal volume (known as the expiratory reserve volume).

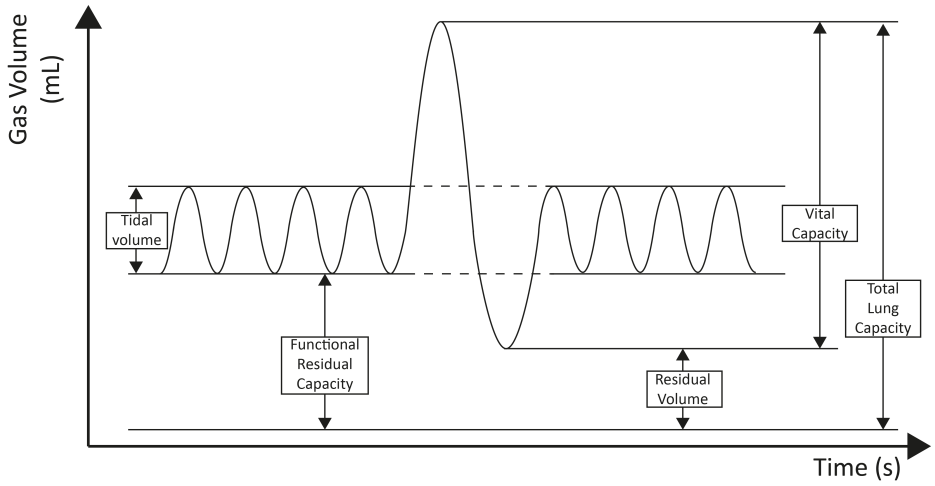

Figure 1.4. Schematized spirometric trace with time plotted against volume indicating the most commonly used measurements. Trace indicates initial normal resting breathing followed by a deep inspiration with full expiration and resumption of normal resting respiration.

The measurement of lung volumes in small animals normally necessitates the use of general anaesthesia and tracheal intubation either orotracheally or directly via a tracheostomy. In anaesthetized animals measurements of lung volumes are recorded at a particular total respiratory system pressure P_{rs}. *TLC* is normally measured while P_{rs} is in the range of 25 – 35 cm H_20 (≈ 2.5 – 3.5 kPa) [4]. *RV* is normally defined as the volume of gas left in the lungs when P_{rs} = -15 cm H_2O (≈ -1.5 kPa). *VC* is then often

characterized as the volume required to inflate the lungs between *RV* and *TLC* and is simply measured by a syringe or by integrating the signal from a pneumotachnograph during the manoeuvre [47]. Comparison of human and rat lung volumes are displayed in Table 1.2.

	Human	**Rat**
Total lung capacity (mL/kg)	80	40
Tidal volume (mL/kg)	7	6
Vital capacity (mL/kg)	65	35
Functional residual capacity (mL/kg)	30	11
Residual volume (mL/kg)	15	6

Table 1.2. Comparison of human and rat lung volumes adapted for total body weight. Values adapted from references [26, 35].

1.3.1.1. Measurement of *FRC* and *RV*

The measurement of FRC and RV necessitates the use of slightly more complicated methods involving either plethysmographic or gas dilution techniques.

Plethysmography

An example arrangement for the calculation of lung volumes using plethysmography is shown in Fig. 1.5. The system utilizes Boyle's law where the volume of a fixed quantity of gas at a constant temperature varies inversely with pressure. Therefore if the airway of the rat is occluded before the start of inspiration, the attempted inhalation will increase the volume in the chest, with a reduction in pressure in the airways, whilst the external pressure in the sealed box surrounding the animal will increase to the same degree. By simultaneously measuring the volume reduction in the box by a pneumotachnograph with the change in pressure in the box or directly across the thorax (the latter by an oesophageal pressure transducer) and the corresponding pressure measurement in the tracheal tube, it is possible to determine the volume inside the chest and hence the *FRC*. This technique can also be adapted to calculate the *RV* by closing the airway after forced expiration. It should however be noted that the plethysmographic techniques can underestimate the values of *FRC* and *RV* due to gas passing into the abdomen during inspiration against the closed airway [45].

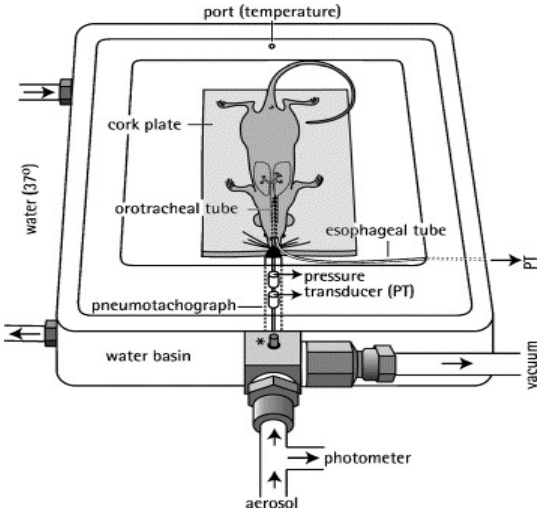

Figure 1.5. Schematic of a body plethysmography device for the rat. Note the intubated rat with use of a pneumotachnograph and pressure transducer (PT) for measurements of airway pressure. Note also the use of an oesophageal tube for measurement of transthoracic pressure. Reproduced with permission from [8].

Gas dilution techniques

The commonest methods to measure *FRC* and *RV* by the gas dilution technique use a tracer gas such as neon [46] or helium [48], which is largely insoluble in blood, therefore remaining in the airspaces. A syringe / spirometer containing a known volume of gas with a small concentration of the tracer is repeatedly inhaled / exhaled by the animal, producing equal concentrations between the lung and the spirometer. The reduction in the concentration of the gas is then used to calculate either the *RV or FRC* depending on how the animal has been ventilated.

1.3.2. Measurement of airway response

Tests of airway hyper-responsiveness (AHR) in small animals require dynamic measurements of lung function to be acquired during broncho-provocative challenges. In small animal models direct challenges of AHR have been the most commonly employed methods although there have been some studies of eucapneic hyperventilation [49] and AHR in relation to cold air [50] and exercise [51]. Direct AHR testing has been demonstrated to increasing quantities of bronchial smooth muscle agonists such as histamine or methacholine (MCh) [52-54] and specific allergens to which the animal has been sensitized [6, 55].

There are several measurements of dynamic lung function in use during broncho-provocation, some are widely accepted whereas others are subject to much debate [5, 7, 42, 56]. The main distinction between the methods is the need for general anaesthesia and invasive instrumentation of the airway.

1.3.2.1. Non-invasive methods

All non-invasive techniques involve the assessment of a conscious breathing animal during the bronchial reactivity challenges. There is inherently more variability in the results due to a combination of subjective factors (e.g. with the assessment of the features of bronchospasm) or with animal movement in the use of plethysmography.

Clinical assessment of bronchospasm

The time for the development of clinical features of bronchospasm such as an increase in the rate and depth of respiration and the time of the first cough (indicating severe bronchospasm) have previously been used [57]. However these measures are inherently difficult to quantify and are often near-lethal end-points with uncertain relevance [5]. Recently the use of the respiratory rate with development of signs of bronchospasm, namely wheeze on auscultation, as assessed by a skilled observer masked to the groups' treatment, has been utilized in a model of exercise-induced asthma in the rat [51]. Despite limited quantifiable data, there was a strong correlation between the severity of features and the treatment groups.

Unrestrained plethysmography- quantity enhanced pause (Penh)

As a development to improve quantifiable data in small animals under near normal conditions, there has been a resurgence in unrestrained plethysmography. The animal is free to move around the plethysmography chamber whilst the box pressure is monitored over prolonged periods of time [58]. Aerosolized bronchoprovocative challenges are delivered to the

chamber for periods of 2 – 5 minutes. The dimensionless quantity *Penh* is derived from the chamber pressures on inspiration and expiration as outlined in Fig. 1.6.

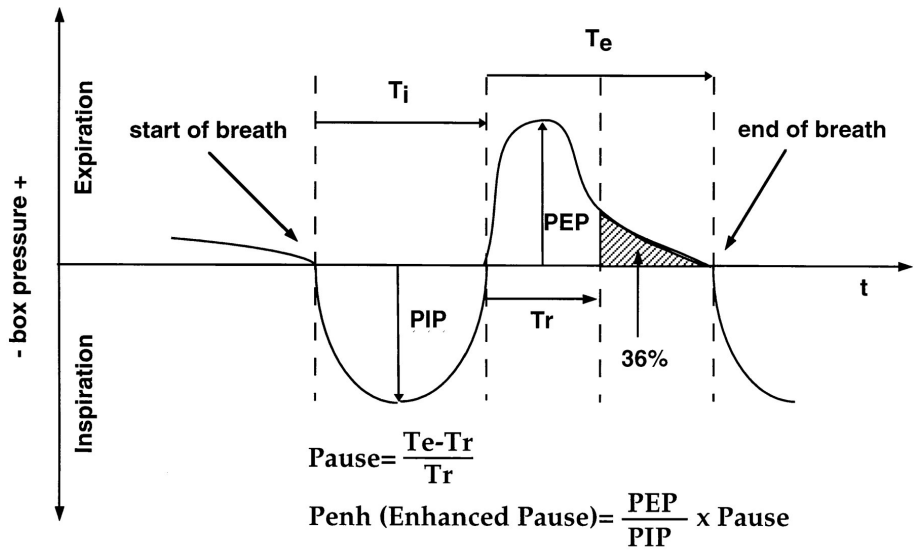

Figure 1.6. Schematic figure of the box pressure wave during the use of unrestrained plethysmography on inspiration and expiration. T_i (inspiratory time (s))- time from start of inspiration to end of inspiration; T_e (expiratory time (s))- time from end of inspiration to start of next the inspiration; *PIP* (peak inspiratory pressure (cm H_20))- maximal negative box pressure occurring during a breath; *PEP* (peak expiratory pressure (cm H_20))- maximal positive box pressure occurring during a breath; T_r (relaxation time (s))- time for the box pressure to decay to 36% of PEP. Reproduced with permission from [58].

Criticism of *Penh* has centred around the difficulty in separating changes in the pressure signal due to animal respiration and those due to changes in gas humidification and temperature as the air moves between the box and the lungs [7, 43, 59] although this can be improved by heating and humidifying the air in the box. More concerning however is the finding that

Penh varies with conditions such as hyperoxia and the timing of ventilation [60]. At present *Penh* is considered to be satisfactory for large scale screening of animals but concerns around its applicability persist.

Restrained plethysmography- tidal midexpiratory flow (EF_{50})

An alternative technique with widespread acceptance is restrained plethysmography on conscious animals. This forms the main battery of testing in safety pharmacology and toxicology studies [42]. The animal is restrained within the plethysmograph as illustrated in Fig. 1.7. The equipment can measure tidal volume (TV), expiratory time (T_e), inspiratory time (T_i), and breathing frequency (f) [61]. Nebulized bronchoprovocative agents are directed to the head exposure chamber after a period of acclimatization.

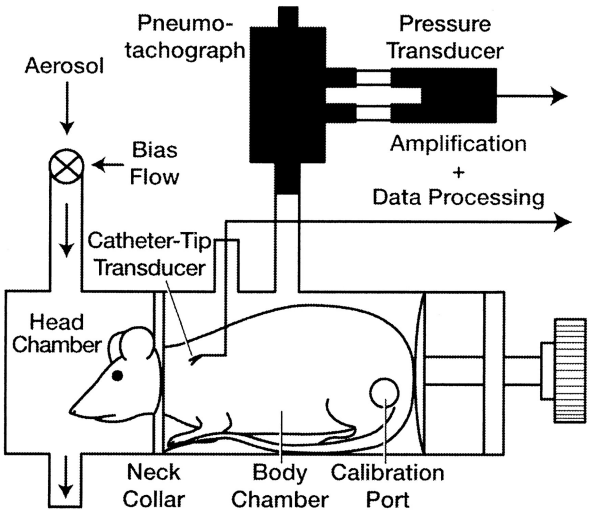

Figure 1.7. Restrained body plethysmography with head chamber exposure system for delivery of aerosolized agents. Changes in the body chamber pressure and volume on inspiration and expiration are recorded. Reproduced with permission from [61].

The key measurement derived from restrained plethysmography in the conscious animal is the tidal midexpiratory flow (EF_{50}) [61, 62]. This

measurement has been noted to correlate well with the 'gold-standard' invasive measurements of lung resistance (R_L) and dynamic lung compliance (C_{dyn}) and does not suffers from the difficulties found with *Penh* [63]. However, it should be noted that sample sizes required for this type of model are large due to significant variation, with recommendations to use at least n = 8 for safety pharmacology studies and n = 16 with asthma models [8].

1.3.2.2. Invasive methods

The use of invasive techniques requires the animal to be intubated and either free-breathing under general anaesthesia or treated with neuromuscular blocking drugs so that the whole respiratory cycle is controlled. Broncho-provocative challenges can be either administered via the aerosolized or intravenous routes. Often these studies are not suitable for repeat studies (unless satisfactory orotracheal intubation can be implemented) with animals usually sacrificed at the end of the procedure [5].

Measurement of airway tone

The simplest method of assessing response to broncho-provocation in the anaesthetized animal is by measuring global airway tone in the trachea [54, 64, 65]. This involves connecting a pressure transducer to the ventilation circuit recording changes in airway pressure before and during the challenge. A small refinement in the technique to stop harmful over-inflation with constant volume ventilation during airway challenges is to allow air overflow once a threshold pressure has been reached and measure the overflow by a pneumotachometer [66].

Plethysmographic assessment of lung resistance and compliance

As mentioned earlier, the 'gold-standard' measurements of lung resistance (R_L) and dynamic lung compliance (C_{dyn}) are the benchmark by which other techniques are measured. Lung compliance (C_L) is a measure of the ease of lung inflation [5, 6] and is dependent on the elasticity of the lung parenchyma and the surface tension forces described earlier. C_L is the gradient of the volume-pressure curve during inspiration. C_{dyn} by comparison is the measure of lung compliance when resistance to airflow may affect the result, such as in case of obstructive disease, therefore in normal lungs C_L and C_{dyn} are very similar. Lung resistance (R_L) is a measure of the frictional resistance to airflow and is the sum of R_{aw} (airway resistance) and R_{tiss} (resistance from the lung tissue). Quantification of R_L and C_{dyn} are usually obtained from measurements of transthoracic pressure recorded by an oesophageal pressure transducer [45] along with measurements of the volume changes within the plethysmography apparatus and flow through the tracheal tube, fitting to the equation:

$$P_{TP}(t) = \dot{V}(t) \times R_L + V(t) \div C_{dyn} + P_0 \quad [1.1]$$

where $P_{TP}(t)$ is the transpulmonary pressure, $\dot{V}(t)$ is the flow and $V(t)$ is the volume inspired at time t with P_o the end expiratory pressure. Airway resistance (R_{aw}) can be calculated if the tissue resistance is measured by using the alveolar capsular pressure [67].

Forced oscillation technique to assess lung resistance and compliance

The low frequency forced oscillation technique (LFOT) has developed as a less severe alternative to the very invasive and technically challenging measurements by plethysmography. The LFOT is able to provide measurements of airway resistance (R_{aw}) and inertance (I) and the peripheral lung tissue components of tissue damping (G) and elastance (H) which are closely related to R_{tiss} and C_{dyn} respecitvely. A brief review of the underlying theory and measurement techniques will be conducted here but for more detailed information the reader is referred to the extensive literature on the topic (see for example [7, 67-70]).

The LFOT compares the linear single-compartment lung model in Eq. 1.1 to the constant phase model of oscillatory data, therefore measuring lung impedence (Z_L):

$$Z_L(\omega) = R_{aw} + j\omega I_{aw} + (G - jH)/\omega^{\alpha} \quad [1.2]$$

where $Z_L(\omega)$ s the lung impedence measured at the angular frequency ω (related to the oscillatory frequency f by $\omega = 2\pi f$) and where $\alpha = (2/\pi)\arctan(H/G)$.

During the experiments a mechanical pressure wave is applied to the air in the lungs by either a mechanically driven piston / syringe (as in Fig. 1.8) [71] or by a plastic tube connected to loud speaker [69]. Alternatively the loud-speaker can be used non-invasively by adapting a body

plethysmography system, allowing the animal to remain conscious (but restrained) [7], however the contribution of the upper airways cannot then be separated, reducing the value of the measurement.

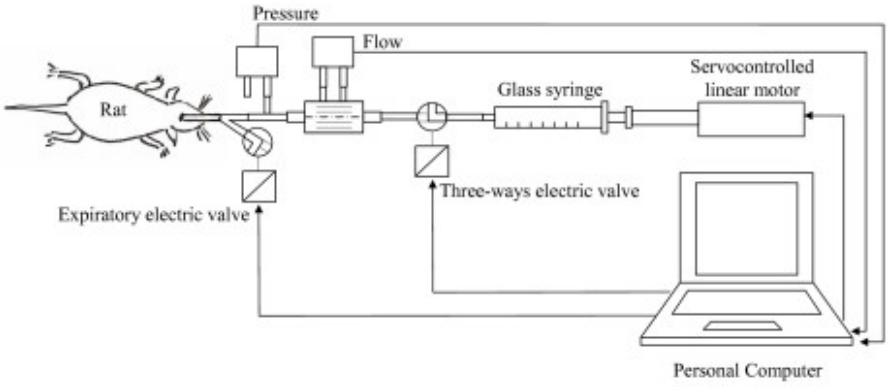

Figure 1.8. Schematic of LFOT technique used in the intubated rat. The Pressure waveform is generated in the servocontrolled syringe when the expiratory valve is closed at end expiration. Pressure and flow are recorded as shown. Reproduced with permission from [71].

At present the LFOT technique is believed to offer the most functional data on airway response with its' ability to partition the central and peripheral respiratory system. It should however be noted that the measurements of R_{aw}, I, G, and H are largely global with significant variation, often requiring large sample sizes [42].

1.3.3. Measuring distribution of ventilation

A key measurement of lung function is the distribution of ventilation, that is, being able to discern the proportion of gas volume from different lung regions. Lung function techniques without the use of imaging have only been able to provide limited information. An example is the single breath oxygen test (Fowler's method [26]) which monitors nitrogen (N_2) washout after breathing in 100 % O_2. From the timing and concentration of N_2 at different time points it is possible to determine where the gas originates (the conducting airways or the alveoli) and the point at which the alveoli open. It has been possible to detect differences in alveolar gas volume between healthy and elastase treated rats (emphysemastous damage) with this technique [72], but further information is limited.

1.3.4. Measuring gas exchange

Another important parameter in the study of lung function is the efficiency of the lungs to allow the passage of gas from the alveoli into the blood. The lung transfer factor (D_L) is a non-spatially resolved measurement initially developed in larger mammals [26]. In small animals this is adapted as the gas volumes are very small. A common method uses a test volume of gas containing a small concentration of carbon monoxide (CO) and an insoluble gas such as neon (Ne) [46]. After inhalation with a 10 s breathhold a sample of the exhaled gas is acquired from the alveolar region and analyzed for Ne and CO concentrations and the ratio used to calculate the transfer factor.

1.4. Lung imaging modalities in small animal models

The plethora of lung function tests highlights the fact that no one test is able to measure all the desired parameters, often requiring a combination of measurements to be performed. The limited regional information of the tests covered in section 1.3 demands further improvements. Consequently there has been increasing attention on the use of lung imaging modalities in small animal models [73]. It will be seen that the use of imaging modalities allows for monitoring of disease progression, often with minimal invasiveness, and the ability to gather increasing amounts of information in the same animal. This has led to the recent expansion of *in vivo* lung imaging facilities. Often the imaging techniques are used in conjunction with biochemical and histological biomarkers and/or the aforementioned *in vivo* measures of lung function. The most widespread functional lung imaging modalities in small animals are micro computed tomography (micro-CT) and magnetic resonance (MR) based. By comparison, nuclear medicine imaging modalities based on single photon emission computed tomography (SPECT) and positron emission tomography (PET) have been hampered by the limited temporal and spatial resolution of both techniques. Nonetheless, some functional information has been garnered by both SPECT and PET such as measurements of: regional gas distribution; ventilation–perfusion differences [74, 75]; permeability of the alveolar membrane [76, 77], and drug deposition and uptake [78, 79].

1.4.1. Micro computed tomography (micro-CT)

Computed Tomography (CT) has been the 'gold standard' of clinical lung imaging for the past 15 - 20 years, however the application of its use to small animal models has been a recent development due to advances in the underlying technology with the development of faster detectors [80] and the increase in dedicated systems for small animals [81]. Scan times of the thorax have been reduced to tens of seconds with resolution < 100 μm isotropic particularly with the successful development of respiratory and cardiac gating strategies [82-84] as breathing rates are normally > 60 breaths/min with heart rates exceeding 200 beats/min in rats (and even faster in mice). Further improvements in gating techniques have allowed for the imaging of free breathing non-intubated, non-ventilated animals [85-87].

Micro-CT uses the attenuation of x-rays by tissue to generate an image. The CT image is created by a series of projections taken at equally spaced angular intervals with the acquired data fed into a filtered back-projection algorithm for reconstruction [81]. Micro-CT produces a series of 2D slice images with voxel values of each image corresponding to the density of the tissue contained, measured in Hounsfield units (HU) with water at 0 HU, air −1000 HU and bone +1000 HU.

Micro-CT is capable of producing fine anatomical lung data, showing thickening in relation to inflammation or fibrosis [81], tumour

development [88], and characterization of airway calibre [89]. Measurements of *FRC* and *TV* in mice have been reported using the change in lung density during the respiratory cycle [86, 90].

Information on regional ventilation has improved with the development of xenon (Xe) enhanced CT, initially developed in larger mammals [91] and scaled down for use in small animals [92, 93]. The use of an inhaled Xe-O_2 mixture necessitates the use of general anaesthesia with intubation and ventilation. As Xe is highly soluble in tissues a correction is required for uptake into the lung parenchyma and blood. The net effect of inhaled Xe is to increase the density of lung tissue thereby improving resolution and further reducing scan times. Using this method it has been possible to image regional ventilation in rats, monitoring the wash-in of Xe on subsequent breaths and providing measurements of regional fractional ventilation, that is, mapping ventilation gradients across the lung [92].

A further recent improvement in micro-CT has been with the application of dual energy CT methods. In this methodology the x-ray absorption properties of heavy elements are utilised where the x-ray attenuation profile is dependent on beam energy [94]. Heavy elements therefore produce different results if two x-ray tube voltages are used and so can be discriminated from surrounding tissue. By simultaneously acquiring attenuation data from two x-ray sources at different voltages with the injection of a contrast agent such as iodine it is possible to improve the contrast of blood vessels and highly perfused tissue. In larger mammals inhaled Xe mixtures have also been used to produce similar contrast

within the lungs, producing data on regional ventilation [95]. Badea et al. simplified the technique by using a post-reconstruction three material decomposition method [96]. Simultaneous image data on air, tissue and blood fractions were produced at different ventilation volumes without the use of inhaled Xe in both *ex vivo* rat lungs and *in vivo* mice lungs with the use of iodinated contrast, however the radiation dose was considered too high for longitudinal studies.

1.4.2. Magnetic resonance imaging (MRI)

In contrast to some of the micro-CT methodologies, MRI with the absence of ionizing radiation allows repeated examinations over prolonged periods of time. In some animal models it is likely that this would be a significant factor as the administration of repeat high doses of radiation could confound the model [86, 97]. In addition the MR methods developed in animals have allowed for longitudinal and 4D imaging in human subjects [98].

However, conventional proton (^{1}H) MRI of the lungs aimed at studying the lung parenchyma has proven challenging, particularly in small animals. Several of the difficulties common to micro-CT including the management of motion artefacts have been resolved by the development of fast image acquisition techniques along with cardiac and respiratory gating technology similar to those used in micro-CT [22, 99-101]. However, the fundamental problems of the low tissue to volume ratio and local magnetic field inhomogeneities associated with the void space of the lungs, producing short T_2 and T_2* relaxation times (see Chapter 2), can result in low sensitivity [102].

Despite the significant difficulties, lung imaging strategies have been developed for proton MRI. Historically sequences used for imaging the lung parenchyma were variants of fast spin echo sequences, such as half fourier single-shot turbo spin echo (HASTE) usually with inversion

recovery preparation [103], where there is a short delay between excitation and acquisition. Resolution is low and there have been few studies in small animals where high magnetic fields are generally utilised [104]. However, fast gradient echo ultra-short echo time (UTE) sequences are also resistant to the susceptibility artefacts and are less time consuming [105]. UTE techniques are rapidly becoming adopted for proton MRI of the lung as hardware development has allowed for echo times ~100 μs or less [105-108]. At present UTE is performed without cardiac or respiratory gating in small animals with averaging over multiple scans, thus far it has not been possible to separate different portions of the respiratory cycle limiting functional information.

Methods utilising contrast agents have been studied to increase the functional information with lung MRI investigations. The use of inhaled paramagnetic contrast agents to shorten the longitudinal relaxation time (T_1) of tissue provides information about distribution of the substance and hence ventilation. In the lung this has mainly involved studies of gadolinium based contrast agents [109-113] and simple inhaled O_2 [114, 115]. Neither agent has yet seen widespread use in small animal models although with improvements in UTE this may be changing [107, 116]. Additionally, UTE imaging has recently been used with inhaled iron oxide nanoparticles to detect inflammation in a mouse model of bacterial lung inflammation [117].

Another method of improving contrast is to introduce a substance into the lung with a higher spin density, therefore increasing the available signal

from within the airspaces themselves. Several fluorinated gases have been investigated [118-120] with the use being recently reported in small mammals [121].

1.4.2.1. Hyperpolarized noble gas MRI

Hyperpolarized (hp) noble gas MRI of the lungs is as an alternative technique for imaging of the lung airspaces [122, 123]. The very high signal enhancement of the order of 10^5 compared to that obtained at thermal equilibrium (see section 2.2.3) permits high resolution images of ventilation compared to the aforementioned MR techniques which has resulted in the rapid adaption of these imaging techniques to the lungs in small animal models [22]. Helium-3 (^{3}He) with its large gyromagnetic ratio (γ), high diffusivity and ability to assume high levels of polarization has been extensively used in lung ventilation imaging studies and in the characterization of alveolar geometry in humans [124-126] with similar measurements available in small animal models [127, 128]. Additional noble gas isotopes, xenon-129 (^{129}Xe) and krypton-83 (^{83}Kr) have attracted increasing attention for hp pulmonary MRI applications partially due to the limited availability of ^{3}He but also because of the ability to interrogate additional physiological parameters [129-133]. The theory behind hp noble gas imaging with a review of the potential applications in small animal imaging will be provided in Chapters 2 and 3.

1.5. Thesis overview

The purpose of this thesis is to demonstrate the utility of hyperpolarized noble gas MRI of the *ex vivo* lung model and to demonstrate that new insights can be garnered from the combination of these technologies. With this in mind, Chapter 2 will illustrate the theoretical basis of MRI and hp noble gas MR imaging.

Following this, Chapter 3 will provide a description of the animal models of respiratory disease used within the context of this thesis, namely models of allergic asthma and emphysema,. This Chapter will also go onto provide a detailed appraisal of the challenges with *in vivo* hp noble gas MRI in small animal models and some of the work already conducted so as to put the *ex vivo* model in context.

Chapters 4 – 6 will then detail the experimental work contained within this thesis. Chapter 4 will document work on the use of the *ex vivo* lung model of healthy rodent lungs with hp ^{129}Xe MRI to study lung function while Chapter 5 continues this work with an *ex vivo* rat lung model of allergic asthma.

In Chapter 6 the novel technique, hp ^{83}Kr MRI, will be introduced which utilises the nuclear electric quadrupole moment to provide surface sensitive contrast [134, 135] not available with hp ^{129}Xe (or hp ^{3}He). This

novel technique is used within this thesis to study the lung microstructure of an *ex vivo* rat model of another obstructive lung disease, emphysema.

Chapter 2: Nuclear magnetic resonance and magnetic resonance imaging applied to hyperpolarized noble gases

2.1. Chapter aims

In order to be able to place the later original research into context it is necessary to understand the principles and concepts behind the methods in use. It is the aim of this chapter to provide the basic concepts of nuclear magnetic resonance (NMR) and magnetic resonance imaging (MRI) to enable an understanding of the details of the original research presented later in this thesis. For this theoretical framework well-established references were heavily utilized [136-139]. This framework then provides the understanding required to explain the methods involved in hyperpolarized (hp) gas imaging where there is a necessary focus on the biomedical techniques and applications. A large part of the review of hp gas imaging is drawn from the peer-reviewed work published in the Journal of Magnetic Resonance article "Perspectives of Hyperpolarized Noble Gas MRI beyond ^{3}He" [133]. Further theoretical background for individual experiments will be provided where necessary in the subsequent chapters.

2.2. Nuclear magnetic resonance (NMR)

2.2.1. Nuclear spin

Nuclei are made up of elementary particles and so possess a quantity called spin (I). Spin values can be integer, half-integer or zero. Nuclei with an odd atomic number or an odd atomic mass number have non-zero spin values and so possess angular momentum and are therefore said to be spin active. Quantum mechanics shows that there are $2I + 1$ possible spin values, ranging from $+I$ to $-I$ so that for $I = 1/2$ nuclei the possible spin values are +1/2 or -1/2. NMR arises from transitions between these nuclear spin energy levels in the presence of a magnetic field.

Nuclei with $I > 1/2$ have an electric quadrupole moment due to the non-spherical distribution of the nucleus resulting in short lifetimes of the nuclear magnetic states because there are magnetic and electric influences on the reorientation of the nucleus in a magnetic field. These quadrupolar nuclei are however sensitive to electric field gradients (EFGs) which shorten the lifetime of the nuclear magnetic state further.

The most commonly used isotope for NMR spectroscopy and MRI is ^{1}H ($I = 1/2$) due to its high natural abundance and its presence in water and other organic molecules. In this thesis, however, nuclei other than ^{1}H are studied, namely ^{129}Xe ($I = 1/2$) and ^{83}Kr ($I = 9/2$). The physical properties of these nuclei compared to ^{1}H and ^{3}He are displayed in Table 2.1.

Nucleus	Spin (I)	Natural abundance (%)	Gyromagnetic ratio (10^6 rad s^{-1} T^{-1})	Resonance frequency at 9.4 T (MHz)
^{1}H	1/2	99.9885	267.52213	400.2282
^{3}He	1/2	0.000137	-203.80159	-304.8987
^{83}Kr	9/2	11.49	-10.3310	-15.4556
^{129}Xe	1/2	26.44	-74.52103	-111.4877

Table 2.1. Physical properties of ^{129}Xe and ^{83}Kr with ^{1}H and ^{3}He for comparison. Values adapted from [140].

A spin active nucleus will display a magnetic moment, μ measured in J T^{-1}, given by:

$$\boldsymbol{\mu} = \gamma \hbar \left[I(I+1) \right]^{1/2} \qquad [2.1]$$

where $\hbar$ is the Planck's constant divided by 2π (1.054571726× 10^{-34} J s). The energy of the magnetic moment in the presence of a magnetic field of strength B (measured in Tesla (T), where 1 T = 10^4 Gauss) is given by:

$$U = -\boldsymbol{\mu}.\boldsymbol{B} \qquad [2.2]$$

where U is the energy in Joules (J). By defining the field B_0 to be along the z-axis the equation reduces to $U = -\mu_z B_0$ with μ_z the component of μ parallel to B_0. The energy of the system then becomes:

$$U = -\gamma \hbar m_z B_0 \qquad [2.3]$$

where m_z is the quantised value of the energy state corresponding to *I*, with $m_z = -I, -I+1, ..., I, I-1, I$. For spin *I* = 1/2 nuclei, there are 2 energy

levels available with $m_z = -1/2$ or $m_z = +1/2$ as shown in Fig. 2.1. The spin energy levels are degenerate but with the application of an external magnetic field separate, a process known as Zeeman splitting.

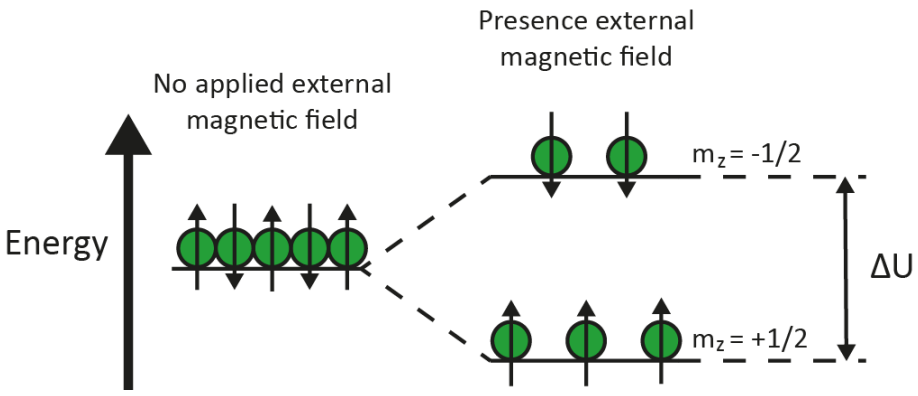

Figure 2.1. Energy level diagram for *I* = 1/2 nuclei. Figure demonstrates Zeeman splitting in the presence of an external magnetic field. Note that nuclei aligned against the field (anti-parallel) possess higher energy than those nuclei aligned with B_0 (parallel).

In the presence of the external magnetic field B_0 the magnetic moment experiences a torque with the result that the spin active nuclei precess around the central axis of B_0 (in this case the z-axis) at an angular frequency, known as the Larmor frequency, equal to $\omega_0 = -\gamma B_0$, where ω_0 is the Larmor frequency in rad s^{-1}. The value of γ determines the direction of precession around B_0.

For an ensemble of spins in the absence of an external magnetic field, the net (bulk) magnetization of the spins within the sample effectively cancel-

out as there is random orientation. If the same sample is however placed in B_0 the spins will tend to align with B_0 and the bulk magnetization vector of the sample, $\boldsymbol{M}$, will be non-zero in the direction of B_0.

2.2.2. Origin of the NMR signal

The application of a radiofrequency (RF) pulse with a frequency (ν) at the Larmor frequency (where $\boldsymbol{\nu} = \boldsymbol{\omega}_0 / 2\boldsymbol{\pi}$) to the spin ensemble located in B_0 will cause a disturbance in the bulk magnetization vector. The bulk magnetization vector will align with the x-y plane due to the induced B_1 field from the RF pulse producing momentary spin coherence (see Fig. 2.2). Subsequently the bulk magnetization will return to equilibrium aligning with B_0 by the relaxation methods to be discussed in section 2.2.4.

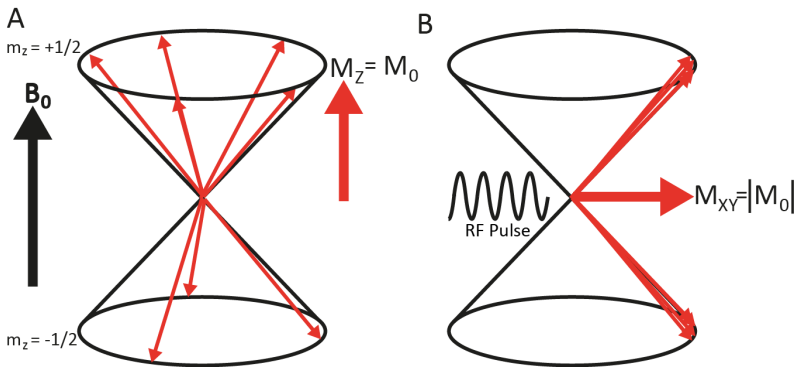

Figure 2.2. Effect of a B_1 field on phase coherence of a sample of spins located in an external magnetic field (B_0) A) Initially spins have random phase and distribution with the effect that M_z is located along the z-axis. B) Result of a 90° RF pulse resonant to the Larmor frequency causes the spins to group together with the production of the transverse component of the bulk magnetization vector (M_{XY}) equal to M_0.

After the B_0 field is removed, there is a return to equilibrium during which time M_{XY} decays with a corresponding increase in M_z. The return of the magnetization to equilibrium is the origin of the free induction decay (FID) signal routinely detected during NMR spectroscopy.

2.2.3. Factors affecting NMR signal intensity

It is possible to increase the intensity of the NMR signal by simply increasing the RF power deposited in the sample. The maximal detectable signal occurs when the bulk magnetization vector has been aligned with the transverse (x-y) plane- the RF pulse effecting this is said to be a 90°

pulse. Higher RF powers cause an excitation in the bulk magnetization beyond the transverse plane but with a reduction in detectable signal. The maximum detectable signal is therefore limited to a greater extent by the bulk magnetization of the sample rather than the strength of the B_1 field.

The magnitude of the equilibrium bulk magnetization M_0 of a sample can be expressed as:

$$M_0 = \frac{N\gamma\hbar P}{2} \qquad [2.4]$$

where N is the number of spins within the sample and P is the polarization. The magnitude of M_0 and hence the detectable NMR signal of a sample of spins is therefore governed by: the gyromagnetic ratio (with ^{1}H and ^{3}He having the largest); the spin density; and the polarization of the sample.

Spin density

The spin density of the sample is simply the number of excitable nuclei present within the sample. Liquids and solids have high densities of atoms compared to the gas phase. For liquid samples of hydrogen molecules such as water the high density combined with the high natural abundance of ^{1}H (> 99% of all available protons) results in high signal intensities. Significant difficulties can however result from experiments performed in the gas phase on low natural abundance nuclei with poor (and sometimes undetectable) NMR signals. Enrichment of samples of low natural

abundance nuclei is sometimes possible at increased cost and often increased experimental complexity.

Polarization

For spin I = 1/2 nuclei in the presence of B_0, the polarization (P) is given by:

$$P = \frac{(N_\uparrow - N_\downarrow)}{(N_\uparrow + N_\downarrow)} \qquad [2.5]$$

where $N_\uparrow$ and $N_\downarrow$ are the number of spins with $m_z = +1/2$ (parallel to B_0) and $m_z = -1/2$ (anti-parallel to B_0) respectively. At ambient temperatures the high temperature approximation of the polarization becomes:

$$P = \frac{|\gamma|\hbar B_0}{2k_B T} \qquad [2.6]$$

where k_B is the Boltzmann constant (1.38066 × 10^{-23} J K^{-1}) and T is the temperature of the system in degrees Kelvin (K). At ambient temperature (~ 20.0 °C / 293.15 K) P is of the order of 10^{-5} for ^{129}Xe in a field of 9.4 T but by reducing the temperature of the sample [141] or by increasing the field strength it is possible to increase P and hence the NMR signal. The improvement in signal intensity by increasing the strength of B_0 has been a driving force in the development of NMR and MRI since their inception [142-144]. There are however methods available to hyperpolarize a sample beyond that obtained at thermal equilibrium, discussed further in section 2.4.

Apparent Polarization

A further additional concept that is used within the context of this thesis is that of the apparent polarization [145]. This concept takes into account the reduction in polarization due to dilution of the spin active nucleus (the noble gas in the context of this thesis). The apparent polarization P_{app} is defined as:

$$P_{app} = P.\left[NG\right] \Big/ \sum_{i} \left[M_i\right] \qquad [2.7]$$

where $\left[NG\right]$ is the noble gas density and $\left[M\right]$ refers to the density of other components in the diluted mixture, such as He or N_2 in the context of this work. The apparent polarization therefore provides a measure of the expected signal from a diluted hp noble gas as compared to a sample of the pure noble gas (assuming identical isotopic distribution).

2.2.4. Relaxation mechanisms

During excitation two processes occur: firstly spins are excited from the $m_z = +1/2$ state to $m_z = -1/2$ with a drop in the polarization and a reduction in the z-component of the bulk magnetization vector (M_Z); secondly spin coherence occurs with the production of a transverse (x-y) component of the bulk magnetization vector (M_{XY}). Different but related relaxation mechanisms govern the return of the bulk magnetization vector (M) to its initial equilibrium.

2.2.4.1. Spin-lattice / longitudinal relaxation and T_1

Spin-lattice relaxation (also called longitudinal relaxation) is the process by which the population reorganizes toward that described by the Boltzmann distribution in Eq. 2.6, that is, the equilibrium polarization is reestablished. This relaxation is brought about by interaction of the spins with their surroundings (the lattice) due to local fluctuations in the magnetic field from the random reorientation of molecules within the lattice. The spin-lattice relaxation is characterized by the time constant T_1 and is defined in the Bloch equation:

$$\frac{dM_z(t)}{dt} = -\frac{(M_z(t) - M_0)}{T_1} \qquad [2.8]$$

where M_0 is the equilibrium value of the bulk magnetization vector. After a 180° RF pulse the solution to Eq. 2.8 is:

$$M_z(t) = M_0\left(1 - 2e^{-t/T_1}\right) \qquad [2.9]$$

The return of the z-component to the equilibrium value M_0 after a 180° pulse is often used to measure the T_1 of a thermally polarized sample through an inversion recovery experiment. In this experiment the magnetization at several points during the recovery of M_Z toward the thermal equilibrium value (M_0) is measured.

2.2.4.2. Spin-spin / transverse relaxation and T_2

Spin-spin relaxation (also called transverse relaxation) is the process by which spin coherence of the ensemble decays towards equilibrium after the RF pulse. At equilibrium due to small differences in the local magnetic field experienced by spins there is random distribution in angular frequencies within the sample resulting in zero net coherence between spins .

On excitation, as described earlier in section 2.2.2 the application of the B_1 field produces net spin coherence with the formation of a transverse component of the bulk magnetization M_{XY} (Fig 2.3a) On removal of B_1 there is relaxation to the initial equilibrium (Fig. 2.3b) brought about by interaction of the spins with each other. Spin-spin relaxation is characterized by the time constant T_2 and is defined by the Bloch equation:

$$\frac{dM_{XY}(t)}{dt} = \frac{M_{XY}(t)}{T_2} \qquad [2.10]$$

After a 90° pulse where $M_{XY}(0) = M_0$ the solution to Eq. 2.10 becomes:

$$M_{XY}(t) = M_0 e^{-t/T_2} \qquad [2.11]$$

In addition to the small variations in the effective value of the magnetic field at each locality due to surrounding spins, in the gas phase T_2 is usually very short due to rapid spin-rotation interactions. In liquids by comparison spin rotation is slower and the magnetic effects of neighbours may cancel with the result that T_2 values can be longer and in some liquids come close to T_1.

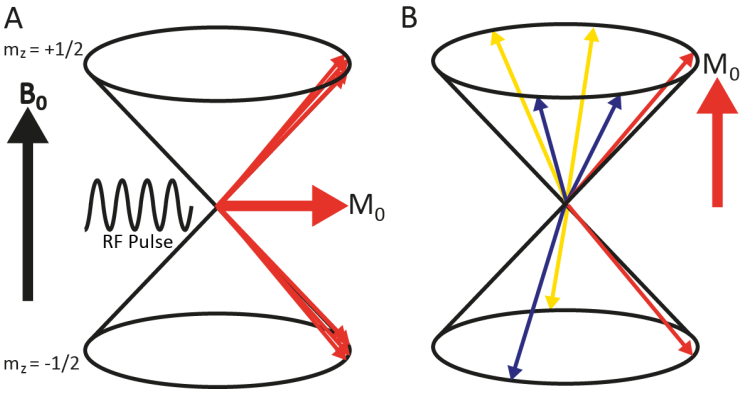

Figure 2.3. Process of spin-spin relaxation. A) During the application of the RF pulse the spins are coherent. B) Return to random distribution of spins with spins precessing at ω_0 (red), faster than ω_0 (yellow) and slower than ω_0 (blue). Note the use of the rotational reference frame where spins rotating at ω_0 appear to be stationary whereas those rotating faster or slower than ω_0 disperse.

In addition to the mechanisms described above, there are also effects due to the inhomogeneity in the external magnetic field (B_0) which contribute to an effective T_2 (T_2*) time constant. The T_2* is calculated from $1/T_2^* = 1/T_2 + 1/T_2'$ where T_2' is the contribution of the B_0

inhomogeneities. The T_2^* can be readily be calculated from the linewidth of the spectra with $\Delta\nu = 1/\pi T_2^*$ at the full-width half maximum (FWHM).

2.3. Magnetic resonance imaging (MRI)

The adaption of NMR spectroscopy to provide spatial distribution of the nucleus of interest forms the foundation of MRI. The fine soft tissue contrast possible with MRI as compared to other non-invasive imaging modalities has resulted in the widespread adoption of MRI in the field of biomedical imaging.

2.3.1. Use of magnetic field gradients for spatial encoding

Spatial encoding of the sample is produced by the use of linear gradients in the x, y and z directions, G_X, G_Y and G_Z respectively. A spin present within a linear gradient will resonate at a frequency proportional to its position within the field according to:

$$\omega = \gamma (B_0 + \Delta x . G_x) \qquad [2.12]$$

where G_x is the strength of the gradient (mT/mm) and Δx is the displacement in mm of the spin from the iso-centre of the gradient in the x direction. By applying gradients in the x, y and z directions it is possible to localize the NMR signal to a particular location within the sample [146, 147].

2.3.2. Spin echo two-dimensional Fourier transform imaging

The use of gradients is best displayed by studying examples of imaging sequences employing their use. Spin echo imaging involves the application of a 90° excitation pulse followed by a 180° refocusing pulse at a time TE/2

(echo time/2) with the production of a spin echo at TE (see Fig. 2.4). The result of the refocusing pulse is to remove the effect of B_0 inhomogeneities with the signal intensity now following T_2 decay rather than T_2* decay. Spatial localization is produced by the read gradient during the acquisition window and by the application of varying strengths of the phase encoding gradient on successive repetitions after a time TR (repetition time).

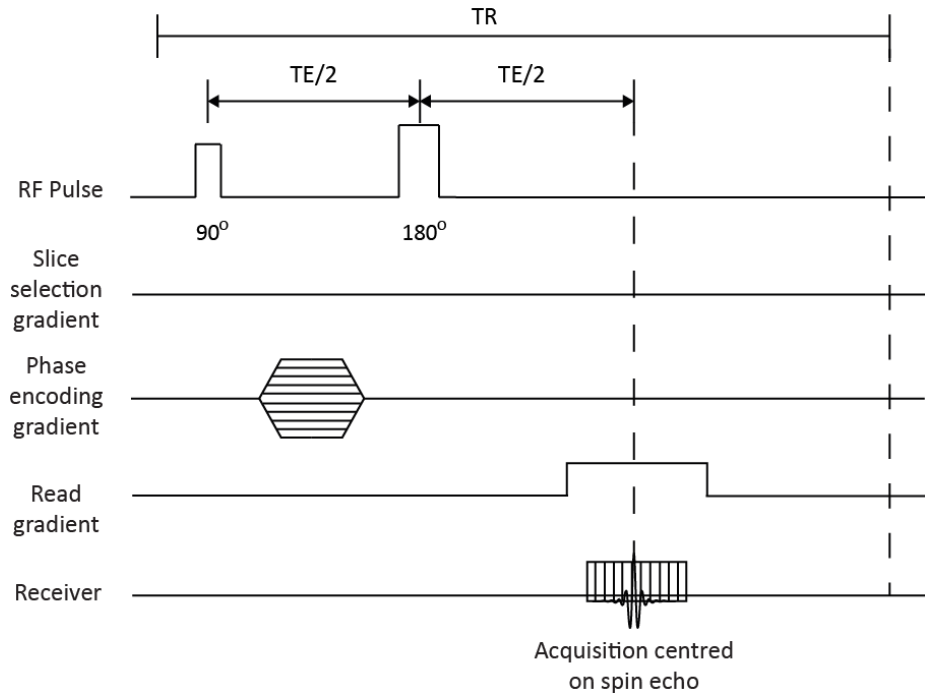

Figure 2.4 Non slice selective spin echo pulse sequence. 90° rectangular RF pulse followed by a 180° rectangular refocusing pulse at TE/2 with formation of the spin echo at TE. Application of the read gradient with opening of the acquisition window centred on the spin echo. After time TR, the process is repeated with different strengths of the phase encoding gradient. Note the length of TR is not representative and is often much longer than TE but has been reduced for ease of display.

The acquired time domain signal is then plotted using the *k*-space (spatial-frequency domain) formalism. The most basic method of traversing *k*-

space, and so acquiring the image data, is by linearly incrementing the phase encoding from negative to positive values on successive TRs (see Fig. 2.5a). More efficient methods have also been described such as centric, radial and spiral (see Fig. 2.5b) where the centre of *k*-space is sampled first before moving to the periphery. These methods have the benefit that contrast between tissues can be improved as the majority of the signal intensity is located in the centre of *k*-space, however there is normally a loss of resolution as the periphery contains the high frequency edge data characteristic of sharp tissue transitions.

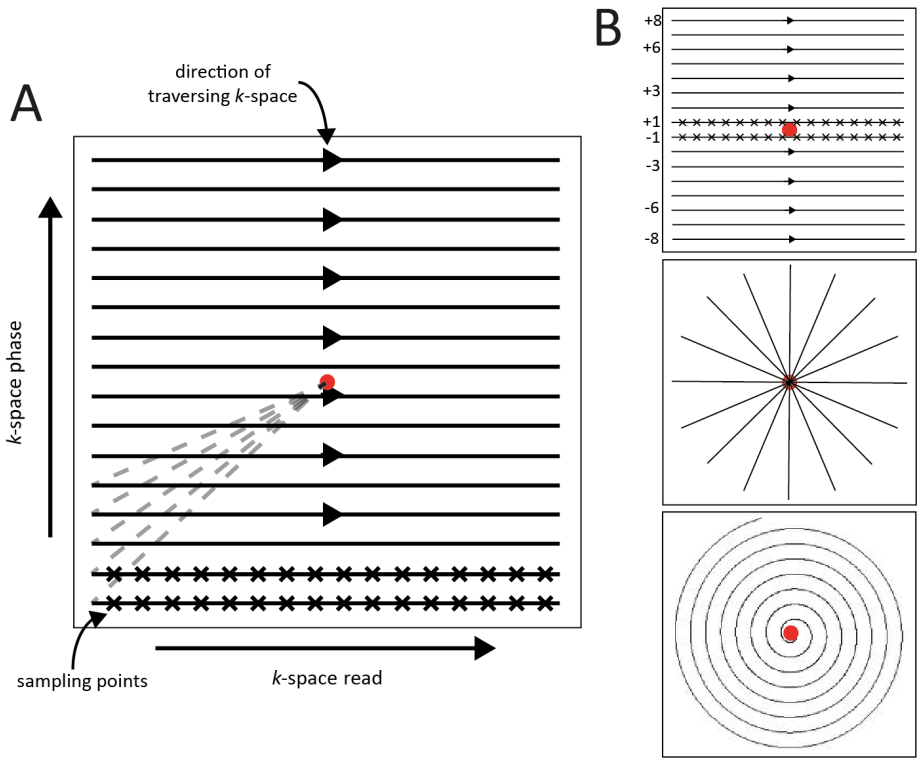

Figure 2.5. Topology and methods of *k*-space sampling. A) Linear sampling of *k*-space from negative to positive read frequencies with successive linear increments of the phase encoding gradient on consecutive TRs. Two dimensional Fourier transform (2DFT) produces a 16 × 16 image matrix. Note each phase encoding step starts at the centre of *k*-space (red dot) with the application of phase and read gradients moving acquisition to the line being sampled (dashed grey line). Note also that points are sampled on all *k*-space lines in a similar fashion. B) Centric acquisition (top) with linear sampling from low to high read phase as in A but with phase encoding steps alternating between positive and negative values from the centre. Radial acquisition (middle) with sampling from the centre to the periphery along 16 radial lines. Spiral acquisition (bottom) with sampling from the centre to the periphery of *k*-space.

2.3.3. Gradient echo imaging

Another widely used imaging technique is that of gradient echo imaging. Rather than refocusing the transverse magnetization with a 180° pulse as in spin echo imaging, gradient echo imaging refocuses the transverse magnetization with the use of a bipolar read gradient (see Fig. 2.6).

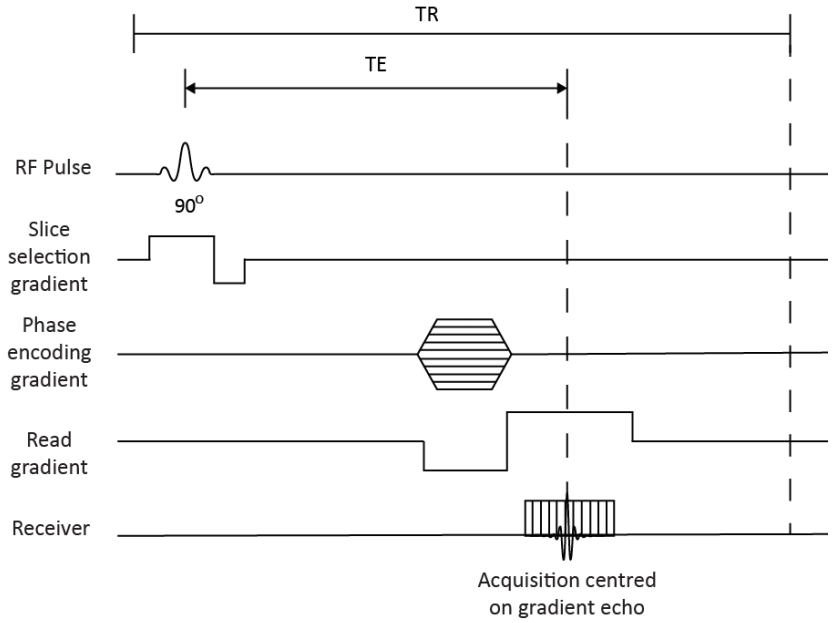

Figure 2.5 Slice selective gradient echo pulse sequence. 90° slice selective pulse followed by gradient refocusing produced by an initial defocusing lobe of the read gradient, switching to a refocusing read gradient. Acquisition again centred on the maximum amplitude of the signal at TE. After time TR, the process is repeated with different strengths of the phase encoding gradient. Note the use of the slice selective gradient with negative compensation lobe to rephase the excited spins.

As T_2* effects are preserved with more rapid signal decay, gradient echo imaging tends to produce lower signal intensities than with similar spin

echo sequences. However as there is no requirement for the refocusing pulse with a long TE, gradient echo sequences can be significantly faster.

2.3.3.1. Fast low angle single shot (FLASH) imaging

The use of gradient echo imaging was improved by the development of the FLASH paradigm [148]. By reducing the power of the excitation pulse (flip angle) to lower values, it has been possible to significantly shorten the TR between phase encoding steps for thermally polarized samples. Saturation due to the application of frequent high power RF pulses would otherwise limit the recovery of signal intensities between excitation pulses. Indeed FLASH protocols were amongst the earliest fast imaging pulse sequences commercially available with modifications of the technique being extensively used in the context of this thesis.

2.4. Hyperpolarized noble gas imaging

As mentioned in Chapter 1, MRI of the gas phase is possible without the use of hyperpolarized (hp) spin states (see for example [119]). However, the density of gases at ambient pressure and temperature is typically reduced by about three orders of magnitude compared to the liquid phase, significantly lowering NMR signal intensities, therefore limiting MRI resolution. Hp spin states, on the other hand, can enhance the NMR signals by many orders of magnitude compared to thermally polarized states and enable gas phase MRI of both dilute spin systems and nuclei with low gyromagnetic ratios. Since the hyperpolarization is almost always produced outside the MRI detection region, the hp gas typically requires some form of transport from the hyperpolarizer to the detection zone and sufficiently long relaxation times are needed to sustain the generated hyperpolarized state until NMR signal detection has occurred. In general slow T_1 relaxation in hp MRI is desirable because signal averaging is not based on relaxation recovery but on renewed delivery of hyperpolarized species for every scan. Unfortunately, most molecules experience fast relaxation in the gas phase due to spin-rotation interactions. A noticeable exception is the group of mono-atomic noble gasses, including ^{3}He, ^{129}Xe and ^{83}Kr, where spin-rotation relaxation only occurs during short-lived interaction with other atoms [149]. Therefore T_1 times of many hours and even days can be possible unless additional relaxation mechanisms are present [149-152].

To date, the most widespread and successful MRI applications of hp noble gasses utilize the isotope ^{3}He (see table 2.1 for physical properties) for preclinical and clinical studies of pulmonary pathophysiology (see for instance [103, 153] for previous reviews). However, the main supply source for ^{3}He is tritium decay in nuclear (fusion) warheads with no viable current alternative in sight. The very high demand for this isotope for many types of applications has therefore led to a ^{3}He supply crisis as evidenced by US congressional hearings [154]. The best remedies to this problem for the MR community may be rigorous ^{3}He recycling whenever possible and the exploration of alternative techniques.

2.4.1. Hp ^{129}Xe MRI

Next to ^{3}He, the most prominent noble gas isotope for hp gas phase MRI is ^{129}Xe (see Table 2.1) that has already found its way into preclinical and clinical usage. Indeed, the first noble gas lung MRI reported by Albert et al. in 1994 utilized hp ^{129}Xe [122]. Xenon is a renewable resource obtained from air liquefaction with a natural abundance of 26.44% ^{129}Xe and isotopic enrichment is available at affordable costs [i.e. currently US$ 200 - 250 per litre gas at ambient pressure and temperature, depending on the fluctuating actual market and specific offers. For comparison, xenon with natural abundance ^{129}Xe isotope distribution typically costs around US$ 10 - 12 per litre gas]. The signal intensity of ^{129}Xe falls short compared to that of hp ^{3}He because of the 2.73 times larger gyromagnetic ratio of ^{3}He and because of the high spin polarizations typically obtained with ^{3}He that exceeded those achieved for ^{129}Xe in the past.

For a hyperpolarized spin system, the NMR signal intensity is proportional to the square of the gyromagnetic ratio assuming identical conditions with respect to the polarization (P), B_0, spectral width, and NMR hardware. However, depending on the particular application, the disadvantage for ^{129}Xe may be reduced at higher field strengths because its smaller gyromagnetic ratios means less shortening of the T_2* times (generally caused by magnetic susceptibility effects in heterogeneous media such as the lungs) and less signal loss in electrically conducting media. Furthermore, due to ever increasing progress in spin exchange optical

pumping (SEOP), very high ^{129}Xe polarization values have now been reached at high production rates [155-159]. This has ultimately reduced the signal to noise (SNR) gap between ^{3}He and ^{129}Xe, directly improving the temporal and spatial resolution of hp ^{129}Xe imaging. Optimization of hardware and MRI protocols leads to further advances in the quality of the MR images. See Fig. 2.6 for an example of the 'evolution' of hp ^{129}Xe lung MRI improvement over the past two decades.

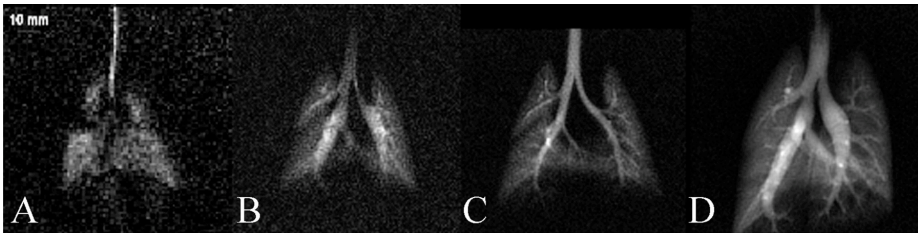

Figure 2.6. Notable improvement in hp ^{129}Xe image resolution over the period 1998-2007. (A) Early image of a rat lung from 1998 with in-plane resolution 0.84 × 0.84 mm^2 and SNR of ~3. (B - D) progressively better image quality as polarization, gas delivery and MR acquisition techniques continue to improve. (D) Image from 2007 with resolution 0.31 × 0.31 mm^2 and an SNR of ~20. Reproduced with permission from [22].

2.4.2. Hp noble gas production

A hyperpolarized spin state is simply a state at very low spin temperature that is not in a thermal equilibrium with the (motional) temperature of the sample. Low spin temperature leads to high population of the ground state ($m_z = +1/2$ for spin $I = 1/2$ nuclei) and thus high magnetization of the spin ensemble that results in very high NMR signal intensity. This state

eventually returns to the thermal equilibrium temperature (i.e. depolarizes). Therefore, T_1 relaxation needs to be slow enough to preserve the state for sufficient periods of time. The hyperpolarized state can, in principle, be generated through rapid heating of a sample that was kept in a thermal equilibrium at very low temperatures (<< 1 K) [141]. Experimentally less demanding, all noble gas isotopes with non-zero nuclear spin can be hyperpolarized through spin exchange optical pumping (SEOP) using alkali metal vapor [160]. Though SEOP typically requires high power laser irradiation it selectively reduces the nuclear spin temperature to values far below 1 K. For this to be useful for MRI, the reactive alkali metal (typically rubidium) needs to be removed before the hp gas transferred for MRI detection [134, 161]. Slow T_1 relaxation is needed to preserve the low spin temperature that is not in a thermal equilibrium with the molecular environment. The nuclear spin polarization of a hyperpolarized sample is best determined through the signal enhancement factor obtained from comparison of the associated hp NMR signal with that of a thermally polarized sample at otherwise identical - or at least at comparable – conditions.

SEOP can be performed either in a stopped flow mode [145, 161, 162] or in a continuous flow mode [156]. Typically SEOP uses a mixture of gases that contain xenon (or krypton) in low concentrations and N_2 and helium (^{4}He) in abundance. Though low noble gas concentration reduces the MR signal intensity hp ^{129}Xe can be concentrated through cryogenic separation [155, 156, 159, 163, 164].

Many advances have been made in continuous flow SEOP leading to very high spin polarization values at high production rates [155-159, 163, 165, 166]. At the pinnacle of current technology, Hersman and co-workers have developed a fully automated SEOP system with cryogenic separation that is capable of producing multiple liters of hp ^{129}Xe per hour with a spin polarization $P_{hp} = 50\%$ [155, 167]. Batch mode SEOP, as a potential low cost alternative, is being further developed using various approaches by other groups [145, 162]. For example high noble gas concentration at low pressures in batch mode SEOP has been recently explored to bypass the need for cryogenic separation [145]. This method produced the equivalent of hp ^{129}Xe gas with $P_{hp} = 14\%$ at a rate of 1.8 cm^3/min using only 23 W of laser power. For hp ^{83}Kr, where cryogenic separation is not feasible due to rapid quadrupolar relaxation in the frozen state, the method allowed for $P_{hp} = 3\%$ at a rate of 2.0 cm^3/min. Since high power solid-state lasers with line-narrowed output are increasingly available [168], lower cost SEOP systems for MRI applications become more feasible. Furthermore, dynamic nuclear polarization (DNP) at 1.2 K was reported as a new approach to generate hp ^{129}Xe state at potentially high volumes [169]. Whatever methodology will ultimately be the most successful, the proliferation of techniques to conveniently and inexpensively polarize noble gases now appears likely.

2.4.3. Hp noble gas phase imaging *in vivo*

Possibly the most useful applications of simple spin density gas phase imaging of hp noble gases are in biomedical studies. The clinically most

useful parameters that can be garnered from static ventilation scans are ventilation defects [170], that is, lung regions with reduced / absent hp gas signal. In patients with chronic obstructive pulmonary disease (COPD) and asthma it is possible to monitor the evolution of these diseases as they progress over time and in response to airway hyperresponsiveness tests. Effective ventilation deduced by hp MRI *in vivo* has been shown to correlate with spirometry data for patients in health and disease [170, 171]. Although the hp noble gas ventilation images may appear dramatic when displaying larger unventilated areas in lungs it should be noted that this might not be necessarily specific to one disease pathology, rather they reveal the extent and severity of heterogeneity in ventilation that may be common in many conditions (Fig. 2.7).

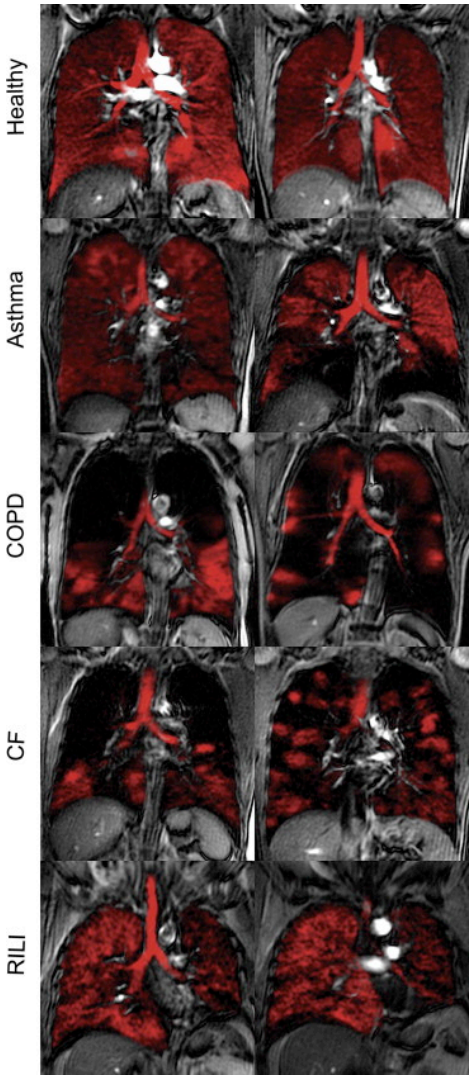

Figure 2.7. *In vivo* human hp ^{129}Xe images in health and disease. Hp ^{129}Xe images (in red) registered onto coronal proton thoracic images from a healthy volunteer and subjects with asthma, chronic obstructive pulmonary disease (COPD), cystic fibrosis (CF) and radiation-induced lung injury (RILI). Reproduced with permission from [172].

Safe *in vivo* delivery of hp noble gases merits special mentioning. In general, static ventilation imaging is performed during a simple breath hold after inhalation of the gas mixture containing a known volume of hp gas. Oxygen, can be added to the hp gas for inhalation but paramagnetic O_2

also leads to an increase in relaxation, for instance T_1 drops to 15 s for ^{129}Xe in breathable oxygen containing mixtures [173]. Special care should be taken as xenon becomes a general anesthetic when its alveolar concentration is in the realm of 70% [174]. However a 70% mixture of xenon with 30% N_2, inhaled for a single breath-hold of 20 - 40 s, will usually only result in an alveolar concentration of xenon ≈ 35% [175]. Moreover, it has been recently reported that 3 – 4 repeated inhalation cycles with undiluted one liter boluses of hp ^{129}Xe are well tolerated in patients with mild to moderate COPD [176].

2.4.4. MR imaging of non-equilibrium spin populations

2.4.4.1. Variable flip angle imaging

The most common *in vivo* hp noble gas imaging protocols are still using the concept of FLASH, as described in section 2.3.3.1, as their core. A valuable addition to the FLASH protocol first developed by Zhou et al. that makes full use of the hp spin state thus leading to a higher image quality is that of variable flip angle (VFA) sequences [177]. The flip angle on each phase increment is governed by the equation:

$$\theta_n = \tan^{-1}\left(\frac{1}{\sqrt{(N-n)}}\right) \qquad [2.12]$$

where θ_n is the flip angle on the nth pulse in a train of N pulses. VFA results in constant signal amplitude (assuming the absence of noticeable T_1 relaxation) until the hp state is completely 'used up' (Fig. 2.8) [177]. Although this methodology has been little used for MRI of lungs to date, as it requires careful calibration of the RF pulse power, it can be

tremendously beneficial for experiments where low signal intensity is a concern [178]. Slice selection with the VFA FLASH sequences have been shown to create slice profile artefacts [179] and in larger coils with inhomogenous excitation, correction is often required [180], however VFA FLASH is extensively utilized in the context of this thesis using small RF coils with relatively homogenous excitation.

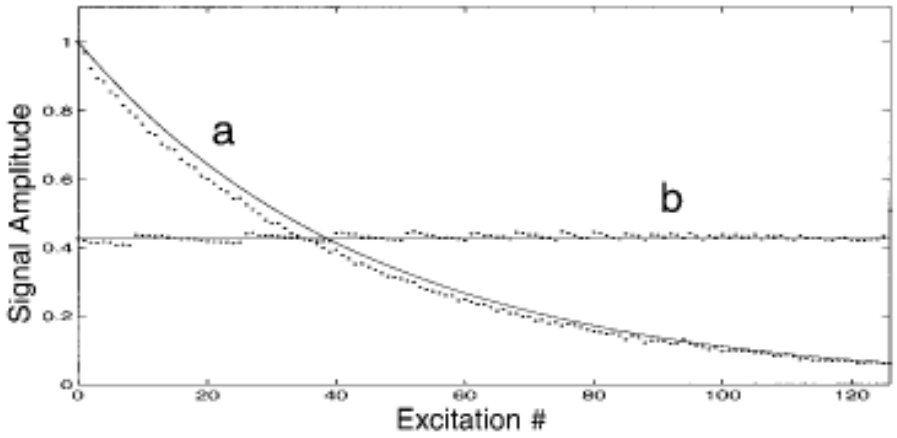

Figure 2.8. Comparison of signal amplitude with trains of 127 pulses using constant flip angle (FLASH) of 12° (a) and variable flip angle (VFA) (b) methods. The filled circles represent the experimental data, solid lines represent theoretical values. Reproduced with permission from [177].

2.4.4.2. Future hp gas imaging strategies

Technological developments in hardware, computing and image reconstruction might lead to orders of magnitude faster data collection and processing compared to the first *in vivo* attempts. Improvements utilizing echo planar imaging (EPI) and spiral imaging acquisition schemes are already in place for dynamic ventilation imaging with hp ^{3}He, however

spatial resolution is usually sacrificed for speed. In addition, three-dimensional (3D) dynamic imaging with hp ^{3}He within one breath-hold has also been reported [181]. These improvements might be translated to hp ^{129}Xe and hp ^{83}Kr given that sufficient advances in SEOP has been achieved.

2.4.5. Apparent diffusion coefficient (ADC) measurements *in vivo*

Diffusion of hp gases in the lungs is restricted by the alveolar walls. For sufficiently short Δ times between the bipolar gradient pulses in pulsed field gradient (PFG) experiments unrestricted diffusion and therefore the self diffusion constant (D_0) of the free gas will be measured. However, as Δ becomes longer, the mean displacement of the gas will be hindered by the pore walls, resulting in a reduced apparent diffusion coefficient (ADC). ADC measurements can therefore provide valuable information about lung morphometry, namely airspace diameter of ventilated lung [182, 183]. Work with ^{3}He (binary diffusion coefficient of dilute ^{3}He in air ($D_{^{3}He-Air}$ = 0.86 cm^2/sec [184]) has shown that in cases of alveolar destruction such as in emphysematous disease the ADC becomes elevated [185, 186]. The ADC measurements for ^{129}Xe ($D_{^{129}Xe-Air}$ = 0.14 cm^2/sec [184]) correlate with those for ^{3}He [128] with ADC values elevated in human COPD phenotypes [187]. Recently it has been found that ^{129}Xe ADC values may actually correlate better than ^{3}He ADC with other lung function testing methods. This may be possibly due to the lower rate of diffusion of xenon leading to less contamination through collateral ventilation from neighbouring alveoli [188]. Note, that the ^{129}Xe self-diffusion coefficient is 6 times smaller than that of ^{3}He therefore larger field gradients are required to

perform the ADC measurements on similar to ^{3}He time scales. This puts a strain on the hardware safety requirements, however experimental strategies have been proposed to circumvent this problem [189]. The use of ADC measurements in small animal lung imaging will be further discussed in Chapter 7.

2.4.6. Dissolved phase ^{129}Xe MR imaging

2.4.6.1. The ^{129}Xe chemical shift

As ^{3}He has a negligible chemical shift and low solubility, its dissolved phase, if any, does not bring any additional information. The situation is different for xenon. Due to its large compressible outer electron shell ^{129}Xe exhibits a significant chemical shift when placed into different chemical environments as compared to the gas phase. The ^{129}Xe NMR chemical shift range is just below 300 ppm for the various materials and solvents that may absorb the xenon atoms [190-193]. Note, that ^{129}Xe NMR signal in the bulk gas phase approximated to zero pressure is typically referenced with 0 ppm and the shift increases by about 0.6 ppm/bar in pure xenon gas at ambient temperature and pressures conditions close to ideal gas behavior. There is an extensive literature covering hyperpolarized ^{129}Xe NMR spectroscopy in addition to work with thermally polarized ^{129}Xe that utilizes the chemical shift as a 'spy' for the environment of the xenon atoms. However, with the recent advances in hyperpolarization of this nucleus, the interrogation of dissolved xenon chemical shift has been utilized for biomedical studies.

The chemical shift of ^{129}Xe is very useful for pulmonary MRI where continuous flow hp ^{129}Xe transport is replaced by usage of the breathing cycle for delivery. When coupled with xenon's high solubility, it is possible to record a distinct signal arising from xenon atoms associated only with parts of lungs where xenon dissolves, i.e. lung tissue and its components. The first *in vivo* hp ^{129}Xe spectra showed four resolved peaks, the initial one located at the gas phase set to 0 ppm and three other peaks were found at 191, 199 and 213 ppm and were attributed to ^{129}Xe dissolved in blood plasma, lung tissue and red blood cells (RBCs) respectively (Fig. 2.9) [129]. The longitudinal relaxation of the peaks associated with the dissolved phase was found to be of the order of seconds thus allowing for the possibility to image xenon incorporated into the tissue components separately from the gas phase [194].

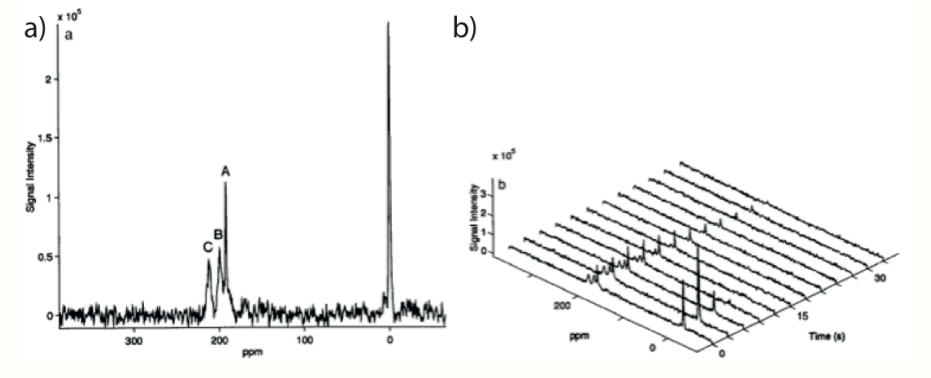

Figure 2.9. Early hp ^{129}Xe spectra and washout dynamics from the rat pulmonary system. (a) hp ^{129}Xe spectra at t = 0 after inhalation of the last xenon bolus. Peak A, B and C at 191, 199, 213 ppm relative to the gas phase peak at 0 ppm attributed to the blood plasma, lung tissue and red blood cells respectively. (b) Temporal dynamics on hp ^{129}Xe washout with the combined effects of ventilation, RF depletion and longitudinal relaxation. Reproduced with permission from [129]

Chemical shift selective MRI of dissolved xenon in lungs is facilitated by the significant frequency shift between ^{129}Xe in the gas phase (around 0 ppm) and in the dissolved phase (191 – 213 ppm) [130]. Unfortunately, xenon in the dissolved phase constitutes only about 1 – 2% of the total inhaled xenon. Therefore, the associated hp ^{129}Xe signal intensity arising from the dissolved phase is fairly weak. Therefore, Fig. 2.9 does not reflect the true intensity of the gas phase peak (for technical reasons - i.e. due excitation in the 200 ppm region) that should be about 50 - 100 times stronger than the dissolved signal. However, the dissolved phase xenon is constantly replenished from the alveolar gas phase through rapid diffusive exchange. This allows for signal averaging with very short delay times in the millisecond regime. Fujiwara and coworkers have demonstrated the use of continuous delivery of hp gas in the mouse lung as a method to

enhance the dissolved phases signal [195, 196]. Single breath-hold and chemical shift selective three-dimensional MRI of the dissolved phases in human volunteers with reasonable spatial resolution have however been reported [197].

This concept can be used for new physiological measurements that probe gas transfer in lungs using xenon as a surrogate for oxygen and may be helpful for early diagnosis of interstitial lung diseases such as idiopathic pulmonary fibrosis (IPF). Due to a thickening of the lung parenchyma that separates the alveolar space from the blood, gas exchange is reduced in these diseases and gas transport requires longer time periods. Driehuys et al. explored the exchange between the alveolar membrane and capillary blood using a technique called xenon alveolar capillary transfer imaging (XACT) [132]. The technique uses chemical shift selective separation between tissue and blood dissolved hp ^{129}Xe utilizing the 14 ppm difference between the two dissolved states. The slowed gas transfer from the alveoli to the blood can be visualized with hp ^{129}Xe if short recycle delays are used as shown in Fig. 2.10.

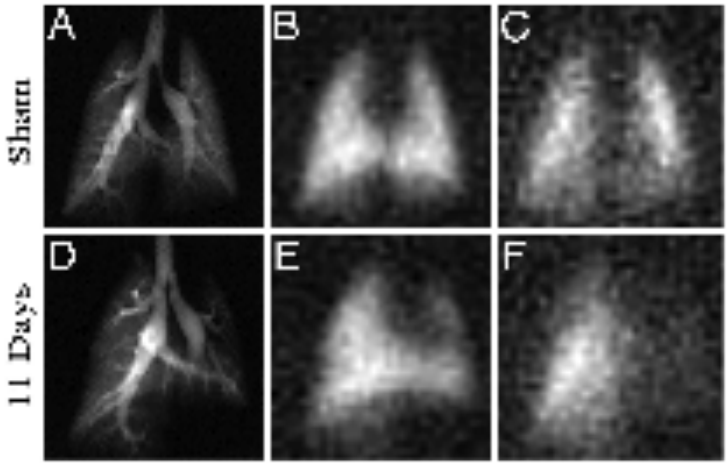

Figure 2.10. Inhaled hp ^{129}Xe images from saline treated rat (sham) and bleomycin treated rat (fibrosis model). Images (A-C) from sham instillation of saline into left lung. (A) Gas phase ^{129}Xe image from airspaces. (B) Tissue phase ^{129}Xe image from lung parenchyma. (C) Red blood cell (RBC) phase ^{129}Xe image. (D-F) Comparable images 11 days after bleomycin instillation left lung with D, E and F representing the gas phase, tissue phase and RBC phase images respectively. Note that the tissue images closely match the gas phase images in both rats whilst the RBC phase images show almost absent uptake of ^{129}Xe by the RBCs in the bleomycin treated lung in the time-frame of the MRI experiment as compared to the sham treated rat, indicating thickening of the alveolar membrane (fibrosis). Reproduced with permission from [132].

The underlying concept of XACT is chemical shift selected recovery of the hp ^{129}Xe signal. This method has been explored by Butler and co-workers to measure surface area to volume ratios (S_A / V_{gas}) in a variety of porous media and has been applied later in a non-spatially resolved manner to study morphometry of healthy human lungs *in vivo* [131, 198]. After a series of selective 90° pulses have destroyed the dissolved phase magnetization, thus creating an initial zero point, the increase of the

dissolved phase signal is recorded as a function of time. Assuming that one dimensional diffusion drives signal growth of the dissolved phase one can deduce the S_A / V_{gas} in lungs as it should be proportional to the normalized intensity of the dissolved phase signal. Recently, this model was refined with lung blood flow corrections and was used to produce additional measurements including alveolar septal thickness (h) [199]. The surface area to volume ratio was found to appropriately decrease in healthy subjects with increasing inhalation volumes and was noted to be lower in patients with COPD, indicating airspace destruction. h was seen to be significantly raised in patients with mild interstitial lung disease.

Xenon transfer contrast (XTC) is an alternative approach to fight the relatively weak hp ^{129}Xe signal originating from the dissolved phase through the usage of indirect detection of the dissolved phase in the gas phase [200]. The underlying principle is that hp ^{129}Xe exchanges not only from the gas phase to the dissolved phase but also vice versa from the tissue into the alveolar space. Therefore, chemical shift selective destruction of the hp ^{129}Xe magnetization (i.e. saturation) in the dissolved phase by 90° pulses can be observed indirectly through a reduction of alveolar hp ^{129}Xe gas phase signal. The advantage is that the alveolar signal is much stronger and hence easier to detect. The reduction of the signal is measured in comparison with experiments without chemical shift selective saturation. Since the concept is based on gas exchange, it allows for regional measurement of gas diffusion into the parenchyma.

To obtain spatial information the XTC preparatory sequences are usually combined with the FLASH imaging protocol. To further maximize the image contrast the signal associated with the dissolved phase can be inverted rather than suppressed [201, 202]. Information is obtained from the decrease of the gas phase signal after multiple exchange times during the XTC sequence as it is proportional to the volume ratio between the lung parenchyma and airspaces. Consequently, the increase of the gas phase signal is indicative of alveolar membrane thickening. With this in mind regional gas exchange was probed in healthy humans and subjects with COPD [202]. Reduced surface area that corresponded to destruction of the airspaces and septal wall thickening resulted in distinctive contrast in XTC images.

2.4.6.2. *In vivo* delivery of dissolved ^{129}Xe as a contrast agent

The high solubility of xenon in saline has allowed hp ^{129}Xe to be added to physiological solutions and then injected as an hp ^{129}Xe containing solution into the blood stream [203]. The T_1 relaxation time of hp ^{129}Xe is in excess of 60 s in saline solution and reduces to 13 s in oxygenated blood and is further shortened in deoxygenated blood [204, 205]. Chemical shift selective imaging of the alveolar space after intravenous injections of saline containing dissolved hp ^{129}Xe allowed comparison of the gas distribution within the *in vivo* rat lung from hp ^{129}Xe delivered by the blood stream (perfusion) and that delivered by direct inhalation (ventilation) (see Figure 2.11). The method suffers from limited xenon signal and is limited by the volume of saline that can be infused *in vivo*. The use of

hollow-fibre membranes has however allowed continuous delivery of xenon [206] and thus has resulted in improved detection of the hp ^{129}Xe dissolved phase in the lungs [207].

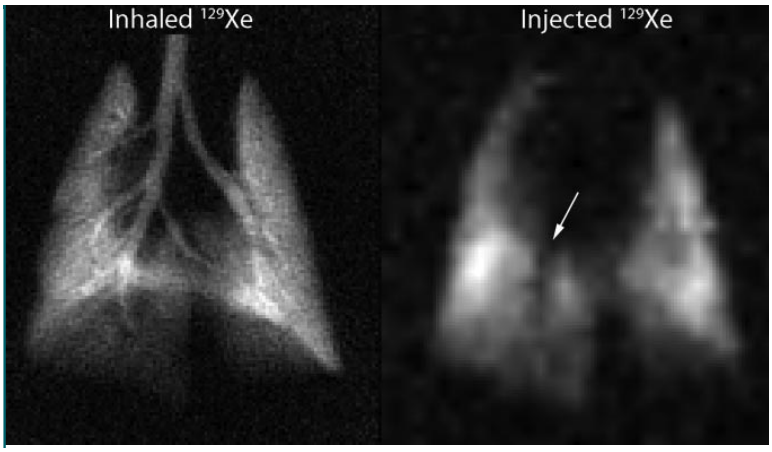

Figure 2.11. Gas phase image from rat lung with directly inhaled hp ^{129}Xe and delivered by injection ^{129}Xe solution. The injected image shows a signal void corresponding to the right main stem bronchus (arrow). Reproduced with permission from [203].

Dissolved phase hp ^{129}Xe imaging can also be applied *in vivo* to non-respiratory body systems and adds a novel complementary investigative tool for neuroimaging [208-211] but as this is not the topic of this thesis it will not be discussed further.

2.4.7. Hp ^{83}Kr MRI.

One of the advantages of hp ^{129}Xe MRI is the associated large chemical shift that is indicative of small distortions in xenon electron cloud and is therefore a valuable 'spy' of the atomic and molecular surroundings. The ^{129}Xe chemical shift is unsurpassed by any other stable noble gas isotope. However, ^{131}Xe, another NMR active and stable xenon isotope, has a nuclear spin $I = 3/2$ and therefore possesses a nuclear electric quadrupole moment that can also serve as a fairly sensitive detector of atomic electron cloud distortions. It is therefore a better "spy" for noble gas – surface interactions than the ^{129}Xe chemical shift and the isotope can provide surface sensitive MRI contrast [212]. Unfortunately, even gas phase collisions cause rapid quadrupolar driven relaxation that leads to short ^{131}Xe T_1 times and therefore rapid decay of the hyperpolarized state [213]. Another noble gas isotope with a nuclear electric quadrupole moment, ^{83}Kr, where quadrupolar relaxation is typically slower than that of ^{131}Xe because of krypton's smaller electron cloud and because of its larger nuclear spin $I = 9/2$. The remarkably long ^{83}Kr gas-phase T_1 times of up to several hundred seconds at ambient pressure allow for hyperpolarization up to 26%. Because of dilution with other gases, the best currently available apparent polarization is 3% [145].

The quadrupole moment dominated longitudinal ^{83}Kr relaxation can be utilized for MR studies of surrounding surfaces since it is susceptible to the surface-to-volume ratio (S/V), surface hydration, and surface temperature

[134]. Hyperpolarized (hp) ^{83}Kr has been shown to provide T_1 relaxation weighted MRI contrast that is highly sensitive to the surface chemistry in low S / V model surface systems. Fig. 2.12 provides an example of surface sensitive contrast in hp ^{83}Kr gas phase MRI.

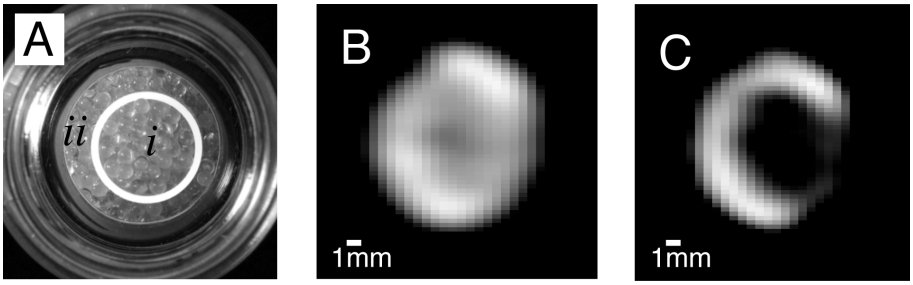

Figure 2.12. Surface sensitive contrast with hp ^{83}Kr MRI. A) Photograph of a sample containing 1.0 mm glass beads with a siliconized, hydrophobic surface in compartment (*i*) and an untreated, hydrophilic surface in compartment (ii). (B) MRI of gas phase hp ^{83}Kr shortly after transfer into the sample. (C) Hp ^{83}Kr MRI as in (B) but after additional 6 s delay time, showing a surface sensitive MRI contrast. The ^{83}Kr quadrupolar relaxation caused by surface interactions leads to T_1 = 9 s in the hydrophobic region (i) and to T_1 = 35 s in the hydrophilic region (ii). Adapted figure, printed with permission from [134].

Hp ^{83}Kr NMR relaxation measurements of excised but actively ventilated rat lungs have been used to study T_1 relaxation as a function of lung inflation [214]. The longitudinal ^{83}Kr relaxation in the distal airways and respiratory zone was found to be independent of the lung inhalation volume and highly reproducible between different specimens. Significantly by removing the effect of the large conducting airways where the S/V is low, therefore focusing on the high S/V regions of the distal airways and lung parenchyma, it was found that the T_1 relaxation times were shortened

from 1.25 ± 0.07 s to 1.00 ± 0.08 s at the same inhalation volume (see Fig. 2.13).

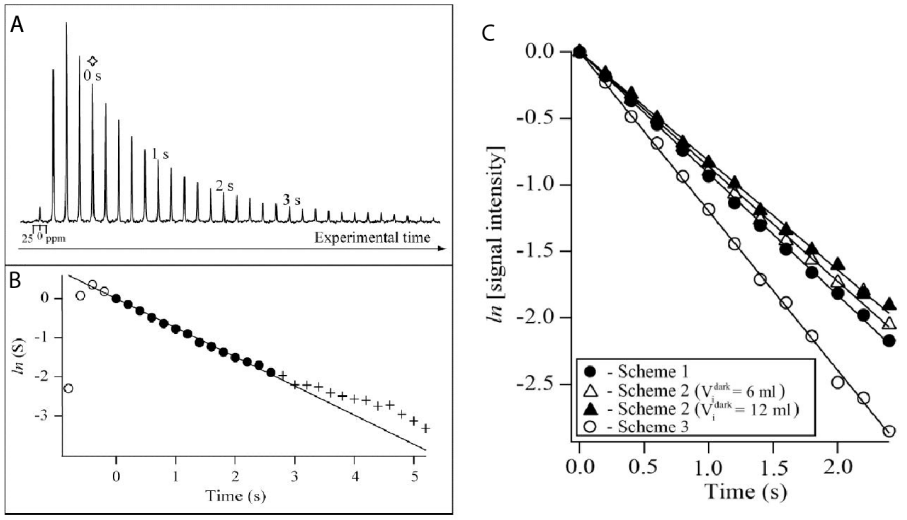

Figure 2.13. Method for measuring hp ^{83}Kr longitudinal (T_1) relaxation in the lung. A) Acquired data during inhalation of hp ^{83}Kr in an *ex vivo* rat lung using a train of constant 12° flip angle pulses. Note the initial increase in signal intensity during inhalation with maximum signal at the peak inhalation volume with subsequent reduction in signal due to T_1 relaxation. B) Natural logarithm of the integrated hp ^{83}Kr signal intensities in A as a function of time. C) By removing the contribution from the large airways the hp ^{83}Kr T_1 decreased (Scheme 3- empty circles), as compared to ventilation schemes where the large airways contributed to the overall measurement (Schemes 1 – 2). Note that in C the signal intensities have been normalized to the value two pulses after the end of inhalation. Reproduced with permission from [214].

It is thought that the ^{83}Kr T_1 in the lung should be long enough for *in vivo* usage of hp ^{83}Kr MRI with rats that typically breathe at a rate of around 1 breath/second while anesthetized. Further, the relaxation should be slower in larger animals as the surface-to-volume ratio decreases with

larger alveoli diameters (recall from section 1.2 that the diameter of rat alveoli is ~90 μm compared to 270 μm in humans).

Recent improvements in SEOP have increased the hp ^{83}Kr signal intensity significantly [145] and enabled coronal lung FLASH MRI of excised rat lungs [215] with spatially resolved measurements of hp ^{83}Kr relaxation [216]. The development of hp ^{83}Kr MRI with the production of spatially resolved T_1 measurements will be discussed in Chapter 6 including the application of the technique to a rat model of emphysema in Chapter 7 where the lung surface to volume ratio is decreased through alveolar destruction.

As some final notes, krypton is obtained from air liquefaction at approximately tenfold lower cost than xenon - i.e. approximately US$ 0.80 – 1.00 per litre gas with a natural abundance of 11.49% (see Table 2.1). Unfortunately, due to rare demand the costs for isotopically enriched ^{83}Kr is currently about US$ 5000 per litre. As a consequence of the extremely low gyromagnetic ratio, ^{83}Kr T_2 relaxation times are typically much longer than that of ^{129}Xe. Furthermore, due to its low γ , the ^{83}Kr T_1 relaxation in rat lungs is not affected by the presence of up to 40% paramagnetic oxygen [214]. Note that although hp ^{83}Kr may dissolve in many tissues, the useful signal associated with its dissolved phase is lost owing to fast quadrupolar relaxation. Finally it should be noted that there are few toxicological concerns for the future clinical applications of hp ^{83}Kr as krypton is chemically inert and does not exhibit anesthetic properties at ambient gas pressure [174, 217].

Chapter 3: Hyperpolarized noble gas MRI of small animal models of respiratory disease

3.1. Chapter Aims

Small animal models as opposed to human studies are often used for disease research and drug development because 1) there is a homogenous aetiology in the animal model as opposed to the heterogeneous aetiologies often present in many human diseases, 2) there is the ability to correlate the results with established histological measurements, and 3) there is the ability to monitor lifetime changes over very short timeframes [218]. However, despite these benefits there are some compromises and important differences between the human diseases and the induced animal model. This Chapter therefore aims to outline the choice of animal models, which will be utilised within the context of this thesis. Furthermore, as has been explored in Chapter 1 the scaling down of lung function and imaging methodologies to small animals produces several technical challenges, making measurements of functional endpoints more difficult in small animals than in larger mammals. The additional complexity performing small animal hyperpolarized (hp) noble gas imaging experiments *in vivo* also necessitates an explanation of the principles and practice to understand the usefulness and potential advantages of the *ex vivo* lung model with hp gas imaging.

3.2. Small animal modeling of respiratory disease

Animal models are the only system available at present for modelling the *in vivo* processes of human asthma and emphysema, facilitating significant contributions towards a better understanding of the pathophysiology of these diseases. These models have allowed mechanistic studies whereby a mediator or process can be investigated. Furthermore, as outlined in Chapter 1, endpoints such as airflow limitation and airway remodelling can be monitored.

Animal models, particularly rodent models, are the ideal candidate for rapid throughput investigation of asthma and emphysema using hp noble gas MR imaging. As mentioned earlier and in Chapter 1, these small animal models are cheaper and easier to set up than human studies and because experimental, unlicensed substances are often being tested, they are a necessary part of the process to gain wider acceptance for human use.

It should be noted that no animal model entirely recreates the human disease as all animal models involve inducing an allergic response in an otherwise healthy animal, often with antigens to which they would not normally be exposed, in the case of small animal asthma models, or inducing acute structural changes in response to a single insult (or series of insults) as in the case of emphysema models. These models aim to mimic some of the mechanistic and/or pathophysiological elements of the disease, which is based on our current incomplete understanding.

3.2.1. Small animal models of asthma

The vast majority of asthma models are of allergic asthma as this is the most predominant form in humans. Sheep are thought to be the most representative models of human asthma allowing multiple inhaled challenges of *Ascaris suum* antigen to which they can become naturally sensitised [219]. The acute and late phase reaction have been well documented with increases in airway hyperresponsiveness (AHR) to bronchoconstrictors and a predominant eosionophilia on bronchoalveolar lavage [220-222].

There are, however, a multitude of rodent models of asthma with the most established centring around mice, rats and guinea pigs [219, 223]. In the context of this thesis allergic asthma with an increase in AHR is the entity to be studied so this will be the focus of following discussion.

3.2.1.1. Ovalbumin model of allergic asthma

The ovalbumin (OVA) model of allergic asthma is currently the best characterised in all rodent species [219, 223-225]. It causes an immune mediated allergic airways disease that replicates many features of human asthma including AHR and can lead to sub-epithelial fibrosis and epithelial and smooth muscle cell changes seen in airway remodelling.

There are a multitude of dosing regimes available. The process typically involves sensitizing the animal by one or two intraperitoneal or

subcutaneous injections of OVA mixed with an adjuvant, usually $Al(OH)_3$ (alum) to prime the desired T-helper 2 cell response.

After sensitization the animals are challenged repeatedly with OVA delivered to the airways. Aerosolized delivery through a nebulizer or by the intra-nasal or intra-tracheal routes can be performed. Within 24 - 48 hours after the airway challenge the maximal allergic response is found in the lungs.

Inter-species differences occur and are summarized in table 3.1. Guinea pigs develop the largest AHR as they have the most muscular airways with high levels of cholinergic (constrictive) and non-cholinergic (relaxant) innervation [224].

Aspect of human asthma modeled	Guinea Pigs	Rats	Mice
IgE dependent	× Mainly IgG_1	✓	Either IgE or IgG_1
Th2 Response	✓	✓	✓
Acute Phase Reaction to antigen	✓	✓	×
Late Phase Reaction to antigen	✓	✓	✓
Acute Airway Response regulators	Histamine Leukotrienes	Serotonin Leukotriene D_4	Serotonin Leukotriene D_1
Airway Hyper-responiveness to bronchoconstrictors	✓ Pronounced	Recorded	Recorded
Pulmonary eosinophilia	✓	✓	✓
Mucus hypersecretion	✓	✓	✓
Airway oedema	✓	✓	✓

Table 3.1.- Summary of aspects human asthma modelled by each of the common rodent ovalbumin models. Adapted from ref. [224].

Guinea pigs would therefore seem to be the ideal model with the most responsive airways and an early phase response regulated by histamine and leukotrienes as it is in humans [226] but the response is mainly IgG_1 mediated and guinea pigs have been shown to suffer seasonal eosinophilia confounding results. In addition, limited transgenic technology has resulted in the guinea pig model falling out of favour.

Mice and rats show considerable strain variation in response to OVA [227-231]. Inbred rat and mice strains with predictable responses to the inflammatory models are used to reduce the effects of genetic variability and hence the number of animals required. In addition, the Brown Norway

rat (BNR) and the Balb/C mouse are the most frequently used as they are known to be high IgE responders. C57/BL6 mice have also been used as they show a similar IgE response and there are many knockout variants available but they have been shown to have less smooth muscle hypertrophy and hyperplasia with less AHR [228].

Rats are often preferable to mice because they are large enough to allow handling and in particular with hp ^{129}Xe MR imaging will facilitate development of imaging techniques in contrast to mice where tidal volumes are very low, adding increasing technical difficulties.

The hallmark of asthma is variable airflow obstruction [232]. BNR rats have been reported to develop, acute and late phase allergic responses to common antigens [224, 233].

Although BNR show the development of tolerance to antigens, the responses are more predictable and initially the airways become increasingly sensitive to bronchoconstrictors with cumulative doses of OVA [230, 234] although it should be noted that this tends to plateau after 3 - 6 challenges in mice and so is likely to be similar in rats due to tolerance [235, 236]. Belvisi and co-workers however noted a difficulty reproducing this AHR to methacholine (MCh) and bradykinin in the BNR, noting that the response that had been found by other groups earlier was rather weak [65]. They postulated that weakening of the BNR response may have been due to methodological issues with the study in terms of animal sensitization protocols or different measurements of AHR. They

also suggested that it is possible that there is variation between BNRs obtained from different suppliers. Allakhverdi et al. did however record considerable bronchial responsiveness to leukotrienes of OVA sensitized BNRs [237].

BNR and Balb/C mice have been noted to develop airway-remodelling changes as seen in humans [238, 239]. A chronic model with loss of the inflammation after cessation of OVA challenges and loss of AHR was seen by Hove et al. in 2009 [228].

3.2.1.2. Alternative models of allergic asthma in the rat

Other common sensitizing agents used in rats and mice are human allergens such as house dust mite (HDM) extract or the fungus *Aspergillus fumigatus* [224, 235, 240]. In addition, the parasite pig roundworm *Ascaris suum* has been used [241].

Of these models most interest has centred around the use of HDM. It like the OVA model involves sensitization of the animal by subcutaneous injection of HDM extract followed by a respiratory challenge [224]. It has been shown that continuous intranasal exposure where the antigen is instilled 5 days per week over 5 - 7 weeks can also produce the same results in mice and that this might be a more comparable model as it mimics more closely the situation with human exposure to antigens [235].

3.2.2. Small animal models of emphysema

Chronic obstructive pulmonary disease (COPD) is a lung disease characterised by the limitation of airflow that interferes with normal breathing and is not fully reversible [1]. There are four different lesions within COPD, namely: emphysema where there is alveolar destruction and a reduction in lung surface area for gas exchange with an associated loss of lung elasticity; small airway remodelling where the distal airways become increasing narrowed, limiting airflow; chronic bronchitis where there is goblet cell proliferation and mucus hypersecretion; and pulmonary hypertension [242]. In the context of this thesis, emphysema with the reduction in lung surface area is the entity being considered so will be the focus of the following discussion.

3.2.2.1. Species differences

In terms of the species of choice for small animal models of emphysema, the guinea pig is generally favoured because it has larger numbers of branching than do rats or mice and alveolisation of guinea pig lungs has been completed at birth, compared to between days 4 – 14 in rats and mice [243]. However it should be noted that for all rodents there are no true respiratory bronchioles present with alveoli only located within the terminal alveolar sacs [244]. This major difference should be borne in mind particularly as smoke related damage in humans suffering from

COPD is seen not only in the terminal alveolar ducts and sacs, but also within the level of the respiratory bronchioles [245].

3.2.2.2. Cigarette smoke exposure model of COPD

Inhalation of cigarette smoke is the major factor linked to the development of COPD in humans [246]. There are over 4000 toxic chemicals and $>10^{15}$ free radicals delivered to the respiratory tract by each puff of cigarette smoke [247, 248]. The cigarette smoke exposure model is therefore considered to be the most clinically relevant of all the animal models currently available with the ability to reproduce the multifaceted response to smoke seen in the vast majority of human COPD [249]. The model takes at least 6 months to develop with the animal either housed within the smoking machine and cigarette smoke delivered continuously or intermittently, or there is daily exposure to cigarette smoke via a nose cone for several hours during model generation [250-252]. There are a plethora of cigarette smoke delivery devices in operation and a variety of cigarette brands being studied, however, all centres report the development of varying degrees of lung damage similar to those found in human COPD with a dose dependence [242]. The emphysematous lesions produced involve dilation of the alveolar ducts and an increase in the number and size of the Pores of Kohn (see Chapter 1, Section 1.2 for details) similar to that in human emphysema [253], however the degree of damage tends to be on the mild – moderate spectrum of human emphysema with little overt tissue destruction [254, 255]. Nonetheless significant small airway remodelling and goblet cell changes within the

airways are produced, characteristic of the chronic bronchitis components of COPD. Furthermore, notable functional changes are seen to develop within animals with reduced airflow and FEV/FVC ratios [256-258].

Generally it is considered that guinea pigs are the best rodent species for the smoke exposure model due, in part, to the aforementioned similarities to the human respiratory system but also because of their ability to develop easily recognisable emphysema and large amounts of goblet cell hyperplasia. However, guinea pigs are expensive to house and keep and, as documented in Section 3.2.1.1., transgenic technology is often limited.

Rats and mice are, by comparison, cheaper with widespread availability of transgenic strains (particularly notable with mice), but it has been noted that rats are a poor species for a cigarette smoke exposure model as they either develop minimal disease or will develop non-specific particle overload when cigarette smoke dosages are increased in an attempt to generate a representative model [259].

3.2.2.3. Elastase model of emphysematous alveolar destruction

The elastase model of emphysema by comparison to the cigarette smoke exposure model produces rapid, dose dependent, emphysematous lung damage, is relatively cheap, and is less technically demanding to implement [242, 249]. The model involves the instillation of an elastolytic enzyme to the lung by either the intra-tracheal or aerosolised route. This model was central in the development of the proteinase – anti-proteinase theory of emphysema and was initially developed after the discovery that humans suffering from α_1-antitrypsin deficiency developed large amounts of emphysematous lung damage [260].

Initially the plant protease papain was utilised but it was found that pancreatic porcine elastase (PPE) or human neutrophil elastase (HNE) are easier to use with less importance placed on the manufacture process [261]. HNE is generally considered better for drug development studies looking at exogenous inhibitors as it is inhibited to a greater degree by α_1-antitrypsin [262].

Both HNE and PPE models produce an initial acute alveolitis with large numbers of neutrophils and lymphocytes, haemorrhage, pulmonary oedema and rupture of the respiratory epithelium. The inflammation peaks at 24 – 48 hours and then largely resolves by 7 days with the development of emphysematous damage until week 8 with notable emphysema that is unresponsive to steroid treatment [263]. The model

also produces the characteristic functional changes of reduced airflow, gas trapping and reduced FEV/FVC ratios seen in human emphysema.

The elastase model of emphysema is considered to be suitable for screening of mechanisms and/or interventions that could apply to human disease when resources are limited and the generation of a 6 month long cigarette smoke exposure model is not possible [242].

3.2.2.4. Other models of emphysema

Several other animal models of emphysema are available including the apoptotic model of emphysema where a drug which interferes with the vascular endothelial growth factor (VEGF) or its receptor is delivered to the lungs [264, 265]. This model, like the starvation model [266, 267], does not tend to produce the characteristic irreversible changes of alveolar destruction seen with the cigarette smoke exposure or elastase models and so will not be covered further within this thesis.

3.3. Requirements for hyperpolarized noble gas MRI in small animals

3.3.1. Anaesthesia and intubation

Anaesthesia is necessary to reduce the stress of imaging experiments and to ensure constant restraint of the animal reducing movement during imaging experiments [268]. In addition, the invasive and technically difficult procedures of rodent intubation and ventilation are necessary for hp gas imaging, requiring deep anaesthesia often with the use of neuromuscular blocking drugs. The use of an anaesthetic in small animals with large surface area to volume ratios can result in hypothermia if constant warming during experiments is not performed [269].

Inhalational anaesthetic agents are commonly used with small animals as cardiovascular function is better maintained. However with hp gas imaging the inhalational route is not commonly used with the requirement for injectable agents, which produce greater degrees of cardiovascular depression and longer recovery times. For instance, intraperitoneal delivery of barbiturates can produce high mortalities in rats and mice [270]. Furthermore, during repeat studies where physical and mental stress can confound experimental results this can become problematic.

As with the other invasive measures of lung function detailed in Chapter 1, endotracheal intubation is required to allow precise control of ventilation volumes, prolonged breath-holds, and in the case of hp gas imaging to

avoid contamination with air (with varying O_2 concentrations). Usually a seal is formed around the endotracheal tube by applying putty around the catheter or if a tracheostomy is performed the endotracheal tube can be secured with a ligature producing a tight seal [23].

3.3.2. Hardware requirements

The challenge of producing images of small lung structures in rodents has produced considerable differences in imaging strategies with significant variation in the image resolution obtained, as will be discussed in section 3.2.4. Nonetheless, using hp ^{3}He MRI, typical *in vivo* resolution in the rat of approximately 300×300 μm^2 with slice thicknesses of < 5 mm is possible [93, 132, 271]. As detailed in Chapter 2, *in vivo* resolution with hp ^{129}Xe imaging tends to vary more between groups due to the technical difficulties in producing high degrees of polarization, but at the pinnacle Driehuys et al. have achieved resolution of the order 310×310 μm^2 in the rat [272]. To achieve this level of resolution requires the MRI hardware to be of the highest standard with dedicated microimaging systems with very homogenous B_0 fields, specialized RF transmit-receive coils (often dual frequency tuned to the noble gas nucleus and ^{1}H) and high quality gradient subsystems [23].

3.3.3. Hp gas compatible ventilators

In addition to the hardware difficulties with the MRI system, there is the additional requirement of MRI compatible ventilation systems that can preferably be operated in strong magnetic fields. Ventilators should be capable of repeatedly delivering precision volumes allowing for reproducible breathing motion [273-275] thereby reducing partial volume blurring and other artefacts such as image ghosting, degrading image resolution and obscuring anatomical detail. Ventilators must have an asynchronous mode where ventilation rate, inspiratory pressures and / or volumes can be set for animal maintenance but with the ability for ventilation to be brought into synchronicity with the MRI system and indeed to trigger the MRI system, allowing for imaging at various stages of the ventilatory cycle.

Unfortunately standard small animal MR compatible ventilation systems are not usually appropriate due to unacceptable degrees of hp gas depolarization before delivery to the animal [275, 276] requiring valves to be made of non-magnetic components. There is also the requirement to mix hp gases as close to the animal as possible due to the paramagnetic effect of O_2, with the O_2 or medical air mixed at the last possible moment [277]. Furthermore, dead space between the ventilator and the lungs should be kept to a minimum to ensure replenishment of air / O_2 and to optimize hp gas delivery to the lung. In the mouse this is a particular problem where tidal volumes are low (approximately 200 μL or one tenth

that in the rat) and due to high pulmonary impedance, problems occur if fine-bore ventilation lines are used. As a solution Chen et al. devised a 'Y' ventilation piece to which the endo-tracheal tube attaches thus significantly reducing the dead space to allow more effective gas delivery and exhalation [278-280].

There are several ventilator and control system in use for this situation. A simplified version is shown in Fig. 3.1 where the hp gas compatible ventilation system is connected to the anaesthetized and intubated rodent and set to constant respiratory rate (*RR*) and tidal volume (*TV)* ventilation with limits put in place if the positive (inspiratory) intermittent pressure (*PIP*) rises too high. As mentioned the ventilator triggers both the release of hp gas and synchronizes the acquisition with the MRI scanner.

One of the most widely used hp gas ventilation systems is that developed by Hedlund et al. at Duke University [275, 281, 282]. The ventilator is controlled by a specifically written LabVIEW® program (National Instruments, Austin, Texas, USA), which allows monitoring and control of such variables as: *PIP*; *RR*; *TV*; inspiratory, expiratory and breath-hold duration; and expiratory venting to passively deflate the lungs to *FRC*. Synchronization of the MRI system with various stages of the respiratory and cardiac cycle is also possible (see section 3.2.4.). In addition, the software provides on screen physiological monitoring from various sources such as electrocardiograph monitoring (ECG), peripheral oxygen saturation (SaO_2), end expired CO_2, and body temperature.

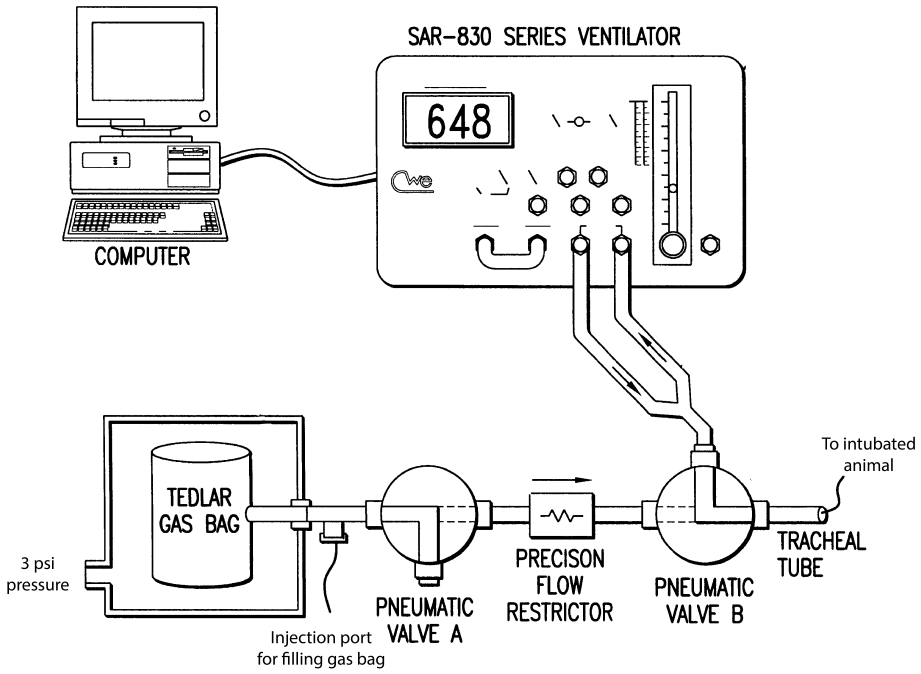

Figure 3.1. Example of small animal hp gas ventilation arrangement. The ventilator is attached to a computer control system to set resting ventilatory parameters with medical air or O_2 and to control pneumatic valves A and B (for switching to delivery hp gas located in the Tedlar® bag) and triggering of MR imaging sequence. The flow restrictor reduces the pressure of gas delivered to the lung and is used to measure volumes of hp gas delivered. Adpated with permission from [283].

The majority of ventilator systems require the hp gas produced by the hyperpolarizer to be collected in a Tedlar® bag (DuPont, Willmington, Delaware, USA) and kept in a non-varying magnetic field to reduce the rate of depolarization [284]. The reservoir containing the hp gas is then placed inside a pressurized chamber to produce a continuous flow of hp gas. The hp gas flow rate is usually governed by a flow restrictor with a pneumotachometer, thereby allowing determination of the volume inspired during each ventilation (see Figure 3.1). Most systems can be used

to deliver inhaled anaesthetic gases whilst hp gas is not being used but this is not routine practice.

3.3.4. Hp gas imaging sequences including respiratory gating

As with micro-CT and proton MRI the rapid respiratory and cardiac rates produce additional challenges for *in vivo* hp gas imaging in small animals often requires acquisition of single images over multiple breaths. Image blurring between breaths is reduced by the high quality, precision ventilators but cannot be totally eliminated due to slight inter-breath differences. Cardiac gating has not been reported in rodents to date but is largely compensated for by signal averaging over multiple breaths. More troublesome however, is the effect of gradient induced diffusion attenuation, particularly with ^{3}He, with the result that radial *k*-space encoding methods have been able to produce higher resolution than more traditional Cartesian methods [22].

Some of the earliest work with hp gas imaging *in vivo* utilized a radially acquired projection reconstruction technique developed from proton MRI sequences [271, 285, 286] where imaging was triggered on each breath of hp ^{3}He. This non-standard paradigm reduced rapid diffusive attenuation seen in the airways with ^{3}He and allowed for a 2D CINE sequence with an in plane resolution of around 195 × 195 μm^2 in the rat over 150 breaths (approximately 2 mins per slice). Images were provided at various stages of the respiratory cycle with averaging over multiple scans to minimize the effect of cardiac motion. By altering the flip angle between images it was

possible to highlight different lung structures producing images with fine detail of the airways [271] and demonstrating changes in regional ventilation and airway calibre after delivery of intravenous methacholine (MCh) in Fischer rats [286].

Similarly Chen et al. followed this up using a 3D anisotropic radially encoded sequence again triggered on the start of ventilation [279]. The group was able to obtain resolution of $70 \times 70 \times 800$ μm^2 in the mouse but required 25 min to collect the images and over 1.2 L of ^{3}He. This was however adapted by the group to significantly shorten image acquisition times in the mouse while avoiding the reduction in SNR due to diffusive attenuation [22, 287]. The technique acquired 20 - 40 radial *k*-space lines per breath, with around 800 radial projections of *k*-space sampled over 40 breaths for a single 2D image, taking around 12 s [22]. The images were able to detect differences in sensitivity to a bolus of MCh between control and ovalbumin sensitized mice and image the time courses after the bolus (see Fig. 3.2). 3D radially acquired images were also produced with anisotropic voxels of 125 × 125 × 1000 μm^3 but requiring 5.8 minutes to produce.

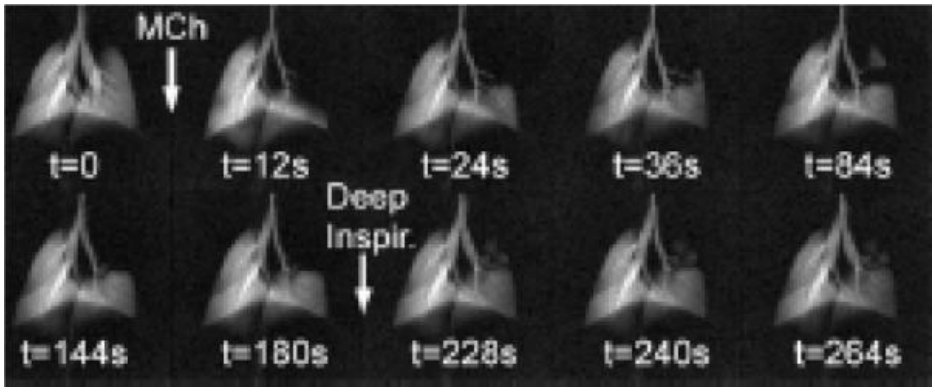

Figure 3.2. Hp ^{3}He non-slice selective coronal images from an un-sensitized C57BL/6 mouse after bolus of 250 µg/kg MCh. Images taken at time after MCh bolus. Note large collapse upper left lung with some improvement over time and after deep inspiration. Reproduced with permission from [280].

More standard methods such as those based on the FLASH (fast-low-angle-shot) gradient echo sequence have been reported with both the constant flip angle [288, 289] and the variable flip angle paradigms [93, 290]. Resolution has been lower in part due to the effect of diffusive attenuation. However application of partial gradient echo [282] and / or Cartesian trajectories which start near the centre of k-space, such as centric acquisition, can help to minimize this effect [23].

3.4. *Ex vivo* hp noble gas MRI

As has been highlighted in this Chapter, there are many difficulties performing hp noble gas MR experiments in small laboratory animals *in vivo*. It will therefore be shown in the subsequent chapters that the technically less demanding *ex vivo* arrangement is capable of producing important and relevant physiological measurements while providing a platform to allow for development of new hp gas MR imaging protocols and techniques which would simply be impractical or infeasible in the living animal.

Chapter 4: Functional hyperpolarized ^{129}Xe MRI of the healthy *ex vivo* rodent lung

The work in this chapter has been published as an article in the peer-reviewed journal PLosONE entitled "Validating Excised Rodent Lungs for Functional Hyperpolarized Xenon-129 MRI" by David M.L. Lilburn, Theodore Hughes-Riley, Joseph S. Six, Karl F. Stupic, Dominick E. Shaw, Galina E. Pavlovskaya, and Thomas Meersmann [291]. Credits for the work were as follows: Dr. Lilburn, Dr. Pavlovskaya and Prof. Meersmann conceived the experiments; Dr. Lilburn, Mr. Hughes-Riley, Mr. Six, Dr. Stupic, Dr. Pavlovskaya and Prof. Meersmann performed the experiments; Dr. Lilburn handled the animals and completed the lung extraction process; Dr. Stupic and Dr. Pavlovskaya designed and constructed the noble gas hyperpolarizer; Dr. Pavlovskaya created and tested the hyperpolarized gas MR imaging sequence; Dr. Lilburn, Dr. Shaw and Prof. Meersmann analyzed the data; and Dr. Lilburn, Dr. Shaw and Prof. Meersmann wrote the paper.

4.1. Introduction

As has been documented in the pervious chapters, the use of animal models of pulmonary diseases is well established in many areas of biomedical research, however *in vivo* functional respiratory measurements of ventilated and anaesthetized small animals are technically challenging to achieve [4, 7, 8]. *Ex vivo* ventilated lungs have been used as a model to investigate airway responses [10-12] and several investigators have since utilized isolated and perfused rodent lungs to study lung vascular function in the absence of systemic interactions [13-19]. In addition isolated and perfused murine lungs have been used to investigate pharmacokinetics of inhaled aerosols [20, 21].

Previously Uhlig et al. have performed technically challenging experiments on the intact *ex vivo* murine lungs examining both the airway and the vascular responses to intravenous delivery of a variety of pharmacologically active substances including methacholine, serotonin, endothelin-1 and leukotriene C_4. [292]. The reported changes in airway resistance and vasoconstriction correlated well with the results obtained from precision cut lung slice models

The significant difficulties performing MR measurements on anaesthetized and ventilated small animals documented in Chapter 3, including logistical concerns when locating MR hardware close to animal experimental facilities, has thus far limited the technique of hyperpolarized noble gas imaging to a few, highly specialized, research centres. The use of *ex vivo*

lung models in conjunction with hp gas MRI therefore offers the opportunity to reduce the experimental complexity. The combination should also facilitate rapid development and testing of hp gas MRI protocols whilst allowing the study of regional lung responses in the absence of systemic effects. Furthermore, *ex vivo* pulmonary MRI allows for tests of lung function using protocols, such as prolonged breath holds or the omission of oxygen, that may be beneficial for obtaining certain parameters but that are not feasible for studies with living animals. Finally, *ex vivo* lung models may reduce the severity of the procedure to the experimental animals minimizing regulatory approval requirements, whilst potentially providing a solid platform for rapid drug development and advancement.

4.2. Materials and Methods

4.2.1. Animal care and preparation

The University of Nottingham Ethical Review Committee approved the study, which was carried out in strict accordance with local animal welfare guidelines and the UK Home Office Animals (Scientific Procedures) Act 1986. All efforts were made to minimize animal suffering.

Healthy male Sprague-Dawley rats (175 - 300 g, n = 20, Charles River UK Ltd, Margate, UK) and Dunkin Hartley guinea pigs (200 - 300 g, n = 8, Harlan UK Ltd, Shardlow, UK) were terminated by overdose of pentobarbital (Sigma-Aldrich Ltd, Gillingham, UK). After confirmation of death, surgery was performed postmortem. A catheter was inserted into the right ventricle or caudal vena cava to permit flushing of the pulmonary circulation with heparin-saline solution (Wockhardt UK Ltd, Wrexham, UK) followed by Dublecco's phosphate buffer solution (D-PBS, Sigma-Aldrich Ltd, Gillingham, UK) to remove the remaining blood from the pulmonary circulation.

The heart and lungs were subsequently removed *en masse*. A plastic adapter tube was placed 5 - 10 mm above the carina and sutured into place. The heart and lungs were then transferred into a custom-built acrylic ventilation chamber with the lungs suspended in 5% glucose solution (weight/volume) (Baxter Healthcare Ltd, Thetford, UK) to minimize dehydration or swelling of the tissues [293] with the trachea

pointing downwards as detailed in Fig. 4.1. In this situation it is known that there is a pressure gradient of no more than 0.5 kPa (5 cm H_2O) from the base to the apex of the lung as the fully expanded lung never exceeded 5 cm in length. The *ex vivo* lungs were checked on repeated inflations with 4 - 5 mL of ambient air for leakage either from the suture around the trachea or the lungs themselves. The lungs were chilled for transportation to the imaging facility with temperature maintained, well above the freezing point, at 278 K. The transfer time from extraction to the experiment facility was approximately 90 min. After transportation, the lungs were then passively warmed to ambient temperature before imaging experiments.

Of the 20 rat lungs extracted, 14 were suitable for *ex vivo* hp ^{129}Xe MR imaging with the others being rejected due to the development of leaks either at the time of extraction or during transport. It should however be noted that the success rate for rat lung extraction improved to close to 80 – 90% by the end of the study once the procedural skill of the operator had significantly improved. By contrast, of the guinea pig lungs harvested, 5 were rejected due to significant gas trapping with the remaining 3 used for *ex vivo* hp ^{129}Xe MR imaging. During the guinea pig work operator dependent issues were not a concern due to significant experience having been developed during the earlier rat lung work.

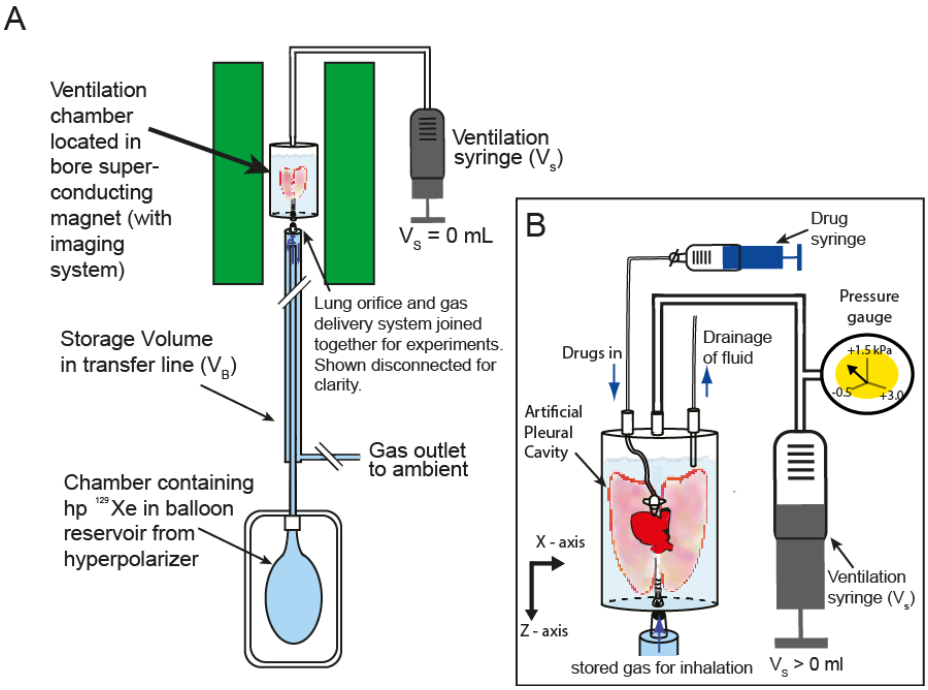

Figure 4.1. Outline of the hyperpolarized ^{129}Xe gas delivery to the *ex vivo* lung. (A) Experimental *ex vivo* setup with hp ^{129}Xe administered from a balloon reservoir chamber into the storage volume (V_B) before being inhaled by the lung. The lung is caused to inhale (exhale) by the negative external 'pleural' pressure applied via the suction volume (V_s) from the ventilation syringe upon the artificial pleural cavity; (B) *Ex vivo* lung submerged with its orifice down (sutured to a cannula) in 5% glucose solution within the ventilation chamber with its posterior-anterior axis aligned in z-direction. In this sketch, a negative pleural caused by V_s pressure (measured on the pressure gauge as indicated) leads to a partial inflation of the *ex vivo* lung, inhaling a selected gas (hp ^{129}Xe, or N_2 or O_2) from the storage volume V_B. Drugs are administered via a cannula sited in the right ventricle with the excess fluid outlet located below the fluid level in the chamber. Ventilation pressures were measured using the pressure gauge attached to the ventilation syringe as indicated in the figure. All resulting MR images shown in subsequent figures are depicted with lung orifice pointing upwards.

4.2.2. Production of hp ^{129}Xe

Hp ^{129}Xe was produced in batch mode using spin exchange optical pumping (SEOP) [160] of a gas mixture containing 25% Xe (enriched to 83% ^{129}Xe, Nova Gas Technologies, Charleston, SC, USA) and 75% N_2 (99.999% pure, Air Liquide, Coleshill, UK). Low pressure SEOP was performed at 40 kPa [294] followed by expansion of the hp gas into the evacuated balloon reservoir in the hp gas extraction unit . The chamber allows for the recompression of the hp gas to ambient pressure and thus makes it available for inhalation as reported in ref. [215]. The hp xenon delivered to the excised rodent lung for inhalation was spin polarized to = 40% with an apparent spin polarization was = (40 ÷ 4) % = 10% once accounting for the fourfold dilution in the dilute xenon mixture (see section 2.2.3. and ref. [294]).

4.2.3. *Ex vivo* lung ventilation

Active inhalation of air or hp ^{129}Xe inside the magnet was accomplished by a small degree of suction provided by a ventilation syringe that causes the lung to inflate as previously demonstrated with hp ^{83}Kr [214, 295]. Briefly, negative pressure was applied to the artificial pleural cavity of the breathing apparatus by creating a desired suction volume V_s within the air filled ventilation syringe shown in Fig. 1. The application of the suction volume V_s typically leads to 'pleural pressures' in the artificial pleural cavity around -0.5 to +3 kPa (-5 to +30 cm H_2O) causing the lungs to inflate and therefore inhale a volume V_i. Due to the use of the compressible fluid

(i.e. air) within the ventilation syringe and the tubing, the inhaled volume V_i was not identical to V_s but was determined experimentally. Following inhalation to V_i, this gas volume was completely exhaled through an increase in the pleural pressure by the reversal of the suction volume to V_s = 0. The exhaled gas was channelled via teflon tubing into a water bell located outside of the magnet. The exhaled gas volume is determined directly by the volume of displaced water. The average V_i values obtained in 3 healthy lungs as a function of the suction volume V_s are listed in Table 4.1.

	Rat weight (g)			
	275	**255**	**300**	
Syringe suction volume, V_s **(mL)**	**Corresponding inhaled volume, V_i (mL)**			**Average V_i (mL)**
0.5 ± 0.1	-	-	0.3 ± 0.1	**0.3** ± 0.1
1.0 ± 0.1	0.3 ± 0.1	0.2 ± 0.1	0.5 ± 0.1	**0.3** ± 0.1
1.5 ± 0.1	-	0.5 ± 0.1	-	**0.5** ± 0.1
2.0 ± 0.1	0.5 ± 0.1	1.2 ± 0.1	1.1 ± 0.1	**0.9** ± 0.2
2.5 ± 0.1	-	1.5 ± 0.1	-	**1.5** ± 0.1
3.0 ± 0.1	1.4 ± 0.1	2.2 ± 0.1	1.7 ± 0.1	**1.8** ± 0.2
4.0 ± 0.1	2.2 ± 0.1	3.3 ± 0.1	2.1 ± 0.1	**2.5** ± 0.2
5.0 ± 0.1	2.9 ± 0.1	3.6 ± 0.1	3.3 ± 0.1	**3.3** ± 0.2
6.0 ± 0.1	3.9 ± 0.1	5.0 ± 0.1	4.2 ± 0.1	**4.4** ± 0.2

Table 4.1. Relationship between syringe suction volume and inhaled gas volume. Applied suction volumes, V_s, with corresponding values for inhaled volume, V_i, determined by the water bell method. Errors listed are experimental relative errors. The omitted values were not determined.

4.2.4. Ventilation Schemes

Prior to hp gas administration the lungs were purged of oxygen. The transfer line with storage volume V_B (Fig. 4.1a) was flushed with N_2 (99.999% pure, Air Liquide, Coleshill, UK) and the lungs were ventilated 8 - 10 times with N_2 to remove any residual O_2. The hp gas was then delivered into the storage volume V_B and a suction created through V_s was applied to the artificial pleural cavity causing the lungs to inhale the hp gas. The maximal V_s applied to create suction was 5 - 6 mL during all experiments, equating to an inhalation volume V_i of 4 - 5 mL depending on the *ex vivo* lung as detailed in Table 4.1. In order to target specific regions of the lung, gas was inhaled at different stages of the ventilation cycle. For instance, a small amount of the hp gas was inhaled at the start of the inhalation followed by 'dark' (non hp) gas, usually N_2, or a small volume of hp gas was inhaled at the end of the inhalation following the initial dark gas inhalation to localize the gas to different regions of the lung.

4.2.5. Bronchoconstriction and reversal

Animals used for airway responsiveness experiments had the catheter used for flushing of the pulmonary circulation retained with the cranial and caudal vena cava ligated to ensure drug delivery to the pulmonary circulation. The cannula was sutured into place and attached to a fine perfluoroalkoxy (PFA) tube passed through a modified ventilation chamber as detailed in Fig. 4.1b with the drug syringe located outside the superconducting magnet.

In order to satisfy tissue metabolic demands, the storage volume V_B was flushed with 50 mL O_2 prior to hp gas delivery whilst the lungs were ventilated 8 – 10 times with the oxygen. This was followed by purging the transfer line with N_2 prior to hp ^{129}Xe delivery as described above.

Bronchoconstriction was achieved by injecting methacholine (Sigma-Aldrich Ltd, Gillingham, UK) through the pulmonary circulation. For rat and guinea pig lungs, 60 μg and 10 μg of methacholine (MCh) dissolved in 1 mL 0.9% saline solution (Baxter Healthcare Ltd, Thetford, UK) were used respectively. The methacholine solutions were delivered using the drug cannula at a rate of 1 mL/minute and were followed by a 2 - 3 mL bolus of 5% glucose solution over 2 – 3 minutes to ensure complete drug delivery through the pulmonary circulation. The MCh dosage for rats was arbitrarily chosen on the basis of previous work where it has been seen that the maximum effect *in vivo* occurs at approximately 100 μg/kg (i.e. 30 μg for a 300 g rat) so a dose double this was chosen to ensure efficacy since the absorption within the *ex vivo* model was unknown [286, 296]. For guinea pigs, it is known that this species is approximately a factor or 3 - 4 more sensitive to MCh [297]. Therefore an appropriately lower dose was chosen, although this was reduced further to 10 μg due to the significant issues with gas trapping seen within some of the guinea pig lungs.

Reversal of bronchoconstriction was produced by flushing the challenged lungs with 5 – 10 mL 5% glucose solution and 1000 μg of salbutamol

(Allen and Hanbury's Ltd, Middlesex, UK) dissolved in 1.0 mL of 0.9% saline solution over 6 – 11 minutes with the lungs from both species of animal.

4.2.6. Pulmonary MRI

Imaging experiments were performed using a 9.4 T vertical bore Bruker® Avance III microimaging system (Bruker Corporation, Billerica, Massachusetts, USA). A custom-built 25 mm low-pass birdcage volume coil tuned to the resonance frequency of ^{129}Xe gas in the lung of 110.69 MHz was used in all experiments. Spectroscopic data were collected using experimental schemes (discussed in Results- section 4.3.) using 3^0 hard pulse of 4.47 μs at 53 W. Images were acquired using a modified variable flip angle (VFA) FLASH gradient echo pulse sequence [177]. Hard pulses of 134 μs and sinc-shaped pulses of 1000 μs at variable power levels were used for non-slice-selective and slice-selective image acquisitions. An individual phase increment was recorded during 2.61 ms; subsequent phase increment acquisitions were separated by 214.5 ms. Therefore the total acquisition time for an image with 128 × 64 resolution was 13.8 s. All coronal images were acquired in 128 × 64 image matrices with field of view (FOV) of 46.9 mm and 30.0 mm in the superior and inferior direction, respectively. Slice thickness in slice-selective imaging experiments was 4 mm with the slice-selective frequency offset corresponding to the excitation of the central slice, selected to transect the lungs through the major airways, that is, the trachea, carina and first order bronchi.

4.2.7. Image processing and analysis

Raw data were analyzed using Prospa© (v. 3.06, Magritek, Wellington, New Zealand) where a sine-bell squared function was used to window the data in both dimensions to result in magnitude images with increased signal to noise ratio (SNR). The images were further processed using IGOR Pro© (Wavemetrics, Lake Oswego, Oregon, USA) as follows. A threshold procedure was applied to remove the background noise. To achieve this, the lower threshold was derived from the mean signal intensity plus two standard deviations obtained from a 10 × 10 voxel region randomly selected outside the lung region within the image limits [298, 299]. This value was subtracted from the intensity in each pixel of the image resulting in reduced noise images. The SNR with the threshold procedure of noise reduction typically improves by a factor of four from ~60 to ~240. Subsequent image analysis was also performed with IGOR Pro©

4.3. Results

4.3.1. Measurement of *ex vivo* lung residual volume

Hp ^{129}Xe MRI and NMR (Nuclear Magnetic Resonance) spectroscopy of excised lungs can be used straightforwardly to measure residual volume (*RV*) of excised lungs. The most basic hp ^{129}Xe protocol that can be used for *RV* determination, using non slice selective and non-spatially resolved 1D NMR spectroscopic measurements is described by Fig. 4.2:

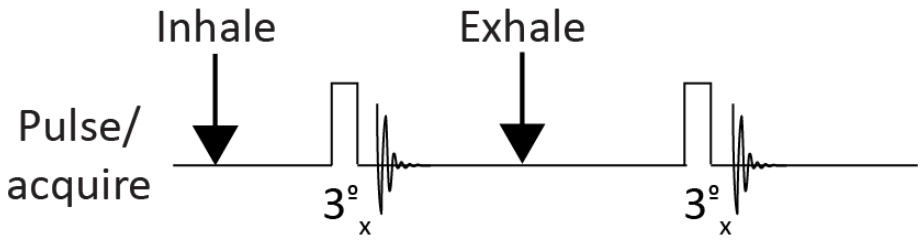

Figure 4.2. Simplified pulse sequence / inhalation diagram indicating the time-steps for acquiring 1D measurements of residual volume (RV). Initial inhalation of hp ^{129}Xe gas followed by 3° rectangular pulse with subsequent full exhale and 3° rectangular pulse. Free induction decay signals are acquired generating measurements of relative signal intensities.

Upon inhalation, the hp gas will be diluted by the gas in the residual volume *RV* (i.e. N_2 or thermally polarized, MRI non-detectable, xenon with N_2) to an unknown hp gas concentration with total volume $V_i + RV$. The residual volume, as defined in this thesis, is composed of the alveolar residual volume and, to a lesser extent, the anatomic dead space in the 'conducting zone'. The hp gas concentration will remain unchanged during exhalation. Therefore the difference between the signal intensities found

between inhalation and exhalation is caused only by the difference in the respective hp gas volumes in the lung and is not affected by the gas mixture. The signal change relates directly to the ratio of gas volume in the inhaled lung to the residual volume *RV*:

$$\frac{V_i + RV}{RV} = \frac{I^{hp}_{inhale}}{I^{hp}_{exhale}} \qquad [4.1]$$

where I^{hp}_{inhale} is the NMR signal intensity recorded with a 3° pulse from a lung with the gas phase volume $V_i + RV$ after inhalation of a V_i volume of hp gas and I^{hp}_{exhale} is the signal intensity from a 3° pulse on exhalation to *RV*.

In order to obtain the residual volume *RV*, the inhaled volume V_i for each lung was determined at a constant suction volume V_s = 5 mL (i.e. $0 \rightarrow 5mL$) using the water displacement method as described in the experimental section. The residual volume can then be calculated using:

$$RV = \frac{I^{hp}_{exhale}}{I^{hp}_{inhale} - I^{hp}_{exhale}} \times V_i \qquad [4.2]$$

The *RV* values obtained for three different, but similar sized, rat lungs are shown in Table 4.2. Please note the underlying assumption is that the lung is ventilated without areas affected by ventilation defects (i.e. non-ventilated lung regions) as further elaborated on in the Discussion section.

The second scheme uses spatially resolved experiments in order to determine the uniformity of ventilation. In this scheme the total MRI signal obtained after full inhalation of hp ^{129}Xe (i.e. V_s = 5 mL, see Fig. 4.3a) is compared with the signal of a second MRI scan obtained in a separate experiment using full inhalation of hp ^{129}Xe followed by immediate complete exhalation (Fig. 4.3b).

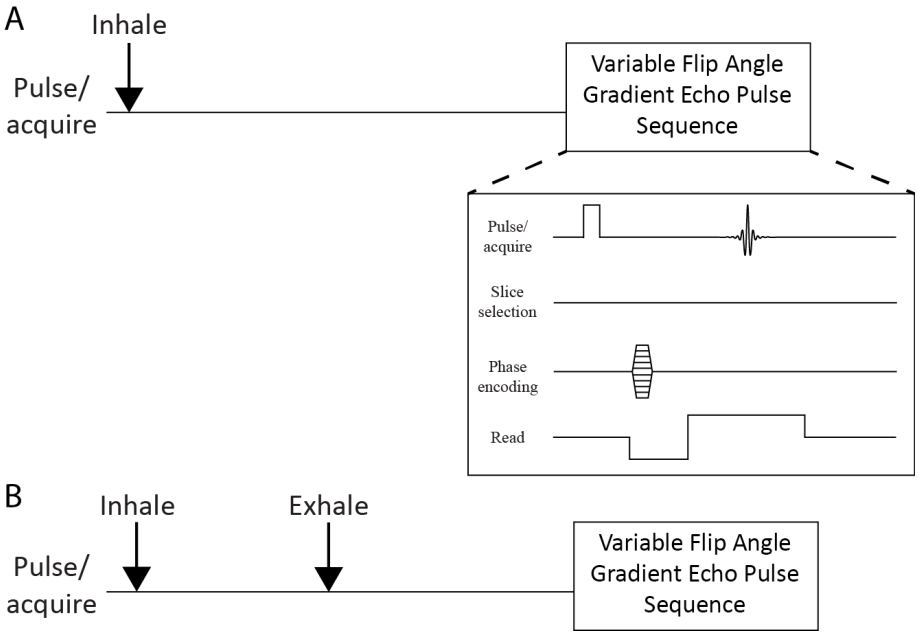

Figure 4.3. Simplified pulse sequence / inhalation diagram indicating the time-steps for acquiring 2D spatially resolved measurements of residual volume (RV). (A) Initial image generated after full inhalation of hp ^{129}Xe gas using non-slice selective VFA GRE pulse sequence. (B) Similar time course with inhalation to the same ventilation syringe (V_s) volume as in (A) but followed by full exhalation.

Coronal non-slice selective VFA FLASH imaging sequences are used in both cases and Fig. 4.4 displays the resulting images. The residual volume can be determined using the total MRI signal intensity resulting from the sum

of intensities from each of the $n \times m$ volume elements (voxels) according to:

$$RV = \frac{\sum_{n \times m} \left[I^{hp}_{exhale} \right]_{n,m}}{\sum_{n \times m} \left[I^{hp}_{inhale} \right]_{n,m} - \sum_{n \times m} \left[I^{hp}_{exhale} \right]_{n,m}} \times V_i \qquad [4.3]$$

where (n, m) is the voxel index, $\sum_{n \times m} \left[I^{hp}_{inhale} \right]_{n,m}$ and $\sum_{n \times m} \left[I^{hp}_{exhale} \right]_{n,m}$ are the summated voxel intensities on inhale and exhale respectively.

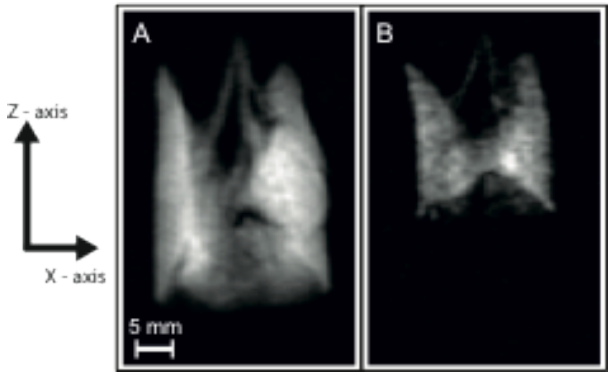

Figure 4.4. Non-slice selective coronal VFA FLASH MR images used for calculation of residual volume (*RV*). (A) Acquired after inhalation to V_s = 5 mL (actual inhalation, V_i = 3.09 mL); (B) Inhalation to V_s = 5 mL followed by full exhalation to V_s = 0 mL (V_i = 0 mL) before the MRI was acquired. Image resolution is 128 × 64 with FOV = 46.9 mm in the longitudinal and FOV= 30.0 mm in the axial dimensions, respectively. In this presentation, the orifice of the lung is pointing up with the posterior-anterior axis aligned with the z-direction.

Since each VFA Flash MRI sequence uses – and therefore destroys – the complete hyperpolarization to record the image, the two MR images for inhalation and inhalation with exhalation need to be acquired in two

separate experiments with separate hp gas deliveries. As a consequence, these measurements may be complicated by fluctuations in the SEOP process leading to a scatter in the obtained hyperpolarization levels. Therefore, the two MR images require a normalization that can be readily accomplished by recording a small flip angle pulse NMR spectrum for calibration purposes after the initial inhalation (V_s = 5 mL) in both experiments as shown below:

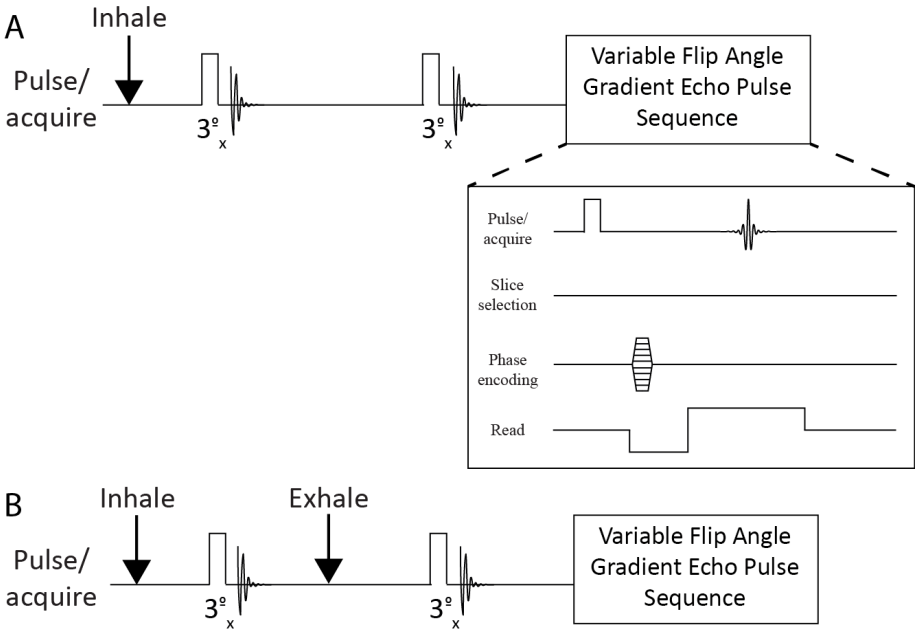

Figure 4.5. Final utilized inhalation / imaging sequence to generate both the 1D and 2D spatially resolved measurements of residual volume (RV). (A) Initial image generated after full inhalation of hp ^{129}Xe gas with two 3° rectangular pulses and followed by non-slice selective VFA GRE pulse sequence. (B) Similar sequence of events as in (A) with inhalation to the same syringe volume (V_s) volume as in (A) but note the full exhalation between the two 3° rectangular pulses.

Note that the sequence in Fig. 4.5b also contains a second small flip angle pulse (after exhalation) that is used for the additional *RV* determination

through the non-spatially resolved (spectroscopic) scheme described in Fig. 4.2. As an additional refinement, the sequence in Fig. 4.5a contains a second 3° pulse – NMR acquisition step after inhalation to ensure that the spin polarization is similarly depleted by an identical number of 3° pulses in both schemes in Fig. 4.5. Values for *RV* obtained through both schemes (i.e. spectroscopic and through MRI) are displayed in Table 2 for three rat lungs with an average value of *RV* = 1.1 ± 0.1 mL and *RV* = 1.0 ± 0.1 mL using the NMR spectroscopic and MRI methods respectively.

Rat Weight (g)	***Inhaled Gas Volume, V_i (mL)***	***Calculated Residual Volume, RV (mL) spectroscopy***	***Calculated Residual Volume, RV (mL), VFA FLASH images***
276	3.65 ± 0.10	1.03 ± 0.08	1.04 ± 0.09
286	3.58 ± 0.10	1.03 ± 0.04	1.07 ± 0.10
266	3.58 ± 0.15	1.22 ± 0.03	0.91 ± 0.07
276	**3.60 ± 0.06**	**1.09 ± 0.03**	**1.01 ± 0.04**

Table 4.2. Experimentally determined *ex vivo* lung residual volume (*RV*). The *ex vivo* lung residual volume, *RV*, calculated using inhaled volume V_i values determined experimentally for the suction volume V_s = 5.0 mL with respective standard errors (n = 4). The *RV* values are derived with standard errors (n = 4) from non-spatially resolved spectroscopic measurements (Eq. 4) and from the non-slice selective coronal VFA FLASH imaging sequence (Eq. 5) are also shown for comparison.

4.3.2. Studying lung ventilation as a function of inhalation volume V_i.

The *ex vivo* lung imaging apparatus described in Fig. 4.1 allows for a large range of ventilation volumes, V_i, to be used for pulmonary hp ^{129}Xe MRI. These experiments can provide insights into how lungs are ventilated regionally as the *ex vivo* model permits 'freezing' of ventilation to take the MR images at various points of the ventilation cycle. In this work we use lungs from similarly sized and healthy Sprague Dawley rats. Non-slice selective coronal MRI images displayed in Fig. 4.6 were acquired as the inhalation volume V_i was increased from 0.3 ml to 5.0 mL (i.e. with the suction volume V_s ranging from 1.0 ml to 6.0 mL). The corresponding integrated intensities $\sum_n \left[I^{hp}_{inhale} \right]_{n,m}$ for each of the m rows are shown to the right of the MR images in Fig. 4.6. The histograms were obtained using a voxel counting algorithm where all voxels across each row were added to give a measure of ventilation as longitudinal position (i.e. along the z axis) from the base to the end of the trachea (Fig. 4.6).

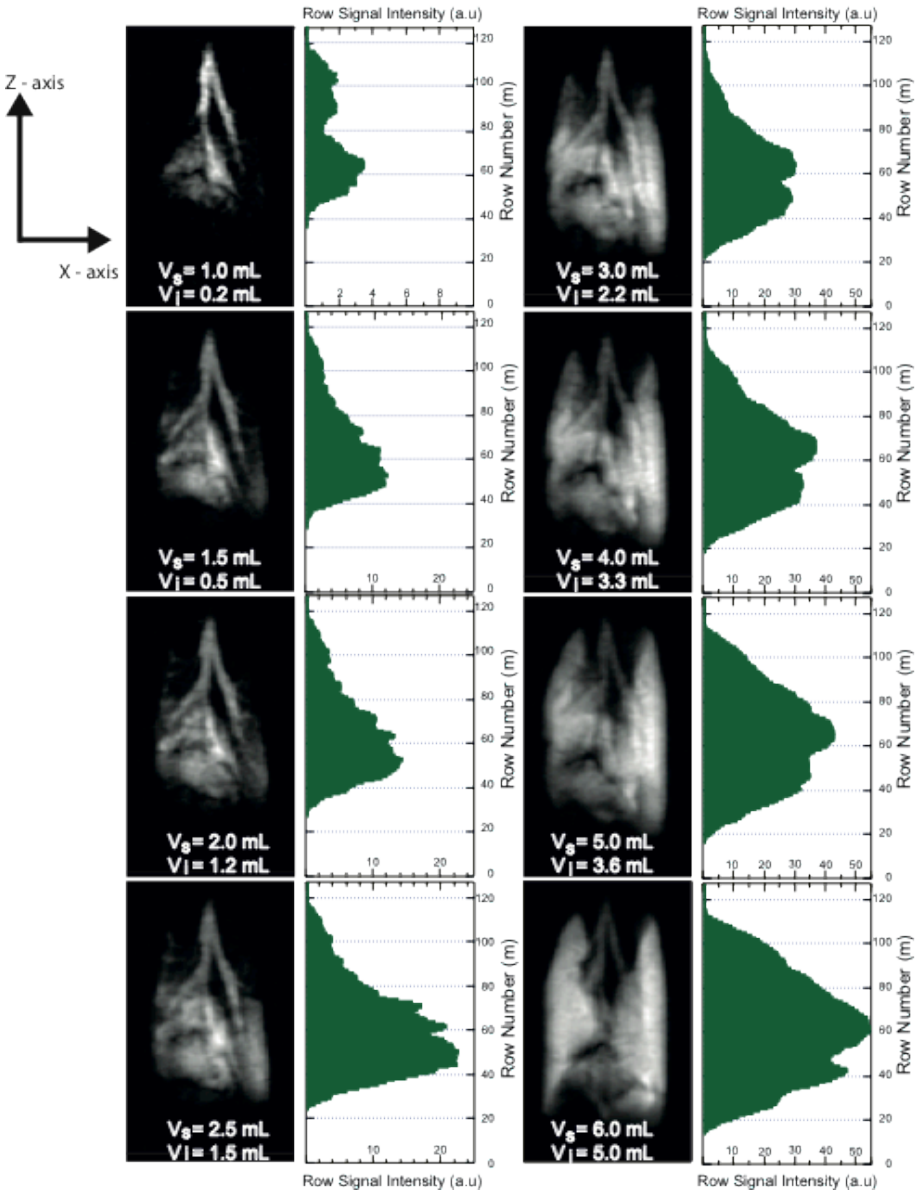

Figure 4.6. Hyperpolarized ^{129}Xe gas distribution on increasing inhalation volumes. Non-slice selective coronal VFA FLASH images as a function of increasing suction volume (V_s) (and inhaled volume (V_i)). The corresponding histograms displaying integrated intensities, $\sum_n \left[I_{inhale}^{hp} \right]_{n,m}$, for each row, *m*, are shown to the right of the images. The vertical axis of the image is parallel to the direction of the B_o field (z-direction) and corresponds to the posterior-anterior axis (base to apex) of the lung in the magnet. Phase encoding was applied transverse to the B_o field direction. As the suction volume increases from 0.5 mL to 6.0 mL the image contrast is greatly

enhanced. The effect is caused by the increasing quantities of inhaled hp gas contained in the lung as the suction volume rises. Matrix 128 × 64 with FOV = 46.9 × 30.0 mm^2.

As can be seen from the histograms in Fig. 4.6, at V_s = 1.0 mL the initial region of lung inflation is largely located in the base of the lung with the majority of the signal resulting from either the base or the major conducting airways. As the base expands between V_s = 1.0 - 2.5 mL the further drop in negative pleural pressure causes adjacent lung regions to inflate and the apices start to display significant inflation at V_s > 2.5 mL. Further inflation increases lung length with signal intensity growing across all lung regions. To better illustrate the inhalation physiology, the histograms of Fig. 4.6 are further processed and presented in a slightly different format in Fig. 4.7.

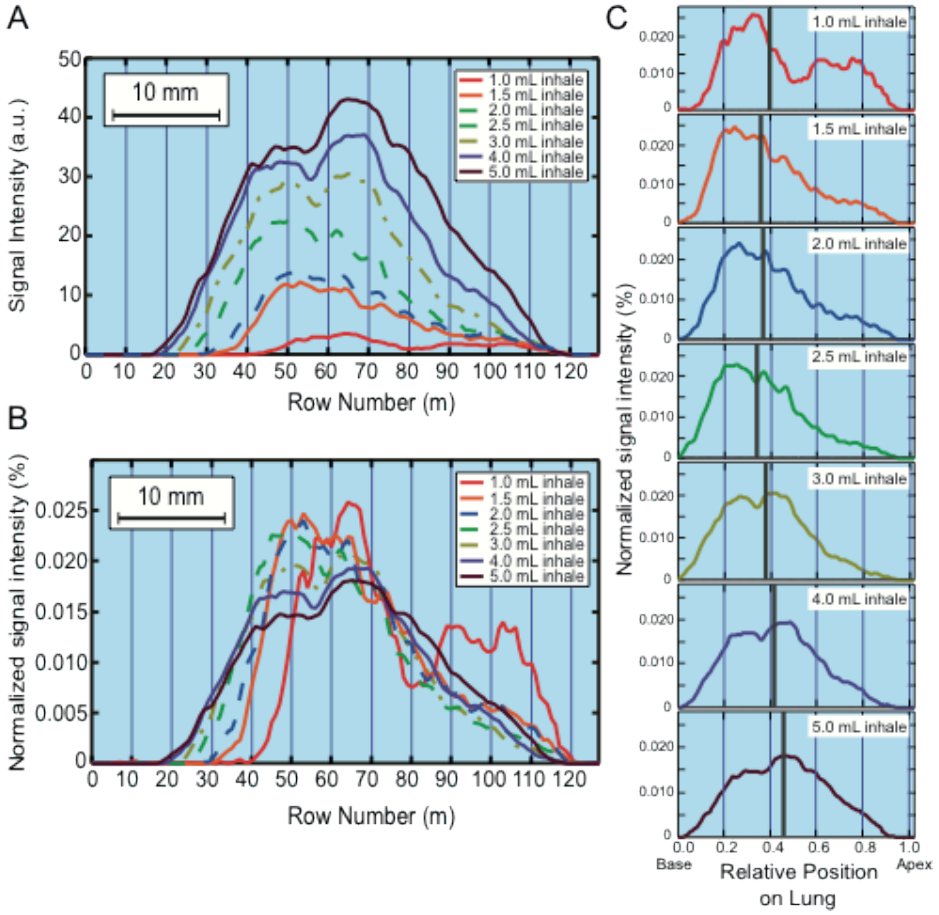

Figure 4.7. Normalization of hyperpolarized ^{129}Xe distribution by total signal intensity and position along the anterior-posterior axis. (A) Integrated signal intensity (taken from Fig. 4.3) in arbitrary units (a.u.) as a function of the image row number *m* (in z-direction); (B) Integrated signal intensity after normalization by the total signal intensity (i.e. the integrated intensity of all voxels, $\sum_{n\times m}\left[I_{inhale}^{hp}\right]_{n,m}$, of the respective MRI); (C) Normalized integrated signal intensity as in (B) but as a function of position along the lung posterior-anterior axis (z-axis) from base to apices. Independent of inhalation volume and actual lung expansion, the 0.0 point refers the base of the lung, whereas 1.0 refers to the apices. The 50% signal intensity position in the lungs is indicated by grey vertical line (C) i.e. 50% of the total signal intensity lies to both sides of the grey line.

It is instructional to normalize each histogram from Fig. 4.6 by the total signal intensity arising from the lung after inhalation of the volume V_i of hp gas, $\sum_{n\times m}\left[I^{hp}_{inhale}\right]_{n,m}$, to allow for better comparison of the regional gas distribution between the various inhalation volumes V_s as shown in Fig. 4.7b. In Fig. 4.7c a further normalization has been performed on the data where the x-axis (row number in the histograms in Fig. 4.7b is divided by the length of the expanding lung to reveal the relative position within the lung. Normalized intensities as a function of relative position within the lung allow for a better visualization of the regional differences in ventilation as the total inhalation volume V_i is changed. Initially at low suction volume V_s = 1.0 mL (V_i = 0.2 mL), it is seen that that the largest portion of the MR signal originates from the base of the lung with a smaller contribution from the larger conducting airways. On increasing inhalation the base receives a growing share of the signal until at V_s = 2.5 mL (V_i = 1.2 mL) the distribution begins to shift from the base towards the apices. The grey line in Fig. 4.7c indicates the position with equal integrated intensity on both sides of this position. This 50% signal intensity position marker serves as an additional aid to visualize regional ventilation of the lung. Initially, this line shifts towards the base of the lung as the suction volume is increased up to V_s = 2.5 mL. This shift reflects the placement of the inhaled gas predominantly into the lung base. With further increasing inhalation causing increasing ventilation of the apices, the line shifts into the opposite direction and at V_s = 5.0 mL (V_i = 3.6 mL) it is centered approximately at the midpoint of the lung.

4.3.3. Timed release of a small quantity of hp ^{129}Xe during constant volume V_i, inhalation.

Ex vivo pulmonary ^{129}Xe MRI also allows for the timed release of a small bolus (0.5 – 1.0 mL) of hp gas during the inhalation period. This method provides further data to support the assertion that the initially inhaled gas localizes to the base of the lung and is directed towards the apices mostly at the end of the inhalation. Two inflation schemes with a total suction volume of V_s = 5.0 mL are employed. For scheme 1 in Fig. 4.8a – c- the initial inhalation consists of a chosen fraction of hp gas, inhaled through application of suction volume $V_{s(hp)}$, followed by 'dark' (i.e. MRI inactive, usually N_2) gas. The dark gas is inhaled after flushing of the storage volume V_B with N_2 and applying suction volume $V_{s(dark)}$. In scheme 2 in Fig. 4.8d - e the delivery order is reversed with the initial dark gas delivery using N_2 and suction volume being $V_{s(dark)}$ followed by hp ^{129}Xe delivery into V_B and suction volume $V_{s(hp)}$. Using ventilation scheme 1 with $V_{s(hp)}$ = 1.0 mL followed by $V_{s(dark)}$ = 4.0 mL, the MRI shows that the hp gas signal is directed to the base. As the ratio $V_{s(hp)}$/ $V_{s(dark)}$ increased, at constant $V_{s(hp)}$+ $V_{s(dark)}$ = V_s = 5.0 mL, the hp gas is progressively found further towards the apices. In scheme 2 the hp gas is directed more to the apical regions of the lung with the hp gas seen in the larger conducting airways. Further increase of the dark gas component in scheme 2 (Fig. 4.8e) results in the hp gas being localized to the conducting airways themselves.

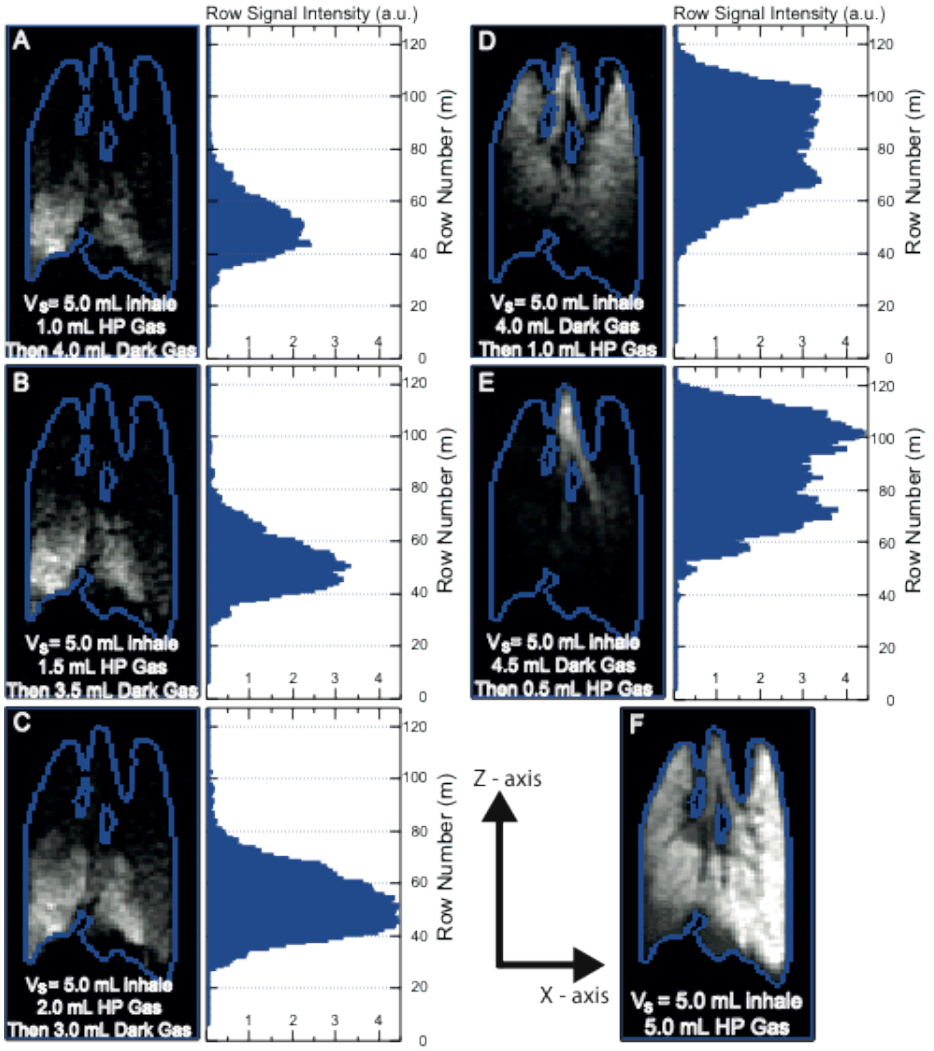

Figure 4.8. Timed release of hyperpolarized ^{129}Xe during constant inhalation volumes. Coronal slice selective VFA FLASH images for directed ventilation schemes with a histogram that displays the integrated intensities in each row are shown to the right of the images. Scheme 1 (A - C)- initial inhalation consists of a known volume of hp gas, $V_{s(hp)}$, followed by dark gas, $V_{s(Dark)}$. Scheme 2 (D - E)- the reversal with the inhalation of $V_{s(Dark)}$ followed by $V_{s(hp)}$. Full 5.0 mL inhalation of hp gas with edge detection using Kirsch operator [300] with window level adjusted to show lower signal intensities (F). Z-axis along B_o in posterior-anterior axis (base to apex) of the lung in the magnet and x-axis along indirect (phase encoding) dimension. Imaging parameters: 4 mm central slice, matrix 128 × 64, FOV = 46.9 × 30.0 mm^2. Positioning of the lung as in Fig. 4.4.

4.3.4. Airway Responsiveness

Excised lung tissue, including lung slices for optical microscopy, has regularly been used to study airway responsiveness to challenges with bronchial smooth muscle agonists such as methacholine (MCh) [301-303]. In this work, it is investigated whether the whole organ can be used many hours post mortem for pulmonary hp ^{129}Xe MRI of MCh challenges. Furthermore, the possibility of the reversal of airway responsiveness by flushing the pulmonary circulation with glucose and salbutamol solutions followed by subsequent challenges and reversals are also explored. Throughout all experiments of lung responsiveness the suction volume V_s was kept constant, with an increase in airway pressures corresponding to changes in the hp ^{129}Xe ventilation images.

4.3.4.1. Positively responding rat lungs

Images obtained from rat lungs, positively responding to MCh challenges, are shown in Figures 4.9 – 4.12. As can be seen from the data, very similar responses were demonstrated on four rat lungs. Initially there is a reduction in signal intensity from lung regions that are poorly ventilated (ventilation defects). On flushing the lung with glucose and salbutamol solutions these are largely seen to recover. There were some differences between the lungs with differing degrees of airway responsiveness evident, with for example the lung in Fig. 4.11 showing initial hyperventilation, likely due to shunting of gas from one region to another. In the later experiments (Fig. 4.11 – 4.12) it became clear that several

cycles of bronchoconstriction followed by reversal could be performed on each rat lung. As can be seen, a subsequent, second challenge produces significant ventilation defects in all of these lungs. After reversal of this second challenge, the third challenge causes the larger amounts of lung to constrict and therefore fail to receive hp gas (Fig. 4.11 and 4.12).

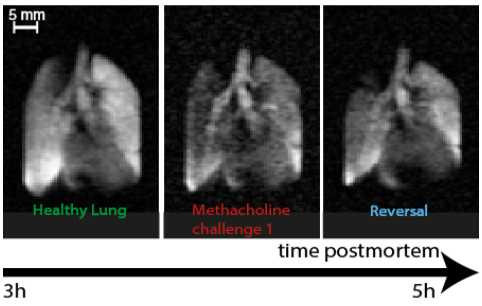

Figure 4.9. Airway responsiveness testing in an excised rat lung. Slice selective VFA FLASH images of positively responding *ex vivo* rat lung after intravenous challenges of 60 µg methacholine with subsequent reversal produced by flushes of intravenous 5% glucose and 1000 µg salbutamol. Imaging parameters: 4 mm central slice, matrix 128 × 64, FOV = 46.9 × 30.0 mm^2. In this presentation, the orifice of the lung is pointing up with the posterior-anterior axis aligned with the z-direction.

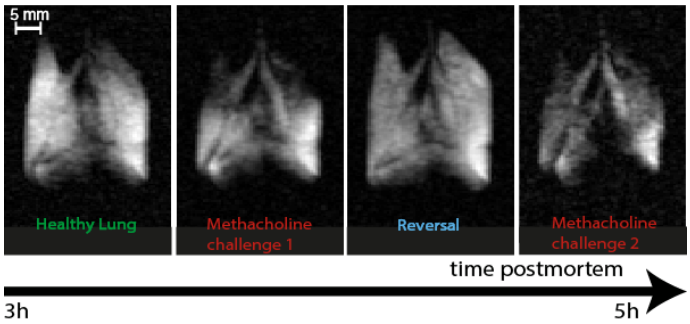

Figure 4.10. Airway responsiveness testing in an excised rat lung. Slice selective VFA FLASH images of positively responding *ex vivo* rat lung demonstrating a response to 60 µg methacholine before and after reversal after reversal with flushes of intravenous 5% glucose and 1000 µg salbutamol. Imaging parameters and lung positioning as in Fig. 4.9.

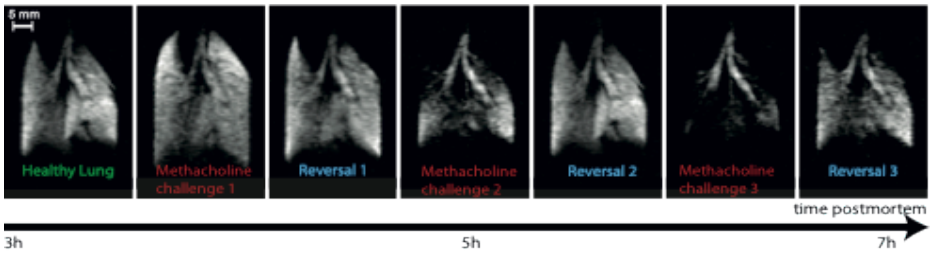

Figure 4.11. Airway responsiveness testing in excised rat lung 2. Slice selective VFA FLASH images of positively responding *ex vivo* rat lung after intravenous challenges of 60 µg methacholine with subsequent reversal produced by flushes of intravenous 5% glucose and 1000 µg salbutamol. Initially the lung developed hyperinflation on the first MCh challenge. This hyperinflation then recovered on reversal with flushing the lung with glucose and salbutamol. A subsequent, second challenge produces significant ventilation defects. After reversal, the third challenge causes the majority of lung tissue to fail to receive hp gas due to the severity of the bronchoconstriction. Imaging parameters and lung positioning as in Fig. 4.9.

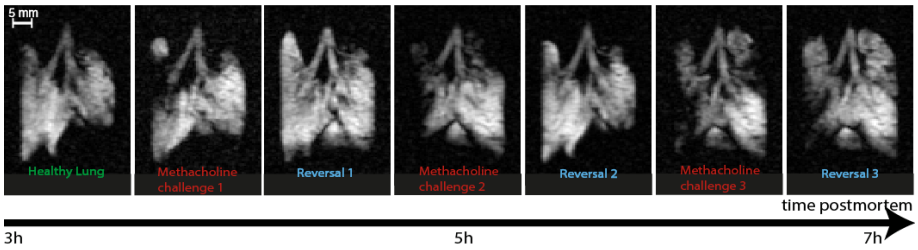

Figure 4.12. Airway responsiveness testing in an excised rat lung 3. Slice selective VFA FLASH images of positively responding *ex vivo* rat lung after intravenous challenges of 60 µg methacholine with subsequent reversal produced by flushes of intravenous 5% glucose and 1000 µg salbutamol. The initial bronchoconstriction resolved after the flush with 5% glucose solution and salbutamol. On subsequent challenges larger amounts of lung tissue were seen to respond on but, as in Fig. 4.11, less improvement is seen on reversal. Imaging parameters and lung positioning as in Fig. 4.9.

4.3.4.2. Poorly and non-responding rat lungs

Despite the success in demonstrating this effect on four rat lungs, subsequent rat lungs (seven in total) showed little or no response to MCh at the dosages under investigation (see Figures 4.13 - – 4.17). Two rat lungs demonstrated a reduced response to MCh challenges with subsequent challenges failing to cause significant ventilation defects (Fig. 4.13). Please note that although this pattern was seen in seven lungs in total, only five are reported here due to an unfortunate hardware crash with a loss of data within the laboratory since these image data were acquired. Furthermore, it should be noted that the Sprague Dawley rats within this work were healthy and had not been sensitized to display any airway hyper-responsiveness. The purpose of this proof of principle study was not to explore airway responsiveness in detail but to demonstrate that responsiveness, if present, can be triggered, observed and reversed for several hours post mortem.

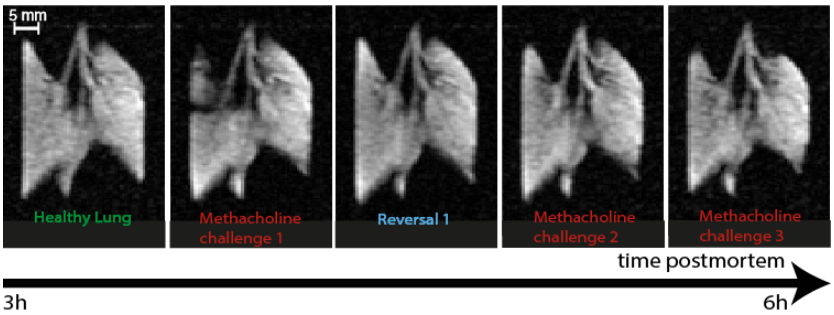

Figure 4.13. Airway responsiveness testing in an excised rat lung. Slice selective VFA FLASH images of a poorly responding *ex vivo* rat lung. The initial intravenous challenges of 60 µg methacholine showed a solitary region of reduced ventilation which subsequently resolved on reversal with intravenous 5% glucose flushes and 1000 µg salbutamol. The rat lung then failed to significantly respond on subsequent challenges with only minor ventilation changes seen. Imaging parameters and lung positioning as in Fig. 4.9.

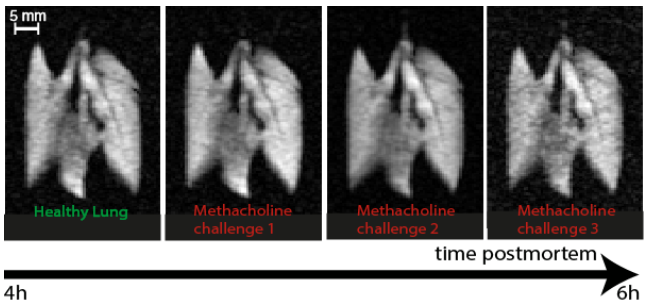

Figure 4.14. Airway responsiveness testing in an excised rat lung. Slice selective VFA FLASH images of a non-responding *ex vivo* rat lung after three intravenous challenges of 60 µg methacholine. Imaging parameters and lung positioning as in Fig. 4.9.

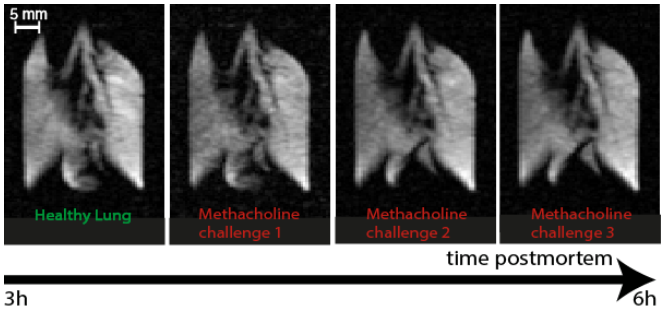

Figure 4.15. Airway responsiveness testing in an excised rat lung. Slice selective VFA FLASH images of a non-responding *ex vivo* rat lung after three intravenous challenges of 60 µg methacholine. Imaging parameters and lung positioning as in Fig. 4.9.

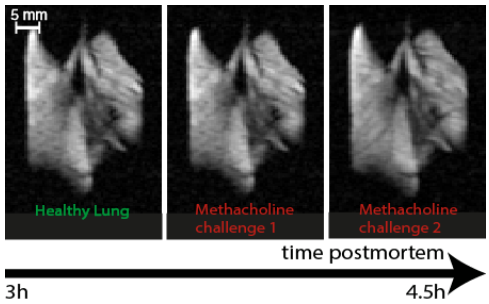

Figure 4.16. Airway responsiveness testing in an excised rat lung. Slice selective VFA FLASH images of a non-responding *ex vivo* rat lung after two intravenous challenges of 60 µg methacholine. Imaging parameters and lung positioning as in Fig. 4.9.

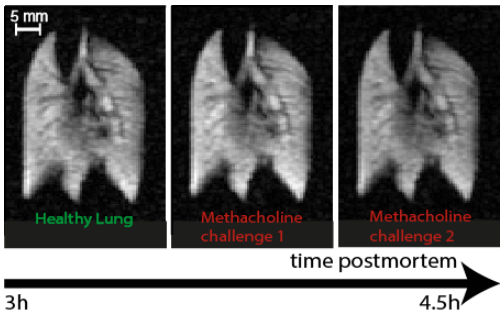

Figure 4.17. Airway responsiveness testing in an excised rat lung. Slice selective VFA FLASH images of a non-responding *ex vivo* rat lung after two intravenous challenges of 60 µg methacholine. Imaging parameters and lung positioning as in Fig. 4.9.

4.3.4.3. Airway responsiveness in guinea pig lungs

Rat lungs were compared to guinea pig lungs as the latter are known to have greater quantities of bronchial smooth muscle [304, 305]. Similar patterns of ventilation defects were produced by smaller dosages of MCh on the three lungs imaged with these again found to be partially reversible with glucose and salbutamol flushes allowing further challenges for several hours post mortem as demonstrated in Fig. 4.18. It was however noted that reversal of the ventilation defects in guinea pig lungs depended more on flushing of residual MCh from the pulmonary circulation rather than significant improvements with salbutamol.

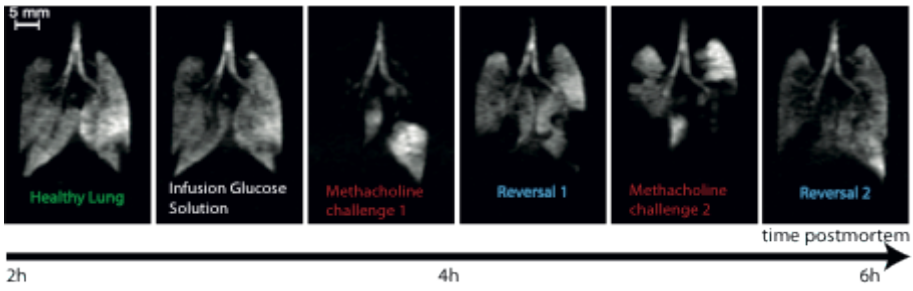

Figure 4.18. Airway responsiveness testing in an excised guinea pig lung. Slice-selective VFA FLASH images of *ex vivo* guinea pig lung after intravenous challenges with 5% glucose solution alone and 20 µg methacholine. Subsequent reversal was produced by flushes of intravenous 5% glucose and 200 µg salbutamol. Images were performed with a constant inhalation syringe (suction) volume of V_S = 5 mL. Imaging parameters: 4 mm central slice, matrix 128 × 64, FOV = 46.9 × 30.0 mm². Positioning of the lung as in Fig. 4.4.

4.4. Discussion

4.4.1. The residual volume, *RV*, of ex vivo lungs.

Residual volume, *RV*, is an important functional parameter used in both animal models of pulmonary disease and in the clinical setting. *RV* is found to decrease in patients with restrictive lung diseases such as fibrotic lung disease and rises in patients with obstructive disease due to hyperinflation. Many methods have been utilized for measurement of *RV* in small animals [4]. In this work, the calculated value of the residual volume of 1.1 ± 0.1 mL using the MR spectroscopic measurements and 1.0 ± 0.1 mL using the spatially resolved MRI method agree within the experimental error. The values are however lower than the 1.26 mL previously determined using body plethysmography [45] and of ~ 1.6 mL with neon dilution [306] for similar sized rats. In the *ex vivo* rodent lung at V_s = 0 mL it is likely that this situation is more akin to an open-chested animal where there is no chest wall recoil holding the airways open with the result that the calculated value of *RV* will be reduced as has been noticed in dog lungs [307]. A further, small contribution to the difference found between our value and previous data is caused by the shortening of the conducting airways (and hence a shorting of the anatomic dead space) as the cannula was sited just above the carina rather than higher below the larynx in the in vivo experiments. On the other hand, it is known that lung compliance decreases with temperature [308] with the result that as the lungs are kept at ambient temperature or just below this will compensate for some of the aforementioned reduction in *RV*. Finally, it has been noted by several

groups that gas trapping is an issue with excised lung tissue used for ventilation studies [10, 309, 310]. Gas trapping had not been a noticeable feature in the current study as no significant gas trapping was seen with prolonged lung ventilation. It its unknown whether the lack of gas trapping is due to differences in the method of organ preparation, smaller total inhaled volume in the current work, or different rat strain used (Sprague-Dawley in the current study). Note that significant gas trapping was seen with some of the guinea pig lungs causing them to be rejected for imaging.

The presented method of *RV* determination is a fast and straightforward addition to hp gas MRI of excised lungs requiring no additional instrumentation. Furthermore, the spatially resolved 2D method could also be modified to reduce the contribution from the signal of the airways (i.e. the anatomical dead space) to the *RV* determination. Some airway contribution to the MRI signal can be taken directly from the images in Fig. 4.4a - b or could be measured in more detail for example through a directed ventilation scheme as in Fig. 4.8e. The directed ventilation scheme can in principle also provide information about regional contributions to the residual volume. Note however, that the underlying assumption made for the *RV* determination in this work is that the hp gas mixes with the 'dark' gas in the residual lung volume uniformly. This requires, that the lungs are being inhaled with hp gas without areas of restricted or obstructed ventilation. Deviations form the expected *RV* in healthy lungs would be indicative of the presence of pulmonary diseases. However this was not further investigated as animal models of disease were beyond the scope of this work.

Measuring functional respiratory parameters, such as *RV in vivo* using hp gas imaging experiments in rodents has proven difficult due to the small gas volumes. The schemes to calculate *RV* developed with the *ex vivo* model in this work may provide a valuable addition to physiological methodology. As an alternative to existing lung function tests, the *ex vivo* hp ^{129}Xe MRI method provides spatially resolved information of the distribution of the *RV* which might provide a sensitive test to identify regions disproportionately affected by the disease process. The hp ^{129}Xe MRI method detailed here, being exceptionally simple, could easily be translated to *in vivo* MRI in the preclinical or clinical setting.

4.4.2. Ventilation physiology using *ex vivo* lungs.

Image data on increasing ventilation volume presented in this work potentially provide new insights into pulmonary physiology. It is shown that ventilation in the *ex vivo* models produces initial ventilation from the bases of the inverted lungs increasing downward towards the apices. Whether this is due to an inherent property of the lung or some element of the experimental set up, for instance, with the lungs submerged in glucose solution with a small pressure gradient of < 0.5 kPa (5 cm H_2O) along the length of the lung, is as yet unknown.

Classical pulmonary physiological theory has tended to explain differences in regional ventilation in humans due to the gravitational effects on pleural pressure resulting in the lower, most dependent, lung regions being under

higher resting pressure and hence on inhalation receive higher volumes of gas [311, 312].

Previous works with SPECT and xenon enhanced CT have shown regional differences in ventilation and changes due to posture in animals [92, 313, 314]. Marcucci et al., using xenon enhanced CT, found that the vertical ventral / dorsal (V/D) ventilation gradient in supine canines where it was noted that the dorsal lung receives the greatest ventilation in the supine position [91]. This gradient was abolished once the animals were placed in the prone position. Interestingly, the group also found a ventilation gradient between the base of the lung and the apex (anterior–posterior) where the base experiences higher levels of ventilation compared to the apex with the animal supine, although this was removed with the animal prone.

Månsson et al. studied V/D fractional ventilation gradients *in vivo* using hp ^{3}He MRI in rats noting a similar V/D gradient in the supine position and reporting the removal of the gradient with the animal prone [315]. Couch et al. subsequently confirmed this in rats using both hp ^{3}He and hp ^{129}Xe, also noting a small positive posterior / anterior (base to apex) fractional ventilation gradient in this work [180].

However recently Kyriazis et al. have noted that in a rat elastase model of emphysema ventilated by positive pressure and imaged using hp ^{3}He, inflation rates at the bases reduced more than at the apices compared to controls despite apparent diffusion coefficients (markers of

emphysematous damage) indicating changes throughout the lung [316]. It is therefore possible that this was due to some inherent elastic property of the lung indicating underlying regional differences.

In this work, the experimental arrangement provides further evidence that regional differences in ventilation may be due to inherent elastic properties of the lung as at values of inhaled volume close to those studied elsewhere (1 - 2 mL in this size of rats), most of the inhaled gas localizes to the bases even when these regions are most superior. Further work to confirm this would be required to see if this situation changed once the lungs were suspended from the trachea without the lungs submerged in solution (i.e. trachea most superior) and also if the lungs were in the supine or prone position as has been performed by other groups with excised lung tissue [309].

4.4.3. Whole organ response to post mortem MCh challenges.

The image data presented in this work confirms post mortem airway responsiveness to MCh challenges and glucose / salbutamol reversal in *ex vivo* rat and guinea pig lungs. Not all of the healthy *ex vivo* rat lungs responded to MCh challenge but those that did respond showed regional ventilation defects at drug dosages similar to those reported elsewhere with a significant increase in sensitivity to methacholine in guinea pig lung tissue. The variation in the airway responsiveness of rat lungs has been documented with review of the literature revealing that there is significant variation in response to MCh amongst rats, especially out-bred strains, when recorded with body plethysmography often requiring very large dosages of MCh [305, 317, 318]. Guinea pig lungs were studied as they are known to have higher levels of bronchial smooth muscle and so are more responsive to MCh [297, 304, 305]. The results confirm this increased airway responsiveness with lungs showing large degrees of bronchoconstriction with one sixth of the dosage. Reversal however appeared to be unaffected by salbutamol and relied more on flushing methacholine from the pulmonary circulation.

The severity of observed bronchoconstriction in some cases in this work is unlikely to be recorded *in vivo* due to the significant physiological deterioration that would result (likely resulting in death before imaging). Therefore the *ex vivo* model offers the opportunity to explore the most extreme of pathophysiological situations for prolonged periods of time in

the absence of systemic effects and considerations. The current model could be further improved to incorporate recirculation of fluid and the use of bubble traps to prevent gas emboli in the lung vasculature [16]. With such improvements and the use of more physiological perfusate the model might be able to last beyond the currently reported 7 - 8 hours.

4.4.4. Spatial resolution of *ex vivo* hp ^{129}Xe MRI.

As a final technical note, the *ex vivo* model may potentially allow for higher resolution of the MR images compared to *in vivo* hp ^{129}Xe MRI that typically relies on signal averaging over multiple breaths. All MR images presented in this proof of concept work are acquired in a single scan without motional artifacts and provide sufficient image spatial resolution using hp ^{129}Xe with an apparent polarization of P_{app} = 10%.

4.5. Conclusions

The aim of this work was to demonstrate the utility of the *ex vivo* pulmonary model for hp ^{129}Xe MRI studies. The pulmonary *ex vivo* model offers a nimble platform for developing and testing novel hp gas MRI protocols before translation of the methods for preclinical *in vivo* studies and ultimately into clinical research. The usage of *ex vivo* whole organs also reduces the regulatory requirements for animal care, handling and monitoring for hp gas MRI experiments. In addition, the ability to investigate lung function, for example in the absence of oxygen and by precise control and freezing of the ventilation cycle, demonstrates that *ex vivo* models offer a new investigative tool for lung physiology in their own right. The imaging of dynamic changes in *ex vivo* whole organ may be of interest for drug development studies or as an additional technique to elucidate airway responses in the absence of systemic effects or considerations, allowing the study of extreme pathophysiology.

Chapter 5: MRI of hyperpolarized xenon-129 in an *ex vivo* rat model of asthma

To illustrate the use of functional *ex vivo* hp ^{129}Xe MRI it was decided to study a rat model of asthma where there is an increase in airway responsiveness to broncho-provocative challenges. Experiments were performed in collaboration with the Pulmonary Biology group at the University of Nottingham. Credits for the work were as follows: Dr. Lilburn and Prof. Meersmann conceived the experiments; Dr. Lilburn, Mr. Six, Ms. Lesbats and Mr. Hughes-Riley performed the MR imaging experiments; Dr. Lilburn, Dr. Tatler, Mr. Habgood and Ms. Lesbats handled the animals, performed the tissue harvesting, and processed the histology; Dr. Lilburn, Dr. Tatler, Dr. Shaw, Dr. Jenkins and Prof. Meersmann analyzed the data; and Dr. Shaw and Prof. Meersmann helped Dr. Lilburn with writing the report.

5.1. Introduction

Asthma is chiefly defined by the cardinal manifestation of variable obstruction of airflow in response to environmental factors [232]. Around 300 million people worldwide suffer from the disease [319] and it is well established that asthma is a leading cause of preventable death [319-321]. Worldwide the prevalence of asthma has risen significantly in the last 40 years [322]. In the UK, rates have increased threefold in school-children between the years 1955 - 2004 [323]. It is estimated that asthma costs the UK health service in excess of £500 million per year due to direct treatment costs and the UK economy more than £1 billion per year due to lost productivity [324].

New insights into the pathophysiology of asthma have been provided over the last 20 -30 years by a variety of molecular and biomedical techniques some of which have resulted in new treatments [325, 326]. Nevertheless new methods for investigating the disease and monitoring treatment outcomes are required as current routine methods suffer from significant variability [327, 328], often do not correlate with the clinical severity of asthma [329, 330], and provide no regional information of lung function [331].

Animal models of asthma are widely used to study the disease [5, 7] and have allowed for significant advances in the understanding and treatment of the condition [39, 43, 332, 333]. There are several animal models of asthma currently in use that displays many features of human asthma

[219, 231, 334, 335]. Nonetheless, as documented in Chapter 3, the ovalbumin (OVA) model of allergic asthma is one of the best characterised of those currently available [224]. Typically animals are sensitized by intraperitoneal or subcutaneous injections of OVA mixed with an adjuvant (usually aluminium hydroxide) to prime a T-helper 2 cell immune response. Subsequent repeat airway challenges of OVA post sensitization produce acute airway inflammation with large numbers of eosinophils [336-338] and an increase in airway sensitivity to broncho-provocative agents such as methacholine (MCh) [55]. Significant differences exist between species and strains of animal [229, 230]. Rats and mice display a greater similarity to the human disease with high IgE titres [228, 234] however levels of airway hyper-responsiveness (AHR) are often low making phenotyping using functional *in vivo* methods difficult [224, 338].

Several imaging methodologies have been used in an effort to enhance phenotyping of OVA induced models including studies of airway inflammation [339] and remodelling [340]. Hyperpolarized (hp) noble gas MRI however has the ability to provide information on lung responses with direct visualization of regional changes in ventilation in small laboratory animals *in vivo* [180, 286-288] which may be useful for studying functional parameters.. To date, much work has demonstrated the utility of technically demanding *in vivo* hp gas imaging experiments. However it has been known for some time that *ex vivo* lung tissue can be used to study airway responses [11, 292, 301]. Furthermore, previous work has explored airway responsiveness in healthy excised rat and guinea pig lungs (see Chapter 4 and ref. [291]). The purpose of this study is to demonstrate that

dynamic functional changes in ventilation may be studied in an OVA model of airway hyper-responsivenes using the less technically demanding *ex vivo* hp ^{129}Xe MRI methodology. Additionally, it will be shown that this arrangement is able to provide useful lung function parameters that will aid functional phenotyping of small animal models of human asthma.

5.2. Materials and Methods

5.2.1. Model Characterization

The University of Nottingham Ethical Review Committee approved the study, which was carried out in strict accordance with local animal welfare guidelines and the UK Home Office Animals (Scientific Procedures) Act 1986. All efforts were made to minimize animal suffering.

Male Brown-Norway rats (150 - 199 g, n = 12) were purchased from Charles River Ltd (Margate, UK). Initial sensitization of all animals was accomplished by intra-peritoneal injections of 2 mg ovalbumin (OVA) with 200 μg aluminium hydroxide (Alum) in 1 mL on day 0 and day 14 [341]. Experimental asthma was induced with subsequent intra-tracheal (i.t.) doses of 500 μg OVA in 1 mL sterile Dublecco's phosphate buffer solution (D-PBS, Sigma-Aldrich Ltd, Gillingham, UK) on days 21 and 23 administered under general anaesthesia (inhaled isofluorane 4% with medical grade oxygen for 3 – 4 minutes). Control animals were similarly treated with 1 mL sterile D-PBS i.t. on days 21 and 23. On day 24 (approximately 24 hours after the last i.t. challenge) animals were weighed and euthanized by overdose of sodium pentobarbital (Sigma-Aldrich Ltd, Gillingham, UK).

Lungs for *ex vivo* hp ^{129}Xe imaging had a cannula inserted into the caudal vena cava to allow flushing of the pulmonary circulation with heparin 100 IU/mL (Wockhardt UK Ltd, Wrexham, UK) in 20 mL 0.9% saline solution

followed by 20 mL D-PBS to remove residual blood from the pulmonary circulation. The heart and lungs were subsequently removed *en masse*. A polytetrafluorethylene (PTFE) adapter tube was inserted 5 - 10 mm above the carina and sutured into place. The heart and lungs were suspended in Hartmann's solution (Baxter Healthcare Ltd, Thetford, UK) in the ventilation chamber with the trachea pointing downwards as detailed in Chapter 4. The *ex vivo* lungs were repeatedly inflated with 5 - 6 mL of room air to check for gas leaks either from the suture around the trachea or the lungs themselves. The lungs were chilled to 278 K for transportation to the imaging facility. After transportation, the lungs were then passively warmed to ambient temperature before imaging experiments. The time from harvest to MR imaging was no more than 5 hours for each *ex vivo* lung.

Of all animals enrolled in the study, six rats were treated with 500 μg OVA i.t., and six control rats were treated using i.t. D-PBS. Of these animals three 500 μg OVA and three D-PBS control rats were used solely for BAL and histological analysis in a satellite group. During the study, one control OVA lung was rejected for *ex vivo* hp ^{129}Xe MR imaging due to gas leakage.

Airway inflammation was quantified in both the satellite group of rats used for histological analysis and in the *ex vivo* lungs used for hp ^{129}Xe MRI after imaging. The satellite group of control and OVA challenged rats had bronchoalveolar lavage (BAL) performed post mortem with 1 mL D-PBS instilled i.t. before subsequent removal. BAL samples were centrifuged at 1500 rpm for 5 minutes with the resulting cell pellet resuspended in 1ml

PBS. Total BAL cell count was performed with a Sceptor cell counter (Millipore, UK). BAL cells were cytospinned and stained using Diff Quik Romanowski stain (Fisher Scientific, UK). % differential inflammatory cells were determined by counting 100 cells at 40x magnification on a light microscope.

Control and OVA challenged lungs from both the satellite hp ^{129}Xe imaging groups (post imaging) were similarly prepared by inflating to forced vital capacity (25 cm $H_2O \approx 2.5$ kPa) with 5% formalin-saline solution (Sigma-Aldrich Ltd, Gillingham, UK) and subsequently wax embedded. Histological analysis included haematoxylin and eosin (H&E) staining to quantify airway inflammation. Quantification was performed using a Nikon Eclipse 90i microscope (Nikon Corporation, Tokyo, Japan) with NIS Elements Ar image analysis software for image capture (v. 3.2, Nikon Corporation, Tokyo, Japan

5.2.2. ^{129}Xe spin exchange optical pumping, compression and transfer

Hp ^{129}Xe was produced in batch mode using spin exchange optical pumping (SEOP) [160] of a gas mixture containing 25% Xe (enriched to 83% ^{129}Xe, Nova Gas Technologies, Charleston, SC, USA) and 75% nitrogen (N_2, 99.999% pure, Air Liquide, Coleshill, UK). SEOP was performed at 40 - 60 kPa followed by expansion of the hp gas into a custom built glass and perspex extraction unit. Hp gas was then compressed to just above ambient pressure before delivery to the lung (further detail of the process can be found in ref. [215] and in subsequent chapters where the technique is used extensively with hp ^{83}Kr) . The hp xenon delivered to the excised lungs for inhalation was spin polarized to P = 40% with an apparent spin polarization P_{app} = 10% [145].

5.2.3. Hp gas inhalation

The ventilation chamber with the *ex vivo* lungs was placed inside the bore of the superconducting magnet and the temperature was kept constant at 293 K throughout the experiments. Active inflation of the lung was accomplished by pulling to a ventilation syringe volume (V_s) of 6 mL. Corresponding inhaled volumes (V_i) were measured separately using the water displacement technique on gas exhalation and can be seen in Table 5.1. To limit potential gas trapping, the *ex vivo* lungs were deflated over 30 - 60 s from V_s = 6 mL to maximum exhalation (V_s = 0 mL) as has been reported elsewhere [10, 309] before hp ^{129}Xe inhalation.

	Identifier	Rat Weight (g)	Inhaled volume, V_i,(mL)
CONTROL	C.1	259	4.2 ± 0.3
	C.2	262	5.0 ± 0.4
OVA CHALLENGED	OVA.1	252	4.9 ± 0.3
	OVA.2	254	4.9 ± 0.4
	OVA.3	270	4.6 ± 0.1

Table 5.1. Demographic data from subjects used for hp ^{129}Xe imaging. Summary of rat weights and inhaled volumes (V_i) ± standard deviation corresponding to inflation (syringe) volume V_s = 6 mL.

5.2.4. Bronchoconstriction and reversal

Animals used for hp ^{129}Xe MRI experiments had the catheter used for flushing of the pulmonary circulation retained. The cranial vena cava was ligated to ensure drug delivery to the pulmonary circulation. The cannula in the caudal vena cava was sutured into place and attached to fine perfluoroalkoxy (PFA) tubing for administration of drugs to the pulmonary circulation as detailed in Chapter 4. Excess fluid was once again removed to keep the fluid level within the ventilation chamber constant during the imaging experiments.

In order to satisfy tissue metabolic demands, the lungs were ventilated 8 – 10 times with the 100% oxygen followed by purging the lungs and transfer line with N_2 prior to hp ^{129}Xe delivery.

Initial hp ^{129}Xe MR imaging was repeatedly performed at baseline to ensure reproducibility of ventilation. Furthermore, 4.5 mL of Hartmann's solution was delivered at a rate of 1 – 2 mL/minute before broncho-provocative challenges to ensure there were no significant changes on hp ^{129}Xe MRI after fluid administration to the lung.

Bronchoconstriction was then achieved by injecting methacholine (MCh, Sigma-Aldrich Ltd, Gillingham, UK) through the pulmonary circulation as detailed previously [291]. Increasing doses of 10, 25, 50, 75, 100, 200, and 400 μg of MCh dissolved in 1 mL 0.9% saline solution followed by a 3.5 mL bolus of Hartmann's solution at a rate of 1 - 2 mL/minute were delivered to the pulmonary circulation before sequential hp ^{129}Xe imaging experiments. The bolus of Hartmann's following the MCh was to ensure complete drug delivery to the lung by flushing out the dead volume in the delivery system. Reversal of broncho-constriction was attempted by flushing the challenged lungs with 30 – 50 mL of Hartmann's solution and 1000 - 1500 μg of salbutamol (Allen and Hanbury's Ltd, Middlesex, UK) in 1.0 – 1.5 mL at a rate of 1 – 2 mL/minute. Note that throughout all experiments the airway pressure was recorded during inhalation and was kept constant between successive images, i.e. was kept at baseline levels throughout the imaging sequence. Typical airway pressures recorded

during inhalation in control and OVA challenged lungs were 2.2 – 2.6 kPa (22 – 26 cm H_2O) and 2.5 – 2.9 kPa (25 – 29 cm H_20) respectively.

5.2.5. MRI protocol

MR imaging experiments were performed using a 9.4 T vertical bore Bruker Avance III microimaging system (Bruker Corporation, Billerica, Massachusetts, USA). A custom-built 25 mm low-pass birdcage volume coil tuned to the resonance frequency of ^{129}Xe gas in the lung of 110.69 MHz was used in all experiments. Images were acquired using a modified variable flip angle (VFA) FLASH gradient echo pulse sequence [177]. Hard pulses of 134 μs and sinc-shaped pulses of 1000 μs at variable power levels were used for non-slice-selective and slice-selective image acquisitions (TE = 1.27 ms, TR = 67.5 ms). All coronal images were acquired in 128 × 64 image matrices with a field of view (FOV) of 47.3 mm and 31.5 mm and a total acquisition time of 4.38 s. Slice thickness in slice-selective imaging experiments was 4 mm with the slice-selective frequency offset corresponding to the excitation of the central slice resulting in nominal resolution of $0.37 \times 0.49 \times 4$ mm^3.

5.2.6. Image reconstruction and analysis

Images were once again processed and reconstructed in Prospa (v. 3.06, Magritek, Wellington, New Zealand) with a sine-bell squared window function applied to the raw data before two-dimensional Fourier transformation and the two dimensional image data were then exported for analysis in IGOR Pro (v. 6.01, Wavemetrics, Lake Oswego, OR, USA).

Subsequent image analysis was also performed with IGOR Pro and is reported in the Results section.

5.3. Results

During the sensitization and challenge protocol (Fig 5.1a) the OVA challenged rats displayed significant clinical features of bronchospasm with marked increases in rate and depth of respiration, which settled within 4 – 6 hours. Histology data revealed a significant response amongst the OVA challenged Brown Norway rats post sensitization, compared to sensitized control animals (Fig. 5.2b). There was significant thickening of the bronchial epithelium with large numbers of inflammatory cells, particularly mononuclear cells, seen on light microscopy. BAL data from the satellite group demonstrated a marked inflammation with a large increase in % differential eosinophil count among the OVA challenged animals (Fig. 5.2). Unfortunately the satellite BAL sample from one of the control lungs did not stain sufficiently to allow calculation of the differential cell count, therefore values are calculated from the other two control lungs.

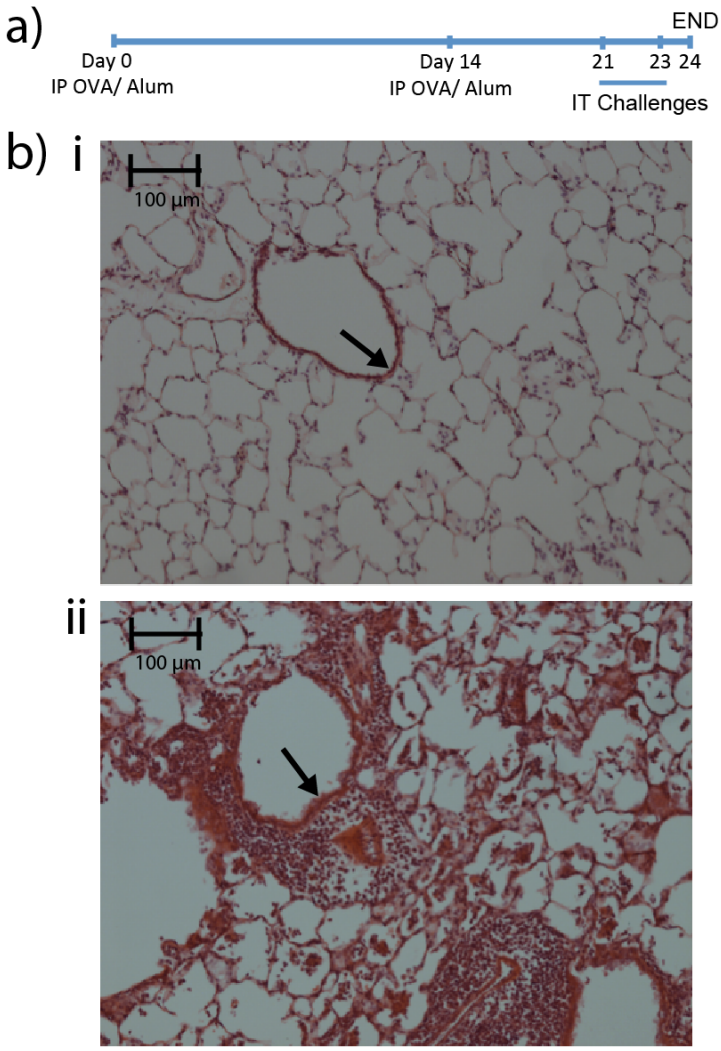

Figure 5.1. Sensitization and challenge protocol with typical light microscopy images of control and OVA challenged lungs. (a) All rats were sensitized with intrapertioneal (IP) injections of 2 mg ovalbumin and 200 µg aluminum hydroxide (Alum) on day 0 and day 14 with subsequent intratracheal (IT) challenges on days 21 and 23 of either 1 mL sterile PBS (control animals) or 1 mL OVA (500 µg/250 µg OVA) with the same OVA dose on each challenge. Animals were euthanized on day 24 for either BAL/histology or *ex vivo* hp ^{129}Xe MRI. (b) Light microscopy image from (i) control (PBS challenged) lung and (ii) 500 µg OVA challenged lung. Note the clear airspaces and thin bronchial walls of the large airways (arrow) in the control lung in contrast to the marked increase in cellular infiltrate particularly around the large airways (arrow) in the OVA challenged lung.

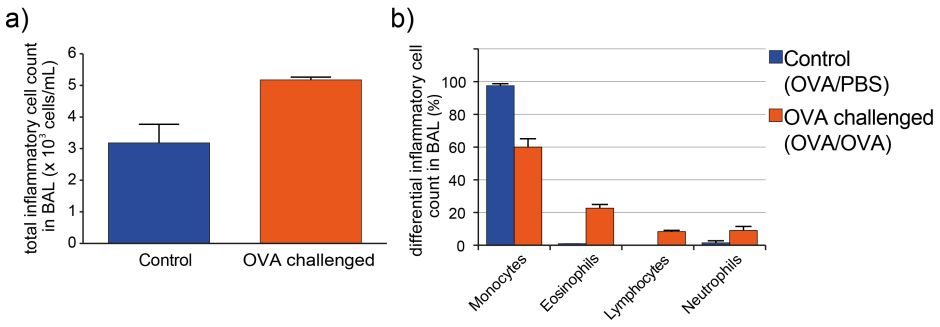

Figure 5.2. Bronchoalveolar lavage (BAL) data. % differential inflammatory cell counts. Mean data with standard deviations (error bars) from satellite (histology) group with BAL performed immediately after death. (a) Note the higher inflammatory cell count in the OVA challenged group (OVA sensitized/OVA challenged) compared to the control group (OVA sensitized/PBS challenged). Similarly note the increased mean % differential eosinophil count in the OVA challenged group (b) indicating allergic inflammation of the airways was present (error bars again represent standard deviation). The control BAL % differential cell count is calculated from a sample size n = 2 compared to n = 3 in the OVA challenged group (see text for detail). Total inflammatory cell counts are from sample sizes n = 3 in both OVA challenged and control groups.

Examples of image datasets acquired from control and OVA challenged animals are displayed in Fig.5.4 and Fig. 5.5 (located in the image plates at the end of the chapter). Images were taken at: baseline; after a 4.5 mL bolus of Hartmann's; on increasing doses of MCh; and on subsequent reversal with flushes of varying volumes of Hartmann's solution and up to 1500 μg of salbutamol. Multiple baseline images (minimum of two) were acquired and visually inspected to ensure a stable reference point for comparison of later image data on increasing MCh dosages. The presence of ventilation defects (regions with absent hp gas signal) was noticeable in one control lung after 200 μg MCh (460 μg cumulative MCh dose) and in

two OVA treated lungs after 50 – 75 μg MCh (85 - 160 μg cumulative MCh dose), however there were noticeable reductions in overall signal intensity in all OVA challenged lungs. Significant reversal was however noted in only one control animal (C.1) and one OVA challenged animal (OVA.1).

As a measure of the reduction in ventilation across the whole lung the mean normalized signal intensity was compared between images. The mean value was calculated by dividing the integral of all voxel values across each image by the total number of image voxels. Mean image values were then normalized to the mean signal intensity of the first baseline image for comparison.

Slice selective and non-slice selective measurement of the mean normalized signal intensity were obtained in control and OVA challenged lungs (see Fig. 5.6). Both values show close correspondence at all points in the time sequences. However the non-slice selective value was used for further comparison between control and OVA challenged lungs as this allowed for monitoring changes in whole lung ventilation.

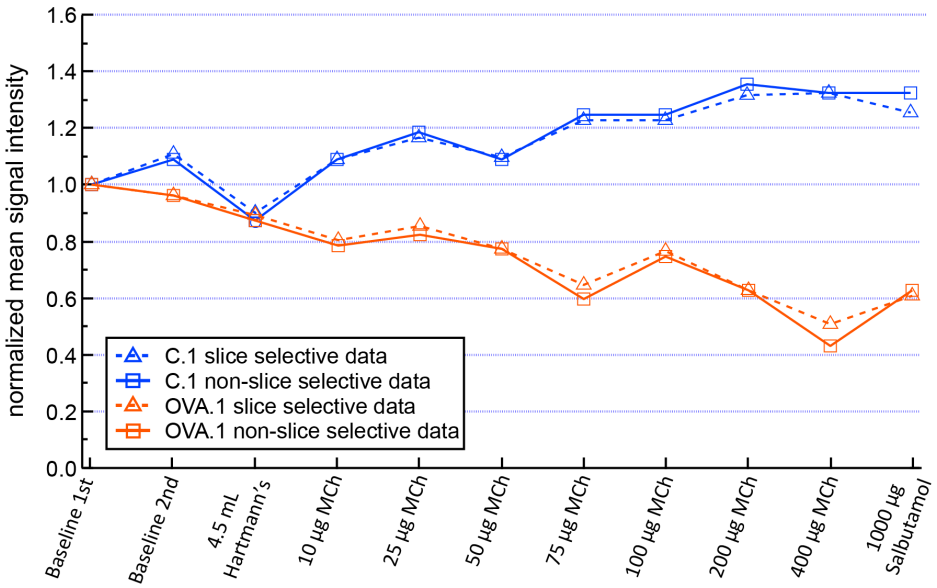

Figure 5.6. Timeline of mean normalized signal intensity in a control and OVA challenged lung. Values from mean normalized signal intensity from images in sequences Fig. 5.4 (rat lung C.1) and Fig. 5.5 (rat lung OVA.1) normalized to the 1st baseline values in each image sequence. Note close approximation between slice selective and non-slice selective datasets in both lungs. There is an increase in normalized mean signal intensity over the sequence in lung control lung, while there is a marked reduction in mean normalized signal intensity over the same sequence of events in the OVA challenged lung.

The time courses of mean normalized signal intensity in all lungs imaged with hp ^{129}Xe MRI are displayed in Fig. 5.7. It can be seen that control animals largely show little or no reduction in mean normalized signal intensity when compared to lungs from the OVA challenged group where there is a >50% reduction by the 400 µg dose of MCh.

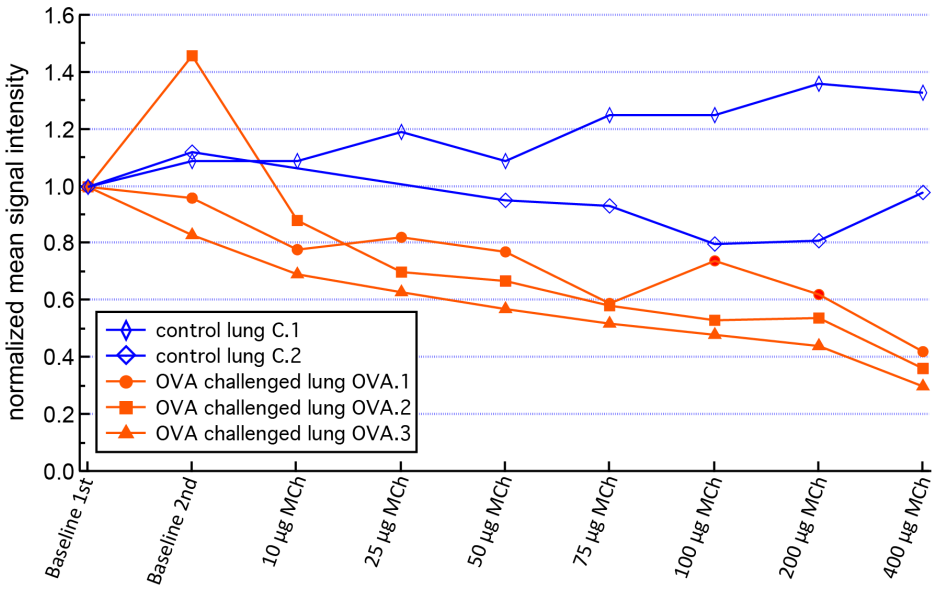

Figure 5.7. Timeline data of mean normalized signal intensity from all lungs using non-slice selective datasets. Values are normalized to 1st baseline image. Note the variation in baseline signal intensities particularly noticeable in lung OVA.2.

To illustrate the change in mean normalized signal intensity as a function of cumulative MCh dose, data was replotted (Fig. 5.8). To compensate for the effect of small fluctuations in the SEOP process upon the signal intensity, the average value from the two baseline images was used for recalculation of the mean normalized signal intensity at each time point. In Fig. 5.8 it can be seen that there is an initial significant drop between a cumulative dose of 10 – 160 µg MCh in the OVA challenged lungs followed by a slow reduction up to the maximum cumulative dose of 860 µg. As sample sizes were small for this proof of principle work only no statistical analysis was possible.

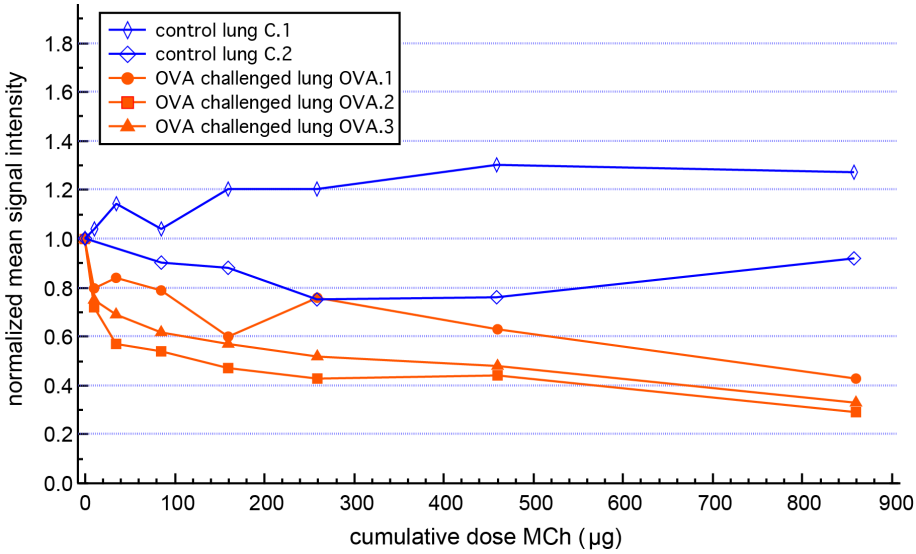

Figure 5.8. Mean normalized signal intensity from all lungs as a function of cumulative methacholine (MCh) dose. Values are normalized to the average baseline value. Note the clear separation between the control and ovalbumin challenged groups particularly at high cumulative MCh dosages.

Further analysis of the data studied the regional changes in ventilation on increasing dosages of MCh and on reversal where it occurred. To compare images on increasing cumulative dose of MCh a difference map was calculated where voxel values from baseline images were subtracted from those on increasing MCh dosages (Fig. 5.9b and Fig. 5.10b). Difference maps on reversal were similarly calculated except that the voxel values in the image corresponding to the 400 µg MCh dose (860 µg cumulative dose MCh) was subtracted from the image acquired on reversal. Note that small inter-breath differences were not rectified by image registration methods for this proof of principle work although this could be attempted in the future to reduce artefacts particularly noticeable at the airways.

The image sequence also allowed for comparison of gas distribution between scans, that is, the fraction of hp gas contained within each lung region. Each image was normalized by dividing each voxel value by the total integrated signal intensity of the image, thereby providing a measure of the fraction of total hp gas signal contained within each voxel. Normalized image matrices at baseline were subtracted from similarly normalized matrices at each dosage of MCh (Fig. 5.9c and Fig. 5.10c). Normalized reversal matrices were produced by subtraction of the normalized matrix corresponding to the 400 μg dose of MCh (860 μg cumulative dose MCh) from that matching the reversal image.

Interestingly using difference maps it was possible to detect ventilation defects before it became visually apparent on the spin density VFA FLASH images in Fig 5.9 (see image plate at end of the Chapter). By comparison the OVA challenged lung (Fig. 5.10- see image plate at end of the Chapter) demonstrated a global reduction in signal intensity across the sequence with small regions at the base of the lung and both apices revealing a marginal increase in signal intensity. However comparing the fraction of hp gas signal these regions contain increasing volumes of the total gas inhaled.

5.4. Discussion

The BAL and histology data with high levels of airway inflammation and large numbers of eosinophils demonstrate that the OVA model used in this study has resulted in an antigen induced allergic airways inflammation, replicating some of the features of human asthma. Intratracheal (i.t.) instillation as utilized in this work is less common than the use of aerosolized methods [65, 230, 234]. Instillation is less technically demanding than aerosolized methods with no requirements for measurement of particle sizes. On the down side, i.t. distribution tends to be less homogenous throughout the lung [5] however this was not considered a disadvantage in this work that focused on MRI methodology. The i.t. OVA dosages used in this study are higher than those used in previous experiments in the rat [237, 341] because it was desired to have a reproducible increase in airway responsiveness to MCh (known to need higher repeat OVA dosages [55]) for confirmation of the *ex vivo* imaging technique. BAL, histology and *ex vivo* hp ^{129}Xe MRI were therefore all performed within 24 - 36 hours post OVA challenges when the maximal allergic response has been reported.

As documented in Chapter 3, Brown Norway rats were chosen for this study as they have been noted to have a pronounced inflammatory response with greater degrees of airway reactivity on OVA challenges [230]. Additionally rats were preferred over mice because the larger inhaled volumes allowed for imaging within one breath using highly polarized hp ^{129}Xe.

Hp ^{129}Xe MR imaging was performed using constant pressure inhalation as this was found to be the most sensitive to changes in ventilation and is similar to that used by other groups *in vivo* [180] although this is not routine practice in the mouse where reductions in tidal volumes (*TV*) would add increasing difficulties to imaging. The use of the manual method (with a syringe pull) did however produce some variation (± 2 cm H_2O) in the inhalation pressures, which could be improved in future by using automated devices.

The ventilation protocol and MCh administration sequence did however demonstrate significant degrees of bronchoconstriction observed through hp ^{129}Xe MRI that could be partially reversed through salbutamol administration (Fig. 5.4 and 5.5). It should be noted that with a >50% reduction in whole lung signal intensities (approximating to a 50% reduction in inhaled gas volumes), the *ex vivo* model has once again allowed imaging of extreme pathophysiology unlikely to be recorded *in vivo* [291]. The wide separation of control and OVA challenged animals on cumulative MCh dosages beyond 160 µg (Fig. 5.8) with *p*-values approaching significance further demonstrates the utility of the *ex vivo* technique. Unfortunately as sample sizes were small, comparison of control and OVA challenged groups remains difficult, although it would seem that the degree of reduction in hp gas signal in healthy lungs is less than that demonstrated in OVA challenged lungs. Further experiments are planned to increase the sample sizes particularly of the control group and also to study the effect of a reduction in the OVA challenge dose.

The regional analysis using difference maps calculated between hp gas distribution at baseline and on increasing dosages of MCh (Fig. 5.9 and 5.10) allows for the visualization of changes in regional ventilation that would be otherwise difficult to identify. It has been shown that changes in ventilation can be seen before they are visually apparent on hp ^{129}Xe spin density images. Furthermore the overall reduction in inhaled hp gas volumes is greater in OVA treated lungs compared to control lungs, although there are large portions of the lung which are able to receive higher gas volumes. Whether this is linked to the degree of inflammation present at each of these regions due to heterogeneity in the OVA model was however beyond the scope of this work.

Previously, Johnson et al. studied the effect of high doses of intravenous (i.v.) MCh (30 μg) on healthy Sprague-Dawley rats using hp ^{3}He MRI [286]. Images with similar degrees of heterogeneity in ventilation to those recorded in this *ex vivo* work after MCh administration were acquired. However the use of a constant *TV* resulted in significant distension of the major airways, resulting in four animals dying from pneumothoraces. It was hypothesised that there was a partitioning in the lung response where gas destined for lung regions with significant constriction was shunted to less constricted zones, with associated hyperinflation. The regional data contained within this Chapter shown in Fig. 5.9 and 5.10 would tend to confirm this result where gas is seen to be increasingly shunted to less constricted regions during rising dosages of MCh, however unlike in the

live animal where the total dose of MCh is limited due to systemic concerns, much higher dosages can be administered repeatedly.

Other studies of asthma models with hp gas MRI have similarly focused on regional responses to MCh in healthy and asthmatic animals rather than the aforementioned whole lung data contained within this Chapter. Driehuys et al. reported a simple pixel counting method to quantify the regional changes in ventilation recorded in OVA sensitized and challenged (asthmatic) mice post MCh (compared to baseline images) [280]. Regional measurements focusing on the lung parenchyma and on the major airways were studied in an effort to quantify the variation in airway response between the two tissues and amongst different lung regions.

Deninger et al. had however previously described the concept of fractional ventilation, defined as the volume of 'new' (hyperpolarized) gas that replaces 'old' (non-hyperpolarized) gas on subsequent ventilations [342]. This concept was subsequently applied to an *Aspergillus fumigatus* mouse model of asthma [288] where there was noted to be a significant reduction in fractional ventilation values across asthmatic mouse lungs with considerable heterogeneity between different lung regions. Subsequent improvements in the technique have resulted in image datasets being acquired using less hp gas and faster acquisition times [180, 289].

Finally Mistry et al. reported a similar methodology to that in use within this Chapter where each voxel within a hp ^{3}He image was normalized by the integral of the signal intensity from a volume within the trachea [343].

Images were thereby less dependent on total image signal intensity (as reported in Fig. 5.9c and 5.10c) providing a measurement of the fraction of hp gas signal contained within each voxel. Subsequent difference maps were similarly generated between baseline images and on increasing dosages of MCh. It was therefore as described in this Chapter possible to visualize regions with reductions or increases in hp gas distribution. Furthermore quantification of changes in airway diameters was also possible. While these methods of regional analysis are similar to those employed within this thesis there are noticeable differences namely: in the previously published results imaging was performed *in vivo* over multiple breaths with the possibility that ventilation would change during the acquisition period of 12 s in mice that breath at a rate of 100 breaths/minute [344]; and in this work normalization for by whole image total signal intensity was performed as tracheal signal intensity on increasing MCh dosages would be expected to change.

5.5. Conclusions

The aim of this work was to demonstrate the ability of *ex vivo* functional hp ^{129}Xe MRI to detect ventilation differences in an ovalbumin rat model of asthma. The validated asthma model allowed for the detection of significant increases in airway responsiveness to intravenous MCh as detected by *ex vivo* hp ^{129}Xe imaging. Large alterations in ventilation were recorded with differences between control and OVA challenged animals on whole lung measurements. Heterogeneity in ventilation was detected across lung regions on delivery of MCh and on reversal images with the *ex vivo* lungs showing redistribution of hp gas on increasing MCh dosages with differences seen between control and OVA challenged animals. This work has therefore shown that the *ex vivo* model allows for simplified hyperpolarized ^{129}Xe MR imaging with useful information of dynamic changes in a small animal model of human asthma.

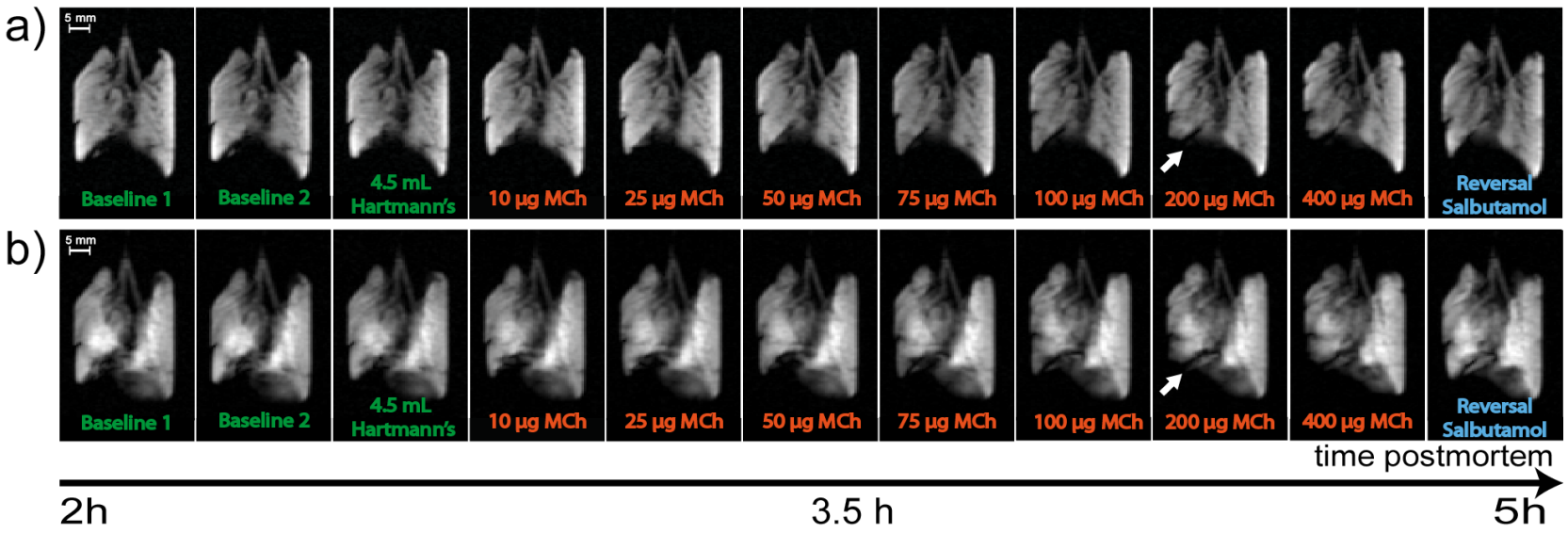

Figure 5.4. VFA FLASH image data from control lung at baseline and on increasing doses methacholine (MCh) with subsequent reversal. (a) Slice selective and (b) non-slice selective image data from control rat C.1. Window levels are uniform for MR signal intensity within both image datasets. Note the close correspondence between baseline images and after flushing with 4.5 mL Hartmann's solution. Noticeable ventilation defect in right lower lobe after 200 µg MCh (white arrows) with subsequent reversal after 1000 µg salbutamol and 29.0 mL Hartmann's solution.

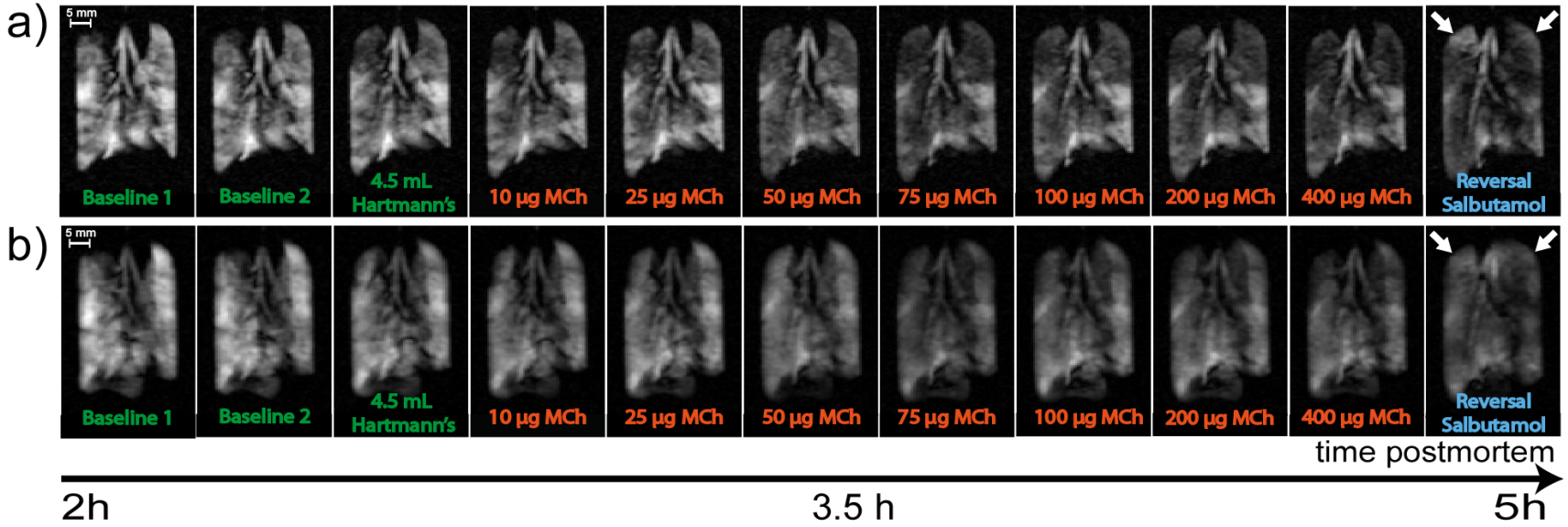

Figure 5.5. VFA FLASH image data from an ovalbumin (OVA) lung at baseline and on increasing doses methacholine (MCh) with subsequent reversal. (a) Slice selective and (b) non-slice selective image data from OVA challenged rat OVA.1. Window levels are once again uniform for MR signal intensity within both image datasets. Note the significant ventilation heterogeneity on the baseline images and a small reduction in signal intensity in the right cranial lobe after flushing with 4.5 mL Hartmann's solution. There is a noticeable reduction in signal intensity on the 50 µg dose of MCh with further significant reductions until 400 µg MCh. Subsequent reversal with 1500 µg salbutamol and 49.0 mL Hartmann's solution when signal increases in the right cranial lobe and the upper portion of the left lobe (white arrows).

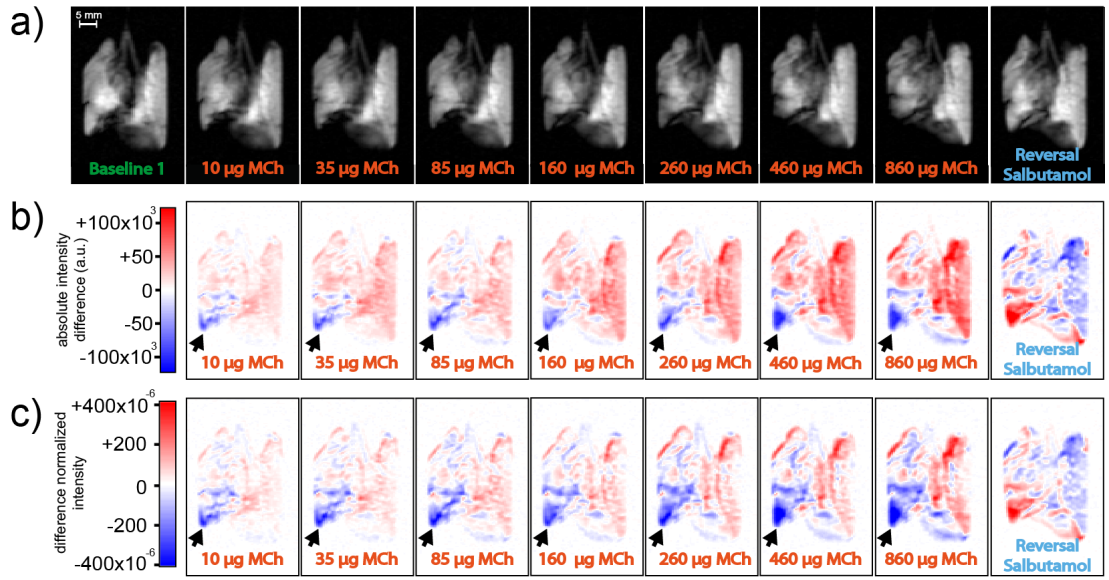

Figure. 5.9. Image data from a control lung with accompanying maps displaying changes in regional ventilation. (a) Non-slice selective VFA FLASH image data from lung C.1 on cumulative dosages of MCh (indicated) and on reversal with flushes of 29 mL Hartmann's solution and 1000 µg salbutamol. (b) Absolute difference maps with difference between baseline image and increasing dosages of MCh and on reversal. Red indicates an increase in absolute hp gas signal intensity while blue indicates a reduction. (c) Difference maps calculated from changes in regional gas fraction as described in the text. Red indicates an increase in the regional fraction of inhaled gas with blue a decrease. Note the reduction in ventilation seen on the difference maps at the right caudal lobe (arrows) where there is a progressive reduction in signal intensity and the fraction of inhaled hp gas between 10 – 460 µg of MCh when it becomes visually apparent on the spin density VFA FLASH image in (a). Other lung regions show an increase in signal intensity and fractional hp gas inhalation. This region then permits hp gas entry on reversal with other lung regions demonstrating a reduction in signal intensity and fraction of inhaled gas.

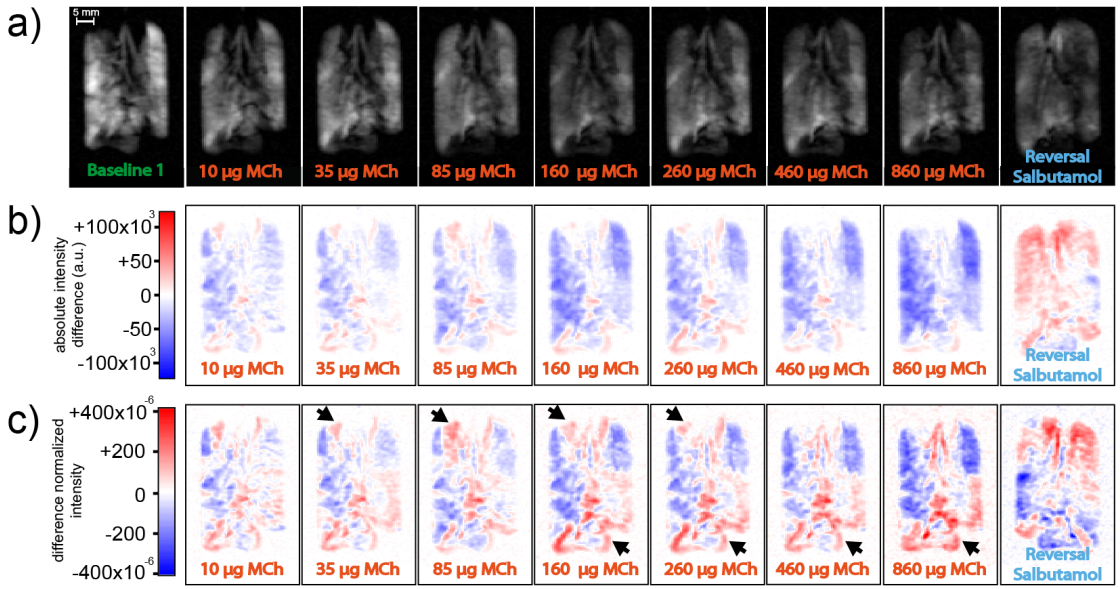

Figure. 5.10. Image data from an OVA challenged lung with accompanying maps displaying changes in regional ventilation. (a) Non-slice selective VFA FLASH image data from lung OVA.1 on cumulative dosages of MCh (indicated) and on reversal with flushes of 49 mL Hartmann's solution and 1500 µg salbutamol. (b) Absolute difference maps and (c) maps indicating changes in the regional fraction of inhaled gas as described in Fig. 5.9. Note the largely global reduction in ventilation seen on the absolute difference maps across the whole lung between 10 – 860 µg with small regions of increased signal intensity at the base of the lung and both apices. However comparing the fraction of hp gas signal in (c) it is clear that these regions (arrows) contain increasing percentage of the total the total gas inhaled. On reversal, hp gas distribution shows a global increase with small reductions in the regions indicated (arrow) with the change in fractional distribution opposite to that seen during the MCh challenges.

Chapter 6: MRI of hyperpolarized krypton-83 surface quadrupolar relaxation (SQUARE) in an *ex vivo* rat model of emphysema

The work contained within this Chapter is a further development of that found in the article published in the peer-reviewed journal Magnetic Resonance Imaging entitled "Pulmonary MRI contrast using Surface Quadrupolar Relaxation (SQUARE) of hyperpolarized ^{83}Kr" by Joseph S. Six, Theodore Hughes-Riley, David M.L. Lilburn, Alan C. Dorkes, Karl F. Stupic, Dominick E. Shaw, Peter G. Morris, Ian P. Hall, Galina E. Pavlovskaya, and Thomas Meersmann [216]. This journal article is reproduced in Appendix 1 for the convenience of the reader and to ensure familiarity with the methodology of the MRI of hp ^{83}Kr surface quadrupolar relaxation in the *ex vivo* rat lung. Within this Chapter the methodology developed in the publication is applied to the study of a rat model of emphysema, where the surface-to-volume (S/V) ratio in the lung parenchyma is decreased. Experiments were performed in collaboration with the Respiratory Pharmacology group at Imperial College London. Credits for the work were as follows: Dr. Lilburn and Prof. Meersmann conceived the experiments; Dr. Lilburn, Mr. Six and Ms. Lesbats performed the MR imaging experiments; Dr. Birrell, Mr. Dubuis and Ms. Yew-Booth handled the

animals and processed the histology while Dr. Lilburn and Dr. Birrell performed the lung harvesting; Dr. Lilburn, Ms. Lesbats, Dr. Birrell, Dr. Shaw, Prof. Belvisi and Prof. Meersmann analyzed the data; and Dr. Birrell, Dr. Shaw and Prof. Meersmann helped Dr. Lilburn with writing the report.

6.1. Introduction

Emphysema is a component of chronic obstructive pulmonary disease (COPD). Worldwide, COPD is the fourth leading cause of death [1]. In the UK it is estimated that COPD causes 25,000 deaths/year [345] with a large proportion of all COPD deaths due to emphysema in particular [346]. The development of emphysema is mainly linked to cigarette smoking with a smaller proportion attributed to pollution, occupational exposure or intrinsic factors [246]. Over time there is significant alveolar destruction with the resulting reduction in surface area for gas exchange with an accompanied loss of lung elasticity. Sufferers develop increasing dyspnoea with intermittent symptom exacerbations, which worsen over time and place significant limitations on physical activity and quality of life [347, 348]. Currently, exposure avoidance/reduction is the only effective treatment to slow or stop the progression of the disease [246, 349]. Unfortunately current routine investigations such as lung function tests often fail to diagnose the disease until the later stages [350] once a significant amount of damage has been done. There is therefore a need for new biomarkers to detect the disease in the early stages and to help separate COPD phenotypes [351].

Investigations of COPD and emphysema in particular have however developed over the past decade with human studies utilizing both computed tomography (CT) [352] and magnetic resonance imaging (MRI) based techniques [126, 353]. High resolution CT and hyperpolarized noble

gas imaging may provide the opportunity to detect the disease in the early stages [186, 354]. Early diagnosis would help with patient management by providing the sufferer timely objective information that they should cease smoking and hence limit further lung damage. Furthermore, early diagnosis offers the opportunity to study and potentially treat the disease when there is the greatest chance of preserving a significant amount of lung function.

Hyperpolarized noble gas MRI using ^{3}He and ^{129}Xe is able to provide measurements of ventilation and is able to delineate poorly ventilated and non-functioning lung regions [133]. Recently visualization of delayed collateral ventilation into lung regions has been performed [355] providing information complementary to CT based techniques. Nonetheless hp ^{3}He and hp ^{129}Xe have been used to provide measurements of the lung microstructure, that is, the apparent diffusion coefficient (ADC) discussed in Chapter 2 [187, 356, 357]. ^{3}He ADC is able to provide measurements of transverse and longitudinal diffusion within the acinus related to the diameters of the alveoli and the terminal bronchioles respectively [358, 359]. ADC is however insensitive to differences in surface composition. As described in Chapter 2, the ^{83}Kr nucleus, unlike ^{3}He and ^{129}Xe, possesses a nuclear electric quadrupole moment and therefore may be used as a probe for electric field gradients. The recent development of hp ^{83}Kr surface quadrupolar relaxation (SQUARE) MRI (as described in Appendix 1 and ref. [216]) may therefore provide a complementary technique allowing for additional information to hp ^{3}He

and ^{129}Xe imaging, such as regional information on the surface composition and surface–to-volume ratio [134, 216].

As mentioned in the previous Chapters, new techniques often require significant testing in animal models before translation to human subjects. Preclinical small animal models are an ideal starting point for ^{83}Kr SQUARE contrast development due to the small volumes of hp ^{83}Kr currently available [145, 216]. The elastase model is an established rodent model of emphysema whereby exposing the lungs to porcine pancreatic elastase (PPE) produces initial inflammation with the subsequent development of airspace enlargement and destruction [249, 253, 263, 360]. The purpose of the work in this Chapter is therefore to study hp ^{83}Kr SQUARE contrast in the elastase model of emphysema in the experimentally less demanding *ex vivo* setup and using the recently improved methodology [216] before development towards *in vivo* applications.

6.2. Materials and Methods

6.2.1. Model Characterization- the elastase model and preparation for *ex vivo* MRI

Male Sprague-Dawley rats (260 - 300 g, n = 22) were purchased from Harlan UK Ltd. (Bicester, UK). Home Office guidelines for animal welfare based on Animals (Scientific Procedures) Act 1986 were strictly observed. Experimental emphysema was induced by instilling one dose of 120 U/kg pancreatic porcine elastase (PPE, Merck Chemicals Ltd, Nottingham, UK) intratracheally at 1 mL/kg directly into the airways under general anaesthesia (inhaled isofluorane 4% with medical grade oxygen for 3 – 4 minutes) [263]. Control animals were similarly treated with 1 mL/kg sterile saline (Fresenius Kabi Ltd, Manor Park, UK) at the same time. At 28 days after intra-tracheal dosing animals were weighed and euthanized by overdose of sodium pentobarbital 200mg/kg intra-peritoneal (Merial Animal Health, Harlow, UK). After confirmation of death, a catheter was inserted into the caudal vena cava to allow flushing of the pulmonary circulation with 20 mL heparin 100 IU/mL (Wockhardt UK Ltd, Wrexham, UK) in 0.9% saline solution (Baxter Healthcare Ltd, Thetford, UK) followed by 20 mL Dublecco's phosphate buffer solution (D-PBS, Sigma-Aldrich Ltd, Gillingham, UK) to remove residual blood from the pulmonary circulation. The heart and lungs were subsequently removed *en masse*.

Lungs for *ex vivo* hp ^{83}Kr imaging had a polytetrafluorethylene (PTFE) adapter tube inserted into the trachea 5 - 10 mm above the carina and sutured into place. The heart and lungs were then suspended in 5%

glucose solution (weight/volume) with the trachea pointing downwards as in the previous chapters. The *ex vivo* lungs were repeatedly inflated with 8 - 10 mL of room air to check for gas leaks either from the suture around the trachea or the lungs themselves. The lungs were chilled to 278 K for transportation to the imaging facility during which time they were repeatedly inflated with 8 -10 mL of air at 30 – 60 minute intervals. Time from lung harvest to the start of imaging was no more than 8 hours for each lung.

Of the 22 rat lungs harvested, 4 were used for histology and 15 of the remaining 18 were suitable for *ex vivo* hp ^{129}Xe MR imaging with the others being rejected due to the development of leaks either at the time of extraction or during transport.

6.2.2. Model Characterization- alveolar cross section measurements

PPE induced changes in air space were measured in both a satellite group of rats and on the *ex vivo* lungs used for hp ^{83}Kr MRI. Lungs from both groups were similarly prepared by inflating to forced vital capacity (25 cm H_2O) with 5% formalin-saline solution (Sigma-Aldrich Ltd, Gillingham, UK). Air-space quantification was performed using an Olympus BX40 microscope and Zeiss image-processing software (Imaging Associates, Bicester, UK) [263]. Using colour-thresholding techniques total parenchymal airspace cross section in μm^2 and the total number of airspaces were measured from 5 random fields per lung lobe. Mean air space area for each field were quantified allowing for calculation of mean values for each lobe. During image analysis fields containing airways or vasculature were excluded. Details of control and PPE treated lungs are shown in Table 6.1 with average measurements of mean alveolar area (MAA) in the satellite group and in those lungs processed post *ex vivo* hp ^{83}Kr MRI.

	Identifier	Rat Weight (g)	Whole lung mean alveolar area (μm²)	Slice or non-slice selective hp ^{83}Kr MRI	Inhaled volume, V_i,(mL)	Inhalation pressure (cm H_20)
CONTROL	C.1	370	30752.0 ± 2797.2	Slice	6.4 ± 0.3	24.8 ± 2.2
	C.2	380	124746.3 ± 71030.6*	Slice	6.4 ± 0.2	29.3 ± 1.3
	C.3	308	31157.2 ± 4348.0	Slice	5.9 ± 0.5	32.3 ± 0.5
	C.4	555	25218.9 ± 1001.6	Non-slice	6.8 ±0.1	21.0 ±0.0
	C.5	400	19095.3 ± 1462.8	Histology	N/A	N/A
	C.6	412	25109.6 ± 3953.5	Histology	N/A	N/A
ELASTASE (PPE) TREATED	E.1	350	44988.9 ± 5444.2	Slice	6.5 ± 0.1	31.7 ± 4.2
	E.2	393	36406.9 ± 11162.7	Slice	6.4 ± 0.3	25.5 ± 1.0
	E.3	385	46261.9 ± 7083.2	Slice	6.6 ± 0.5	27.2 ± 2.4
	E.4	390	62769.6 ± 11162.7	Non-slice	6.3 ± 0.3	26.0 ± 0.0
	E.5	508	68223.0 ±10760.4	Non-slice	6.1 ± 0.6	-
	E.6	513	36405.3 ± 10352.7	Non-slice	6.1 ± 0.2	-
	E.7	416	57714.6 ± 10036.8	Slice and Non-slice	6.9 ± 0.3	-
	E.8	440	44804.2 ± 5872.5	Non-slice	7.3 ± 0.4	-
	E.9	454	27892.4 ± 10898.2	Slice	7.1 ± 0.2	-
	E.10	382	47670.8 ± 14451.6	Histology	N/A	N/A
	E.11	436	107926.5 ± 61889.7	Histology	N/A	N/A

Table 6.1. Demographic data from satellite subjects (histology) and those used for hp ^{83}Kr imaging. Summary of rat weights, whole lung mean alveolar area ± standard deviation of the mean, inhaled volumes (V_i) ± standard deviation corresponding to inflation (syringe) volume V_s = 8 mL with associated inhalation pressures ± standard deviation at V_s = 8 mL. *Recalculated value for C.2 from 3 lung lobes excluding 2 outlier values = 28514.2 ± 3991.7 μm². Note that different hp ^{83}Kr imaging was performed (slice selective or non-slice selective imaging) on lungs as indicated in the

Table. No values for V_i were determined in the histology groups. Values omitted were not measured.

6.2.3. ^{83}Kr spin exchange optical pumping, compression and transfer

Hp ^{83}Kr was produced in batch mode by SEOP as described in detail in chapter 6 and in ref. [145]. All MR imaging was performed using enriched ^{83}Kr (99.925% ^{83}Kr, CHEMGAS, Boulogne, France) to improve the available signal intensity. A 15% krypton 85% N_2 (99.999% purity, Air Liquide, Coleshill, UK) mixture was used to reduce the consumption of expensive isotopically enriched ^{83}Kr. SEOP build times of 12 minutes, corresponding to ~92% of the steady state polarization were once again used to reduce the experimental duration. The extraction unit described in Appendix 1 and ref. [215] was utilised to allow for below ambient pressure SEOP with enhanced ^{83}Kr spin polarization [145] (see Fig. 6.1). Further reductions in the transfer container volume between the SEOP cell and the lungs allowed for SEOP at 55 – 65 kPa with an increase in the available polarization in the lower concentration ^{83}Kr gas mixture. Overall, the method produced approximately 12 - 16 mL of hp gas every 12 minutes for lung imaging with an approximate apparent spin polarization of P_{app} = 2.5%, when accounting for losses during the extraction procedure [145].

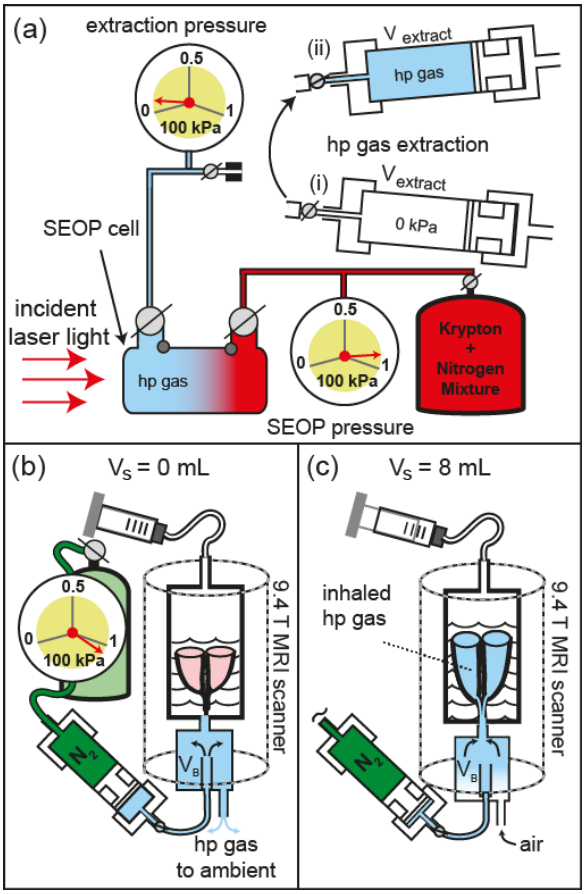

Fig. 6.1. Hp krypton-83 gas extraction and transfer from the SEOP cell in the hyperpolarizer to the lungs (ambient pressure). (a) A pre-evacuated volume $V_{extract}$ = 790 cm^3 in the extraction unit (i) was filled to approximately 6 kPa during hp gas extraction from the SEOP cell in the hyperpolarizer (operating at 90 – 100 kPa) (ii). (b) The extraction unit was moved to the MRI scanner and the N_2 gas operated piston pressurized the hp gas mixture to a slightly above ambient pressure. The hp gas was then pushed through connecting tubing into a storage container (V_B). (c) Inhalation of the hp gas was accomplished by pulling to volume V_s = 8 mL on the ventilation syringe to expand the lung as has been previously demonstrated. Modified with permission from Fig. 1 in Appendix 1 and ref. [216].

6.2.4. Hp gas inhalation

The ventilation chamber described in Chapters 4 and 5 was again utilised with the lungs suspended in a 5% glucose solution (weight/volume) (Baxter Healthcare Ltd, Thetford, UK). The chamber was then placed inside the bore of the superconducting magnet and the temperature was kept constant at 295 K throughout the experiments. Active inflation of the lung was accomplished by pulling to a ventilation syringe volume (V_s) of 8 mL (Fig. 6.1a). Corresponding inhaled volumes (V_i) were measured separately using the water displacement technique on gas exhalation and can be seen in Table 6.1. To limit gas trapping (particularly noticeable in the PPE treated lungs) the *ex vivo* lungs were deflated over 30 - 60 s from V_s = 8 mL to maximum exhalation (V_s = 0 mL) as has been reported elsewhere [10, 309] before hp ^{83}Kr inhalation.

6.2.5. MRI protocol

MRI experiments were performed using a vertical bore 9.4 T Bruker Avance III microimaging system (Bruker Corporation, Billerica, Massachusetts, USA) with a Bruker 30 mm double saddle probe tuned to 15.40 MHz corresponding to the resonance frequency of ^{83}Kr gas in the lung. Images were acquired by means of 32 phase encoding gradient increments using a variable flip angle (VFA) FLASH protocol (TE = 1.8 ms, TR = 12.6 ms) [177]. The imaging protocol had a total acquisition time 0.405 s limiting the T_1 decay during acquisition.

Coronal images were acquired into 64 × 32 matrices resulting in a field of view (FOV) of 50.9 mm in the longitudinal (frequency encoding) and 40.7 mm in the transverse (phase encoding) directions, respectively. To acquire a non-slice selective image, 0.3 ms rectangular hard RF pulses of variable power levels were used for excitation. The slice selective images utilized 2 ms sinc-shaped pulses of variable power to selectively excite a 3 mm central coronal slice of the lung, resulting in resolution of $0.80 \times 1.27 \times 3$ mm^3.

To obtain T_1-weighted images and demonstrate SQUARE pulmonary MRI contrast two schemes were utilised. Scheme 1 employed the paradigm seen in Appendix 1 with each imaging sequence started after a programmed time delay after inhalation t_d = 0.0 s, 0.5 s, 1.0 s, 1.5 s or 2.0 s. The inhalation itself was accomplished manually by reducing the pressure in the artificial pleural cavity using the ventilation syringe as previously

described [214, 291]. Slight alternations in the timing (approximately ± 0.2 s) of the manual inhalation procedure were deemed acceptable. However it became clear that images taken at t_d = 0.0 s showed considerable variation due to timing difficulties and were thus discounted from the analysis. As a result of this finding, five images were performed at t_d = 0.2 s, 0.7 s, 1.2 s, 1.7 s or 2.2 s after inhalation in later experiments (see Fig. 6.1). In all imaging experiments in scheme 1 each individual image was acquired from a single inhalation cycle and subsequent VFA FLASH acquisition (NEX = 1) with no signal averaging. As a proof of principle for future development scheme 2 was developed to allow for two images to be performed during one inhalation cycle with an inter-image duration of 1.4 s thus abolishing artefacts as a result of inter-breath volume and timing differences (see Fig. 6.3a-b). Due to the need for larger signal intensities, this technique permitted only non-slice selective imaging but was used to for comparison to the data from experiments in scheme 1 where non-slice selective imaging had been performed.

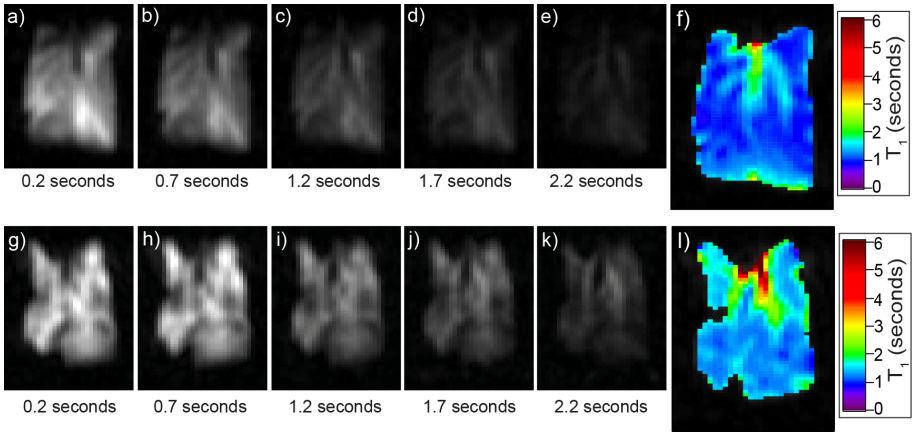

Figure 6.2. Series of hp ^{83}Kr MR images with resultant T_1 map in control and PPE treated lungs using scheme 1. Each image was acquired using a new delivery of hp ^{83}Kr. (a) VFA FLASH MRI with no slice selection in control lung C.4. .(b – e) MR images as in (a) with a relaxation delay, t_d, between hp gas inhalation and acquisition as indicated in the figure. Note that the major airways are less affected than the lung parenchyma by increasing t_d values. (f) Resultant T_1 map for the control lung. (g – k) Similarly acquired VFA FLASH MRI with no slice selection in PPE treated lung E.4 as in (a – e). Note the heterogeneity in ventilation displayed in the elastase treated lungs as compared to the control. (l) Resultant T_1 map in the PPE treated lungs.

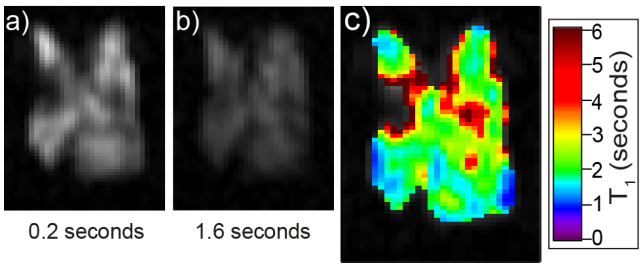

Figure 6.3. Series of two hp ^{83}Kr MR images acquired with scheme 2 and the resultant T_1 map from the PPE treated lung in Fig. 7.1. (a) VFA FLASH MRI with no slice selection in the PPE treated lung shown in Fig. 7.1 (lung E.4). (b) MR images as in (a) with a relaxation delay of t_d = 1.4 s after the first image. (c) Resultant T_1 map for images in (a – b). The reduced quality of data fit results in significantly higher T_1 values than that produced by scheme 1. Note the removal of non-sensical T_1 values < 0 s from the resulting T_1 map.

6.2.6. Image reconstruction and analysis

Images were once again processed and reconstructed in Prospa (v. 3.06, Magritek, Wellington, New Zealand) with a sine-bell squared window function applied to the raw data before two-dimensional Fourier transformation. The two dimensional image data were then exported for analysis in IGOR Pro (v. 6.01, Wavemetrics, Lake Oswego, OR, USA). Intermittent random noise was at times problematic with occasional noise spikes recorded in some of the slice selective data in the centre of the FOV. This data was excluded from any analysis of T_1 values and later improved RF shielding prevented further problems. Furthermore, random noise around 15.0 MHz leaked into some of the image data but the result on mean T_1 calculation was minimal and subsequent analysis of regional T_1 measurements avoided these regions.

Using scheme 1 T_1 maps were created using the set of either four or five images at increasing delay times (depending on the protocol) combined into a three dimensional matrix as in Appendix 1. T_1 values were calculated by logarithmic linear regression analysis and plotted to the resultant T_1 matrix (Fig. 6.2f and 6.2l). T_1 values calculated outside the lung region were masked as these were essentially noise. Thresholds based on the relative signal-to-noise ratios between the non-slice and slice-selective datasets were therefore applied for the masking. The threshold was set to 15.0% of the maximum signal intensity at t_d = 0.2 s for non-slice selective data (SNR approximately 60 – 70) and 20.0% at t_d = 0.2 s or 0.5 s for slice selective (SNR approximately 45 – 55). Noise far removed from the lung

remaining after the mask was also removed. The final T_1 maps displayed in Fig. 6.2f and 6.2l were then overlaid onto the lung at delay time t_d = 0.2 s for clarity of presentation. A further image-processing step was applied to the T_1 maps of the slice selective images where the discernable large airways were removed from any subsequent analysis to focus on the lung parenchyma. T_1 maps were similarly created using the images acquired under scheme 2 with logarithmic linear regression analysis across the two images. Calculation of the image threshold using the two images acquired in one inhalation cycle was performed similarly with a threshold of 20.0% applied to the image at t_d = 0.2 s due to the significant drop in available signal to noise ratio (SNR). Further image processing and statistical analysis were performed using IGOR Pro and SPSS (IBM, New York, USA) and are reported in the Results section. Probability (p) values less than 0.05 were deemed significant.

6.3. Results

6.3.1. Alveolar cross section measurements

Example histology from control and elastase treated lungs is displayed in Fig. 6.4. Mean alveolar areas (MAAs) were calculated from such images. The average whole lung MAA for the control group was 26,641.2 ± 1,844.9 μm^2 (mean ± standard error) compared to 53,626.0 ± 7,212.3 μm^2 for the PPE treated group. Both the Mann-Whitney U-test and Kolmogorov Smirnov test for independent samples reached significance (p = 0.003 and p =0.007 respectively), indicating that the distribution of MAAs was different between control and PPE treated groups.

However, the means for the control and PPE treated lungs in the imaged sample were 28,910.6 ± 1,360.9 μm^2 and 47,582.8 ± 4,418.0 μm^2 respectively, with the samples not being significantly different (p = 0.064 for the Mann-Whitney U-test and p = 0.057 for the Kolmogorov Smirnov test). Representation of the distribution of whole lung MAA in the sample of control and PPE treated lungs used for hp ^{83}Kr MRI is displayed in Fig. 6.5a.

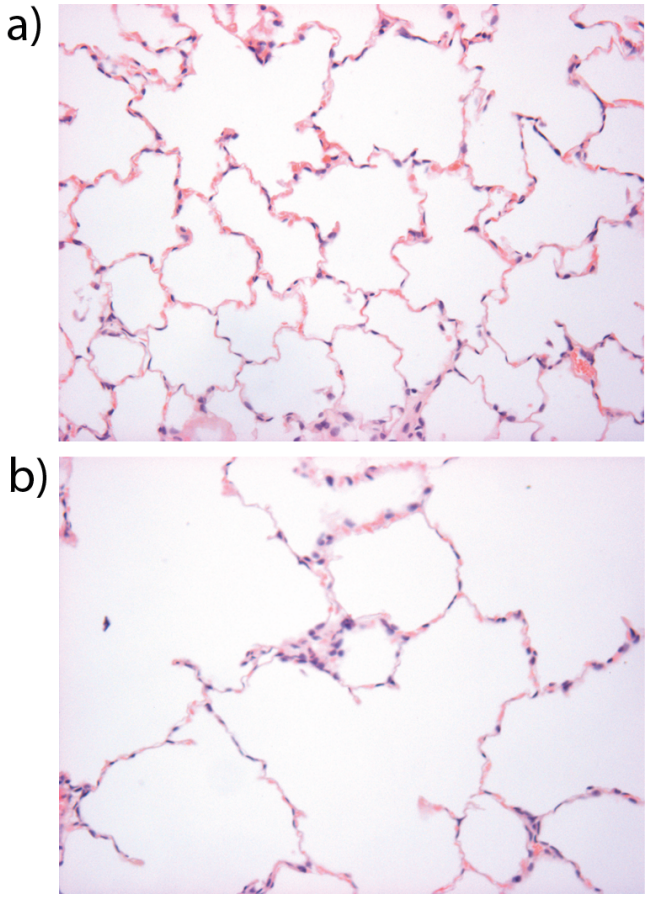

Figure 6.4. Low power light microscopy image of a) control lung and b) elastase treated lung. Note the widespread destruction of alveoli in the elastase treated lung with much larger effective airspace area.

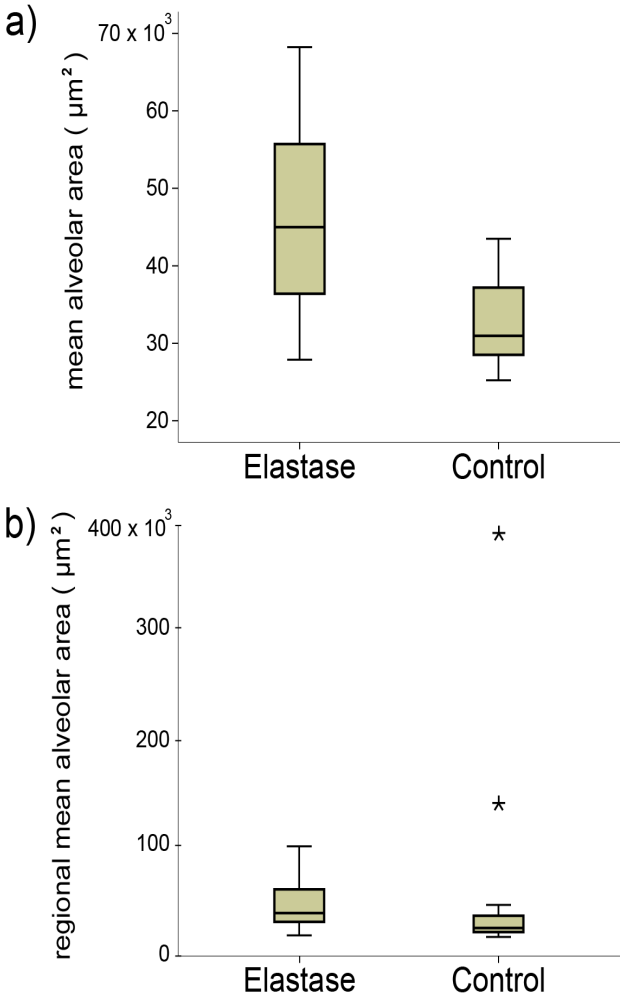

Figure 6.5. Box and whisker plots comparing a) whole lung MAAs of control and PPE treated rats lungs used for hp ^{83}Kr MRI and b) regional (lobar) MAAs of control and PPE treated rats lungs used for hp ^{83}Kr MRI. Whiskers represent maximum and minimum values**.** Note the out-lying regional (lobar) values (asterisks) in the control lung cohort (both from lung C.2- see text for details).

Variation in lobar values was higher in PPE treated lungs in both the histology (satellite) group and those used in *ex vivo* hp ^{83}Kr MRI (Fig. 6.5b). The control lungs showed similar lobar values in all lungs (histology and imaged groups) with the exception of 2 lobes in control lung C.2 (see Fig. 6b). As these lobar values were clearly outlier values, with MAA values far higher than the maximum of any of the PPE treated lobar values, they were discounted from subsequent analysis. These high values were thought to be due to errors during tissue processing as the lungs had appeared normal at the time of tissue harvest and on imaging. Examples of the

variation in both the lobar MAA measurements with corresponding T_1 maps are displayed in Fig. 6.6.

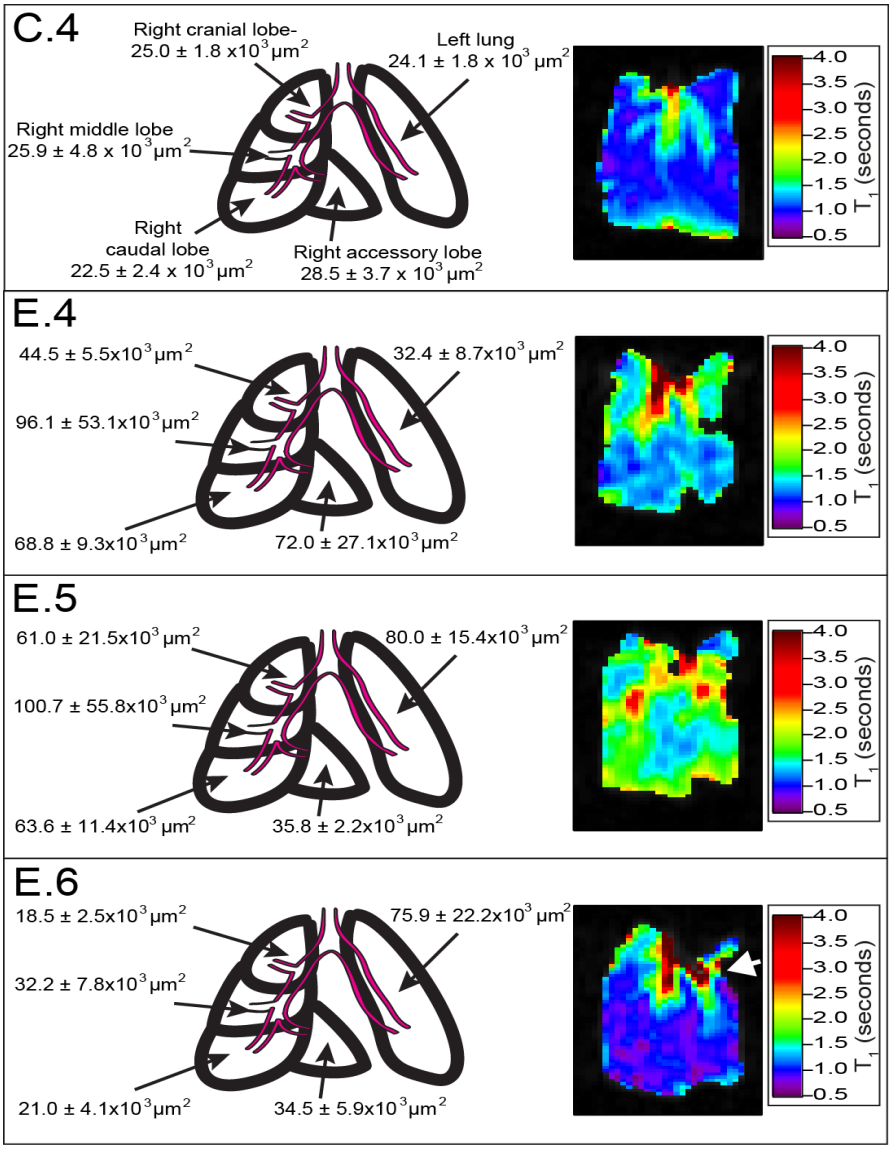

Figure 6.6. Mean regional alveolar area (MAA) values with corresponding T_1 maps demonstrating range 0.5 – 4.0 s. Schematic of rat lung anatomy illustrating principle measurements of lobar MAA and corresponding T_1 maps produced from non-slice selective datasets as in Fig. 6.2. Lungs as identified in figure with one control lung (C.4) and three elastase treated lungs (E.4 – E.6). Note that E.6 has similar regional MAA and T_1 values to those seen in lung C.4 with the exception of the left upper lobe where there is a large ventilation defect (white arrow).

6.3.2. T_1 map histogram analysis

Data from T_1 maps were then used for histogram analysis with frequencies of T_1 values within 0.15 s intervals calculated. Normalization for the total number of voxel values in each T_1 map allowed for comparison between lungs with different degrees of ventilation on MR imaging. Histograms were calculated for slice selective data before and after removal of the major airways in both control and PPE lungs (Fig. 6.7). Furthermore average histograms were calculated for the control and PPE treated groups of animals and used for comparison of the slice selective data where sample sizes permitted (Fig. 6.8).

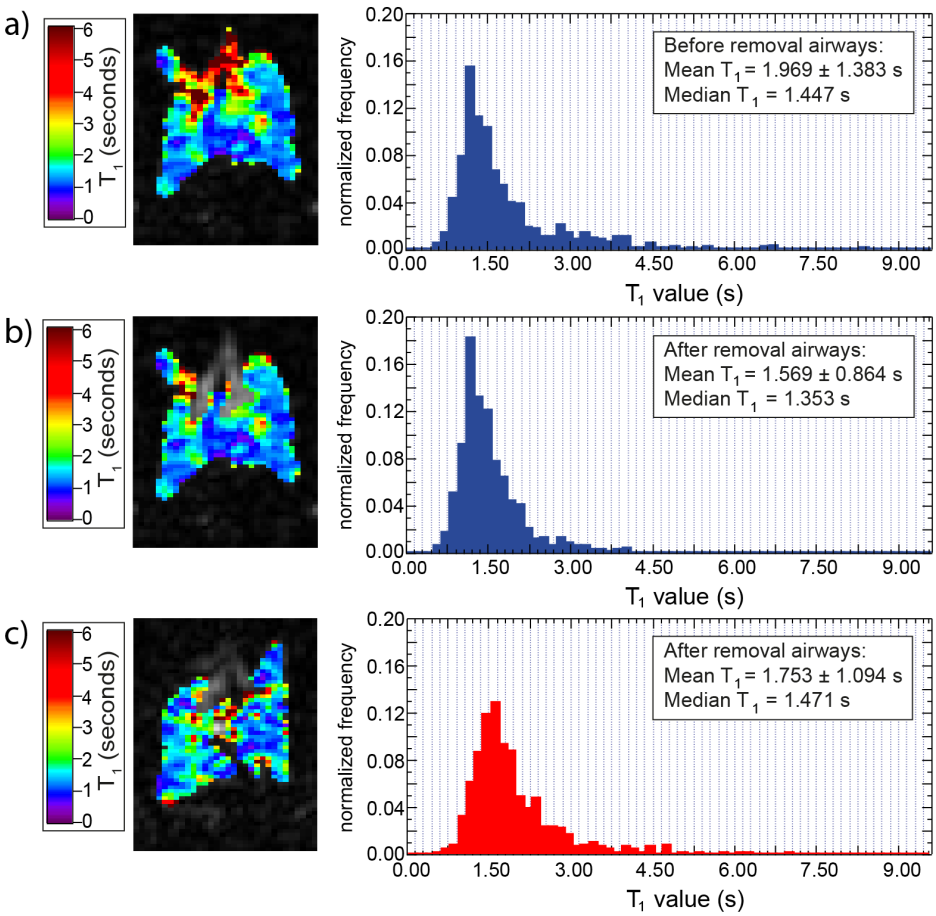

Figure 6.7. Histogram analysis of T_1 values. Slice selective dataset from the same control lung (a) before and (b) after removal of the major airway values with accompanying histograms of T_1 values. Mean ± standard deviation and the median value as indicated. (c) Slice selective data from PPE treated lung after removal airway of values. Note the greater spread of values with slightly higher mean and median values in the PPE treated lung.

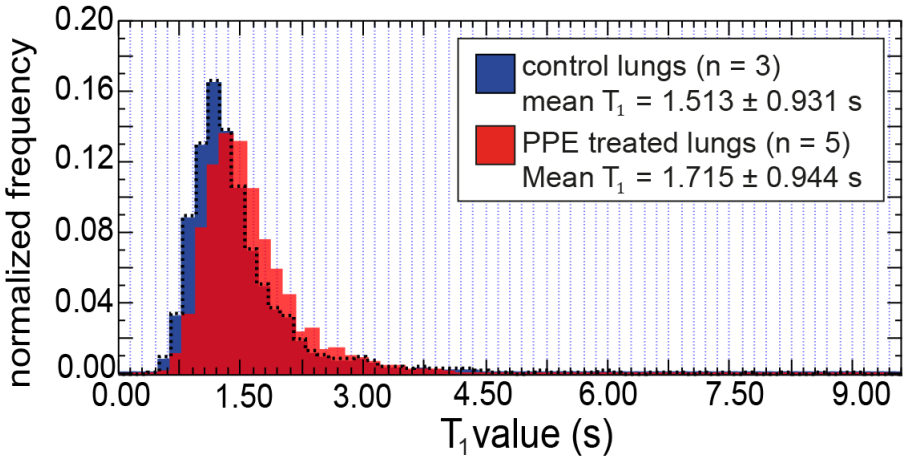

Figure 6.8. Histogram analysis of average T_1 data between control and elastase (PPE) treated groups. Note the shift toward higher T_1 values with the elastase treated lungs (red) and the slightly higher mean value compared to the control lungs (blue and with dashed outline). Errors are ± standard deviation.

6.3.3. Whole lung MAA and T_1 measurements

Due to the variation in the MAA of the PPE treated lungs it was decided to compare MAA values from the whole sample against the T_1 values obtained from *ex vivo* hp ^{83}Kr MRI. It is possible to calculate the average T_1 values by integrating across the entire thresholded T_1 map for comparison to the mean histological data. Assuming a simple spherical model of the alveolus, $S/V \propto R^{-1}$ (where R is the alveolar radius) with $T_1 \propto (S/V)^{-1}$. Therefore as $MAA \propto R^2$, it would be expected that $T_1 \propto \sqrt{MAA}$. Average T_1 values for non-slice and slice selective datasets (before and after removal of the major airways in slice selective data) are displayed in Fig. 6.9 with the corresponding square root of the whole lung mean alveolar areas. The results of linear regression analysis with data weighting according to the

inverse of the standard deviation of the T_1 values ($1/\sigma_{T_1}$) are displayed in Table 6.2.

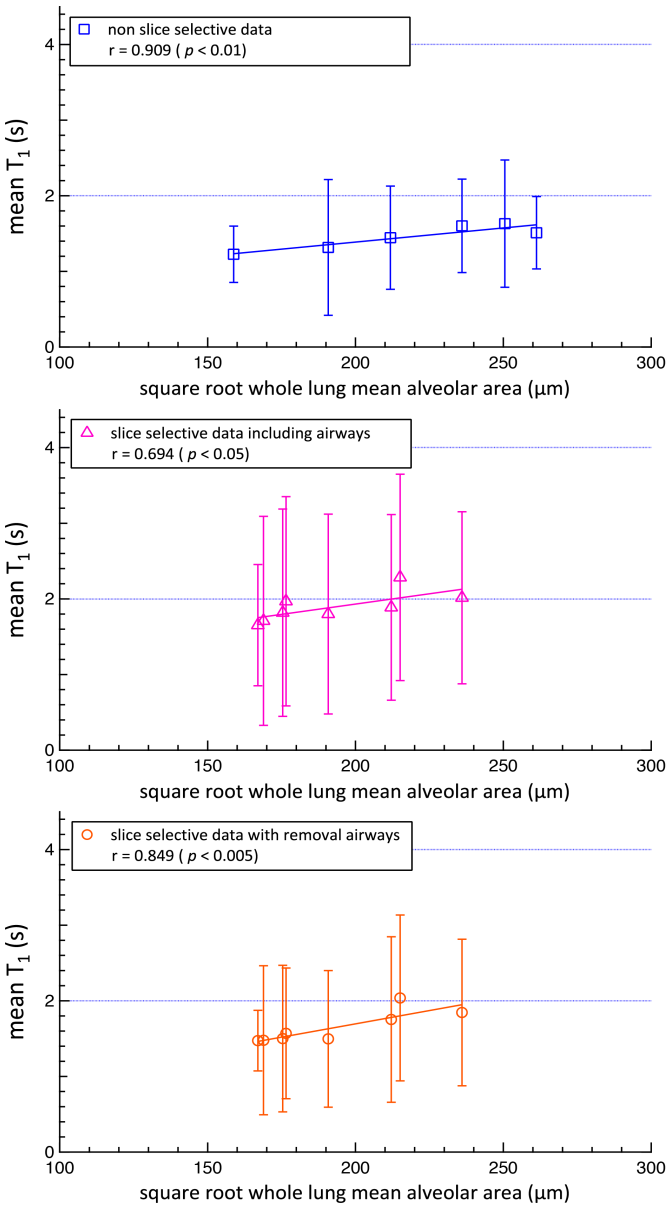

Figure 6.9. Mean T_1 plotted against the square root whole lung mean alveolar area. (a) Non-slice selective data (squares); (b) slice selective data including airway values (triangles) and (c) after manual removal of airways (circles). Values of linear correlation coefficient and significance levels of the least squares solutions indicated in figure. Note error bars represent the standard deviation of the mean T_1 values.

	Slope (s/μm)	Intercept (s)	r
Non-slice selective T_1 data	$3.7\times10^{-3} \pm 0.9\times10^{-3}$	0.64 ± 0.18	r = 0.909 ($p < 0.01$)
Slice selective T_1 data including major airways	$5.4\times10^{-3} \pm 2.3\text{-}\times10^{-3}$	0.84 ± 0.45	r = 0.694 ($p < 0.05$)
Slice selective T_1 data with major airways removed	$7.0\times10^{-3} \pm 1.8\times 10^{-3}$	0.29 ± 0.35	r = 0.849 ($p < 0.005$)

Table 6.2. Results of linear regression analysis in Fig. 7.7. Equation of the linear regression solution has the form: mean T_1 (s) = Slope × $\sqrt{whole\ lung\ MAA}$ + intercept, with accompanying linear correlation coefficients (r) values.

6.3.4. Regional MAA and T_1 measurements

Due to the significant inter-subject variation in whole lung MAA in the PPE treated group (as seen in Fig. 7.4), lobar MAAs were then compared to regional T_1 values from 20 voxel regions of interest (ROIs) corresponding to each lobe in all lungs. ROIs were selected at least one pixel from discernable major airways and the outer limit of the lung to avoid values where inter-breath differences could have affected the results. If the lobe could not be identified (as in the case of the accessory lobe in all image data sets) or was not present in the image then no value was calculated. Areas of random noise were similarly avoided. The resultant regional T_1 values for non-slice and slice selective image datasets were then matched to the corresponding square root of the lobar mean alveolar area (Fig. 6.10). The two outlier lobar MAAs from lung C.2 mentioned in the

Materials and Methods section were not included in the analysis. The results of linear regression analysis with data weighting according to $1/\sigma_{T_1}$ are displayed in Table 6.3.

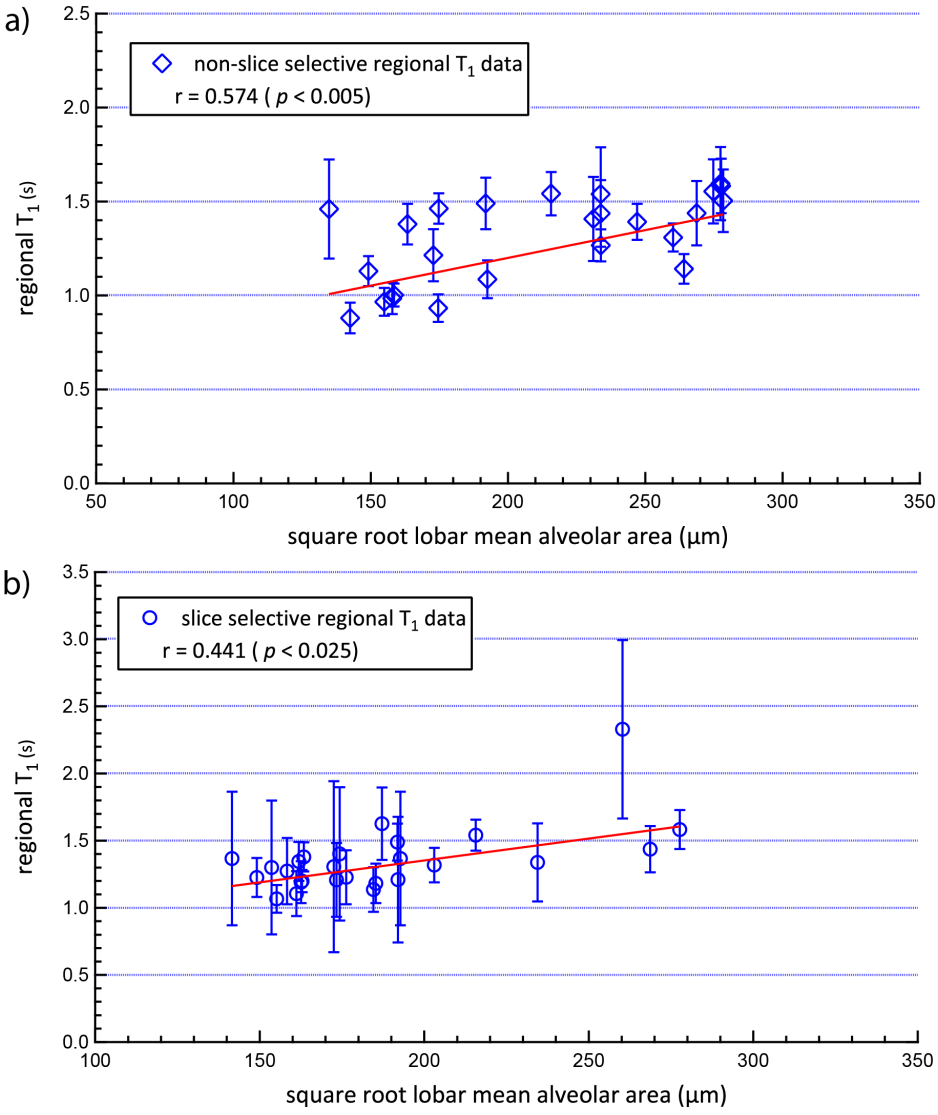

Figure 6.10. Correlation between mean regional T_1 and the square root of the lobar mean alveolar area. (a) Non-slice selective regional data and (b) slice selective data from control and PPE treated animals with respective least squares solution and linear correlation coefficients (r). Errors represent ± standard error of the mean values.

	Slope (s/μm)	Intercept (s)	r
Non-slice selective T_1 data	$3.0\times10^{-3} \pm 0.4\times10^{-3}$	0.64 ± 0.09	r = 0.574 ($p < 0.005$)
Slice selective T_1 data with major airways removed	$3.3\times10^{-3} \pm 0.9\times 10^{-3}$	0.70 ± 0.18	r = 0.441 ($p < 0.025$)

Table 6.3. Results of linear regression analysis in Fig. 7.8. Equation of the linear regression solution has the form: mean T_1 (s) = Slope × $\sqrt{regional\ MAA}$ + intercept, with accompanying linear correlation coefficients (r) values.

6.4. Discussion

The previously developed methodology of hp ^{83}Kr SQUARE MR imaging has, for the first time, permitted meaningful imaging of an *ex vivo* model of respiratory disease and measurement of regional hp ^{83}Kr T_1 values within lungs displaying a spectrum of alveolar degradation.

Variation within the elastase model

There was clear variation among the PPE treated group demonstrated by the four times greater standard error of the mean MAA in the PPE group and the large spread of whole lung MAA displayed in Fig. 6.5 where some PPE treated rats had values similar to control animals. Furthermore significant intra-subject variation within different lung regions was evident, further confounding analysis. However histology post *ex vivo* hp ^{83}Kr MRI was similar to that from non imaged lungs showing that the imaging technique itself was not the cause of this variation and thus is a valid technique for study of changes in the lung microstructure.

It has been noted in prior experiments that the degree of emphysematous damage in PPE treated animals can vary depending on the protocol [361], including delay between dosing and tissue chararcterization [362]. It has also been noted that young animals, as have been used in this study, may be more resistant to the effects of endotracheal PPE with Karlinsky et al. noting that airspace densities in young hamsters (less than 3 weeks old) showed less reduction in airspace densities despite being treated with the same dosages of PPE as older hamsters (7 – 8 weeks old), possibly due to

higher levels of endogenous α_1-antitypsiin and/or the ability to grow new alveoli [363]. Therefore further analysis of hp ^{83}Kr MR imaging results focused on the PPE treated and control animals as a single group with a range of MAA thus allowing for confirmation of the imaging technique to detect differences in MAA rather than between cohorts.

Hp ^{83}Kr spin density images of PPE treated lungs with significant emphysematous changes revealed significant heterogeneity. This finding was not unexpected since ventilation defects (lung regions with poor hp gas signal) have been reported in human emphysema [186, 188, 364] and animal models of the disease [127, 186, 365]. Emphysematous regions are believed to either fail to inflate due to airway obstruction or undergo little volume change during normal inhalation, thereby contributing to non-ventilated dead space with low uptake of the inhaled hp gas [366]. The pattern of ventilation defects with hp ^{3}He and ^{129}Xe has been recently studied [188, 357] where it has been noted that larger ventilation defects are seen on hp ^{129}Xe spin density imaging, thought to be due to the lower diffusivity of Xe (diffusion coefficient $D_{^{129}Xe-Air} = 0.14\ cm^2 s^{-1}$ calculated for an 83% enriched ^{129}Xe mixture in air at T = 310 K and atmospheric pressure using a Leonard-Jones 6 – 12 potential to approximate for interatomic interactions [367], compared to $D_{^{3}He-Air} = 0.86\ cm^2 s^{-1}$ for pure ^{3}He at identical conditions). Indeed, the high diffusivity of ^{3}He with the relatively long T_1 time of hp ^{3}He in the lung has recently allowed for visualization of delayed collateral ventilation of obstructed lung regions in emphysematous patients [355]. ^{83}Kr by comparison has similar diffusivity

to xenon with a diffusion coefficient $D_{^{83}Kr-Air} = 0.17\ cm^2 s^{-1}$ (99.925% enriched ^{83}Kr in air). It is therefore unlikely that the severely affected lung regions would be probed as effectively with hp ^{83}Kr which could lead to underestimation of regional T_1 values.

Distribution of T_1 measurements

Due to the spread of PPE induced emphysematous damage with a range in MAAs, total T_1 voxel data did not permit separation of the two groups of animals with similar means and distributions albeit with a trend to a higher regional T_1 values in the PPE treated group (Fig. 6.8).

Whole lung mean T_1 measurements

There is moderate correlation between the mean T_1 and $\sqrt{whole\ lung\ MAA}$ in the non-slice selective and slice selective data with and without the major airway values. Removing the airways to focus on the lung parenchyma increases the correlation to levels obtained with the higher SNR non-slice selective images. Interestingly there is a greater dependence on $\sqrt{MAA}$ (slope) in the slice selective data, particularly after removal of the airways, possibly because the contribution of the lung periphery (with presumably larger amounts of healthy lung) is removed from the T_1 value.

The theoretical y-intercept values in Table 6.2, that is the minimum T_1 measurable in the lung, are within good agreement. Interestingly all intercepts are non-zero which indicates that factors other than the mean

airspace area may be significant. However, as would be expected, by reducing the contribution of the airways in the slice selective data the minimum T_1 is also reduced. Possible causes of this non-zero intercept could be the contribution from the small airways within the lung and/or the lung surface composition itself.

The small airways would permit gas diffusion in the presence of a reduction in alveolar dimensions. This hypothesis would fit with the measurements of non-isotropic ADC measurements [358, 368] where during experimental durations of the order of 1.8 ms, spins are expected to diffuse out of the alveoli and into the airways. Therefore the situation in the lung with an extensive network of terminal bronchioles would produce a minimum hp ^{83}Kr T_1 value dependent upon the airway calibre. Further experiments would therefore be required to quantify the contribution of diffusion within the acinus during the experimental timeframes used in this Chapter. Faster imaging sequences and the use of the one breath method (imaging scheme 2) would produce less diffusive attenuation and could minimise this effect.

Regional T_1 measurements

By comparing the lobar measurements of MAA to corresponding regional T_1 values it can be seen that SQUARE MR imaging is able to detect differences in regional surface-to-volume changes in small amounts of lung tissue. The technique would therefore allow for the use of smaller numbers of animals by, for instance, inducing disease in one lung (right or left) as has been performed elsewhere [132, 316, 368].

Elastase rodent models of emphysema have been studied with micro-CT [369, 370] and proton MR based techniques [106, 371, 372]. Both methods have so far been able to detect reductions in lung tissue density. Retrospective gated micro-CT of anaesthetized, free-breathing, non-intubated control and TIMP-3 knockout mice was however also able to produce measurements of major airway diameters and spirometric indices such as forced residual capacity (*FRC*) and tidal volume (*TV*). Proton MRI methods however have suffered from lower spatial and temporal resolution compared to the micro-CT methods. However, using an ultra-short TE radial sequence the reduction in alveolar surface area in a murine elsastase model was quantified by an decrease in the T_2* in the elastase treated mice providing information beyond simple reduction in tissue density [372].

Hyperpolarized noble gas MR imaging by comparison produces information on gas distribution within the lung and is therefore able to delineate ventilated lung regions. Hp ^{3}He and ^{129}Xe MRI have been

similarly studied in rodent elastase models and have provided information of spirometric indices and regional ventilation [316]. In addition, hp noble gas imaging has sufficient sensitivity to measure lung morphology at the acinar level using the ADC in the rat [127, 365, 373] and more recently in the mouse [374]. ^{3}He ADC has also been able to detect the early onset of emphysema in a rat elastase model [362].

ADC is however insensitive to differences in surface composition and therefore the technique of hp ^{83}Kr SQUARE with its ability to provide additional information on surface composition and surface-to-volume ratios [134, 216] would provide another tool for characterization of the lungs. Spatial resolution is obviously reduced compared to hp ^{3}He and ^{129}Xe methodologies with nominal hp ^{83}Kr resolution of $0.80 \times 1.27 \times 3$ mm^3 but as mentioned this is likely to improve with advances in hyperpolarization and imaging techniques. Nonetheless, current resolution has proved sensitive to detect regional histological differences using small amounts of lung tissue.

MR imaging of hyperpolarized ^{83}Kr SQUARE

The value of performing the imaging over subsequent inhalations is seen when comparing the resulting T_1 maps of scheme 1 and scheme 2. In this early proof of principle work it has been shown to be possible to obtain SQUARE contrast on a single inhalation as in ADC measurements, but current available polarizations and imaging strategies only allow for two non-slice selective images per breath producing poor data fits of non-monoexponential T_1 relaxation. However as polarization technology and

imaging strategies improve it may become possible to acquire higher numbers of images in one breath to combat these difficulties.

Random noise was occasionally a problem in the non-shielded MR laboratory during *ex vivo* hp ^{83}Kr imaging with intermittent noise spikes recorded in early data and RF leaks on one of the imaging days. The effect on T_1 analysis was however minimal with little consequence on the calculated mean T_1 values and regional T_1 analysis. Enhanced hp ^{83}Kr signal intensities and further improvements in RF shielding (including of the MR facility itself) would however mitigate these problems in the future.

6.5. Conclusions

The aim of this work was to demonstrate the ability of hp ^{83}Kr SQUARE MRI to measure the reduction of surface-to-volume ratio in a rat elastase model of emphysema. The use of the simpler *ex vivo* model has allowed for rapid confirmation of the imaging technique to provide reproducible T_1 measurements related to changes in the lung microstructure in both a global and regional manner. It has therefore been shown that hp ^{83}Kr SQUARE MRI may be able provide additional complementary information of changes in surface-to-volume ratio and surface composition to the other lung imaging techniques currently in use.

Chapter 7: Conclusions

Pulmonary hyperpolarized (hp) noble gas magnetic resonance imaging (MRI) has seen increasing development and utility since its' inception two decades ago [125, 375]. However, as described in Chapters 2 and 3, the application of this relatively new lung imaging modality to small animal models is technically challenging. The use of *ex vivo* lung models have allowed for the investigation of functional respiratory measurements in small animals [11, 16, 376, 377] but had yet to be utilized with hp noble gas MRI.

The purpose of this thesis has been threefold: 1) demonstrate that the *ex vivo* lung model allows for a reduction in the experimental complexity of hp noble gas MRI in small animals thereby facilitating the development and testing of novel imaging protocols and technologies; 2) establish that the *ex vivo* rodent lung model permits the study of lung structure and function in healthy and disease models of human disease with hp noble gas MRI and that the combination can provide additional benefits and insights to *in vivo* techniques; 3) make evident the utility of hp noble gas MRI as a tool to study respiratory physiology and improve the understanding of pulmonary disease.

The *ex vivo* lung model presented within this work, based upon that developed by Stupic et al. [214], allowed for the study of pulmonary physiology using hp ^{129}Xe and hp ^{83}Kr MR imaging in intact lungs from both healthy rodents and rat models of respiratory disease. The usage of the *ex vivo* lung model reduced the regulatory requirements for animal care, handling and monitoring during hp gas MRI experiments. Furthermore the *ex vivo* model allowed for the generation of lung models at different sites to that where the imaging took place, permitting hp noble gas imaging experiments which would otherwise not have been possible during the term of this thesis.

Novel hp ^{129}Xe imaging protocols were developed in Chapter 4 to provide measurements of functional respiratory parameters such as the residual volume (*RV*) and to gather information of regional gas distribution in healthy excised rodent lungs on increasing inhalation and directed small probe volumes of hp gas. Functional measurements of changes in hp ^{129}Xe distribution during intravenous deliveries of the bronchoconstricting agent methacholine (MCh) to the pulmonary circulation were also acquired in rat and guinea pig lungs, with reversal images obtained after intravenous delivery of salbutamol.

The latter developed methodology then allowed for the study of whole lung and regional responses in an *ex vivo* ovalbumin (OVA) model of human asthma with hp ^{129}Xe in Chapter 5. Acquired MR image data provided information on the changes in whole lung and regional ventilation on increasing dosages of MCh and on reversal with salbutamol.

New image data analysis techniques were developed in an effort to improve the functional information obtained with notable differences seen between the control and OVA challenged lungs. The work demonstrated that the *ex vivo* model allowed for simplified hyperpolarized ^{129}Xe MR imaging and that the technique could provide useful information of the dynamic changes in a small animal model of human asthma.

The *ex vivo* model also provided the platform to develop the novel lung imaging technique of hp ^{83}Kr surface quadrupolar relaxation (SQUARE) MRI (detailed in Appendix 1 and ref. [216]). The developed hyperpolarization and delivery methodology, with improved signal intensity, was sufficient to produce disease specific contrast in the study of an excised rat model of emphysema in Chapter 6. In this work the first potential application of hp ^{83}Kr SQUARE MRI in the field of respiratory medicine was demonstrated. The technique was noted to be sensitive to both inter-subject and intra-lung differences in the S/V in healthy control lungs and lungs with varying degrees of emphysematous damage. The use of the simpler *ex vivo* model allowed for rapid confirmation of the imaging technique to provide reproducible T_1 measurements related to changes in the lung microstructure in both a global and regional manner.

While it has been shown that the *ex vivo* lung model allows for a simplification in the hp noble gas experimental complexity and has been seen to provide additional benefits and insights beyond those available *in vivo*, it is not the author's contention that the *ex vivo* model should replace *in vivo* hp gas techniques and measurements. The development of *in vivo*

techniques is fundamental to the development of safe clinical hp noble gas MR imaging protocols and is necessary for the widespread acceptance of the imaging modality. It is however hoped that *ex vivo* hp noble gas MRI has a potential role to facilitate the rapid development of both translational pre-clinical (small animal model) and human *in vivo* methods.

Future technical developments to improve hp ^{129}Xe and ^{83}Kr MRI

There are a number of improvements in the design of both the hyperpolazier and the extraction and delivery apparatus that would allow for improvements in future *ex vivo* studies and the start of *in vivo* studies using both hp ^{129}Xe and ^{83}Kr within the Translational Imaging group at the University of Nottingham. For example, a compression apparatus made purely of glass as opposed to acrylic would limit depolarization of hp gas (particularly surface sensitive hp ^{83}Kr) increasing available signal intensities for MR imaging. The delivery technique itself is labour intensive and subject to operator error and would therefore benefit from computer automation to reduce variations between hp gas deliveries.

Furthermore, improvements in the underlying spin exchange optical pumping (SEOP) process using the low pressure method are required to produce larger quantities of hyperpolarized gas with greater levels of polarization especially if larger animals, e.g. rabbits or dogs, are to be used. Also, currently hp gas imaging frequency is limited by the build times of the hp gas using the batch mode operation of the hyperpolarizing systems (typically 6 – 8 minutes between image with hp ^{129}Xe and 8 – 12 minutes with hp ^{83}Kr) with the result that potential functional data is not acquired

because of this limiting factor. Therefore improvements with larger gas volumes (currently up to 35 mL hp gas is produced per hyperpolarizer cycle) or reduced build times could be implemented if higher laser powers beyond the 23 – 30 W used in this work are utilized [216]. The initial steps towards this end have already occurred with a new hyperpolarizer designed and constructed by Dr. Stupic, Mr. Six, Mr. Dorkes, and Dr. Lilburn using a high power laser (~100 W output at the SEOP cell) for installation in the small animal MRI unit located in the Brain and Body Centre at the University of Nottingham to allow for high quality hp noble gas MRI *in vivo* with both hp ^{129}Xe and hp ^{83}Kr.

There are also a number of improvements in the hp gas MRI protocols used within the context of this thesis that would increase the utility of the *ex vivo* model and potentially provide greater amounts of functional data. A notable improvement would be in the imaging strategies in use. Currently limitations of the variable flip angle (VFA) fast-low-angle-shot technique using simple linear k-space sampling are evident with difficulties in reducing imaging durations beyond those used within this thesis. Therefore further improvements would need the use of either faster imaging sequences such as echo-planar imaging (EPI) based techniques or partial Fourier k-space methods. Alternative k-space filling trajectories such as the centric, radial or spiral methods detailed in Chapter 2 would also be of benefit in hp ^{83}Kr imaging due to the short T_1 times in the lung, where the centre of k-space with the tissue contrast data acquired at the expense of the periphery of k-space, with significant increases in the signal-to-noise ratio (SNR) of acquired hp ^{83}Kr images.

Future work, particularly with hp ^{83}Kr, would also benefit from the construction of improved imaging coils. The currently used Bruker® double saddle coil has poor sensitivity in the centre of the coil where the lung is located, limiting image resolution. Therefore improved volume coils such as those employing birdcage or quadrature designs would help increase hp ^{83}Kr image quality. The use of phased array detection coils with the implementation of compressed sensing techniques would be similarly beneficial for hp ^{129}Xe imaging.

Potential human usage of hyperpolarized ^{83}Kr SQUARE MRI

A final note is required on the potential human application of hp ^{83}Kr MR imaging. As has already been mentioned, the ultimate the purpose of developing hp ^{83}Kr MRI is to produce a biomarker of lung disease, particularly emphysema, in the early stages when there is the greatest chance of limiting further respiratory decline. To this end it is prudent to discuss the potential for applying the developed methods in humans.

As mentioned, hp ^{83}Kr MRI is technically challenging with only small volumes of hp ^{83}Kr with sufficient polarization having been produced. Furthermore, the MR imaging itself is difficult due to the rapid relaxation noted in the rat lung, where the T_1 is on the order of 1 – 2 s. These hurdles are not insignificant to overcome but, as has been documented, steps are already underway to deal with the technical issues surrounding them with improvements in hyperpolarizer design and MR imaging techniques. Furthermore, it should be remembered that in humans the alveolar

diameter is on the order of 270 μm [33] as opposed to approximately 90 μm in the rat lung [32]. As a result of this increase in alveolar geometry it should be expected that the T_1 of hp ^{83}Kr should similarly increase by a factor of three as has been noted in model systems [378], reducing the rapid signal loss and making MR imaging more feasible.

References:

[1] (WHO) W H O 2011 World Health Statistics 2011.

[2] Gibson G J, Loddenkemper R, Lundback B and Sibille Y 2013 Respiratory health and disease in Europe: the new European Lung White Book *Eur Respir J* **42** 559-63

[3] Weibel E R 2009 What makes a good lung? The morphometric basis of lung function *Swiss Medical Weekly* **139** 375-86

[4] Oneil J J and Raub J A 1984 Pulmonary-Function Testing in Small Laboratory Mammals *Environ Health Persp* **56** 11-22

[5] Raeburn D, Underwood S L and Villamil M E 1992 Techniques for Drug Delivery to the Airways, and the Assessment of Lung-Function in Animal-Models *J Pharmacol Toxicol* **27** 143-59

[6] Hoymann H G 2006 New developments in lung function measurements in rodents *Experimental and Toxicologic Pathology* **57 Suppl 2** 5-11

[7] Bates J H and Irvin C G 2003 Measuring lung function in mice: the phenotyping uncertainty principle *J Appl Physiol* **94** 1297-306

[8] Hoymann H G 2007 Invasive and noninvasive lung function measurements in rodents *J Pharmacol Toxicol Methods* **55** 16-26

[9] Irvin C G and Bates J H 2003 Measuring the lung function in the mouse: the challenge of size *Respir Res* **4** 4

[10] Frazer D G and Weber K C 1976 Trapped Air in Ventilated Excised Rat Lungs *J Appl Physiol* **40** 915-22

[11] Greenwald S E, Collino C E and Berry C L 1988 Invitro Determination of Lung Airway Compliance in Small Animals *Medical & Biological Engineering & Computing* **26** 497-502

[12] Struhar D and Harbeck R J 1990 An Apparatus for the Measurement of Lung-Volume and Compliance in Mice *Laboratory Animals* **24** 328-31

[13] Herget J and Chovanec M 2010 Isolated perfused murine lung: A well characterized preparation for studying lung vascular function *Drug Discovery Today: Disease Models* **7** 131-5

[14] Herget J and Mcmurtry I F 1985 Effects of Ouabain, Low K+, and Aldosterone on Hypoxic Pressor Reactivity of Rat Lungs *Am J Physiol* **248** H55-H60

[15] Herget J and Mcmurtry I F 1987 Dexamethasone Potentiates Hypoxic Vasoconstriction in Salt Solution-Perfused Rat Lungs *Am J Physiol* **253** H574-H81

[16] Uhlig S and Wollin L 1994 An Improved Setup for the Isolated-Perfused Rat Lung *J Pharmacol Toxicol* **31** 85-94

[17] von Bethmann A N, Brasch F, Nusing R, Vogt K, Volk H D, Muller K M, Wendel A and Uhlig S 1998 Hyperventilation induces release of cytokines from perfused mouse lung *Am J Resp Crit Care* **157** 263-72

[18] Barrenschee M, Lex D and Uhlig S 2010 Effects of the TLR2 agonists MALP-2 and Pam3Cys in isolated mouse lungs *Plos One* **5** e13889

[19] Siegl S and Uhlig S 2012 Using the one-lung method to link p38 to pro-inflammatory gene expression during overventilation in C57BL/6 and BALB/c mice *Plos One* **7** e41464

[20] Ewing P, Eirefelt S J, Andersson P, Blomgren A, Ryrfeldt A and Gerde P 2008 Short inhalation exposures of the isolated and perfused rat lung to respirable dry particle aerosols; The detailed pharmacokinetics of budesonide, formoterol, and terbutaline *Journal of Aerosol Medicine and Pulmonary Drug Delivery* **21** 169-80

[21] Selg E, Ewing P, Acevedo F, Sjoberg C O, Ryrfeldt A and Gerde P 2012 Dry Powder Inhalation Exposures of the Endotracheally Intubated Rat Lung, Ex Vivo and In Vivo: The Pulmonary Pharmacokinetics of Fluticasone Furoate *J Aerosol Med Pulm Drug Deliv*

[22] Driehuys B and Hedlund L W 2007 Imaging techniques for small animal models of pulmonary disease: MR microscopy *Toxicol Pathol* **35** 49-58

[23] Santyr G E, Lam W W, Parra-Robles J M, Taves T M and Ouriadov A V 2009 Hyperpolarized noble gas magnetic resonance imaging of the animal lung: Approaches and applications *Journal of Applied Physics* **105**

[24] Hebel R and Stromberg M W 1977 *Anatomy of the Laboratory Rat*: The Williams and Wilkins Company)

[25] Churg A M, Myers J L, Tazelaar H D and Wright J L 2005 *Thurlbeck's Pathology of the Lung* (New York: Thieme Medical Publishers, Inc.)

[26] West J 2008 *Respiratory Physiology: The Essentials*: Lippincott Williams and Wilkins)

[27] Prange H D 1996 *Respiratory physiology : understanding gas exchange* (New York: Chapman & Hall)

[28] Dejours P 1981 *Principles of Comparative Respiratory Physiology*: Elsevier / North-Holland Biomedical Press)

[29] Yeh H C, Schum G M and Duggan M T 1979 Anatomic Models of the Tracheobronchial and Pulmonary Regions of the Rat *Anat Rec* **195** 483-92

[30] Deljo D 2010 Plućni acinusi.

[31] Slomianka L 2009 H&E Staining Human Alveolus. School of Anatomy and Human Biology - The University of Western Australia)

[32] Mercer R R, Laco J M and Crapo J D 1987 3-Dimensional Reconstruction of Alveoli in the Rat Lung for Pressure-Volume Relationships *J Appl Physiol* **62** 1480-7

[33] Haefelibleuer B and Weibel E R 1988 Morphometry of the Human Pulmonary Acinus *Anat Rec* **220** 401-14

[34] 1991 *Comparative Biology of the Normal Lung* vol 1: Telford Press)

[35] Schulz H and Mühle H 2000 *The Laboratory Rat,* ed G J Krinke: Academic Press)

[36] McBride J T 2000 *Treatise on Pulmonary Toxicology.,* ed R A Parent: CRC Press) pp 49-61

[37] Sweet C S, Emmert S E, Seymour A A, Stabilito I I and Oppenheimer L 1987 Measurement of Cardiac-Output in Anesthetized Rats by Dye Dilution Using a Fiberoptic Catheter *J Pharmacol Method* **17** 189-203

[38] Mason R J and Lewis J F 2005 *Murray and Nadel's Textbook of Respiratory Medicine,* ed R Mason*, et al.*: Elsevier Saunders) pp 301-29

[39] Cazzola M, Page C P, Calzetta L and Matera M G 2012 Pharmacology and Therapeutics of Bronchodilators *Pharmacol Rev* **64** 450-504

[40] Kesler B S and Canning B J 1999 Regulation of baseline cholinergic tone in guinea-pig airway smooth muscle *J Physiol-London* **518** 843-55

[41] Canning B J and Fischer A 2001 Neural regulation of airway smooth muscle tone *Resp Physiol* **125** 113-27

[42] Hoymann H G 2012 Lung function measurements in rodents in safety pharmacology studies *Front Pharmacol* **3** 156

[43] Glaab T, Taube C, Braun A and Mitzner W 2007 Invasive and noninvasive methods for studying pulmonary function in mice *Resp Res* **8**

[44] Palecek F 1969 Measurement of Ventilatory Mechanics in Rat *J Appl Physiol* **27** 149-&

[45] Lai Y L and Hildebrandt J 1978 Respiratory mechanics in the anesthetized rat *J Appl Physiol* **45** 255-60

[46] Takezawa J, Miller F J and Oneil J J 1980 Single-Breath Diffusing-Capacity and Lung-Volumes in Small Laboratory Mammals *J Appl Physiol* **48** 1052-9

[47] Crosfill M L and Widdicombe J G 1961 Physical Characteristics of Chest and Lungs and Work of Breathing in Different Mammalian Species *J Physiol-London* **158** 1-&

[48] Roy C H, Barnes R J, Heath M F and Sensky P L 1992 A Modified Helium Dilution Technique for Measuring Small Lung Gas Volumes *J Dev Physiol* **17** 87-92

[49] Koyama S, Ohtsuka A and Horie T 1992 Eucapnic Hyperventilation-Induced Bronchoconstriction in Rabbits *Tohoku J Exp Med* **168** 611-9

[50] Jammes Y, Barthelemy P, Fornaris M and Grimaud C 1986 Cold-Induced Bronchospasm in Normal and Sensitized Rabbits *Resp Physiol* **63** 347-60

[51] Kodesh E, Zaldivar F, Schwindt C, Tran P, Yu A, Camilon M, Nance D M, Leu S Y, Cooper D and Adams G R 2011 A rat model of exercise-induced asthma: a nonspecific response to a specific immunogen *Am J Physiol-Reg I* **300** R917-R24

[52] Dimaria G U, Wang C G, Bates J H T, Guttmann R and Martin J G 1987 Partitioning of Airway Responses to Inhaled Methacholine in the Rat *J Appl Physiol* **62** 1317-23

[53] Martin T R, Gerard N P, Galli S J and Drazen J M 1988 Pulmonary Responses to Bronchoconstrictor Agonists in the Mouse *J Appl Physiol* **64** 2318-23

[54] McNamara A, Pulido-Rios M T, Hegde S S and Martin W J 2011 Application of the classical Einthoven model of bronchoconstriction to the study of inhaled bronchodilators in rodents *J Pharmacol Toxicol* **63** 89-95

[55] Bellofiore S and Martin J G 1988 Antigen Challenge of Sensitized Rats Increases Airway Responsiveness to Methacholine *J Appl Physiol* **65** 1642-6

[56] Bates J, Irvin C, Brusasco V, Drazen J, Fredberg J, Loring S, Eidelman D, Ludwig M, Macklem P, Martin J, Hantos Z, Hyatt R, Lai-Fook S, Leff A, Solway J, Lutchen K, Suki B, Mitzner W, Pare P, Pride N and Sly P 2004 The use and misuse of Penh in animal models of lung disease *Am J Resp Cell Mol* **31** 373-4

[57] Herxheimer H 1952 Repeatable Microshocks of Constant Strength in Guinea-Pig Anaphylaxis *J Physiol-London* **116** P28-P

[58] Hamelmann E, Schwarze J, Takeda K, Oshiba A, Larsen G L, Irvin C G and Gelfand E W 1997 Noninvasive measurement of airway responsiveness in allergic mice using barometric plethysmography *Am J Respir Crit Care Med* **156** 766-75

[59] Lundblad L K, Irvin C G, Adler A and Bates J H 2002 A reevaluation of the validity of unrestrained plethysmography in mice *J Appl Physiol (1985)* **93** 1198-207

[60] Petak F, Habre W, Donati Y R, Hantos Z and Barazzone-Argiroffo C 2001 Hyperoxia-induced changes in mouse lung mechanics: forced oscillations vs. barometric plethysmography *J Appl Physiol (1985)* **90** 2221-30

[61] Glaab T, Daser A, Braun A, Neuhaus-Steinmetz U, Fabel H, Alarie Y and Renz H 2001 Tidal midexpiratory flow as a measure of airway hyperresponsiveness in allergic mice *Am J Physiol Lung Cell Mol Physiol* **280** L565-73

[62] Glaab T, Hoymann H G, Hohlfeld J M, Korolewitz R, Hecht M, Alarie Y, Tschernig T, Braun A, Krug N and Fabel H 2002 Noninvasive measurement of midexpiratory flow indicates bronchoconstriction in allergic rats *J Appl Physiol (1985)* **93** 1208-14

[63] Glaab T, Ziegert M, Baelder R, Korolewitz R, Braun A, Hohlfeld J M, Mitzner W, Krug N and Hoymann H G 2005 Invasive versus noninvasive

measurement of allergic and cholinergic airway responsiveness in mice *Respir Res* **6** 139

[64] Dixon W E and Brodie T G 1903 Contributions to the physiology of the lungs. Part I. The bronchial muscles, their.innervation, and the action of drugs upon them. *J Physiol-London* **29** 97-173

[65] Underwood S L, Haddad E B, Birrell M A, McCluskie K, Pecoraro M, Dabrowski D, Webber S E, Foster M L and Belvisi M G 2002 Functional characterization and biomarker identification in the Brown Norway model of allergic airway inflammation *British Journal of Pharmacology* **137** 263-75

[66] Konzett H and Rössler R 1940 Versuchsanordung zu untersuchungen an der bronchialmuskulatur. *Naunyn-Schmiedeberg's Archives of Experimental Pathology and Pharmacology* **192** 71-4

[67] Tomioka S, Bates J H T and Irvin C G 2002 Airway and tissue mechanics in a murine model of asthma: alveolar capsule vs. forced oscillations *J Appl Physiol* **93** 263-70

[68] Peslin R and Fredberg J 1986 *Handbook of Physiology. The Respiratory System III.,* ed P T Macklem and J Mead pp 145-77

[69] Petak F, Hantos Z, Adamicza A, Asztalos T and Sly P D 1997 Methacholine-induced bronchoconstriction in rats: Effects of intravenous vs. aerosol delivery *J Appl Physiol* **82** 1479-87

[70] Hantos Z, Daroczy B, Suki B and Nagy S 1987 Low-Frequency Respiratory Mechanical Impedance in the Rat *J Appl Physiol* **63** 36-42

[71] Dellaca R L, Zannin E, Sancini G, Rivolta I, Leone B E, Pedotti A and Miserocchi G 2008 Changes in the mechanical properties of the respiratory system during the development of interstitial lung edema *Resp Res* **9**

[72] Likens S A and Mauderly J L 1982 Effect of Elastase or Histamine on Single-Breath N2 Washouts in the Rat *J Appl Physiol* **52** 141-6

[73] Brown R H, Irvin C G, Allen G B, Shapiro S D, Martin W J, Kolb M R J, Hyde D M, Nieman G F, Ishii M, Kadlecek S J, Driehuys B, Rizi R R, Wu A M, Weber W A and Stout D B 2008 Advances in Small Animal Imaging Application to Lung Patholphysiology. In: *ATS,* pp 591-600

[74] Jobse B N, Rhem R G, McCurry C A J R, Wang I Q and Labiris N R 2012 Imaging Lung Function in Mice Using SPECT/CT and Per-Voxel Analysis *Plos One* **7**

[75] Jobse B N, Rhem R G, Wang I Q, Counter W B, Stampfli M R and Labiris N R 2013 Detection of Lung Dysfunction Using Ventilation and Perfusion SPECT in a Mouse Model of Chronic Cigarette Smoke Exposure *J Nucl Med* **54** 616-23

[76] Turi G J, Ellis R, Wattie J N, Labiris N R and Inman M D 2011 The effects of inhaled house dust mite on airway barrier function and sensitivity to inhaled methacholine in mice *Am J Physiol-Lung C* **300** L185-L90

[77] Wu Y J, Kotzer C J, Makrogiannis S, Logan G A, Haley H, Barnette M S and Sarkar S K 2011 A Noninvasive [Tc-99m]DTPA SPECT/CT Imaging Methodology as a Measure of Lung Permeability in a Guinea Pig Model of COPD *Mol Imaging Biol* **13** 923-9

[78] Oberdorster G, Cox C and Gelein R 1997 Intratracheal instillation versus intratracheal inhalation of tracer particles for measuring lung clearance function *Exp Lung Res* **23** 17-34

[79] Moller W, Felten K, Sommerer K, Scheuch G, Meyer G, Meyer P, Haussinger K and Kreyling W G 2008 Deposition, retention, and translocation of ultrafine particles from the central airways and lung periphery *Am J Resp Crit Care* **177** 426-32

[80] Greschus S, Kiessling F, Lichy M P, Moll J, Mueller M M, Savai R, Rose F, Ruppert C, Gunther A, Luecke M, Fusenig N E, Semmler W and Traupe H 2005 Potential applications of flat-panel volumetric CT in morphologic and functional small animal imaging *Neoplasia* **7** 730-40

[81] Johnson K, Badea C, Hedlund L and Johnson G A 2008 Imaging Techniques for Small Animal Imaging Models of Pulmonary Disease: Micro-CT (vol 35, pg 9, 2007) *Toxicol Pathol* **36** 895-

[82] Badea C, Hedlund L W and Johnson G A 2004 Micro-CT with respiratory and cardiac gating *Med Phys* **31** 3324-9

[83] Walters E B, Panda K, Bankson J A, Brown E and Cody D D 2004 Improved method of in vivo respiratory-gated micro-CT imaging *Phys Med Biol* **49** 4163-72

[84] Badea C T, Johnston S, Johnson B, Lin M, Hedlund L W and Johnson G A 2008 A dual micro-CT system for small animal imaging *Proc SPIE* **6913** 691342

[85] Ford N L, Nikolov H N, Norley C J, Thornton M M, Foster P J, Drangova M and Holdsworth D W 2005 Prospective respiratory-gated micro-CT of free breathing rodents *Med Phys* **32** 2888-98

[86] Ford N L, Martin E L, Lewis J F, Veldhuizen R A W, Drangova M and Holdsworth D W 2007 In vivo characterization of lung morphology and function in anesthetized free-breathing mice using micro-computed tomography *J Appl Physiol* **102** 2046-55

[87] Guo X L, Johnston S M, Qi Y, Johnson G A and Badea C T 2012 4D micro-CT using fast prospective gating *Phys Med Biol* **57** 257-71

[88] Cody D D, Nelson C L, Bradley W M, Wislez M, Juroske D, Price R E, Zhou X, Bekele B N and Kurie J M 2005 Murine lung tumor measurement using respiratory-gated micro-computed tomography *Invest Radiol* **40** 263-9

[89] Artaechevarria X, Perez-Martin D, Ceresa M, de Biurrun G, Blanco D, Montuenga L M, van Ginneken B, Ortiz-de-Solorzano C and Munoz-Barrutia A 2009 Airway segmentation and analysis for the study of mouse models of lung disease using micro-CT *Phys Med Biol* **54** 7009-24

[90] Mitzner W, Brown R and Lee W 2001 In vivo measurement of lung volumes in mice *Physiol Genomics* **4** 215-21

[91] Marcucci C, Nyhan D and Simon B A 2001 Distribution of pulmonary ventilation using Xe-enhanced computed tomography in prone and supine dogs *J Appl Physiol* **90** 421-30

[92] Lam W W, Holdsworth D W, Du L Y, Drangova M, McCormack D G and Santyr G E 2007 Micro-CT imaging of rat lung ventilation using continuous image acquisition during xenon gas contrast enhancement *J Appl Physiol* **103** 1848-56

[93] Santyr G E, Couch M J, Lam W W, Ouriadov A, Drangova M, McCormack D G and Holdsworth D W 2011 Comparison of hyperpolarized (3)He MRI with Xe-enhanced computed tomography imaging for ventilation mapping of rat lung *NMR Biomed* **24** 1073-80

[94] Johnson T R, Krauss B, Sedlmair M, Grasruck M, Bruder H, Morhard D, Fink C, Weckbach S, Lenhard M, Schmidt B, Flohr T, Reiser M F and Becker C R 2007 Material differentiation by dual energy CT: initial experience *Eur Radiol* **17** 1510-7

[95] Chae E J, Seo J B, Goo H W, Kim N, Song K S, Lee S D, Hong S J and Krauss B 2008 Xenon ventilation CT with a dual-energy technique of dual-source CT: initial experience *Radiology* **248** 615-24

[96] Badea C T, Guo X, Clark D, Johnston S M, Marshall C D and Piantadosi C A 2012 Dual-energy micro-CT of the rodent lung *Am J Physiol Lung Cell Mol Physiol* **302** L1088-97

[97] Rube C E, Uthe D, Schmid K W, Richter K D, Wessel J, Schuck A, Willich N and Rube C 2000 Dose-dependent induction of transforming growth factor beta (TGF-beta) in the lung tissue of fibrosis-prone mice after thoracic irradiation *Int J Radiat Oncol Biol Phys* **47** 1033-42

[98] Biederer J, Hintze C, Fabel M and Dinkel J 2010 Magnetic Resonance Imaging and Computed Tomography of Respiratory Mechanics *Journal of Magnetic Resonance Imaging* **32** 1388-97

[99] Hedlund L W, Johnson G A, Karis J P and Effmann E L 1986 MR "microscopy" of the rat thorax *J Comput Assist Tomogr* **10** 948-52

[100] Brau A C, Hedlund L W and Johnson G A 2004 Cine magnetic resonance microscopy of the rat heart using cardiorespiratory-synchronous projection reconstruction *J Magn Reson Imaging* **20** 31-8

[101] Mai W, Badea C T, Wheeler C T, Hedlund L W and Johnson G A 2005 Effects of breathing and cardiac motion on spatial resolution in the microscopic imaging of rodents *Magn Reson Med* **53** 858-65

[102] Su S, Saunders J K and Smith I C P 1995 Resolving Anatomical Details in Lung Parenchyma: Theory and Experiment for a Structurally and Magnetically Inhomogeneous Lung Imaging Model *Magn Reson Med* **33** 760-5

[103] Kauczor H U ed 2009 *MRI of the Lung*: Springer)

[104] Kveder M, Zupancic I, Lahajnar G, Blinc R, Suput D, Ailion D C, Ganesan K and Goodrich C 1988 Water Proton Nmr Relaxation Mechanisms in Lung-Tissue *Magn Reson Med* **7** 432-41

[105] Beckmann N, Tigani B, Mazzoni L and Fozard J R 2001 MRI of lung parenchyma in rats and mice using a gradient-echo sequence *Nmr in Biomedicine* **14** 297-306

[106] Takahashi M, Togao O, Obara M, van Cauteren M, Ohno Y, Doi S, Kuro-o M, Malloy C, Hsia C C and Dimitrov I 2010 Ultra-short Echo Time (UTE) MR Imaging of the Lung: Comparison Between Normal and Emphysematous Lungs in Mutant Mice *Journal of Magnetic Resonance Imaging* **32** 326-33

[107] Togao O, Ohno Y, Dimitrov I, Hsia C C and Takahashi M 2011 Ventilation/Perfusion Imaging of the Lung Using Ultra-short Echo Time (UTE) MRI in an Animal Model of Pulmonary Embolism *Journal of Magnetic Resonance Imaging* **34** 539-46

[108] Bell L C, Johnson K M, Fain S B, Wentland A, Drees R, Johnson R A, Bauman G, Francois C J and Nagle S K 2013 Simultaneous MRI of lung structure and perfusion in a single breathhold *J Magn Reson Imaging*

[109] Montgomery A B, Paajanen H, Brasch R C and Murray J F 1987 Aerosolized Gadolinium-Dtpa Enhances the Magnetic-Resonance Signal of Extravascular Lung Water *Invest Radiol* **22** 377-81

[110] Haage P, Adam G, Misselwitz B, Karaagac S, Pfeffer J G, Glowinski A, Dohmen S, Tacke J and Gunther R W 2000 Aerosolized gadolinium-DTPA for demonstration of pulmonary ventilation in MR imaging of the lung. *Rofo-Fortschritte Auf Dem Gebiet Der Rontgenstrahlen Und Der Bildgebenden Verfahren* **172** 323-8

[111] Haage P, Adam G, Karaagac S, Pfeffer J, Glowinski A, Dohmen S and Gunther R W 2001 Mechanical delivery of aerosolized gadolinium-DTPA for pulmonary ventilation assessment in MR imaging *Invest Radiol* **36** 240-3

[112] Haage P, Karaagac S, Spuntrup E, Truong H T, Schmidt T and Gunther R W 2005 Feasibility of pulmonary ventilation visualization with aerosolized magnetic resonance contrast media *Invest Radiol* **40** 85-8

[113] Suga K, Ogasawara N, Okada M, Matsunaga N and Arai M 2002 Regional lung functional impairment in acute airway obstruction and pulmonary embolic dog models assessed with gadolinium-based aerosol

ventilation and perfusion magnetic resonance imaging *Invest Radiol* **37** 281-91

[114] Edelman R R, Hatabu H, Tadamura E, Li W and Prasad P V 1996 Noninvasive assessment of regional ventilation in the human lung using oxygen-enhanced magnetic resonance imaging *Nature Medicine* **2** 1236-9

[115] Loffler R, Muller C J, Peller M, Penzkofer H, Deimling M, Schwaiblmair M, Scheidler J and Reiser M 2000 Optimization and evaluation of the signal intensity change in multisection oxygen-enhanced MR lung imaging *Magn Reson Med* **43** 860-6

[116] Zurek M, Johansson E, Risse F, Alamidi D, Olsson L E and Hockings P D 2013 Accurate T mapping for oxygen-enhanced MRI in the mouse lung using a segmented inversion-recovery ultrashort echo-time sequence *Magn Reson Med*

[117] Strobel K, Hoerr V, Schmid F, Wachsmuth L, Loffler B and Faber C 2012 Early detection of lung inflammation: exploiting T1-effects of iron oxide particles using UTE MRI *Magnetic resonance in medicine : official journal of the Society of Magnetic Resonance in Medicine / Society of Magnetic Resonance in Medicine* **68** 1924-31

[118] Kuethe D O, Caprihan A, Fukushima E and Waggoner R A 1998 Imaging lungs using inert fluorinated gases *Magn Reson Med* **39** 85-8

[119] Kuethe D O, Caprihan A, Gach H M, Lowe I J and Fukushima E 2000 Imaging obstructed ventilation with NMR using inert fluorinated gases *J Appl Physiol* **88** 2279-86

[120] Schreiber W G, Eberle B, Laukemper-Ostendorf S, Markstaller K, Weiler N, Scholz A, Heussel C P, Thelen M and Kauczor H U 2001 Dynamic F-19-MRI of pulmonary ventilation using sulfur hexafluoride (SF6) gas *Magn Reson Med* **45** 605-13

[121] Carrero-Gonzalez L, Kaulisch T and Stiller D 2013 In Vivo Diffusion-Weighted MRI Using Perfluorinated Gases: ADC Comparison Between Healthy and Elastase-Treated Rat Lungs *Magn Reson Med* **70** 1761-4

[122] Albert M S, Cates G D, Driehuys B, Happer W, Saam B, Springer C S and Wishnia A 1994 Biological Magnetic Resonance Imaging Using Laser Polarized Xe-129 *Nature* **370** 199-201

[123] Middleton H, Black R D, Saam B, Cates G D, Cofer G P, Guenther R, Happer W, Hedlund L W, Johnson G A, Juvan K and Swartz J 1995 Mr-Imaging with Hyperpolarized He-3 Gas *Magn Reson Med* **33** 271-5

[124] Altes T A, Powers P L, Knight-Scott J, Rakes G, Platts-Mills T A E, de Lange E E, Alford B A, Mugler J P and Brookeman J R 2001 Hyperpolarized He-3 MR lung ventilation imaging in asthmatics: Preliminary findings *Journal of Magnetic Resonance Imaging* **13** 378-84

[125] Fain S B, Korosec F R, Holmes J H, O'Halloran R, Sorkness R L and Grist T M 2007 Functional lung imaging using hyperpolarized gas MRI *Journal of Magnetic Resonance Imaging* **25** 910-23

[126] Fain S, Schiebler M L, McCormack D G and Parraga G 2010 Imaging of Lung Function Using Hyperpolarized Helium-3 Magnetic Resonance Imaging: Review of Current and Emerging Translational Methods and Applications *Journal of Magnetic Resonance Imaging* **32** 1398-408

[127] Chen X J, Hedlund L W, Moller H E, Chawla M S, Maronpot R R and Johnson G A 2000 Detection of emphysema in rat lungs by using magnetic resonance measurements of He-3 diffusion *P Natl Acad Sci USA* **97** 11478-81

[128] Mata J F, Altes T A, Cai J, Ruppert K, Mitzner W, Hagspiel K D, Patel B, Salerno M, Brookeman J R, de Lange E E, Tobias W A, Wang H T J, Cates G D and Mugler J P 2007 Evaluation of emphysema severity and progression in a rabbit model: comparison of hyperpolarized He-3 and Xe-129 diffusion MRI with lung morphometry *J Appl Physiol* **102** 1273-80

[129] Sakai K, Bilek A M, Oteiza E, Walsworth R L, Balamore D, Jolesz F A and Albert M S 1996 Temporal dynamics of hyperpolarized Xe-129 resonances in living rats *Journal of Magnetic Resonance Series B* **111** 300-4

[130] Swanson S D, Rosen M S, Coulter K P, Welsh R C and Chupp T E 1999 Distribution and dynamics of laser-polarized Xe-129 magnetization in vivo *Magn Reson Med* **42** 1137-45

[131] Patz S, Muradian I, Hrovat M I, Ruset I C, Topulos G, Covrig S D, Frederick E, Hatabu H, Hersman F W and Butler J P 2008 Human pulmonary imaging and spectroscopy with hyperpolarized Xe-129 at 0.2T *Acad Radiol* **15** 713-27

[132] Driehuys B, Cofer G P, Pollaro J, Mackel J B, Hedlund L W and Johnson G A 2006 Imaging alveolar-capillary gas transfer using hyperpolarized Xe-129 MRI *P Natl Acad Sci USA* **103** 18278-83

[133] Lilburn D M L, Pavlovskaya G E and Meersmann T 2013 Perspectives of hyperpolarized noble gas MRI beyond He-3 *J Magn Reson* **229** 173-86

[134] Pavlovskaya G E, Cleveland Z I, Stupic K F and Meersmann T 2005 Hyperpolarized Krypton-83 as a New Contrast Agent for Magnetic Resonance Imaging *P Natl Acad Sci USA* **102** 18275-9

[135] Cleveland Z I, Stupic K F, Pavlovskaya G E, Repine J E, Wooten J B and Meersmann T 2007 Hyperpolarized Kr-83 and Xe-129 NMR relaxation measurements of hydrated surfaces: Implications for materials science and pulmonary diagnostics *Journal of the American Chemical Society* **129** 1784-92

[136] Abragam A 1983 *Principles of Nuclear Magnetism* (Oxford, UK: Oxford University Press)

[137] Callaghan P T 1991 *Principles of Nuclear Magnetic Resonance Microscopy* (New York: Oxford University press)

[138] Levitt M H 2001 *Spin Dynamics: Basics of Nuclear Magnetic Resonance* (West Sussex, UK: John Wiley & Sons, LTD)

[139] McRobbie D W, Moore E A, Graves M J and Prince M R 2006 *MRI From Picture to Proton* (Cambridge, U.K.: Cambridge University Press)

[140] Harris R K, Becker E D, De Menezes S M C, Goodfellow R and Granger P 2001 NMR nomenclature. Nuclear spin properties and conventions for chemical shifts - (IUPAC recommendations 2001) *Pure and Applied Chemistry* **73** 1795-818

[141] Krjukov E V, O'Neill J D and Owers-Bradley J R 2005 Brute force polarization of Xe-129 *Journal of Low Temperature Physics* **140** 397-408

[142] Fu R, Brey W W, Shetty K, Gor'kov P, Saha S, Long J R, Grant S C, Chekmenev E Y, Hu J, Gan Z, Sharma M, Zhang F, Logan T M, Bruschweller R, Edison A, Blue A, Dixon I R, Markiewicz W D and Cross T A 2005 Ultra-wide bore 900 MHz high-resolution NMR at the National High Magnetic Field Laboratory *J Magn Reson* **177** 1-8

[143] Frayne R, Goodyear B G, Dickhoff P, Lauzon M L and Sevick R J 2003 Magnetic resonance imaging at 3.0 Tesla: Challenges and advantages in clinical neurological imaging *Invest Radiol* **38** 385-402

[144] Schick F 2005 Whole-body MRI at high field: technical limits and clinical potential *European Radiology* **15** 946-59

[145] Six J S, Hughes-Riley T, Stupic K F, Pavlovskaya G E and Meersmann T 2012 Pathway to Cryogen Free Production of Hyperpolarized Krypton-83 and Xenon-129 *Plos One* **7**

[146] Lauterbur P C 1973 Image formation by induced local interactions: examples employing nuclear magnetic resonance. *Nature* **242** 2

[147] Mansfield P and Maudsley A A 1977 Medical Imaging by Nmr *Brit J Radiol* **50** 188-94

[148] Haase A, Frahm J, Matthaei D, Hanicke W and Merboldt K D 1986 Flash Imaging - Rapid Nmr Imaging Using Low Flip-Angle Pulses *J Magn Reson* **67** 258-66

[149] Anger B C, Schrank G, Schoeck A, Butler K A, Solum M S, Pugmire R J and Saam B 2008 Gas-phase spin relaxation of Xe-129 *Physical Review A* **78** 043406

[150] Jacob R E, Morgan S W, Saam B and Leawoods J C 2001 Wall relaxation of He-3 in spin-exchange cells *Physical Review Letters* **87**

[151] Cleveland Z I and Meersmann T 2008 Density-independent contributions to longitudinal relaxation in Kr-83 *Chemphyschem* **9** 1375-9

[152] Cleveland Z I and Meersmann T 2008 Binary-collision-induced longitudinal relaxation in gas-phase Kr-83 *Journal of Chemical Physics* **129** 244304

[153] Lipson D A and van Beek E J R eds 2005 *Functional Lung Imaging* vol 200: Taylor and Francis Group)

[154] Woods J C 2010 Congressional Hearing: "Caught by Surprise: Causes and Consequences of the Helium-3 Supply Crisis" *Testimony before the House Committee on Science and Technology, Subcommittee on Investigations and Oversight*

[155] Hersman F W, Ruset I C, Ketel S, Muradian I, Covrig S D, Distelbrink J, Porter W, Watt D, Ketel J, Brackett J, Hope A and Patz S 2008 Large

production system for hyperpolarized Xe-129 for human lung imaging studies *Acad Radiol* **15** 683-92

[156] Driehuys B, Cates G D, Miron E, Sauer K, Walter D K and Happer W 1996 High-volume production of laser-polarized Xe-129 *Applied Physics Letters* **69** 1668-70

[157] Shah N J, Unlu T, Wegener H P, Halling H, Zilles K and Appelt S 2000 Measurement of rubidium and xenon absolute polarization at high temperatures as a means of improved production of hyperpolarized Xe-129 *Nmr in Biomedicine* **13** 214-9

[158] Zook A L, Adhyaru B B and Bowers C R 2002 High capacity production of > 65% spin polarized xenon-129 for NMR spectroscopy and imaging *J Magn Reson* **159** 175-82

[159] Schrank G, Ma Z, Schoeck A and Saam B 2009 Characterization of a low-pressure high-capacity 129Xe flow-through polarizer *Physical Review A* **80** 063424

[160] Walker T G and Happer W 1997 Spin-exchange optical pumping of noble-gas nuclei *Review of Modern Physics* **69** 629-42

[161] Raftery D, Long H, Meersmann T, Grandinetti P J, Reven L and Pines A 1991 High-Field NMR of Adsorbed Xenon Polarized by Laser Pumping *Physical Review Letters* **66** 584-7

[162] Whiting N, Eschmann N A, Goodson B M and Barlow M J 2011 (129)Xe-Cs (D(1), D(2)) versus (129)Xe-Rb (D(1)) spin-exchange optical pumping at high xenon densities using high-power laser diode arrays *Physical Review A* **83** 053428

[163] Ruset I C, Ketel S and Hersman F W 2006 Optical pumping system design for large production of hyperpolarized Xe-129 *Physical Review Letters* **96** 053002

[164] Kuzma N N, Patton B, Raman K and Happer W 2002 Fast nuclear spin relaxation in hyperpolarized solid Xe-129 *Physical Review Letters* **88** 147602

[165] Raftery D, MacNamara E, Fisher G, Rice C V and Smith J 1997 Optical pumping and magic angle spinning: Sensitivity and resolution enhancement for surface NMR obtained with laser-polarized xenon *Journal of the American Chemical Society* **119** 8746-7

[166] Haake M, Pines A, Reimer J A and Seydoux R 1997 Surface-enhanced NMR using continuous-flow laser-polarized xenon *Journal of the American Chemical Society* **119** 11711-2

[167] F.W. H 2012 Portable Automated Polarizer for Clinical Production of Hyperpolarized Xenon-129. In: *XeMat,* (Dublin

[168] Whiting N, Nikolaou P, Eschmann N A, Barlow M J, Lammert R, Ungar J, Hu W, Vaissie L and Goodson B M 2012 Using frequency-narrowed, tunable laser diode arrays with integrated volume holographic gratings for spin-exchange optical pumping at high resonant fluxes and xenon densities *Applied Physics B-Lasers and Optics* **106** 775-88

[169] Comment A, Jannin S, Hyacinthe J N, Mieville P, Sarkar R, Ahuja P, Vasos P R, Montet X, Lazeyras F, Vallee J P, Hautle P, Konter J A, van den Brandt B, Ansermet J P, Gruetter R and Bodenhausen G 2010 Hyperpolarizing Gases via Dynamic Nuclear Polarization and Sublimation *Physical Review Letters* **105** 018104

[170] Woodhouse N, Wild J M, Paley M N J, Fichele S, Said Z, Swift A J and van Beek E J R 2005 Combined helium-3/proton magnetic resonance imaging measurement of ventilated lung volumes in smokers compared to never-smokers *Journal of Magnetic Resonance Imaging* **21** 365-9

[171] van Beek E J R, Dahmen A M, Stavngaard T, Gast K K, Heussel C P, Krummenauer F, Schmiedeskamp J, Wild J M, Sogaard L V, Morbach A E, Schreiber L M and Kauczor H U 2009 Hyperpolarised (3)He MRI versus HRCT in COPD and normal volunteers: PHIL trial *Eur Respir J* **34** 1311-21

[172] Shukla Y, Wheatley A, Kirby M, Svenningsen S, Farag A, Santyr G E, Paterson N A M, McCormack D G and Parraga G 2012 Hyperpolarized Xe-129 Magnetic Resonance Imaging: Tolerability in Healthy Volunteers and Subjects with Pulmonary Disease *Acad Radiol* **19** 941-51

[173] Jameson C J, Jameson A K and Hwang J K 1988 Nuclear-Spin Relaxation by Intermolecular Magnetic Dipole Coupling in the Gas-Phase - Xe-129 in Oxygen *Journal of Chemical Physics* **89** 4074-81

[174] Cullen S C and Gross E G 1951 The Anesthetic Properties of Xenon in Animals and Human Beings, with Additional Observations on Krypton *Science* **113** 580-2

[175] Latchaw R E, Yonas H, Pentheny S L and Gur D 1987 Adverse Reactions to Xenon-Enhanced Ct Cerebral Blood-Flow Determination *Radiology* **163** 251-4

[176] Driehuys B, Martinez-Jimenez S, Cleveland Z I, Metz G M, Beaver D M, Nouls J C, Kaushik S S, Firszt R, Willis C, Kelly K T, Wolber J, Kraft M and McAdams H P 2012 Chronic Obstructive Pulmonary Disease: Safety and Tolerability of Hyperpolarized Xe-129 MR Imaging in Healthy Volunteers and Patients *Radiology* **262** 279-89

[177] Zhao L, Mulkern R, Tseng C H, Williamson D, Patz S, Kraft R, Walsworth R L, Jolesz F A and Albert M S 1996 Gradient-echo imaging considerations for hyperpolarized Xe-129 MR *Journal of Magnetic Resonance Series B* **113** 179-83

[178] Cleveland Z I, Pavlovskaya G E, Stupic K F, Wooten J B, Repine J E and Meersmann T 2008 Detection of Tobacco Smoke Deposition by Hyperpolarized Krypton-83 MRI *Magnetic Resonance Imaging* **26** 270-8

[179] Deppe M H and Wild J M 2012 Variable flip angle schedules in bSSFP imaging of hyperpolarized noble gases *Magn Reson Med* **67** 1656-64

[180] Couch M J, Ouriadov A and Santyr G E 2012 Regional ventilation mapping of the rat lung using hyperpolarized (129) Xe magnetic resonance imaging *Magn Reson Med*

[181] Holmes J H, Korosec F R, Du J, Sorkness R L, Grist T M, Kuhlman J E and Fain S B 2007 Imaging of lung ventilation and respiratory dynamics in a single ventilation cycle using hyperpolarized he-3 MRI *Journal of Magnetic Resonance Imaging* **26** 630-6

[182] Parra-Robles J, Ajraoui S, Deppe M H, Parnell S R and Wild J M 2010 Experimental investigation and numerical simulation of (3)He gas diffusion in simple geometries: Implications for analytical models of (3)He MR lung morphometry *J Magn Reson* **204** 228-38

[183] Sukstanskii A L, Conradi M S and Yablonskiy D A 2010 He-3 lung morphometry technique: Accuracy analysis and pulse sequence optimization *J Magn Reson* **207** 234-41

[184] Chen X J, Moller H E, Chawla M S, Cofer G P, Driehuys B, Hedlund L W and Johnson G A 1999 Spatially resolved measurements of

hyperpolarized gas properties in the lung in vivo. Part I: Diffusion coefficient *Magn Reson Med* **42** 721-8

[185] Swift A J, Wild J M, Fichele S, Woodhouse N, Fleming S, Waterhouse J, Lawson R A, Paley M N J and Van Beek E J R 2005 Emphysematous changes and normal variation in smokers and COPD patients using diffusion He-3 MRI *European Journal of Radiology* **54** 352-8

[186] Fain S B, Panth S R, Evans M D, Wentland A L, Holmes J H, Korosec F R, O'Brien M J, Fountaine H and Grist T M 2006 Early emphysematous changes in asymptomatic smokers: Detection with He-3 MR imaging *Radiology* **239** 875-83

[187] Driehuys B, Kaushik S S, Cleveland Z I, Cofer G P, Metz G, Beaver D, Nouls J, Kraft M, Auffermann W, Wolber J and McAdams H P 2011 Diffusion-Weighted Hyperpolarized (129)Xe MRI in Healthy Volunteers and Subjects With Chronic Obstructive Pulmonary Disease *Magn Reson Med* **65** 1155-65

[188] Kirby M, Svenningsen S, Owrangi A, Wheatley A, Farag A, Ouriadov A V, Santyr G E, Etemad-Rezai R, Coxson H O, McCormack D G and Parraga G 2012 Hyperpolarized 3He and 129Xe MR Imaging in Healthy Volunteers and Patients with Chronic Obstructive Pulmonary Disease *Radiology*

[189] Sukstanskii A L and Yablonskiy D A 2012 Lung morphometry with hyperpolarized 129Xe: Theoretical background *Magn Reson Med* **67** 856-66

[190] Ratcliffe C I 1998 Xenon NMR *Annual Reports on NMR Spectroscopy* **36** 123-221

[191] Springuel-Huet M A, Bonardet J L, Gedeon A and Fraissard J 1999 Xe-129 NMR overview of xenon physisorbed in porous solids *Magnetic Resonance in Chemistry* **37** S1-S13

[192] Bartik K, Choquet P, Constantinesco A, Duhamel G, Fraissard J, Hyacinthe J N, Jokisaari J, Locci E, Lowery T J, Luhmer M, Meersmann T, Moudrakovski I L, Pavlovskaya G E, Pierce K L, Pines A, Ripmeester J A, Telkki V V and Veeman W S 2005 Xenon NMR as a probe for microporous and mesoporous solids, polymers, liquid crystals, solutions, flames, proteins, imaging *Actualite Chimique* 16-34

[193] Moudrakovski I L, Wang L Q, Baumann T, Satcher J H, Exarhos G J, Ratcliffe C I and Ripmeester J A 2004 Probing the geometry and interconnectivity of pores in organic aerogels using hyperpolarized Xe-129 NMR spectroscopy *Journal of the American Chemical Society* **126** 5052-3

[194] Albert M S, Schepkin V D and Budinger T F 1995 Measurement of Xe-129 T1 in Blood to Explore the Feasibility of Hyperpolarized Xe-129 Mri *Journal of Computer Assisted Tomography* **19** 975-8

[195] Wakayama T, Kitamoto M, Ueyama T, Imai H, Narazaki M, Kimura A and Fujiwara H 2008 Hyperpolarized Xe-129 MRI of the mouse lung at a low xenon concentration using a continuous flow-type hyperpolarizing system *Journal of Magnetic Resonance Imaging* **27** 777-84

[196] Hori Y, Kimura A, Wakayama T, Kitamoto M, Imai F, Imai H and Fujiwara H 2009 3D Hyperpolarized Xe-129 MRI of Mouse Lung at Low Xenon Concentration using a Continuous Flow-type Hyperpolarizing System: Feasibility for Quantitative Measurement of Regional Ventilation *Magnetic Resonance in Medical Sciences* **8** 73-9

[197] Cleveland Z I, Cofer G P, Metz G, Beaver D, Nouls J, Kaushik S S, Kraft M, Wolber J, Kelly K T, McAdams H P and Driehuys B 2010 Hyperpolarized Xe-129 MR Imaging of Alveolar Gas Uptake in Humans *Plos One* **5**

[198] Butler J P, Mair R W, Hoffmann D, Hrovat M I, Rogers R A, Topulos G P, Walsworth R L and Patz S 2002 Measuring surface-area-to-volume ratios in soft porous materials using laser-polarized xenon interphase exchange nuclear magnetic resonance *Journal of Physics-Condensed Matter* **14** L297-L304

[199] Patz S, Muradyan I, Hrovat M I, Dabaghyan M, Washko G R, Hatabu H and Butler J P 2011 Diffusion of hyperpolarized (129)Xe in the lung: a simplified model of (129)Xe septal uptake and experimental results *New Journal of Physics* **13** 015009

[200] Ruppert K, Brookeman J R, Hagspiel K D and Mugler J P 2000 Probing lung physiology with xenon polarization transfer contrast (XTC) *Magn Reson Med* **44** 349-57

[201] Ruppert K, Mata J F, Brookeman J R, Hagspiel K D and Mugler J P 2004 Exploring lung function with hyperpolarized Xe-129 nuclear magnetic resonance *Magn Reson Med* **51** 676-87

[202] Dregely I, Mugler J P, Ruset I C, Altes T A, Mata J F, Miller G W, Ketel J, Ketel S, Distelbrink J, Hersman F W and Ruppert K 2011 Hyperpolarized Xenon-129 Gas-Exchange Imaging of Lung Microstructure: First Case Studies in Subjects With Obstructive Lung Disease *Journal of Magnetic Resonance Imaging* **33** 1052-62

[203] Driehuys B, Moller H E, Cleveland Z I, Pollaro J and Hedlund L W 2009 Pulmonary Perfusion and Xenon Gas Exchange in Rats: MR Imaging with Intravenous Injection of Hyperpolarized Xe-129 *Radiology* **252** 386-93

[204] Albert M S, Balamore D, Kacher D F, Venkatesh A K and Jolesz F A 2000 Hyperpolarized Xe-129 T-1 in oxygenated and deoxygenated blood *Nmr in Biomedicine* **13** 407-14

[205] Venkatesh A K, Zhao L, Balamore D, Jolesz F A and Albert M S 2000 Evaluation of carrier agents for hyperpolarized xenon MRI *Nmr in Biomedicine* **13** 245-52

[206] Baumer D, Brunner E, Blumler P, Zanker P P and Spiess H W 2006 NMR spectroscopy of laser-polarized Xe-129 under continuous flow: A method to study aqueous solutions of biomolecules *Angewandte Chemie-International Edition* **45** 7282-4

[207] Cleveland Z I, Moller H E, Hedlund L W, Nouls J C, Freeman M S, Qi Y and Driehuys B 2012 In Vivo MR Imaging of Pulmonary Perfusion and Gas Exchange in Rats via Continuous Extracorporeal Infusion of Hyperpolarized Xe-129 *Plos One* **7**

[208] Swanson S D, Rosen M S, Agranoff B W, Coulter K P, Welsh R C and Chupp T E 1997 Brain MRI with laser-polarized Xe-129 *Magn Reson Med* **38** 695-8

[209] Nakamura K, Kondoh Y, Wakai A, Kershaw J, Wright D and Kanno I 2005 Xe-129 spectra from the heads of rats with and without ligation of the external carotid and pterygopalatine arteries *Magn Reson Med* **53** 528-34

[210] Kershaw J, Nakamura K, Kondoh Y, Wakai A, Suzuki N and Kanno I 2007 Confirming the existence of five peaks in Xe-129 rat head spectra *Magn Reson Med* **57** 791-7

[211] Zhou X, Sun Y P, Mazzanti M, Henninger N, Mansour J, Fisher M and Albert M 2011 MRI of stroke using hyperpolarized Xe-129 *Nmr in Biomedicine* **24** 170-5

[212] Pavlovskaya G, Blue A K, Gibbs S J, Haake M, Cros F, Malier L and Meersmann T 1999 Xenon-131 surface sensitive imaging of aerogels in liquid xenon near the critical point *J Magn Reson* **137** 258-64

[213] Stupic K F, Cleveland Z I, Pavlovskaya G E and Meersmann T 2011 Hyperpolarized Xe-131 NMR spectroscopy *J Magn Reson* **208** 58-69

[214] Stupic K F, Elkins N D, Pavlovskaya G E, Repine J E and Meersmann T 2011 Effects of pulmonary inhalation on hyperpolarized krypton-83 magnetic resonance T-1 relaxation *Phys Med Biol* **56** 3731-48

[215] Hughes-Riley T, Six J S, Lilburn D M, Stupic K F, Dorkes A C, Shaw D E, Pavlovskaya G E and Meersmann T 2013 Cryogenics free production of hyperpolarized Xe and Kr for biomedical MRI applications *J Magn Reson* **237C** 23-33

[216] Six J S, Hughes-Riley T, Lilburn D M, Dorkes A C, Stupic K F, Shaw D E, Morris P G, Hall I P, Pavlovskaya G E and Meersmann T 2013 Pulmonary MRI contrast using Surface Quadrupolar Relaxation (SQUARE) of hyperpolarized Kr *Magn Reson Imaging*

[217] Hachulla A L, Pontana F, Wemeau-Stervinou L, Khung S, Faivre J B, Wallaert B, Cazaubon J F, Duhamel A, Perez T, Devos P, Remy J and Remy-Jardin M 2012 Krypton Ventilation Imaging Using Dual-Energy CT in Chronic Obstructive Pulmonary Disease Patients: Initial Experience *Radiology* **263** 253-9

[218] Takahashi M, Kubo S, Kiryu S, Gee J and Hatabu H 2007 MR microscopy of the lung in small rodents *European Journal of Radiology* **64** 367-74

[219] Zosky G R and Sly P D 2007 Animal models of asthma *Clinical and Experimental Allergy* **37** 973-88

[220] Abraham W M 1989 Effect of Nedocromil Sodium on Antigen-Induced Airway Responses in Allergic Sheep *Drugs* **37** 78-86

[221] Long W M, Yerger L D, Abraham W M and Lobel C 1990 Late-Phase Bronchial Vascular-Responses in Allergic Sheep *J Appl Physiol* **69** 584-90

[222] Fujimoto K, Kubo K, Okada K, Kobayashi T, Sekiguchi M and Sakai A 1996 Effect of the 21-aminosteroid U-74006F on antigen-induced bronchoconstriction and bronchoalveolar eosinophilia in allergic sheep *Eur Respir J* **9** 2044-9

[223] Szelenyi I 2000 Animal models of bronchial asthma *Inflammation Research* **49** 639-54

[224] Stevenson C S and Belvisi M G 2008 Preclinical animal models of asthma and chronic obstructive pulmonary disease *Expert Rev Respir Med* **2** 631-43

[225] 2002 *Animal Models for Asthma: Contributions from the Workshop on Animal Models in Asthma, Hannover, January 24-25, 2003* (Hannover: Karger)

[226] Roquet A, Dahlen B, Kumlin M, Ihre E, Anstren G, Binks S and Dahlen S E 1997 Combined antagonism of leukotrienes and histamine produces predominant inhibition of allergen-induced early and late phase airway obstruction in asthmatics *Am J Resp Crit Care* **155** 1856-63

[227] Shinagawa K and Kojima M 2003 Mouse model of airway remodeling - Strain differences *Am J Resp Crit Care* **168** 959-67

[228] Van Hove C L, Maes T, Cataldo D D, Gueders M M, Palmans E, Joos G F and Tournoy K G 2009 Comparison of Acute Inflammatory and Chronic Structural Asthma-Like Responses between C57BL/6 and BALB/c Mice *International Archives of Allergy and Immunology* **149** 195-207

[229] Pauwels R, Vanderstraeten M, Weyne J and Bazin H 1985 Genetic-Factors in Non-Specific Bronchial Reactivity in Rats *Eur J Respir Dis* **66** 98-104

[230] Hylkema M N, Hoekstra M O, Luinge M and Timens W 2002 The strength of the OVA-induced airway inflammation in rats is strain dependent *Clinical and Experimental Immunology* **129** 390-6

[231] Kucharewicz I, Bodzenta-Lukaszyk A and Buczko W 2008 Experimental asthma in rats *Pharmacological Reports* **60** 783-8

[232] Boushey H, Corry D, JV F, EG B and Woodruff P 2005 *Murray and Nadel's Textbook of Respiratory Medicine,* ed R Mason*, et al.*: Elsevier Saunders) pp 1168-216

[233] Waserman S, Olivenstein R, Renzi P, Xu L J and Martin J G 1992 The Relationship between Late Asthmatic Responses and Antigen-Specific Immunoglobulin *J Allergy Clin Immun* **90** 661-9

[234] Haczku A, Chung K F, Sun J, Barnes P J, Kay A B and Moqbel R 1995 Airway Hyperresponsiveness, Elevation of Serum-Specific Ige and Activation of T-Cells Following Allergen Exposure in Sensitized Brown-Norway Rats *Immunology* **85** 598-603

[235] Mehlhop P D, van de Rijn M, Goldberg A B, Brewer J P, Kurup V P, Martin T R and Oettgen H C 1997 Allergen-induced bronchial hyperreactivity and eosinophilic inflammation occur in the absence of IgE in a mouse model of asthma *Proc Natl Acad Sci U S A* **94** 1344-9

[236] Zosky G R, von Garnier C, Stumbles P A, Holt P G, Sly P D and Turner D J 2004 The pattern of methacholine responsiveness in mice is dependent on antigen challenge dose *Resp Res* **5**

[237] Allakhverdi Z, Allam M and Renzi P M 2002 Inhibition of antigen-induced eosinophilia and airway hyperresponsiveness by antisense oligonucleotides directed against the common beta chain of IL-3, IL-5, GM-CSF receptors in a rat model of allergic asthma *Am J Resp Crit Care* **165** 1015-21

[238] Salmon M, Walsh D A, Koto H, Barnes P J and Chung K F 1999 Repeated allergen exposure of sensitized Brown-Norway rats induces airway cell DNA synthesis and remodelling *Eur Respir J* **14** 633-41

[239] Temelkovski J, Hogan S P, Shepherd D P, Foster P S and Kumar R K 1998 An improved murine model of asthma: selective airway inflammation, epithelial lesions and increased methacholine responsiveness following chronic exposure to aerosolised allergen *Thorax* **53** 849-56

[240] Johnson J R, Wiley R E, Fattouh R, Swirski F K, Gajewska B U, Coyle A J, Gutierrez-Ramos J C, Ellis R, Inman M D and Jordana M 2004 Continuous exposure to house dust mite elicits chronic airway inflammation and structural remodeling *Am J Resp Crit Care* **169** 378-85

[241] Misawa M, Takenouchi K, Abiru T, Yoshino Y and Yanaura S 1987 Strain Difference in an Allergic-Asthma Model in Rats *Japanese Journal of Pharmacology* **45** 63-8

[242] Wright J L, Cosio M and Churg A 2008 Animal models of chronic obstructive pulmonary disease *Am J Physiol Lung Cell Mol Physiol* **295** L1-15

[243] Massaro D and Massaro G D 2007 Developmental alveologenesis: longer, differential regulation and perhaps more danger *Am J Physiol Lung Cell Mol Physiol* **293** L568-9

[244] Pinkerton K E, Dodge D E, Cederdahl J, Haselton C, Peake J, Singh G and Plopper C G 1992 Bronchiolarization of the Rodent Lung Following Life-Span Exposure to Ozone *Faseb J* **6** A939-A

[245] Niewoehner D, Kleinerman J and Rice D 1974 Pathologic-Changes in Peripheral Airways of Young Cigarette Smokers *Am Rev Respir Dis* **109** 725-

[246] Mannino D M and Buist A S 2007 Global burden of COPD: risk factors, prevalence, and future trends *Lancet* **370** 765-73

[247] Pryor W A, Hales B J, Premovic P I and Church D F 1983 The Radicals in Cigarette Tar - Their Nature and Suggested Physiological Implications *Science* **220** 425-7

[248] Church D F and Pryor W A 1985 Free-Radical Chemistry of Cigarette-Smoke and Its Toxicological Implications *Environ Health Persp* **64** 111-26

[249] Stevenson C S and Birrell M A 2011 Moving towards a new generation of animal models for asthma and COPD with improved clinical relevance *Pharmacology & Therapeutics* **130** 93-105

[250] Teague S V, Pinkerton K E, Goldsmith M, Gebremichael A, Chang S, Jenkins R A and Moneyhun J H 1994 Sidestream Cigarette-Smoke Generation and Exposure System for Environmental Tobacco-Smoke Studies *Inhal Toxicol* **6** 79-93

[251] Coggins C R E 1998 A review of chronic inhalation studies with mainstream cigarette smoke in rats and mice *Toxicol Pathol* **26** 307-14

[252] Coggins C R E 2007 An updated review of inhalation studies with cigarette smoke in laboratory animals *Int J Toxicol* **26** 331-8

[253] Kuhn C and Tavassoli F 1976 Scanning Electron-Microscopy of Elastase-Induced Emphysema - Comparison with Emphysema in Man *Lab Invest* **34** 2-9

[254] Wright J L, Postma D S, Kerstjens H A M, Timens W, Whittaker P and Churg A 2007 Airway remodeling in the smoke exposed guinea pig model *Inhal Toxicol* **19** 915-23

[255] Cavarra E, Bartalesi B, Lucattelli M, Fineschi S, Lunghi B, Gambelli F, Ortiz L A, Martorana P A and Lungarella G 2001 Effects of cigarette smoke in mice with different levels of alpha(1)-proteinase inhibitor and sensitivity to oxidants *Am J Respir Crit Care Med* **164** 886-90

[256] Takubo Y, Guerassimov A, Ghezzo H, Triantafillopoulos A, Bates J H T, Hoidal J R and Cosio M G 2002 alpha(1)-antitrypsin determines the pattern of emphysema and function in tobacco smoke-exposed mice parallels with human disease *Am J Resp Crit Care* **166** 1596-603

[257] Guerassimov A, Hoshino Y, Takubo Y, Turcotte A, Yamamoto M, Ghezzo H, Triantafillopoulos A, Whittaker K, Hoidal J R and Cosio M G 2004 The development of emphysema in cigarette smoke-exposed mice is strain dependent *Am J Resp Crit Care* **170** 974-80

[258] Wright J L and Churg A 1990 Cigarette-Smoke Causes Physiological and Morphological-Changes of Emphysema in the Guinea-Pig *Am Rev Respir Dis* **142** 1422-8

[259] Stevenson C S, Docx C, Webster R, Battram C, Hynx D, Giddings J, Cooper P R, Chakravarty P, Rahman I, Marwick J A, Kirkham P A, Charman C, Richardson D L, Nirmala N R, Whittaker P and Butler K 2007 Comprehensive gene expression profiling of rat lung reveals distinct acute and chronic responses to cigarette smoke inhalation *Am J Physiol-Lung C* **293** L1183-L93

[260] Carrell R W, Jeppsson J O, Laurell C B, Brennan S O, Owen M C, Vaughan L and Boswell D R 1982 Structure and Variation of Human Alpha-1-Antitrypsin *Nature* **298** 329-34

[261] Lieberman J 1976 Elastase, collagenase, emphysema, and alpha1-antitrypsin deficiency *Chest* **70** 62-7

[262] Lafuma C, Frisdal E, Harf A, Robert L and Hornebeck W 1991 Prevention of leucocyte elastase-induced emphysema in mice by heparin fragments *Eur Respir J* **4** 1004-9

[263] Birrell M A, Wong S, Hele D J, McCluskie K, Hardaker E and Belvisi M G 2005 Steroid-resistant inflammation in a rat model of chronic

obstructive pulmonary disease is associated with a lack of nuclear factor-kappa B pathway activation *Am J Resp Crit Care* **172** 74-84

[264] Tuder R M, Petrache I, Elias J A, Voelkel N F and Henson P M 2003 Apoptosis and emphysema - The missing link *Am J Resp Cell Mol* **28** 551-4

[265] Voelkel N F, Vandivier R W and Tuder R M 2006 Vascular endothelial growth factor in the lung *Am J Physiol-Lung C* **290** L209-L21

[266] Sahebjami H and Vassallo C L 1979 Effects of Starvation and Refeeding on Lung-Mechanics and Morphometry *Am Rev Respir Dis* **119** 443-51

[267] Sahebjami H and Wirman J A 1981 Effects of Starvation on Experimental Emphysema *Chest* **80** 351-

[268] Hildebrandt I J, Su H and Weber W A 2008 Anesthesia and other considerations for in vivo imaging of small animals *Ilar J* **49** 17-26

[269] Fueger B J, Czernin J, Hildebrandt I, Tran C, Halpern B S, Stout D, Phelps M E and Weber W A 2006 Impact of animal handling on the results of F-18-FDG PET studies in mice *J Nucl Med* **47** 999-1006

[270] Lukasik V M and Gillies R J 2003 Animal anaesthesia for in vivo magnetic resonance *Nmr in Biomedicine* **16** 459-67

[271] Chen B T, Brau A C S and Johnson G A 2003 Measurement of regional lung function in rats using hyperpolarized (3)helium dynamic MRI *Magn Reson Med* **49** 78-88

[272] Driehuys B, Pollaro J and Cofer G P 2008 In vivo MRI using real-time production of hyperpolarized Xe-129 *Magn Reson Med* **60** 14-20

[273] Hedlund L, Deitz J, Nassar R, Herfkens R, Dahlke J, Vock P, Kubek R, Charles C, Effmann E and Putman C 1985 Optimizing Quality of Magnetic-Resonance Images by Scan Synchronous Ventilation *Invest Radiol* **20** S47-S

[274] Hedlund L W, Deitz J, Nassar R, Herfkens R, Vock P, Dahlke J, Kubek R, Effmann E L and Putman C E 1986 A Ventilator for Magnetic-Resonance-Imaging *Invest Radiol* **21** 18-23

[275] Hedlund L W, Cofer G P, Owen S J and Johnson G A 2000 MR-compatible ventilator for small animals: computer-controlled ventilation for proton and noble gas imaging *Magnetic Resonance Imaging* **18** 753-9

[276] de Alejo R P, Ruiz-Cabello J, Villa P, Rodriguez I, Perez-Sanchez J M, Peces-Barba G and Cortijo M 2005 A fully MRI-compatible animal

ventilator for special-gas mixing applications *Concepts in Magnetic Resonance Part B-Magnetic Resonance Engineering* **26B** 93-103

[277] Hedlund L W, Moller H E, Chen X J, Chawla M S, Cofer G P and Johnson G A 2000 Mixing oxygen with hyperpolarized He-3 for small-animal lung studies *Nmr in Biomedicine* **13** 202-6

[278] Johnson G A, Chen B T and Yordanov A T 2005 Ventilation-synchronous magnetic resonance microscopy of pulmonary structure and ventilation in mice *Magn Reson Med* **53** 69-75

[279] Chen B T, Yordanov A T and Johnson G A 2005 Ventilation-synchronous magnetic resonance microscopy of pulmonary structure and ventilation in mice *Magn Reson Med* **53** 69-75

[280] Driehuys B, Walker J, Pollaro J, Cofer G P, Mistry N, Schwartz D and Johnson G A 2007 He-3 Mri in Mouse Models of Asthma *Magn Reson Med* **58** 893-900

[281] Hedlund L W and Johnson G A 2002 Mechanical ventilation for imaging the small animal lung *ILAR journal / National Research Council, Institute of Laboratory Animal Resources* **43** 159-74

[282] Dugas J P, Garbow J R, Kobayashi D K and Conradi M S 2004 Hyperpolarized He-3 MRI of mouse lung *Magn Reson Med* **52** 1310-7

[283] Albert M S, Venkatesh A K and Ward III C F 2002 Method and apparatus for delivering a measured of a gas. In: *United States Patent,* (U.S.: The Brigham and Women's Hosptial, Inc., Boston, MA (US))

[284] Moller H E, Cleveland Z I and Driehuys B 2011 Relaxation of hyperpolarized Xe-129 in a deflating polymer bag *J Magn Reson* **212** 109-15

[285] Viallon M, Cofer G P, Suddarth S A, Moller H E, Chen X J, Chawla M S, Hedlund L W, Cremillieux Y and Johnson G A 1999 Functional MR microscopy of the lung using hyperpolarized He-3 *Magn Reson Med* **41** 787-92

[286] Johnson G A and Chen B T 2004 Dynamic lung morphology of methacholine-induced heterogeneous bronchoconstriction *Magn Reson Med* **52** 1080-6

[287] Thomas A C, Potts E N, Chen B T, Slipetz D M, Foster W M and Driehuys B 2009 A robust protocol for regional evaluation of methacholine

challenge in mouse models of allergic asthma using hyperpolarized He-3 MRI *Nmr in Biomedicine* **22** 502-15

[288] Haczku A, Emami K, Fischer M C, Kadlecek S, Ishii M, Panettieri R A and Rizi R R 2005 Hyperpolarized He-3 MRI in asthma: Measurements of regional ventilation following allergic sensitization and challenge in mice - Preliminary results *Acad Radiol* **12** 1362-70

[289] Emami K, Kadlecek S J, Woodburn J M, Zhu J L, Yu J S, Vahdat V, Pickup S, Ishii M and Rizi R R 2010 Improved Technique for Measurement of Regional Fractional Ventilation by Hyperpolarized (3)He MRI *Magn Reson Med* **63** 137-50

[290] Santyr G E, Lam W W and Ouriadov A 2008 Rapid and efficient mapping of regional ventilation in the rat lung using hyperpolarized He-3 with Flip Angle Variation for Offset of RF and Relaxation (FAVOR) *Magn Reson Med* **59** 1304-10

[291] Lilburn D M L, Hughes-Riley T, Six J S, Stupic K F, Shaw D E, Pavlovskaya G E and Meersmann T 2013 Validating Excised Rodent Lungs for Functional Hyperpolarized Xenon-129 MRI *Plos One* **8**

[292] Martin C, Held H D and Uhlig S 1999 Characterization of pulmonary responses in mice: Comparison of lung slices and perfused lung *Am J Resp Crit Care* **159** A871-A

[293] Faridy E E 1973 Effect of Hydration and Dehydration on Elastic Behavior of Excised Dogs Lungs *J Appl Physiol* **34** 597-605

[294] Six J S, Hughes-Riley T, Stupic K F, Pavlovskaya G E and Meersmann T 2012 Pathway to Cryogen Free Production of Hyperpolarized Krypton-83 and Xenon-129 *PLOS ONE* **7** e49927

[295] Cleveland Z I, Pavlovskaya G E, Elkins N D, Stupic K F, Repine J E and Meersmann T 2008 Hyperpolarized Kr-83 MRI of lungs *J Magn Reson* **195** 232-7

[296] Armstrong S R, Briones S, Horger B, Richardson C L, Jaw-Tsai S and Hegde S S 2008 Pharmacological analysis of the interaction of antimuscarinic drugs at M(2) and M(3) muscarinic receptors in vivo using the pithed rat assay *Naunyn-Schmiedeberg's archives of pharmacology* **376** 341-9

[297] Buchheit K H, Hofmann A and Fozard J R 1995 Salbutamol-induced airway hyperreactivity in guinea pigs is not due to a loss of its bronchodilator effect *European journal of pharmacology* **287** 85-8

[298] Kauczor H U, Markstaller K, Puderbach M, Lill J, Eberle B, Hanisch G, Grossmann T, Heussel C P, Schreiber W and Thelen M 2001 Volumetry of ventilated airspaces by He-3 MRI preliminary results *Invest Radiol* **36** 110-4

[299] Woodhouse N, Wild J M, van Beek E J R, Hoggard N, Barker N and Taylor C J 2009 Assessment of Hyperpolarized He-3 Lung MRI for Regional Evaluation of Interventional Therapy: A Pilot Study in Pediatric Cystic Fibrosis *Journal of Magnetic Resonance Imaging* **30** 981-8

[300] Kirsch R A 1971 Computer Determination of Constituent Structure of Biological Images *Comput Biomed Res* **4** 315-&

[301] Martin C, Uhlig S and Ullrich V 1996 Videomicroscopy of methacholine-induced contraction of individual airways in precision-cut lung slices *Eur Respir J* **9** 2479-87

[302] Sturton R G, Trifilieff A, Nicholson A G and Barnes P J 2008 Pharmacological characterization of indacaterol, a novel once daily inhaled beta(2) adrenoceptor agonist, on small airways in human and rat precision-cut lung slices *Journal of Pharmacology and Experimental Therapeutics* **324** 270-5

[303] Ressmeyer A R, Larsson A K, Vollmer E, Dahlen S E, Uhlig S and Martin C 2006 Characterisation of guinea pig precision-cut lung slices: comparison with human tissues *Eur Respir J* **28** 603-11

[304] Patra A L 1986 Comparative anatomy of mammalian respiratory tracts: the nasopharyngeal region and the tracheobronchial region *J Toxicol Environ Health* **17** 163-74

[305] Lauzon A and Martin J 2008 *Airway Smooth Muscle in Asthma and COPD: Biology and Pharmacology,* ed K F Chung: John Wiley & Sons) pp 160-79

[306] Takezawa J, Miller F J and Oneil J J 1978 Lung-Volumes and Single Breath Diffusing-Capacity for Carbon-Monoxide Measured in Small Laboratory Mammals *Am Rev Respir Dis* **117** 405-

[307] Kleinman L I, Siebens A A and Poulos D A 1964 Minimal Air in Dogs *J Appl Physiol* **19** 204-&

[308] Horie T, Ardila R and Hildebra.J 1974 Static and Dynamic Properties of Excised Cat Lung in Relation to Temperature *J Appl Physiol* **36** 317-22

[309] Hughes J M B and Rosenzweig D Y 1970 Factors Affecting Trapped Gas Volume in Perfused Dog Lungs *J Appl Physiol* **29** 332-&

[310] Frazer D G, Stengel P W and Weber K C 1979 Effect of Pulmonary-Edema on Gas Trapping in Excised Rat Lungs *Resp Physiol* **38** 325-33

[311] Milic-Emili J, Henderson J, Dolovich M B, Trop D and Kaneko K 1966 Regional Distribution of Inspired Gas in Lung *J Appl Physiol* **21** 749-59

[312] Michels D B, Friedman P J and West J B 1979 Radiographic Comparison of Human-Lung Shape during Normal Gravity and Weightlessness *J Appl Physiol* **47** 851-7

[313] Ball W C, Newsham L G S, Stewart P B and Bates D V 1962 Regional Pulmonary Function Studied with Xenon133 *J Clin Invest* **41** 519-&

[314] Orphanidou D, Hughes J M B, Myers M J, Alsuhali A R and Henderson B 1986 Tomography of Regional Ventilation and Perfusion Using Krypton 81m in Normal Subjects and Asthmatic-Patients *Thorax* **41** 542-51

[315] Mansson S, Deninger A J, Magnusson P, Pettersson G, Olsson L E, Hansson G, Wollmer P and Golman K 2005 He-3 MRI-based assessment of posture-dependent regional ventilation gradients in rats *J Appl Physiol* **98** 2259-67

[316] Kyriazis A, Rodriguez I, Nin N, Izquierdo-Garcia J L, Lorente J A, Perez-Sanchez J M, Pesic J, Olsson L E and Ruiz-Cabello J 2012 Dynamic Ventilation He-3 MRI for the Quantification of Disease in the Rat Lung *Ieee Transactions on Biomedical Engineering* **59** 777-86

[317] Eidelman D H, Dimaria G U, Bellofiore S, Wang N S, Guttmann R D and Martin J G 1991 Strain-Related Differences in Airway Smooth-Muscle and Airway Responsiveness in the Rat *Am Rev Respir Dis* **144** 792-6

[318] Wang C G, Almirall J J, Dolman C S, Dandurand R J and Eidelman D H 1997 In vitro bronchial responsiveness in two highly inbred rat strains *J Appl Physiol* **82** 1445-52

[319] Beasley R, Masoli M, Fabian D, Holt S and Program G 2004 The global burden of asthma: executive summary of the GINA Dissemination Committee Report *Allergy* **59** 469-78

[320] Sidebotham H J and Roche W R 2003 Asthma deaths; persistent and preventable mortality *Histopathology* **43** 105-17

[321] Harrison B, Stephenson P, Mohan G and Nasser S 2005 An ongoing Confidential Enquiry into asthma deaths in the Eastern Region of the UK, 2001-2003 *Prim Care Respir J* **14** 303-13

[322] Braman S S 2006 The global burden of asthma *Chest* **130** 4S-12S

[323] Anderson H R, Gupta R, Strachan D P and Limb E S 2007 50 years of asthma: UK trends from 1955 to 2004 *Thorax* **62** 85-90

[324] National.Asthma.Campaign 1999 National Asthma Audit 1999/2000.

[325] Dahlen S E, Bjork J, Hedqvist P, Arfors K E, Hammarstrom S, Lindgren J A and Samuelsson B 1981 Leukotrienes promote plasma leakage and leukocyte adhesion in postcapillary venules: in vivo effects with relevance to the acute inflammatory response *Proc Natl Acad Sci U S A* **78** 3887-91

[326] Diamant Z, Boot J D and Virchow J C 2007 Summing up 100 years of asthma *Respir Med* **101** 378-88

[327] Hruby J and Butler J 1975 Variability of Routine Pulmonary-Function Tests *Thorax* **30** 548-53

[328] Rozas C J and Goldman A L 1982 Daily Spirometric Variability - Normal Subjects and Subjects with Chronic-Bronchitis with and without Air-Flow Obstruction *Archives of Internal Medicine* **142** 1287-91

[329] Bacharier L B, Strunk R C, Mauger D, White D, Lemanske R F and Sorkness C A 2004 Classifying asthma severity in children - Mismatch between symptoms, medication use, and lung function *Am J Resp Crit Care* **170** 426-32

[330] Spahn J D, Cherniack R, Paull K and Gelfand E W 2004 Is forced expiratory volume in one second the best measure of severity in childhood asthma? *Am J Resp Crit Care* **169** 784-6

[331] Castro M, Fain S B, Hoffman E A, Gierada D S, Erzurum S C, Wenzel S and Sever N H L B I 2011 Lung imaging in asthmatic patients: The picture is clearer *J Allergy Clin Immun* **128** 467-78

[332] Smith L J 2001 Comparative efficacy of inhaled corticosteroids and antileukotriene drugs in asthma *Biodrugs* **15** 239-49

[333] Barnes P J 2002 Scientific rationale for inhaled combination therapy with long-acting beta(2)-agonists and corticosteroids *Eur Respir J* **19** 182-91

[334] Kurucz I and Szelenyi I 2006 Current animal models of bronchial asthma *Current Pharmaceutical Design* **12** 3175-94

[335] Fuchs B and Braun A 2008 Improved mouse models of allergy and allergic asthma - Chances beyond ovalbumin *Curr Drug Targets* **9** 495-502

[336] Haczku A, Moqbel R, Jacobson M, Kay A B, Barnes P J and Chung K F 1995 T-Cells Subsets and Activation in Bronchial-Mucosa of Sensitized Brown-Norway Rats after Single Allergen Exposure *Immunology* **85** 591-7

[337] Underwood S L, Raeburn D, Lawrence C, Foster R, Webber S and Karlsson J A 1997 RPR 106541, a novel, airways-selective glucocorticoid: effects against antigen-induced CD4(+) T lymphocyte accumulation and cytokine gene expression in the brown Norway rat lung *British Journal of Pharmacology* **122** 439-46

[338] Belvisi M G, Underwood S L, Haddad E B, Birrell M A, McCluskie K, Pecoraro M, Dabrowski D, Webber S E and Foster M L 2002 Functional characterization and biomarker identification in the Brown Norway model of allergic airway inflammation *British Journal of Pharmacology* **137** 263-75

[339] Bianchi A, Ozier A, Ousova O, Raffard G and Cremillieux Y 2013 Ultrashort-TE MRI longitudinal study and characterization of a chronic model of asthma in mice: inflammation and bronchial remodeling assessment *NMR Biomed* **26** 1451-9

[340] Lederlin M, Ozier A, Montaudon M, Begueret H, Ousova O, Marthan R, Berger P and Laurent F 2010 Airway remodeling in a mouse asthma model assessed by in-vivo respiratory-gated micro-computed tomography *Eur Radiol* **20** 128-37

[341] Carvalho C, Jancar S, Mariano M and Sirois P 1999 A rat model presenting eosinophilia in the airways, lung eosinophil activation, and pulmonary hyperreactivity *Exp Lung Res* **25** 303-16

[342] Deninger A J, Mansson S, Petersson J S, Pettersson G, Magnusson P, Svensson J, Fridlund B, Hansson G, Erjefeldt I, Wollmer P and Golman K 2002 Quantitative measurement of regional lung ventilation using 3He MRI *Magn Reson Med* **48** 223-32

[343] Mistry N N, Thomas A, Kaushik S S, Johnson G A and Driehuys B 2010 Quantitative Analysis of Hyperpolarized He-3 Ventilation Changes in Mice Challenged With Methacholine *Magn Reson Med* **63** 658-66

[344] Venegas J G, Schroeder T, Harris S, Winkler R T and Melo M F V 2005 The distribution of ventilation during bronchoconstriction is patchy and bimodal: A PET imaging study *Respiratory Physiology & Neurobiology* **148** 57-64

[345] Executive H a S 2013 Chronic Obstructive Pulmonary Disease (COPD) in Great Britain 2013. Health and Safety Executive)

[346] barnes P J 2000 Chronic Obstructive Pulmonary Disease *New England Journal of Medicine* **343** 269-80

[347] Seemungal T A R, Donaldson G C, Paul E A, Bestall J C, Jeffries D J and Wedzicha J A 1998 Effect of exacerbation on quality of life in patients with chronic obstructive pulmonary disease *Am J Resp Crit Care* **157** 1418-22

[348] Blinderman C D, Homel P, Billings J A, Tennstedt S and Portenoy R K 2009 Symptom Distress and Quality of Life in Patients with Advanced Chronic Obstructive Pulmonary Disease *J Pain Symptom Manag* **38** 115-23

[349] Pauwels R A, Buist A S, Calverley P M, Jenkins C R and Hurd S S 2001 Global strategy for the diagnosis, management, and prevention of chronic obstructive pulmonary disease. NHLBI/WHO Global Initiative for Chronic Obstructive Lung Disease (GOLD) Workshop summary *Am J Respir Crit Care Med* **163** 1256-76

[350] Vestbo J, Anderson W, Coxson H O, Crim C, Dawber F, Edwards L, Hagan G, Knobil K, Lomas D A, MacNee W, Silverman E K and Tal-Singer R 2008 Evaluation of COPD Longitudinally to Identify Predictive Surrogate End-points (ECLIPSE) *Eur Respir J* **31** 869-73

[351] Han M K, Agusti A, Calverley P M, Celli B R, Criner G, Curtis J L, Fabbri L M, Goldin J G, Jones P W, MacNee W, Make B J, Rabe K F, Rennard S I, Sciurba F C, Silverman E K, Vestbo J, Washko G R, Wouters E F M and Martinez F J 2010 Chronic Obstructive Pulmonary Disease Phenotypes The Future of COPD *Am J Resp Crit Care* **182** 598-604

[352] Litmanovich D, Boiselle P M and Bankier A A 2009 CT of pulmonary emphysema--current status, challenges, and future directions *Eur Radiol* **19** 537-51

[353] Ley-Zaporozhan J, Ley S and Kauczor H U 2008 Morphological and functional imaging in COPD with CT and MRI: present and future *European Radiology* **18** 510-21

[354] Irion K L, Marchiori E, Hochhegger B, Porto N D, Moreira J D, Anselmi C E, Holemans J A and Irion P O 2009 CT Quantification of Emphysema in Young Subjects with No Recognizable Chest Disease *Am J Roentgenol* **192** W90-W6

[355] Marshall H, Deppe M H, Parra-Robles J, Hillis S, Billings C G, Rajaram S, Swift A, Miller S R, Watson J H, Wolber J, Lipson D A, Lawson R and Wild J M 2012 Direct visualisation of collateral ventilation in COPD with hyperpolarised gas MRI *Thorax* **67** 613-7

[356] Salerno M, de Lange E E, Altes T A, Truwit J D, Brookeman J R and Mugler J P 2002 Emphysema: Hyperpolarized Helium 3 Diffusion MR Imaging of the Lungs Compared with Spirometric Indexes,ÄîInitial Experience1 *Radiology* **222** 252-60

[357] Kirby M, Svenningsen S, Kanhere N, Owrangi A, Wheatley A, Coxson H O, Santyr G E, Paterson N A M, McCormack D G and Parraga G 2013 Pulmonary ventilation visualized using hyperpolarized helium-3 and xenon-129 magnetic resonance imaging: differences in COPD and relationship to emphysema *J Appl Physiol* **114** 707-15

[358] Yablonskiy D A, Sukstanskii A L, Leawoods J C, Gierada D S, Bretthorst G L, Lefrak S S, Cooper J D and Conradi M S 2002 Quantitative in vivo assessment of lung microstructure at the alveolar level with hyperpolarized He-3 diffusion MRI *P Natl Acad Sci USA* **99** 3111-6

[359] Woods J C, Choong C K, Yablonskiy D A, Bentley J, Wong J, Pierce J A, Cooper J D, Macklem P T, Conradi M S and Hogg J C 2006 Hyperpolarized

He-3 diffusion MRI and histology in pulmonary emphysema *Magn Reson Med* **56** 1293-300

[360] Snider G L, Lucey E C and Stone P J 1986 Animal-Models of Emphysema *Am Rev Respir Dis* **133** 149-69

[361] Wright J L, Cosio M and Churg A 2008 Animal models of chronic obstructive pulmonary disease *Am J Physiol-Lung C* **295** L1-L15

[362] Emami K, Cadman R V, Woodburn J M, Fischer M C, Kadlecek S J, Zhu J L, Pickup S, Guyer R A, Law M, Vahdat V, Friscia M E, Ishii M, Yu J S, Gefter W B, Shrager J B and Rizi R R 2008 Early changes of lung function and structure in an elastase model of emphysema - a hyperpolarized He-3 MRI study *J Appl Physiol* **104** 773-86

[363] Karlinsky J B, Goldstein R H, Catanese A and Snider G L 1986 Young Hamsters Are More Resistant Than Adults to Endotracheally Instilled Porcine Pancreatic Elastase *Exp Lung Res* **11** 229-43

[364] van Beek E J R, Wild J M, Kauczor H U, Schreiber W, Mugler J P and de Lange E E 2004 Functional MRI of the lung using hyperpolarized 3-helium gas *Journal of Magnetic Resonance Imaging* **20** 540-54

[365] Peces-Barba G, Ruiz-Cabello J, Cremillieux Y, Rodriguez I, Dupuich D, Callot V, Ortega M, Arbo M L R, Cortijo M and Gonzalez-Mangado N 2003 Helium-3 MRI diffusion coefficient: correlation to morphometry in a model of mild emphysema *Eur Respir J* **22** 14-9

[366] Hogg J C, Nepszy S J, Macklem P T and Thurlbec.Wm 1969 Elastic Properties of Centrilobular Emphysematous Space *J Clin Invest* **48** 1306-&

[367] Hirschfelder J O, Curtiss, C. F. and Bird R B 1954 *Molecular Theory of Gases and Liquids* (New York: John Wiley and Sons, Inc.)

[368] Tanoli T S K, Woods J C, Conradi M S, Bae K T, Gierada D S, Hogg J C, Cooper J D and Yablonskiy D A 2007 In vivo lung morphometry with hyperpolarized He-3 diffusion MRI in canines with induced emphysema: disease progression and comparison with computed tomography *J Appl Physiol* **102** 477-84

[369] Froese A R, Ask K, Labiris R, Farncombe T, Warburton D, Inman M D, Gauldie J and Kolb M 2007 Three-dimensional computed tomography imaging in an animal model of emphysema *Eur Respir J* **30** 1082-9

[370] Ford N L, Martin E L, Lewis J F, Veldhuizen R A W, Holdsworth D W and Drangova M 2009 Quantifying lung morphology with respiratory-gated micro-CT in a murine model of emphysema *Phys Med Biol* **54** 2121-30

[371] Quintana H K, Cannet C, Zurbruegg S, Ble F X, Fozard J R, Page C P and Beckmann N 2006 Proton MRI as a noninvasive tool to assess elastase-induced lung damage in spontaneously breathing rats *Magn Reson Med* **56** 1242-50

[372] Zurek M, Boyer L, Caramelle P, Boczkowski J and Cremillieux Y 2012 Longitudinal and noninvasive assessment of emphysema evolution in a murine model using proton MRI *Magn Reson Med* **68** 898-904

[373] Xu X J, Boudreau M, Ouriadov A and Santyr G E 2012 Mapping of 3He apparent diffusion coefficient anisotropy at sub-millisecond diffusion times in an elastase-instilled rat model of emphysema *Magn Reson Med* **67** 1146-53

[374] Ishii M, Emami K, Xin Y, Barulic A, Kotzer C J, Logan G A, Chia E, MacDuffie-Woodburn J P, Zhu J L, Pickup S, Kuzma N, Kadlecek S, Podolin P L and Rizi R R 2012 Regional function-structure relationships in lungs of an elastase murine model of emphysema *J Appl Physiol* **112** 135-48

[375] Mugler J P and Altes T A 2013 Hyperpolarized 129Xe MRI of the human lung *Journal of Magnetic Resonance Imaging* **37** 313-31

[376] Frazer D G, Morgan J, Khoshnood B and Weber K C 1979 Gas Trapping in the Excised Lungs of Mice, Hamsters, Rats, Rabbits, and Cats *Am Rev Respir Dis* **119** 309-

[377] Frazer D G, Weber K C and Franz G N 1985 Evidence of Sequential Opening and Closing of Lung Units during Inflation-Deflation of Excised Rat Lungs *Resp Physiol* **61** 277-88

[378] Cleveland Z I and Meersmann T 2007 Studying porous materials with krypton-83 NMR spectroscopy *Magnetic Resonance in Chemistry* **45** S12-S23

Appendix 1: Pumlonary MRI contrast using surface quadrupolar relaxation (SQUARE) of hyperpolarized Kr-83

The work in this Appendix is the article published in the peer-reviewed journal Magnetic Resonance Imaging entitled "Pulmonary MRI contrast using Surface Quadrupolar Relaxation (SQUARE) of hyperpolarized ^{83}Kr" by Joseph S. Six, Theodore Hughes-Riley, David M.L. Lilburn, Alan C. Dorkes, Karl F. Stupic, Dominick E. Shaw, Peter G. Morris, Ian P. Hall, Galina E. Pavlovskaya, and Thomas Meersmann [1]. Credits for the work were as follows: Prof. Meersmann conceived the experiment; Mr. Six, Mr. Hughes-Riley and Dr. Lilburn performed the experiments; Dr. Lilburn handled the animals and completed the lung extraction process; Mr. Hughes-Riley and Mr. Dorkes designed the gas extraction unit fabricated by Mr. Dorkes; Mr. Six, Mr. Hughes-Riley, Dr. Lilburn and Dr. Pavlovskaya analyzed the data; Dr. Stupic and Dr. Pavlovskaya designed and constructed the hyperpolarizer; Dr. Shaw, Prof. Morris, and Prof. Hall were greatly consulted on the design of the experiments; with Mr. Six, Mr. Hughes-Riley, Dr. Lilburn and Prof. Meersmann writing the manuscript.

Inclusion of this publication as Appendix within this thesis is justified because the thesis author performed a significant amount of the work, including writing and preparing the manuscript. Furthermore the development of *ex vivo* hp ^{83}Kr MRI detailed in the publication led onto the research contained within Chapter 7 where the new methodology was applied to an *ex vivo* elastase model of human emphysema.

Pulmonary MRI contrast using surface quadrupolar relaxation (SQUARE) of hyperpolarized ^{83}Kr.

Joseph S. Six[a,b], Theodore Hughes – Riley[a,b], David M.L. Lilburn[a,b], Alan C. Dorkes[a,c], Karl F. Stupic[‡a,b], Dominick E. Shaw[d], Peter G. Morris[a,c], Ian P. Hall[b], Galina E. Pavlovskaya[a,b], and Thomas Meersmann[*a,b]

[a]Sir Peter Mansfield Magnetic Resonance Centre;

[b]School of Clinical Sciences;

[c]School of Physics and Astronomy;

[a,b,c]University of Nottingham, Nottingham, NG7 2RD, United Kingdom;

[d]City Hospital Nottingham, Nottingham Respiratory Research Unit, Nottingham NG5 1PB, United Kingdom

[‡]Present address: Division of Magnetics, National Institute of Standards and Technology, Boulder, Colorado, USA, 80305

[*]Corresponding author: Thomas Meersmann, University of Nottingham, Sir Peter Mansfield Magnetic Resonance Centre, Nottingham, NG7 2RD, United Kingdom, telephone +44 (0) 115 9514747, fax: +44 (0) 115 9515166

email: Thomas.Meersmann@Nottingham.ac.uk

Abstract

Hyperpolarized ^{83}Kr has previously been demonstrated to enable MRI contrast that is sensitive to the chemical composition of the surface in a porous model system. Methodological advances have lead to a substantial increase in the ^{83}Kr hyperpolarization and the resulting signal intensity. Using the improved methodology for spin exchange optical pumping of isotopically enriched ^{83}Kr, internal anatomical details of *ex vivo* rodent lung were resolved with hyperpolarized ^{83}Kr MRI after krypton inhalation. Different ^{83}Kr relaxation times were found between the main bronchi and the parenchymal regions in *ex vivo* rat lungs. The T_1 weighted hyperpolarized ^{83}Kr MRI provided a first demonstration of surface quadrupolar relaxation (SQUARE) pulmonary MRI contrast.

1. Introduction

Pulmonary MRI with hyperpolarized (hp) ^{129}Xe [1] and hp ^{3}He [2] are emerging techniques for spatially resolved measurement of lung function that cannot be obtained by alternative non-invasive methods. Both non-radioactive isotopes have a nuclear spin I = 1/2 that can be hyperpolarized through laser-based methods [3, 4] to obtain sufficient MRI signal intensity for high resolution imaging of the lung. Various MRI protocols can be used to generate complementary contrast from the two isotopes. For example, because of its high diffusivity, ^{3}He is thus far preferred for contrast relating to changes in alveolar lung structure (i.e. ADC contrast) [5-8]. The ^{3}He spin relaxation is more affected by the presence of paramagnetic O_2 than that of any other noble gas isotope and the ^{3}He T_1 relaxation can therefore be used for partial pressure measurement of pulmonary oxygen [9-11]. On the other hand, the large chemical shift range of ^{129}Xe leads to distinguishable MR signals between tissue dissolved and gas phase xenon [12] thus enabling the visualization of gas transport through the parenchyma [13]. The isotope ^{129}Xe generally possesses a relatively high solubility, has a relaxation times of T_1 = 13 s in oxygenated blood [14], and can be functionalized to serve as a biosensor for certain target molecules [15] with potential applications for pulmonary MRI and beyond. The development of hp pulmonary MRI is therefore not only a quest for higher signal intensity and better spatial resolution but also a pursuit for novel sources of contrast that probe different structural and functional aspects of lungs in health and disease [11, 16].

Using a third noble gas isotope, namely ^{83}Kr, longitudinal (T_1) relaxation weighted MRI contrast was previously shown to be indicative of the specific surface treatment in a porous model system [17]. Unlike ^{3}He and ^{129}Xe, the ^{83}Kr nucleus possesses a nuclear spin I = 9/2 and thus a non-vanishing electric quadrupole moment that serves as a probe for electric field gradients (EFGs). The EFGs are predominantly generated during brief collision and adsorption events of the noble gas atoms with the surrounding surfaces, resulting in rapid T_1 relaxation that is detected in the gas phase. The ^{83}Kr surface quadrupolar relaxation (SQUARE) MRI contrast is affected by the surface to volume ratio (S/V), surface composition, surface temperature, and surface adsorption of molecules [16-18]. On the down side, quadrupolar relaxation also restricts the hp ^{83}Kr signal intensity and applications of hp ^{83}Kr MRI were limited thus far to conceptual studies showing low resolution images [17, 19] with little chance to provide data about internal structure or function of the lung.

In recent work, spin exchange optical pumping (SEOP) of a mixture of 5% krypton with 95% N_2 achieved a ^{83}Kr spin polarization of P = 26%, corresponding to a 59,000 fold signal increase compared to the thermal equilibrium ^{83}Kr signal at 9.4 T field strength [20]. SEOP at low krypton concentration was used because high krypton density [Kr] adversely affects SEOP but, unfortunately, fast quadrupolar driven ^{83}Kr T_1 relaxation in the condensed state generally prevents the cryogenic separation of hp krypton from the gas mixture [21]. The high gas dilution caused a 20 fold reduction of the MRI signal and it is instructional to define the apparent polarization P_{app} that takes the dilution into account [20]:

$$P_{app} = P \cdot \left[NG \right] \Big/ \sum_i \left[M_i \right] \qquad [1]$$

where [NG] is the noble gas density (here, krypton) and [Mi] refers to the density of other components in the hp gas mixture (i.e. N_2 in this work). The apparent polarization provides a measure of the expected signal from a diluted hp noble gas. The example above (P = 26%) leads to P_{app}=1.3% and thus to the same signal of pure krypton gas with P =1.3% (assuming identical isotopic composition).

As an alternative to dilution, the density [Kr] can be lowered in concentrated krypton mixtures by reducing the SEOP gas pressure [20]. In the current work, this method was modified to extract below ambient pressure hp gas mixture from the SEOP cell followed by compression to ambient pressure for pulmonary imaging. Hp ^{83}Kr produced with this method was utilized to study SQUARE contrast in an excised rat lung.

2. Materials and methods

2.1. ^{83}Kr spin exchange optical pumping.

Spin exchange optical pumping (SEOP) with rubidium produced hp ^{83}Kr via batch mode as described in detail elsewhere [20]. Spin polarization measurements used natural abundance krypton gas (99.995% purity; 11.5% ^{83}Kr; Airgas, Rednor, PA, USA), whereas the MR images presented in this publication utilized enriched ^{83}Kr (99.925% ^{83}Kr, CHEMGAS, Boulogne, France) for improved signal intensity. A 25% krypton - 75% N_2 (99.999% purity, Air Liquide, Coleshill, UK) mixture was used for SEOP because it was previously proven to lead to high hp ^{83}Kr signal intensities [20] and allowed for economical usage of the expensive isotopically enriched ^{83}Kr gas.

Spin polarization was determined by comparison of the hp gas signal in a single pulse experiment with that from a thermally polarized krypton gas [20]. In baseline polarization measurements the hp gas was transferred by gas expansion directly into a pre-evacuated borosilicate glass cell located in the r.f. detection coil without usage of the extraction unit. Spin polarization measurements were acquired after 8 minutes of SEOP and images were acquired after 12 minutes of SEOP, corresponding to ~80% and ~92% of the steady state polarization (reached after 18 minutes [20]) respectively, to reduce experimental time.

2.2. HP gas extraction, compression and transfer.

To utilize the enhanced ^{83}Kr spin polarization of below ambient pressure SEOP [20] an extraction unit was designed and built that extracted the hp gas from the SEOP cell and then delivered the gas for pulmonary imaging as shown in Fig. 1. At 90 – 100 kPa SEOP cell pressure this method produced approximately 35 - 40 cm^3 of hp gas mixture every 12 minutes for lung imaging. Alternatively, in the spin polarization measurements the hp gas was injected into an NMR detection cell to measure the ^{83}Kr spin polarization after the compression process.

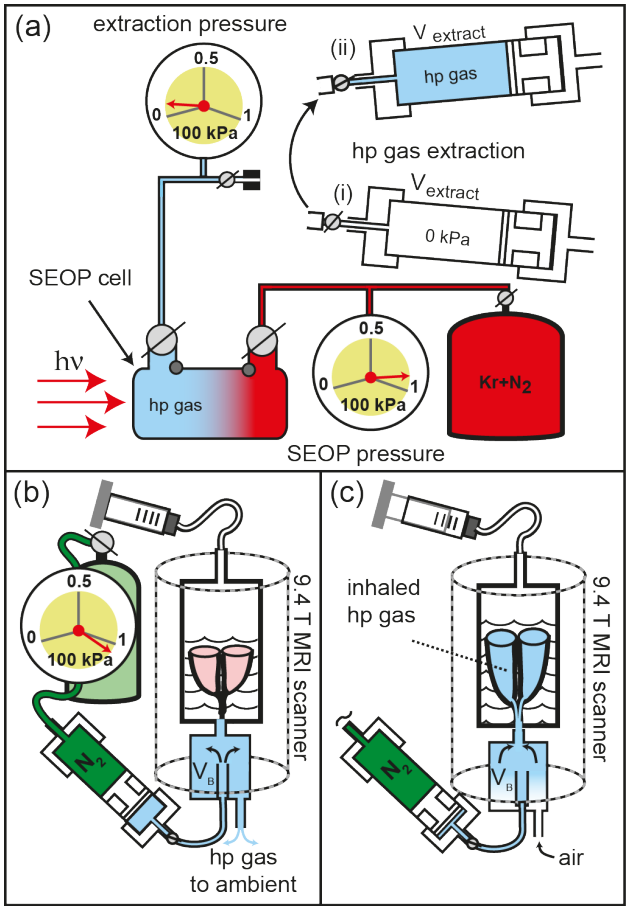

Fig. 1. Hp krypton extraction and transfer from the SEOP cell, operating at 90 – 100 kPa, to the lungs at ambient pressure. (a) A pre-evacuated volume $V_{extract}$ = 790 cm^3 in the extraction unit (i) was filled to approximately 6 kPa during hp gas extraction (ii). (b) The extraction unit was moved to the MRI scanner and the N_2 gas operated piston pressurizes the hp gas mixtures to a pressure slightly above ambient. The hp gas was then pushed through connecting tubing into a storage container (V_B). The lung was located upside down in glucose solution within the breathing apparatus with the trachea connected to V_B. (c) A slight suction on the breathing apparatus (substituting for the pleural cavity) caused the lung to expand and to inhale the hp gas.

2.3. HP gas inhalation.

A ventilation chamber with the lung suspended in a 5% glucose solution (weight/volume) (Baxter Healthcare Ltd, Thetford, UK) was placed inside the MR magnet and kept at a constant temperature of 295 K. Active inflation of the lung was achieved by producing a negative pressure above the glucose solution from pulling a ventilation syringe to 10 cm^3 as shown in Fig. 1c (see further explanation in ref. [27]). The corresponding inhaled volume of 8 cm^3 was measured through exhalation causing water displacement in a water bell.

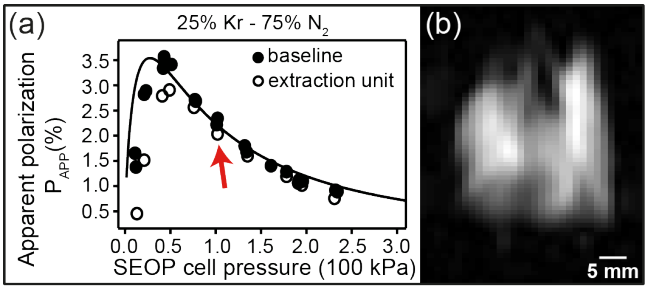

Fig. 2. (a) The apparent ^{83}Kr spin polarization P_{app} as a function of SEOP cell pressure using the extraction unit for compression (open circles) and baseline data without the extraction unit (filled circles). The arrow indicates the pressure used for imaging experiments. Curve fitting was adapted from ref. [20]. (b) Variable flip angle (VFA) FLASH hp ^{83}Kr MRI of an excised rat lungs at 9.4 T without signal averaging (NEX =1, no slice selection, SNR = 51) using isotopically enriched ^{83}Kr (99.925%).

2.4. MRI protocol

MRI experiments were performed using a vertical bore 9.4 T Bruker Avance III microimaging system (Bruker Corporation, Billerica, Massachusetts, USA). Imaging experiments utilized a Bruker 30 mm double

saddle probe tuned to 15.4002 MHz corresponding to the resonance frequency of ^{83}Kr gas in the lung. Images were acquired by means of 32 phase encoding gradient increments using a variable flip angle (VFA) FLASH protocol (TE = 4.2 ms, TR = 19.2 ms) that neglected T_1 decay; the flip angle of the ith increment (θ_i) was calculated by $\theta_i \approx \tan^{-1}\left(1/\sqrt{32-i}\right)$ [28]. The imaging protocol had a total acquisition time 0.615 s limiting the T_1 decay during acquisition.

Coronal images were acquired into 64 × 32 matrices resulting in a field of view (FOV) of 50.9 mm in the longitudinal (frequency encoding) and 40.7 mm in the transverse (phase encoding) directions, respectively. To acquire a non-slice selective image, 0.3 ms rectangular hard pulses of variable power levels were used for excitation. The slice selective images utilize 2 ms sinc-shaped radio frequency pulses of variable power to selectively excite a 3 mm central coronal slice of the lung, resulting in a nominal resolution of 0.80 × 1.27 × 3 mm^3. To obtain T_1-weighted images and demonstrate SQUARE pulmonary MRI contrast the imaging sequence was started with a programmed time delay (t_d) of 0.0 s, 0.5 s, 1.0 s or 1.5 s after inhalation. The inhalation itself was accomplished manually by reducing the pressure in the artificial pleural cavity using the ventilation syringe as described in ref. [27]. Slight alternations in the timing (approximately ± 0.2s) of the manual inhalation procedure were deemed acceptable. Note that the uncertainty in the exact timing of the images can be eliminated by future improved MRI protocols that record multiple images within one inhalation cycle. In this work, each individual image was acquired from a

single inhalation cycle and subsequent VFA FLASH acquisition (NEX = 1) with no signal averaging. Slice selective images demonstrating SQUARE MRI contrast (Fig. 3a-d) and the resulting T_1 map (Fig. 3e) were acquired using a single animal.

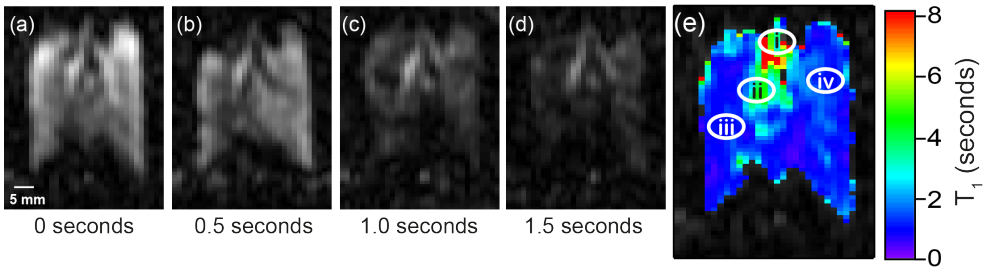

Fig. 3. Series of hp ^{83}Kr MR images demonstrating SQUARE contrast. A new delivery of hp ^{83}Kr was provided for each image shown. (a) VFA FLASH MRI as in Fig. 2b but with 3 mm slice selection. (b – d) MR images as in (a) with a relaxation delay, t_d, between hp gas inhalation and acquisition as indicated in the figure. The major airways are visibly less affected than the alveolar space by increasing t_d values. (e) Graphical representation of the T_1 values calculated from the signal decay in (a – d) for each volume element (voxel). Decay curves for each of the voxels located at positions i – iv in (e) are shown in Fig. 4.

2.5. Image reconstruction and analysis

Images were processed and reconstructed in Prospa (v. 3.06, Magritek, Wellington, New Zealand) by applying a sine-bell squared window function to the raw data before two-dimensional Fourier transformation. The two dimensional image data were exported for further analysis using IGOR Pro (v. 6.01, Wavemetrics, Lake Oswego, OR, USA).

To construct the T_1 map shown in Fig. 3e the image data were combined into a three dimensional matrix having two spatial dimensions (the slice selective images) and one time dimension (the delay before acquisition). Data were then converted into a half logarithmic scale for linear regression analysis of signal intensity as a function of time that resulted in spatially resolved T_1 values (Fig. 4). T_1 values calculated outside the lung region were composed solely of background noise and are consequently insignificant. Therefore, these data were removed by applying a threshold set to 15.4% of the maximum signal intensity on the lung image for t_d = 0 s and then applying the resulting mask to the T_1 map. It is important to note that noise far removed from the lung remaining after the mask was also removed. The final T_1 map was then overlaid onto the lung at delay time t_d = 0 s for clarity of presentation.

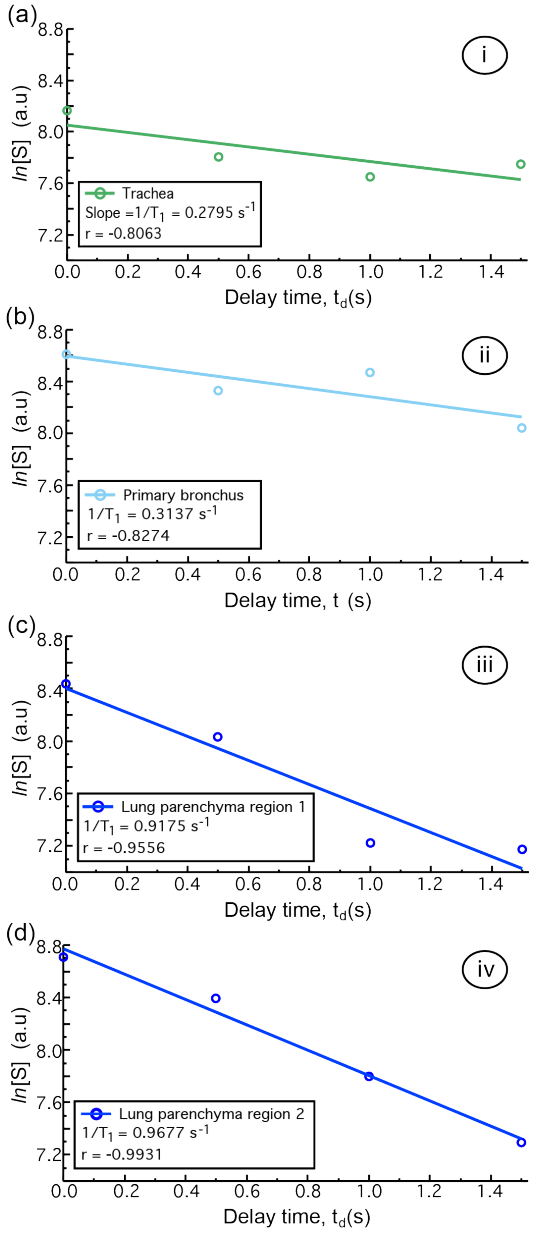

Fig. 4. Selected T_1 decay data from representative locations indicated in Fig. 3e. Position (a) trachea corresponding to point (i) in Fig 3e, (b) major bronchus corresponding to point (ii) in Fig. 3e, and (c - d) lung parenchyma corresponding to points (iii) – (iv) in Fig. 3e. Data are displayed with the natural logarithm of the signal intensity (*S*) as a function of time. The resultant least squares linear regression solution with linear correlation coefficients, r, and $1/T_1$ rates (i.e. slopes) for each location are also shown.

2.6. Animal care and preparation

Male Sprague-Dawley rats (350 - 400 g, Charles River UK Ltd, Margate, UK) were euthanized by overdose of pentobarbital (Sigma-Aldrich Ltd, Gillingham, UK) in accordance with local animal welfare guidelines and A(SP)A 1986 (Animals for Scientific Procedures Act 1986). Immediately after confirmation of death, a catheter was inserted into the caudal vena cava to allow flushing of the pulmonary circulation with 20 – 30 cm^3 heparin 100 IU/cm^3 (Wockhardt UK Ltd, Wrexham, UK) in 0.9% saline solution (Baxter Healthcare Ltd, Thetford, UK) followed with phosphate buffer solution (PBS, Sigma-Aldrich Ltd, Gillingham, UK) in order to remove residual blood from the pulmonary circulation.

The heart and lungs were removed *en masse*. A polytetrafluorethylene (PTFE) adapter tube was inserted 5 - 10 mm above the carina and sutured into place. The heart and lungs were suspended in 5% glucose solution (weight/volume) with the trachea pointing downwards in a custom-built acrylic ventilation chamber, as detailed in Fig. 1. The *ex vivo* lungs were repeatedly inflated with 8 - 10 cm^3 of room air to check for leakage either from the suture around the trachea or the lungs themselves. For the presented work the lung harvesting procedure was completed with 100% success of removing the lungs intact. Normally with a skilled operator the *ex vivo* technique results in over 90% of lungs being suitable for imaging. The lungs were chilled to 278 K for transportation to the imaging facility.

3. Results and discussion

The pure gas phase relaxation time of ^{83}Kr is sufficiently long with T_1 times of several minutes at ambient pressure [16] to permit hp gas extraction and transfer. However, as the ^{83}Kr relaxation is accelerated by the presence of surfaces, the contact of the hp gas with any material during this process needs to be minimized. Pumps, that have been used for extraction and compression of ^{3}He after metastable exchange optical pumping (MEOP) [22], typically require many compression cycles to transfer the entire hp gas volume [22-25]. For the extraction and compression of the quadrupolar hp ^{83}Kr a pneumatically operated piston within a large volume cylinder was designed that used a single extraction – compression cycle as shown in Fig. 1.

This design is conceptually similar to the gas pressure driven 'syringe' using a Teflon piston as applied previously by Rosen et al. [26] for the transfer of hp ^{129}Xe following cryogenic gas separation. However, the extraction unit in this work needed to attain vacuum conditions of less than 0.2 kPa prior to hp gas extraction from the SEOP cell and, following extraction, was required to compress the hp gas to ambient pressure. Therefore, this unit operates at a high pressure differential and an O-ring seal equipped acrylic piston provides gas tight isolation of the two compartments of the extraction unit. The setup allowed for the extraction of about 3/4 of the hp gas from the SEOP cell in a single expansion - compression cycle. The losses in polarization caused by compression, shown in Fig. 2a, were negligible at SEOP pressures above 75 kPa and were

still acceptable down to 50 kPa. Using a 25% krypton - 75% N_2 mixture for a SEOP duration of 8 minutes at a pressure of 50 kPa, the apparent spin polarization P_{app} = 2.9% was found after extraction and transfer of the hp gas into a sample cell as seen in Fig. 2.

For the MRI, an SEOP cell pressure of 90 – 100 kPa was used, even though the attained apparent polarization of P_{app} = 2.0% was only about 2/3 the maximum possible value (Fig 2a, red arrow). The higher SEOP pressure ensured that the quantity of the produced hp gas (i.e. 40 cm^3 hp gas at ambient pressure) was sufficient to match the actual inhaled volume and the dead volume in the gas transfer system.

After SEOP with isotopically enriched ^{83}Kr followed by extraction, compression, and delivery of the gas mixture into the (ambient pressure) storage chamber (V_B) located underneath the breathing apparatus, 8 cm^3 of the hp gas were inhaled by the excised lungs using the breathing apparatus shown in Fig. 1b and 1c (see also ref. [27]). The signal intensity was sufficient to provide anatomical details, such as the shape of the lung lobes and the distinction of major airways, using a variable flip angle (VFA) FLASH MRI protocol [28] without slice selection but also without signal averaging having SNR = 51 as shown in Fig. 2b. Further experimental details of the MRI protocol, animal usage and SEOP are described in the **Materials and methods** section.

After the addition of 3 mm slice selection to the VFA FLASH MRI protocol, the major airways could clearly be recognized in a single acquisition (i.e.

NEX = 1) as show in Fig. 3a. Furthermore, the obtained signal intensity was sufficient to permit the proof of principle study of ^{83}Kr SQUARE contrast in lungs. Fig. 3b – 3d show the same 3 mm slice selective hp ^{83}Kr images as Fig. 3a, but with a delay period t_d between inhalation and start of the image acquisition ranging from 0.5 s – 1.5 s (t_d = 0 s in Fig. 3a). A new bolus of hp ^{83}Kr was delivered for each of the images. As a clear trend observed directly in these four images (Fig. 3a – 3d), the signal originating from the major airways was less affected by the delay time than the rest of the lung. The cause for the slower relaxation was presumably the smaller surface to volume (S/V) ratio in the airways as opposed to the alveolar space.

Smaller airways were not resolved but contribute to the contrast observed in the MR images. Fig. 3e shows a T_1 relaxation time map obtained from the t_d dependent signal decay of each volume element in Fig. 3a – 3d. The longitudinal relaxation time (averaged over 20 voxel) for the trachea is T_1 = 5.3±1.9 s and T_1 = 3.0±0.9 s for the main stem bronchus. The relaxation times measured in lung parenchyma adjacent to the major airways and in the periphery of the lung are T_1 = 1.1±0.2 s and T_1 = 0.9±0.1 s respectively. The observed T_1 data are in reasonable agreement with previous, spatially unresolved bulk measurements of ^{83}Kr T_1 relaxation in excised rat lungs that also demonstrated that the addition of up to 40% of O_2 did not significantly alter the T_1 times [27].

SQUARE originates from surfaces but its effect is detected in the gas phase due to rapid exchange. It is however not known to what depth the alveolar surface, that is comprised of surfactant molecules and proteins, followed

by a water layer, cell tissue, and the vascular system (filled with phosphate buffer solution in this work), is probed by the SQUARE effect. The relaxation of the water dissolved krypton is too slow, i.e. T_1 = 100 ms at 298 K [29], to be a major contributor to the observed T_1 values in the alveolar region, given the small quantity of water dissolved krypton. SQUARE may therefore originate from a deeper layer (i.e. cell tissue) or from the outer surfactant layer. The answer to this question could have profound impact on potential usage of SQUARE for disease related contrast but its exploration is beyond the scope of this work.

As Figs. 2 and 3 demonstrate, the extraction technique from low pressure (90 – 100 kPa) SEOP cells works well, generating reproducibly P_{app} = 2.0% with a line narrowed laser providing 23.3 W of power incident at the SEOP cell. This resulted in an approximately 10 fold increase in MR signal intensity as compared to the previously published results on hp ^{83}Kr MRI in excised rat lungs [19]. An additional factor of 8.7 improvement in signal to noise ratio was achieved by using isotopically enriched to 99.925% ^{83}Kr gas. Not surprisingly for a spin system with P_{app} = 2%, the obtained resolution fell short compared to ventilation hp ^{129}Xe MRI. However, the ^{83}Kr signal intensity was strong enough to allow for surface sensitive contrast in excised lungs while retaining structural resolution. The voxel resolution obtained with the slice selective hp ^{83}Kr MRI is 0.80 X 1.27 X 3 mm^3, (SNR = 23.8 for t_d = 0 s) and is therefore similar to dissolved phase ^{129}Xe pulmonary MRI that uses the small fraction (typically 1 – 2%) of inhaled xenon dissolved in tissue and blood.

The applied laser power of 23.3 W (incident at the SEOP cell) can be increased significantly due to recent advances in solid state laser technology and may thus improve the quantity of the produced hp gas and its spin polarization. Larger volume SEOP cells could be used to produce larger quantities of hp gas volumes at lower pressures if the power density of the laser irradiation is maintained across the larger cross section. Alternatively, the volume of hp gas can also be increased if several SEOP units of the current cell size and laser power operate in parallel. The amount of hp gas needed per inhalation cycle may additionally be reduced by optimizing the ambient pressure storage container (V_B), consequently allowing for lower SEOP cell pressures that result in higher spin polarization with the current setup.

A potential drawback of the presented methodology is that the lungs may become contaminated by rubidium vapors during the rapid delivery of hp gas from the SEOP cell. Therefore, the extraction unit was tested at various locations for rubidium residues through pH measurements (ColorpHast). Although more elaborate testing is required, and it appears that most of the rubidium tends to condense in the tubing located before the extraction unit. The use of additional rubidium filters that make use of the high reactivity of the alkali metal may improve the situation further but was not explored.

4. Conclusions

Using improved hp ^{83}Kr production methodology, SQUARE MRI contrast was demonstrated between airways and alveolar regions. Lung pathology related contrast was not attempted as animal models of pulmonary disease were beyond the scope of this proof of concept study. However, the produced signal intensity will be sufficient to attempt disease specific contrast in pathophysiology and to explore whether hp ^{83}Kr is of supplemental diagnostic value to hp ^{3}He and hp ^{129}Xe MRI. The potential usage of hp ^{83}Kr as a novel contrast agent should be investigated for disorders such as emphysema where the lung surface to volume ratio (S/V) is reduced [30, 31], or generally for the broad spectrum of diseases which exhibit significant changes in lung surface chemistry, for example acute lung injury (ALI), acute respiratory syndrome (ARDS) [32] and cystic fibrosis (CF) [33]. Two final notes with regard to practicalities of hp ^{83}Kr MRI: (1) Krypton gas (natural abundance of 11.5% ^{83}Kr) is a renewable resource generated as a by-product of air liquefaction, available at approximately € 1 per liter (at ambient pressure). Unfortunately, isotopically enriched ^{83}Kr is costly (approximately € 4000/L) at the current low demand for production. (2) There are little toxicological concerns for future clinical applications as krypton is chemically inert and does not exhibit anesthetic properties at ambient gas pressure [34, 35].

5. Acknowledgments

This work was supported in part by the Medical Research Council under Grant No. G0900785 and by the Royal Society through the Paul Instrument Fund.

References:

[1] M.S. Albert, G.D. Cates, B. Driehuys, W. Happer, B. Saam, C.S. Springer, A. Wishnia, Biological Magnetic-Resonance-Imaging Using Laser Polarized Xe-129, Nature, 370 (1994) 199-201.

[2] H. Middleton, R.D. Black, B. Saam, G.D. Cates, G.P. Cofer, R. Guenther, W. Happer, L.W. Hedlund, G.A. Johnson, K. Juvan, J. Swartz, Mr-Imaging with Hyperpolarized He-3 Gas, Magn. Reson. Med., 33 (1995) 271-275.

[3] D. Raftery, H. Long, T. Meersmann, P.J. Grandinetti, L. Reven, A. Pines, High-Field NMR of Adsorbed Xenon Polarized by Laser Pumping, Phys. Rev. Lett., 66 (1991) 584-587.

[4] T.G. Walker, W. Happer, Spin-exchange optical pumping of noble-gas nuclei, Rev. Mod. Phys., 69 (1997) 629-642.

[5] B.T. Saam, D.A. Yablonskiy, V.D. Kodibagkar, J.C. Leawoods, D.S. Gierada, J.D. Cooper, S.S. Lefrak, M.S. Conradi, MR imaging of diffusion of He-3 gas in healthy and diseased lungs, Magn. Reson. Med., 44 (2000) 174-179.

[6] M. Salerno, E.E. de Lange, T.A. Altes, J.D. Truwit, J.R. Brookeman, J.P. Mugler, Emphysema: Hyperpolarized Helium 3 Diffusion MR Imaging of the Lungs Compared with Spirometric Indexes--Initial Experience, Radiology, 222 (2002) 252-260.

[7] A.L. Sukstanskii, M.S. Conradi, D.A. Yablonskiy, He-3 lung morphometry technique: Accuracy analysis and pulse sequence optimization, J. Magn. Reson., 207 (2010) 234-241.

[8] J. Parra-Robles, S. Ajraoui, M.H. Deppe, S.R. Parnell, J.M. Wild, Experimental investigation and numerical simulation of (3)He gas diffusion in simple geometries: Implications for analytical models of (3)He MR lung morphometry, J. Magn. Reson., 204 (2010) 228-238.

[9] A.J. Deninger, B. Eberle, M. Ebert, T. Grossmann, G. Hanisch, W. Heil, H.U. Kauczor, K. Markstaller, E. Otten, W. Schreiber, R. Surkau, N. Weiler, He-3-MRI-based measurements of intrapulmonary p(O2) and its time course during apnea in healthy volunteers: first results, reproducibility, and technical limitations, NMR Biomed., 13 (2000) 194-201.

[10] M.C. Fischer, Z.Z. Spector, M. Ishii, J. Yu, K. Emami, M. Itkin, R. Rizi, Single-acquisition sequence for the measurement of oxygen partial pressure by hyperpolarized gas MRI, Magn. Reson. Med., 52 (2004) 766-773.

[11] G.E. Santyr, W.W. Lam, J.M. Parra-Robles, T.M. Taves, A.V. Ouriadov, Hyperpolarized noble gas magnetic resonance imaging of the animal lung: Approaches and applications, J. Appl. Phys., 105 (2009) 102004.

[12] J.P. Mugler, T.A. Altes, I.C. Ruset, I.M. Dregely, J.F. Mata, G.W. Miller, S. Ketel, J. Ketel, F.W. Hersman, K. Ruppert, Simultaneous magnetic resonance imaging of ventilation distribution and gas uptake in the human lung using hyperpolarized xenon-129, Proc. Natl. Acad. Sci. U. S. A., 107 (2010) 21707-21712.

[13] B. Driehuys, G.P. Cofer, J. Pollaro, J.B. Mackel, L.W. Hedlund, G.A. Johnson, Imaging alveolar-capillary gas transfer using hyperpolarized Xe-129 MRI, Proc. Natl. Acad. Sci. U. S. A., 103 (2006) 18278-18283.

[14] M.S. Albert, D. Balamore, D.F. Kacher, A.K. Venkatesh, F.A. Jolesz, Hyperpolarized Xe-129 T-1 in oxygenated and deoxygenated blood, NMR Biomed., 13 (2000) 407-414.

[15] M.M. Spence, S.M. Rubin, I.E. Dimitrov, E.J. Ruiz, D.E. Wemmer, A. Pines, S.Q. Yao, F. Tian, P.G. Schultz, Functionalized xenon as a biosensor, Proc. Natl. Acad. Sci. U. S. A., 98 (2001) 10654-10657.

[16] D.M.L. Lilburn, G.E. Pavlovskaya, T. Meersmann, Perspectives of hyperpolarized noble gas MRI beyond 3He, J. Magn. Reson., (2012).

[17] G.E. Pavlovskaya, Z.I. Cleveland, K.F. Stupic, T. Meersmann, Hyperpolarized Krypton-83 as a New Contrast Agent for Magnetic Resonance Imaging, Proc. Natl. Acad. Sci. U. S. A., 102 (2005) 18275-18279.

[18] Z.I. Cleveland, K.F. Stupic, G.E. Pavlovskaya, J.E. Repine, J.B. Wooten, T. Meersmann, Hyperpolarized ^{83}Kr and ^{129}Xe NMR Relaxation Measurements of Hydrated Surfaces: Implications for Materials Science and Pulmonary Diagnostics, J. Am. Chem. Soc., 129 (2007) 1784-1792.

[19] Z.I. Cleveland, G.E. Pavlovskaya, N.D. Elkins, K.F. Stupic, J.E. Repine, T. Meersmann, Hyperpolarized Kr-83 MRI of lungs, J. Magn. Reson., 195 (2008) 232-237.

[20] J.S. Six, T. Hughes-Riley, K.F. Stupic, G.E. Pavlovskaya, T. Meersmann, Pathway to Cryogen Free Production of Hyperpolarized Krypton-83 and Xenon-129, PLoS ONE, 7 (2012) e49927.

[21] D.F. Cowgill, R.E. Norberg, Spin-Lattice Relaxation and Chemical-Shift of Kr-83 in Solid and Liquid Krypton, Phys. Rev. B, 8 (1973) 4966-4974.

[22] R.S. Timsit, J.M. Daniels, E.I. Dennig, A.K.C. Kiang, A.D. May, An Experiment to Compress Polarized 3He Gas, Can. J. Phys., 49 (1971) 508-516.

[23] J. Becker, W. Heil, B. Krug, M. Leduc, M. Meyerhoff, P.J. Nacher, E.W. Otten, T. Prokscha, L.D. Schearer, R. Surkau, Study of Mechanical Compression of Spin-Polarized He-3 Gas, Nucl. Instrum. Methods Phys. Res. Sect. A-Accel. Spectrom. Dect. Assoc. Equip., 346 (1994) 45-51.

[24] T.R. Gentile, G.L. Jones, A.K. Thompson, R.R. Rizi, D.A. Roberts, I.E. Dimitrov, R. Reddy, D.A. Lipson, W. Gefter, M.D. Schnall, J.S. Leigh,

Demonstration of a compact compressor for application of metastability-exchange optical pumping of He-3 to human lung imaging, Magn. Reson. Med., 43 (2000) 290-294.

[25] H. Imai, J. Fukutomi, A. Kimura, H. Fujiwara, Effect of reduced pressure on the polarization of Xe-129 in the production of hyperpolarized Xe-129 gas: Development of a simple continuous flow mode hyperpolarizing system working at pressures as low as 0.15 atm, Concepts Magn. Reson., Part B, 33B (2008) 192-200.

[26] M.S. Rosen, T.E. Chupp, K.P. Coulter, R.C. Welsh, S.D. Swanson, Polarized Xe-129 optical pumping/spin exchange and delivery system for magnetic resonance spectroscopy and imaging studies, Rev. Sci. Instrum., 70 (1999) 1546-1552.

[27] K.F. Stupic, N.D. Elkins, G.E. Pavlovskaya, J.E. Repine, T. Meersmann, Effects of pulmonary inhalation on hyperpolarized krypton-83 magnetic resonance T-1 relaxation, Phys. Med. Biol., 56 (2011) 3731-3748.

[28] L. Zhao, R. Mulkern, C.H. Tseng, D. Williamson, S. Patz, R. Kraft, R.L. Walsworth, F.A. Jolesz, M.S. Albert, Gradient-echo imaging considerations for hyperpolarized Xe-129 MR, J. Magn. Reson. Ser. B., 113 (1996) 179-183.

[29] R.K. Mazitov, K.M. Enikeev, A.V. Ilyasov, Magnetic-Resonance and Relaxation of Nuclei of Atomic Krypton in Liquid Solutions, Zeitschrift Fur Physikalische Chemie Neue Folge, 155 (1987) 55-68.

[30] W.M. Thurlbeck, Internal Surface Area and Other Measurements in Emphysema, Thorax, 22 (1967) 483-496.

[31] G.D. Massaro, D. Massaro, Retinoic acid treatment abrogates elastase-induced pulmonary emphysema in rats, Nature Medicine, 3 (1997) 675-677.

[32] A. Gunther, C. Siebert, R. Schmidt, S. Ziegler, F. Grimminger, M. Yabut, B. Temmesfeld, D. Walmrath, H. Morr, W. Seeger, Surfactant alterations in severe pneumonia, acute respiratory distress syndrome, and cardiogenic lung edema, Am. J. Respir. Crit. Care Med., 153 (1996) 176-184.

[33] J.J. Smith, S.M. Travis, E.P. Greenberg, M.J. Welsh, Cystic fibrosis airway epithelia fail to kill bacteria because of abnormal airway surface fluid, Cell, 85 (1996) 229-236.

[34] S.C. Cullen, E.G. Gross, The Anesthetic Properties of Xenon in Animals and Human Beings, with Additional Observations on Krypton, Science, 113 (1951) 580-582.

[35] A.-L. Hachulla, F.o. Pontana, L. Wemeau-Stervinou, S. Khung, J.-B. Faivre, B. Wallaert, J.-F.o. Cazaubon, A. Duhamel, T. Perez, P. Devos, J. Remy, M. Remy-Jardin, Krypton Ventilation Imaging Using Dual-Energy CT in Chronic Obstructive Pulmonary Disease Patients: Initial Experience, Radiology, 263 (2012) 253-259.